Motto:

"Writing is not like painting where you add. It is not what you put on the canvas that the reader sees. Writing is more like a sculpture where you remove, you eliminate in order to make the work visible. Even those pages you remove somehow remain."

Elie Wiesel (1928 – Rumanian-born American Writer)

DECLARATION

This Thesis titled "Microscopic Characterisation of Photonic Devices" is a report on research conducted by the author at Victoria University from January 1999 to January 2004 under the supervision of Associate Professor Gregory Baxter and Associate Professor Ann Roberts. This is my own work and has not been submitted previously, in whole or in part in respect of any other academic award.

Copyright in all images and text is retained by the Author and reproduction is governed by the *Copyright Act 1968 (Cth)*.

I declare that this thesis is less than 100,000 words in length, inclusive of tables, maps, bibliographies, footnotes and appendices.

This thesis was prepared using Microsoft Word for Windows98, version 4.0 on a Compaq Laptop Computer PC, including automatic equation, figure numbering and integrated bibliography management. This choice was due to facility importing high quality TIFF images and bibliography management system such as EndNote (version 5.0). Illustrations were created using Adobe Illustrator 9.0 and imported as TIFF images, whilst all graphs were produced using MICROCAL ORIGIN 6.0 and MAPLE 6.

Nicoleta M. Dragomir

Submitted: Wednesday, 10 march 2004

Emended: Friday 19 November 2004

AKNOWLEDGMENTS

There may be only one author credited on the title page of this dissertation but it would never have been completed without the support of many people I have had the fortune to know. The number of years spent at Victoria University in particular at the Optical Technology Research Laboratory (OTRL) have had their low and high points (though happily many more of the latter) and has been a blessing to have been surrounded by great friends with whom to share the moments.

The goal of a PhD program is not only to accomplish specific research goals but also to train one as a scientist. Special thanks go to Assoc. Prof. Gregory Baxter whose supervision style gave me the support and patience that has contributed to this second goal. I thank him for the generous gift of his time, for constant encouragements and astonishing speed in reading the nearly finished product when time was short. In addition he has entrusted me tremendous amount of freedom to set my own goals and seek my own solutions to problems whilst at the same time has always been approachable and encouraging when I got stuck.

I owe a huge debt of gratitude to Assoc. Prof. Ann Roberts of University of Melbourne, who acted as a second supervisor over the past two years and whose energy and sense of fellowship has been everything one could wish for in an advisor. She provided sound academic guidance throughout and introduced me to the world

of science. She served as an example and an inspiration in ways extending beyond the academic, and I owe an inestimable debt for her patience and kindness.

I am very privileged to record my thanks to my former supervisor, Dr. Peter Farrell, for constantly brainstorming me and for his original mixture of personal independence and upfront supervision. Chapter four on refractive index reconstruction is the result of detailed collaboration with Peter without whom it would not have materialised into the form it has.

It is a pleasure to record my gratitude to the members of the OTRL community in general for their good humour and helpful suggestions. In particular I would like to express my appreciation of help given to me by Dr. Scott Wade starting with the period when he was a research fellow at City University in London and then continuing with the time when he came back at OTRL. In addition to manufacturing some of the Bragg gratings investigated in this Thesis, he has also prepared the annealed optical fibre samples. Also appreciated is Dr. Darol Garchev's contribution for manufacturing the very first Bragg grating samples investigated during this work. Many thanks go to Mr. Donald Ermel for the construction of the fibre rotation mount, to Mr. Hayrettin Arisoy for his contribution to the temperature controlled system for this mount, and to Ms. Claire Rollinson for her patience in using this gear during her Honours year. Chapter five of this thesis could not have existed without the direct contribution of all these people and the resources they brought to bear on the problem.

The department has been a very warm and friendly place, and fellow students I met here have helped me along the way. The administrative and technical personnel are greatly appreciated: Mr. Alex Shelamoff, Mr. Abdurrahman Kuzucu, Mr. Hayrettin Arisoy for their invaluable involvement in the project and in particular for their

support throughout the third year labs. My very sincere thanks go to Ms. Maria Pylnyk for her unending cheerful presence.

I had the valuable opportunity to work with Dr. Gerard Monnom of University of Nice, France, and am grateful for providing me with some special fibre samples, including the Bragg fibre, and for many illuminating discussions during his visit at OTRL.

I thank Ms. Coral Ware for her patience in successfully solving all the "little challenging tasks" required during the literature search and to Ms. Claire Rollinson and Ms. Angela Rojter for reading parts early drafts of this Thesis and for their constructive comments.

Thanks also go to Ms. Magda Michna and to Mr. Eric Ampem-Lassen of University of Melbourne for their collaboration on the project during their Phd candidature. Having the opportunity to share ideas with them was a refreshing and fascinating experience from which all of us benefited.

I have also been fortunate to benefit from a Victoria University Postgraduate Scholarship Programme that generously provided financial support for this research. I thank Assoc. Prof. Neil Barnett, the Former Head of School of Communications and Informatics for supporting my candidature. In addition I am most grateful to Head of School of Electrical Engineering Assoc. Prof. Aladin Zayegh and Assoc. Prof. Stephen Collins, for providing me with the opportunity to act as coordinator of the third year optics laboratory in my final stage of the Ph.D candidature.

I also extend my gratitude and admiration to all my teachers throughout my early educational years for bringing inspiration and passiong on the passion for science and mathematics.

Last but not least, millions of thanks go to the most two significant people in my life: my husband, Sever and my son, Sergiu, who have provided me with their unfailing support and belief in me through the many stages of this candidature process. Their love has been the source and the strength of my life. Sever has been patient with me in my moments of self-doubt and hesitation and he has spent countless hours alone during the past years enduring the final stages of the process, often only watching from distance as I pondered over each word, each comma, and each turn of phrase. He has been the kind of support that any PhD student would wish for, and more. His loving support, incessant cheerfulness and excellent cooking skills never failed to brighten up even the most difficult of thesis-writing days. Words cannot express neither my gratitude nor my love for him.

In all cases my contribution to these collaborations was substantial and direct, and unless otherwise stated in the text, the work presented in this Thesis is the product of my own work.

Nicoleta Dragomir

Victoria University of Technology, Melbourne
Friday 19 November 2004

ABSTRACT

The work presented in this thesis sets out to explore the optical properties of optical fibres by means of non-invasive microscopic techniques such as Differential Interference Contrast (DIC) microscopy. It seeks to provide the fibre optic industrial and research community with an alternative tool that is cost effective, having the accuracy and robustness of the existing techniques in addition to being non-destructive relative to the optical fibre. The development of non-invasive microscopic imaging methods for exploring the physical properties of optical fibres is essential as alternative methods to the well-known standard ones that are often destructive.

Accurate knowledge of physical properties of actual fibers is critical for the development of more sophisticated devices. In addition there are specific areas of optical fibre technology, such as the fabrication of optical fibre Bragg gratings that benefit from this research. Currently manufacturers of fibre Bragg gratings are largely limited in their knowledge by information obtained from performance characterization.

This Thesis has researched the possibility of non-destructively reconstructing the refractive index profile of an optical fibre by means of DIC microscopy. For this purpose calibrations of critical elements of the microscope that are essential for

refractive index reconstruction have been performed. Furthermore sensitivity of DIC imaging of an optical fibre to various parameters, such as the refractive index of the embedding immersion fluid, and the fibre orientation in the field of view of the objective have also been investigated.

The results provide evidence that DIC is a powerful research tool in studying the refractive index of optical fibres; in particular it may be adequate for small core diameter optical fibres. The reconstruction method uses an analytical approach based on the Leibniz theorem in conjunction with knowledge of the geometry of the fibre and of the imaging elements of the microscope.

The refractive index profile of various optical fibres, such as the SMF-28, FSS and DCI-PBG, has been obtained from the analysis of DIC images of these fibres. Notable was that the reconstructed refractive index profile of the studied fibres was in very good agreement with the one obtained by alternative methods. Of importance was the measurement of the refractive index changes of optical fibres used in fluorescence-based temperature sensing which have been subjected to annealing.

A major contribution of this work is the framework and methodology proposed and implemented in relation to the non-invasive imaging of an in-fibre Bragg grating (FBG). The methodology is in fact a novel application of DIC imaging to direct visualization of an FBG, in particular the imaging of a Type I FBG, which has never imaged before due to its very low refractive index variation, which makes it difficult to be imaged with virtually any other technique.

FBGs characterization is generally based on the assumption that they are uniformly distributed as planes across the fibre core and as such the refractive index modulation can be described by a one-dimensional model in the axial direction of

the optical fibre. The measurements performed on Type I FBGs, written by a phase mask method, presented in this work demonstrate for the first time a complex structure within the FBG. By taking two orthogonal images of the same FBG it was unveiled that the grating has a periodicity in both axial and radial directions; and that the axial direction has a periodicity equal with that of the phase mask pitch whilst the radial periodicity is related to the so called Talbot diffraction pattern. Further, this structure is normally due to the interference of the diffracted orders coming from the phase mask suggesting that there is a relationship between the beating orders.

The work presented in this Thesis provides an invaluable framework for future investigations of fibre Bragg gratings of various types. The results obtained so far may be useful in explaining birefringence effects observed by other groups of researchers in particular in the strain sensors area. Having knowledge of the internal structure of an in-fibre Bragg grating may also lead to improved and more versatile intragrating sensing using FBGs. Work on discovering FBG's three-dimensional structure is ongoing.

TABLE OF CONTENTS

Declaration ii

Aknowledgments iii

Abstract vii

Table of Contents x

List of Figures xv

List of Tables xxviii

1 Introduction 1

1.1 Overview 1

1.2 Problem Statement (Rationale) 1

1.3 Significance of the Study 3

1.4 Solving the Problem 5

1.5 The Objectives of the Research 5

1.6 The Structure of the Thesis 6

2 A Review of Refractive Index Profiling of Optical Fibres 9

2.1 Overview 9

2.2 The Optical Fibre: General 9

2.2.1 The Operational Characteristics of Optical Fibres *11*
2.3 Refracted Near Field Technique 15
2.4 Atomic Force Microscopy 18
2.5 Near Field Scanning Optical Microscopy 19
2.6 Quantitative Phase Microscopy 20
2.7 Interference Microscopy - Axial Interferometry 24
2.8 Transverse Interferometric Methods 26
2.8.1 The Phase Stepping Technique *28*
2.8.2 Variable-Wavefront Interferometry *29*
2.9 Summary 33
3 Aspects of the Research Method 37
3.1 Overview 37
3.2 Data Acquisition 37
3.3 Differential Interference Contrast Microscope Operation 40
3.3.1 Principle of Differential Interference Contrast Imaging *41*
3.3.2 Optical Components of a Differential Interference Contrast Microscope *43*
3.4 Calibration of the Microscope 45
3.4.1 Sliding Wollaston Prism Calibration *46*
3.4.2 Wavefront Shear Characterisation *47*
3.5 Sensitivity Measurements in a Differential Interference Contrast Imaging System 58
3.5.1 Sensitivity of DIC Imaging to Refractive Index of the Immersion Fluid *59*
3.5.2 Sensitivity of DIC Imaging to the Orientation of the Fibre *65*
3.6 Summary 66
4 Estimation of the Refractive Index 68
4.1 Overview 68
4.2 The Imaging Model 68

4.3 Recovering Refractive Index from DIC Images of Optical Fibres.....71
4.3.1 Sample Selection.....*74*
4.3.2 Experimental DIC Images of Optical Fibres.....*75*
4.3.3 Reconstructed Refractive Index of Optical Fibres.....*78*
4.4 The Bragg Fibre.....81
4.5 Annealing Effects in Optical Fibres.....85
4.6 Accuracy Considerations.....91
4.7 Summary.....93
5 Fibre Bragg Grating Characterisation 96
5.1 Overview.....96
5.2 The Optical Fibre Bragg Grating.....97
5.3 Refractive Index Change.....99
5.3.1 Photosensitivity.....*101*
5.3.2 Classification of Fibre Bragg Gratings.....*105*
5.4 Fabrication of Fibre Bragg Gratings 117
5.5 Characterisation Methods 121
5.5.1 Direct Methods *122*
5.5.2 Scanning Electron Microscopy *123*
5.5.3 Atomic Force Microscopy *125*
5.5.4 Scanning Near-Field Optical Microscopy.....*127*
5.5.5 The Half-Shade Polarising Technique.....*129*
5.5.6 Indirect Methods *132*
5.6 Measurement of the Index Modulation along an Optical Fibre Bragg Grating 146
5.6.1 Optical Sectioning of a Fibre Bragg Grating.....*153*
5.7 Diffracted Field Produced by a Phase Mask.....164

5.8 The Talbot Effect – The Repeated Self-Imaging of a Diffraction Grating 170
5.9 Summary 177
6 Concluding Remarks 180
6.1 Summary of Research Presented in this Thesis 180
6.2 Directions for Further Work 183
6.2.1 Improving Quality of Images 184
6.2.2 Quantifying the Thermal Diffusion Processes: Fusion Splices 185
6.2.3 Quantify the Shear Modulus of Optical Fibres 186
6.2.4 Periodicity of Light in Three Dimensions 186
6.2.5 Bragg Grating Resonance 186
6.2.6 Fibre Bragg Gratings Birefringence 188
6.2.7 Multipeaked FBG 189
6.3 Summary 190
7 Appendices 191
7.1 Appendix A: Sample Preparation and Mounting 191
7.1.1 Choice of Optical Fibres 191
7.1.2 Stripping the Plastic Jacket 193
7.2 Appendix B: Plane-Wave Expansion 194
7.3 Appendix C: Diffraction Pattern in a Defocused Plane 196
7.4 Appendix D: Fresnel-Kirchhoff Formulation of Talbot Effect 199
7.5 Appendix E: Characterisation of the Phase Mask 201
7.6 Appendix F: The Temperature Controlled Rotation Stage 204
7.7 Appendix G: Companion Publications 208
8 Glossary, Symbols and Acronyms 211
8.1 Glossary of Terms 211
8.2 Symbols 217

8.3 Abbreviations 218

9 References 220

LIST OF FIGURES

Figure 2.1. Schematic diagram of a typical optical fibre in cross-section. (Figure after Future Fibre Technologies Pty.Ltd. http://www.fft.com/backgrnd.html). 10

Figure 2.2. Ray trace of the light propagating in a refracted ray scanner. The basic components are the photodetector (PD), condensing lens (Cond), opaque stop (OS), index matching block (IB) with index n_6, specimen with index $n_4(x, y)$, index matching fluid (IF) with index $n_3 = n_5$ and coverslip (CS) with index n_2..... 17

Figure 2.3. Schematic representation of the sub-wavelength aperture used in near-field scanning optical microscopy..... 19

Figure 2.4. The mounting system used in the TIE imaging technique of an optical fibre (after (Barty 2000)) . The fibre sample has been placed in a pool of matching index fluid formed between two other identical fibres located on either side to ensure the parallelism between the cover slip and the microscope slide. 22

Figure 2.5. Sample arrangement used to observe tilted fringes in a reflected microscope with monochromatic light. Fringes are formed by reflection from the top mirror bottom surface and the bottom mirror top surface. The resultant interference pattern is that of a wedge, modified by the refractive index variation of the optical fibre..... 25

Figure 2.6. Transverse ray tracing through the inhomogeneous rod-like medium of unit radius. The test object is characterized by a radially symmetric index profile *n(r)* related to the function $u(r) = n(r) \times r$. 27

Figure 2.7. Optical System of the Pluta interference microscope with continuous variable wavefront shear. Notations are as follows: polarisers P, A; half-waveplates H_1, H_2; Wollaston prisms W_1, W_2; compensator Wollaston prisms Q_1, Q_2; Objective Ob; condenser C and object plane OP. 31

Figure 2.8. The liquid wedge interferometer used in multiple-beam Fizeau fringe in transmission and the produced interference fringe shift. Both the wedge angle ε and the interferometric gap thickness t are adjustable in order to produce sharp parallel fringe perpendicular to the fibre axis. 32

Figure 3.1. The measurement system. The microscope is an inverted Olympus FluoView IX Infinity Corrected Optical System, equipped with high resolution Nomarski optics. The photomultiplier tube is coupled to the microscope via a fibre bundle. The image output is converted to numerical format and recorded on a computer NT workstation. The computer controls the fine focus of the microscope in the *z*-direction via a piezo-stepper motor. The stepper motor translates the objective of the microscope in *0.1* μ*m* increments along the optical axis. 39

Figure 3.2. Interference between two monochromatic coherent light waves. The resultant intensity, as measured by the detector, reaches a maximum amplitude (I_M) when the two waves are in phase ($\Delta\phi=0$), and a minimum (I_m) when the waves are π out of phase due to the detector dark current. 41

Figure 3.3. An example of imaging of a simple object through a DIC microscope. ϕ_1 and ϕ_2 represent the two wavefronts resulting from the object shifted with respect to each other as a result of the lateral shear introduced by the microscope. The intensity as seen in the DIC image is dependent on the phase difference between these two wavefronts. 42

Figure 3.4. Schematic of DIC configuration in the Olympus IX inverted microscope. The DIC microscope is equipped with special optics that convert phase differences to amplitude differences: the polariser and analyser that create the necessary conditions for interference, and two Wollaston prisms that split and then recombine the illuminating beam into two components separated at the specimen's plane by a very small lateral shear. The orientation of the analyser is set such that its direction of light vibration is at 90° with respect to the polariser's direction of vibration, in other words the polars are crossed. The sliding Wollaston prism is placed such that its fringes are in the front focal plane of the objective lens. When the two prisms are perfectly aligned, as illustrated here, then the bias retardation between the two components of the sheared beam is zero. A translation of the sliding Wollaston prism (illustrated by the red arrow) along the direction of the shear produces a nonzero bias value. 44

Figure 3.5. Effect of the slider prism position on intensity. The microscope was set up to image an apparently empty volume of the specimen with crossed polarisers. Intensities were measured as a function of slider prism position and averaged over a *512* × *512* (*0.28* μm pixel size) region. The slider has been advanced 20 steps per turn. 46

Figure 3.6. Determination of shear of the *40* × */0.85* - *NA* lens. (a) An enlargement of a DIC image of a polystyrene microsphere (*365 nm* in diameter) in monochromatic light of *488 nm* with bias setting equal to $\pi/2$ radians. The DIC image was enlarged using linear interpolation for display purposes and shows a bright and dark spot at the edges of the bead. The direction of the shear is along the *135* degree angle. (b) Line profile along the shear direction. The lateral shift (shear) introduced by the microscope is determined by measuring the distance between the centre of the bright spot and the centre of the dark spot.....49

Figure 3.7. The experimental arrangement for the collection mode NSOM utilizing a stepper motor for controlling the objective probe separation. No cover slip was present in the focal region of the objective.....51

Figure 3.8. (a) Separation of the polarisation states after propagation of a Gaussian beam through the polariser, the Wollaston prism and the objective; measured optical intensity from scans in the axial plane using a near field probe. (b) Cross sectional profile along the shear direction; solid line plots the measured intensity profile; dashed line plots the Gaussian fit.....52

Figure 3.9. Schematic representation illustrating the geometry of the collection near-field optical setup. The plane of scanning is represented by the dashed arrow and is situated at a height z_s from the focal plane. The two propagating fields, orthogonal to each other, are represented by $\mathbf{E_1}$ and $\mathbf{E_2}$ respectively. 53

Figure 3.10. Calculated light field intensity in a differential intensity microscope: (a) in focus; (b) out of focus at a distance ~*0.6* μ*m* from the focal plane. (c) and (d) intensity plot contours of the diffraction pattern displayed in (a) and (b) respectively, showing equal strength beams. The distance between the centres of the two bright spots, in each case, is equal to the lateral shear s. The direction of the shear was considered to be along the *135*-degree angle. The scale bar is approximately *1* μ*m*. 58

Figure 3.11. Effect of refractive index of the embedding fluid in the measured DIC image of an optical fibre. The far right column shows a line profile through the middle of the images on the far left. The images presented here are raw, uncorrected for the characteristic non-uniform illumination of DIC imaging therefore in the intensity line profile one can easily observe a linear intensity component near the axis of the fibre.....62

Figure 3.12. Effect of temperature change on the DIC image of an optical fibre in the case of very well index matched situation. The measurements were taken at *24.10* ºC and at *29.40* ºC in figure (a) and (b) respectively with the fibre immersed in index

matching oil $n_{O2} = 1.4576$. A plot profile of the normalised intensity shows little difference for the two measurements. Here the presence of some horizontal lines degrades the quality of the images, it is believed that they are caused by the aliasing of the scan period with periodic fluctuations in the laser. 64

Figure 3.13. Measured DIC images of an optical fibre. Images were acquired with a $40 \times /0.85 - NA$ and a $0.55\ NA$ condenser with the aperture partially closed at different orientations of the fibre. (b) the fibre is rotated by 45 degrees clockwise from position (a); (c) the fibre is rotated by 45 degrees clockwise from position (b); (d) the fibre is rotated by 45 degrees clockwise from position (c). The section images are cuts through the three-dimensional images and are at the best focus of the objective lens. The horizontal lines are possible due to aliasing of the scan with the periodic fluctuations in the laser; they disappeared after the laser has been changed. 66

Figure 4.1. (a) Diagram of the cross sectional area of a uniform cylindrically symmetric optical fibre in oil and (b) the DIC image intensity when focussed in the plane containing the fibre centre; r_c represents the core radius, R represents the fibre radius. The refractive index of the oil is temperature controlled and matches the refractive index of the clad. A and B are defined in the text. 72

Figure 4.2. (a) The refractive index profile of 3M-FSN -3224; (b) Phase profile recovered by QPM phase imaging technique (after (Barty 2000)). 74

Figure 4.3. Panel (a) shows the measured DIC image of the central region of the SMF-28 optical fibre acquired with an Olympus UplanApo $40 \times /0.85$ - NA dry lens. The scan area is $36 \times 36\ \mu m$. The minimum and maximum intensity in the image is mapped to black and white respectively. Panel (b) shows a horizontal line-profile through the above image. 76

Figure 4.4. A collection of four measured DIC images of optical fibres. The name of each fibre is indicated above its image. The images in each figure cover an area of 140×140 μ*m* along the fibre with an effective pixel size of 0.28×0.28 μ*m*. 77

Figure 4.5. Measured differential interference contrast image of the central region of the SMF 28 optical fibre acquired with a $40 \times /0.85$ - *NA* dry lens, 488 nm illumination wavelength. The scan area in (a) is 140×140 μ*m*; (b) represents the rectangular area outlined in (a); the dimension of the image is 36×36 μ*m*. The minimum and maximum intensity in each image is mapped to black and white respectively. Horizontal line-profiles through the images in (a) and (b) are plotted in (c) and (d) respectively. The horizontal lines evident in the image are possibly due to aliasing of the scan with the periodic fluctuations in the laser, they disappeared after the laser had been replaced. 78

Figure 4.6. Refractive index profile of the SMF 28 optical fibre reconstructed from DIC image presented in Figure 4.5. 79

Figure 4.7. Comparison of refractive index profiles of the refractive index obtained for FSS fibre using three different techniques. 80

Figure 4.8. (a) Cross-sectional view of a Bragg fibre. The fibre consists of a low-index core surrounded by a cladding formed by seven alternating layers of dielectric media of high and low refractive indices. (b) Refractive index profile of an ideal DCI-PBG fibre. 82

Figure 4.9 Quantitative comparison of the measured and computed DIC images of DCI-PBG fibre. (a) Measured DIC of the central region of the fibre representing a 140 μm × 140 μm transverse section of the fibre; (b) Modelled DIC image computed from the refractive index data of the preform from which the fibre has been drawn; (c) A comparison of profiles through the computed and real DIC images (continuous and dashed lines respectively). Note that the real and computed

DIC images are indistinguishable by eye, and that the line profile through both the images shows an excellent agreement. 84

Figure 4.10. Extraction of refractive index profiles from DIC data. Known and reconstructed index profile (preform and DIC lines respectively) for the DCI-PBG fibre 85

F 87

Figure 4.12. The effect of annealing on the refractive index profiles of (a) Yb^{3+}-doped fibre and (b) SMF-28™ fibre, obtained using DIC imaging. 89

Figure 5.1. Statistics showing the fibre Bragg gratings technologies are the most widely studied topic in the field of optical fibre sensors (Source: Lee, 2003). FOG refers to fibre optic gyroscopes. 98

Figure 5.2. Schematic representation of a fibre Bragg grating. (a) a straight short-period grating; (b) a slanted short-period grating; and (c) a long-period grating. The period of the grating is Λ. For the slanted grating the planes of the grating form an angle θ with the normal to the fibre axis (after ((Riant 2003)**).** 106

Figure 5.3. Refractive index dependence on UV fluence for Type I and Type IIA FBG written in high Ge-doped fibre. When the Ge-doped core is exposed to UV light the refractive index increases giving rise to, what is referenced in literature, a positive index change. With continued UV exposure the index change saturates and then starts decreasing. This later formation has been classified as Type IIA producing a so-called negative index change (after (Salik 2001)) 108

Figure 5.4. Spectral characteristics of a Type I Bragg grating (after (Othonos and Kalli 1999a)). 109

Figure 5.5. Spectral characteristics of a Type II Bragg grating (after (Archambault, Reekie and Russel 1993a)). The transmission spectrum shows that Type II gratings pass wavelengths longer than the Bragg wavelength, whilst shorter wavelengths are

coupled into the cladding. The reflection spectrum is broad showing complex resonance peaks. 110

Figure 5.6. A non-symmetric UV-induced refractive index into the photosensitive fibre core resulting from a left side exposure of the fibre (Renner 2001).....116

Figure 5.7. UV absorption spectra of a GeO_2:SiO_2 optical preform slice (~100 μm thick) before (Line (i) dashed) and after UV exposure line (iii) and (ii). Line (ii) and (iii) represent the absorption spectra around and after 30 min of UV exposure respectively (Atkins, Misrahi *et al.*, 1993). 116

Figure 5.8. Schematic of the phase mask method used for the production of the fibre Bragg gratings. The coherent UV beam splits at a zeroth-order nulled phase mask (approx *3.5%*). The resulting beams, predominantly contained in the +1 and -1 diffracted orders, with approximately 38% of the total light intensity found divided in the two orders, interfere to produce the periodic pattern that photoimprints the gratings in the optical fibre. The phase mask period determines the grating period: if the period of the phase mask grating is Λ, the period of the photo-imprinted index grating is Λ/2. 119

Figure 5.9. Schematic diagram illustrating the configuration in the NPL microscope for measuring birefringence. The circle at the top of the diagram represents the field of view as it appears to the observer; a small rotation, θ, of the quarter-wave plate produces unequal intensities into the hemispheres (after (Raine, Feced *et al.* 1999)). 130

Figure 5.10 Schematic representation of the side-diffraction Bragg grating characterisation system (source (Krug, Stolte and Ulrich 1995)).....137

Figure 5.11. Schematic configuration of an OLCR Bragg grating characterization system (after (Hui, Thomas *et al.* 2003)). The setup is basically a Michelson interferometer with a movable reference mirror in the reference arm, and the device under test, i.e. the FBG, in the test arm.....139

Figure 5.12. Schematic configuration of an OSDR Bragg grating characterisation system (after (Brinkmeyer, Stolze and Johlen 1997)). The light from a tunable laser diode is launched into the grating under test. A localised phase shift is produced at position z_s, by heating the grating with a focused He-Ne laser beam, which is also moved along the grating of length L. The He-Ne light is chopped at a certain frequency and the light from the grating is synchronously detected. 140

Figure 5.13. Schematic diagram of the phase mask system used to record and measure Bragg gratings. The optical source to illuminate the FBG was a Laser diode pumped Amplified Spontaneous Emission EDFA. Light transmitted through the grating is fed to the optical spectrum analyser through an optical coupler. The unused ports of the grating fibre and the optical coupler are index matched to avoid light reflected at the fibre-air interface. 147

Figure 5.14. Spectral transmittance of a fibre Bragg grating (coded FBG1-DG1) fabricated in standard telecommunications fibre that was pre-soaked in hydrogen (~2.5 mol. %). The UV light source was a 244 nm CW laser and the phase mask had a 1.06 μm pitch. The transmission spectrum exhibits some loss on the low-wavelength side of the Bragg wavelength.....150

Figure 5.15. Measured DIC image of the fibre core with a blazed Bragg grating (FBG1-DG1). The tilt of the grating determine the coupling efficiency and the bandwidth of the light that is tapped out. 151

Figure 5.16. Line profile from four gratings imaged in Figure 5.11. 153

Figure 5.17. Schematic of the light path through sample in the DIC microscope used.....154

Figure 5.18. The sectioning property of DIC imaging containing a FBG is clearly evident in this stack of 12 consecutive horizontal sections through the fibre. The sections are separated by *0.8* μ*m* and represent a scanned area of *35* × *35* μ*m*. The top left section was taken from the bottom of the fibre while the bottom right image

is from the top, as light travels from the bottom to the top. Note that all the images are raw data - no image processing has been performed (Dragomir, Roberts *et al.* 2002).....156

Figure 5.19. Measured DIC images of FBG2-DG2 with different axial orientation of the fibre. The images are *145* × *157* pixels and *140* × *150* pixels respectively with *0.069* μ*m* pixel size. The second image is obtained by rotating the fibre approximately *90* degrees from position 1.....158

Figure 5.20. Evolution of the transmission spectra of Bragg grating labelled FBG-CR1 with exposure time. A noticeable change in transmission at around 1534.17 nm was observed after 1.48 min exposure, then the reflectance increases significantly with further exposure whilst the centre Bragg resonance shifts towards longer wavelengths. The peak reflectivity of approximately 97 % at 1534.46 nm has a spectral width of 0.5 nm.....159

Figure 5.21. Reflectance and refractive index modulation of grating FBG3 - CR1 at different UV radiation time. The nearly linear response of the refractive index modulation with increasing exposure time is a characteristic of Type I gratings.160

Figure 5.22. Schematic diagram identifying the direction of the microscope beam used for the images represented in Figure 5.22.....161

Figure 5.23. Measured DIC images of the core region containing the FBG l - CR1 Bragg grating, recorded for two different fibre orientations. (a) The fibre position has been selected so that the image is taken from a direction parallel to that of the writing UV laser beam.; (b) The same FBG as in (a) recorded after the fibre has been rotated by *90* degrees about its axis. The images' dimensions are *1024* × *1024* pixels covering *47* × *47* μ*m*; *x* and *z* represents distance across and along the fibre respectively. (c) and (d) The intensity distribution for a region of approximately 130 μm^2 within the core of the fibre represented in panels (a) and (b) respectively. The

contour graph displayed on the bottom plane of both panels (c) and (d) clearly emphasises the different features observed in panels (a) and (b). 162

Figure 5.24. Line profile through grating represented in Figure 5.22a showing a period of the grating equal with that of the phase mask used for grating fabrication. 164

Figure 5.25. Diffracted field distribution in a plane parallel with an ideal phase mask (i.e. only the interference of the ± 1 orders is present) for an illumination wavelength of $\lambda = 244\ nm$ having a line width of $\Delta\lambda = 1$ nm. (a) and (b) are two examples of finite spatial coherence less then 300 μm having the beam incidence divergence of $\Delta\phi = 1.6$ and $2\ mrad$ respectively. (c) Beam incidence divergence of $\Delta\phi = 0.85\ mrad$, characteristic to our FBG writing conditions, in which case the spatial coherence length is approximately $606.97\ \mu m$. (d) As the above but with perfect spatial coherence $\Delta\phi = 0$. Distances x and y are measured in μm units while the intensity, normalized to unity is expressed in arbitrary units.....166

Figure 5.26. Fringe visibility as a function of the incident beam divergence. Evidently for a perfect spatial coherence at the mask, i.e. divergence → 0 the fringe visibility is the highest. A spatial coherence length of approx 600 μm characterized the illumination light used to write gratings for this work.....167

Figure 5.27. Fluence distribution in a plane parallel to the surface of a phase mask with various order efficiencies. (a) Excluding the zeroth order and having 48% in the first-order; (b) first-order as in (a) and including a very small zeroth order and second order of 0.05% and 1.5% respectively; (c) similar strength of the zeroth and second order contributions of 8% but having the first-order of 38%; (d) 5% in the zeroth order, 37% in the first and 10% in the second orders – characteristic to the phase mask used for FBG writing in this work. Units for x and z are expressed in μm.169

Figure 5.28. (a) Diffraction geometry from a grating. The Talbot effect occurs in the region where the diffracted orders overlap, the shaded region in (b). (b) Geometrical

representation of the region over which the Talbot effect occurs due to the coherent overlapping of the diffracted orders illustrated in (a). $\delta = \lambda / \Delta\phi$ represents the spatial coherence length at the grating; $\Delta\phi$ is the incident beam divergence. 173

Figure 5.29. Numerically calculated intensity for the propagation of the optical field diffracted from a 1.06 μm period grating in free space. The images show a 5 × 5 μm free area space, representing the corresponding diffraction pattern for various distances from the grating, (a) z=35 to 40 μm, (b) z = 60 to 65 μm. The pattern's repeat distance is 3.05 μm. The phase mask is along the bottom of the image. 176

Figure 5.30. Cross-section of Figure 5.28b along the phase mask through fringes corresponding to (a) z = 61.2 μm and (b) z = 62.725 μm. The distance x is expressed in μm. 176

Figure 5.31. Cross-section of Figure 5.28b normal to the phase mask through two sets of Talbot peaks. The distance z is expressed in μm. 177

Figure 6.1. Transmission spectra of a Bragg reflector extended over the spectral range *600* nm to *1600* nm (after (Malo, Johnson et al. 1993)). The transmission dips that occur at *1535, 1030, 770* and *620* nm suggest a period of the grating equal to that of the phase mask.....187

Figure 7.1 . Measured transversal (*x - y*) image through a *1.06* μm period.....202

Figure 7.2. Measured axial *(x - z)* image through a 1.06 μm period phase mask demonstrating the Talbot diffraction pattern at 488 nm wavelength. The image represents an $x \times y$ section of *6.1 × 17.1* μ*m*. The phase mask is along the top of the picture and the propagation of light travels from top to bottom. The centres of the high elevations on the phase mask are positioned directly below of the lowest full row of maxima. The pattern repeat distance is *4.5 ± 0.03* μm, which matches the calculated value of *4.605* μm illustrating a strong zeroth order diffraction (for *488* nm).....202

Figure 7.3. Cross section of Fig. 7.1 (along line AB) normal to the phase mask, through sets of Talbot maxima, showing the same period with the phase mask, i.e. ~*1.06* μm. 203

Figure 7.4 . Transverse (a) and axial (b) images of a region with defect in the phase mask. The axial image shows that in the distorted regions, marked by circles, a missing line in the grating limits the number of self-images. The disturbance is due to the fact that each diffracted order separates from the others at increasing distance, thus limiting the distance at which there still is interference. 203

Figure 7.5. Measured image of an FBG presenting a defect. The unexpected structure may be due to defects of rulings surface in the phase mask, as shown, for example in Figure 7.4. 204

Figure 7.6. Schematic of the temperature controlled rotation stage. The smooth angular rotation of the fibre placed in matching oil between two cover slips has been achieved by combining a home made fibre chuck rotator with a fibre chuck. This way 360 degrees of initial fibre rotation have been provided whilst the optical fibre sample is kept within the working distance of the microscope objective (600 μm) and lateral constrained motion to within a 350 μm × 350 μm field of view of the objective. This combination is attached directly on top-side of the temperature controlled stage. A graduated knob and vernier scale allows initial setting of the rotation angle. 206

LIST OF TABLES

Table 2.1. Summary of methods used for refractive index profiling of optical fibres 34

Table 3.1. Characteristics of immersion fluids used as embedding agent measured at 25 ºC. 59

Table 4.1. Several optical fibres imaged using DIC. Refractive indices n_1 and n_2 of the surrounding medium and the fibre structure respectively, maximum optical path length (Max.OPL), and maximum phase (Max. Phase) of the fibre core were studied under monochromatic light of λ = 488 nm wavelength. The OPL was computed from $(n_2 - n_1)t$ where t is the maximum thickness of the fibre, which is across its core diameter. The phase was computed from $(2\pi/\lambda)\cdot OPL$. 75

Table 4.2. Comparison of results obtained from DIC images and manufacturers' specifications. 90

Table 4.3. Summary of advantages and disadvantages of refractive index profile reconstruction of optical fibres from differential interference contrast images...94
Table 5.1. Sensitivity of the photoinduced index change for various enhancement methods. 102
Table 5.2 Summary of direct techniques used for FBG characterisation. 143
Table 5.3. Parameters of the FBGs considered in this work. The values obtained for the refractive index modulation amplitude have been calculated using Eq. 5.7.149
Table 7.1. Optical fibres used in imaging experiments in this thesis. 192

1 Introduction

1.1 Overview

This chapter provides an overview of this research and background to the thesis. It begins by explaining the rationale of the work by putting it into context, and then proceeds to put forward the background of this research, offering a justification for its relevance and defining the aims and objectives. Also discussed is the approach followed to achieve these objectives. This chapter argues that the development of a non-destructive imaging methodology should be based on direct observation of the object under the study. Finally the structure of the thesis is outlined.

1.2 Problem Statement (Rationale)

Most notable among the successes of optical-fibre sensing technology, as it evolved in the final decade of the 20th century was the development of fibre Bragg grating sensors. From their beginning, fibre Bragg gratings have

remained a hot topic and despite a great accumulation of scientific information since their first trials as sensors, very little has been discovered about their detailed internal structure.

It has been reported that the market share of strain sensors is predicted to grow by up to 40% per year from 2001 due mainly to the progress in fibre grating sensors; the global market of fibre-optic sensors of US$350 or below 1% million in 1997 (Willsch 2001) is expected to reach more than $50 billion by 2008 (Fernando *et. al.* 2002).

Fibre Bragg gratings have a myriad of applications. They are used extensively in the telecommunications industry as dispersion compensators and add/drop multiplexers but also due to their inherent advantages such as small size and weight, inert nature, electromagnetic interference immunity, low cost, high performance, robustness and accuracy, they have found substantial applications as sensors, particularly of temperature and strain, due to the fact that the measurand, (a strain, pressure or temperature) change is encoded as a wavelength shift.

Areas of interest of fibre Bragg gratings sensors include monitoring/recording the actual seismic response in structure analysis used in earthquake detection, pipeline monitoring and leakage detection; early fire detection and surveying; monitoring and controlling of air conditioning systems; detecting and locating leakages in sealing elements; locating water seepage paths in the underground; measuring of static and dynamic deformations of hydraulic structures; long term monitoring of processes in the environment and geosphere; surveying of the setting process and deformation measurements on engineering systems such as bridges, tunnels, historical buildings, nuclear power plants and slopes (Ferdinand *et. al.* 2002).

Many groups worldwide have the capability to fabricate a variety of Bragg gratings designed for specific applications such as the ones mentioned above. However, assessing the quality of a Bragg grating, in other words, the problem of synthesizing or reconstructing the fibre Bragg grating structure, its grating period and index modulation, is to date indirectly evaluated from the device reflectivity or transmission characteristics (Poladian 2000) with a coupled mode analysis based on a simplified longitudinal distribution of the ultraviolet induced refractive index perturbations in the core of the fibre. Inferring the microscopic properties from the device performance is a classical inverse problem and it is known that a wide variety of Bragg grating parameters can give rise to similar reflection spectra (Poladian 1997), consequently limiting the manufacturer's ability to optimise the manufacturing process. Furthermore, future applications of fibre Bragg gratings currently being researched (Erdogan 1998), will require more detailed structure than those used as simple reflectors or simple dispersion compensators. This represents a serious gap in the knowledge required for the efficient use of such devices.

Consequently, microscopic data will provide crucial insight enabling the successful development of these devices. If the grating structure is appropriately described, modelled and fabricated, the grating long-term stability can be more rigorously assessed and improved and more versatile intragrating sensing may be realised.

1.3 Significance of the Study

The intent of this research study was twofold and is intimately connected to the continuing development of novel optical fibres including advances in synthesizing novel materials as well as improvements in their theoretical

understanding. Firstly this research was designed to provide information on how microscopic techniques can be employed in profiling the optical fibre by non-destructively imaging it. It is well known that commercially available techniques suffer from various deficiencies lacking on providing accurate measurements and particularly being limited when complex fibre structure is involved. There is clearly a need to develop an alternative reliable technique. The proposed technique offers the basis for new instrumentation. From this work the researchers learn about the specific steps needed to be considered for imaging an optical fibre and determine its fibre properties and their relation to fibre performance. This work is also important and particularly needed because it builds on the ongoing work of the Optical Technology Research Laboratory (OTRL) at Victoria University of Technology, in collaboration with the Optics Group at the University of Melbourne, in the development of a large range of fibre based devices including rare earth doped optical fibres as optical amplifiers and temperature sensors.

The second intent of this work was to provide information on the process of grating formation in an optical fibre. Despite the fact that much research has been conducted trying to understand the microscopic mechanism of fibre Bragg grating formation in the past twenty years, only limited systematic results have been obtained in relation to the FBG structure. This is particularly true for Type I FBGs. The information from this work has already influenced the development of a deeper understanding of fibre Bragg grating fabrication. This understanding, in turn, provides insight and direction for improving not only the manufacture of fibre Bragg gratings but also understanding certain unusual aspects of their operation as sensors. The information encourages and/or persuades designers and manufacturers to better assess the various aspects and needs of their sensors in order to improve their design, implementation and evaluation. Locally, such a study is needed because the work within OTRL also

involves researching and constructing a wide range of fibre Bragg grating structures as sensors fabricated in diverse types of fibres, used for strain, temperature, position and motion measurements.

1.4 Solving the Problem

As this thesis argues, microscopy techniques, particularly Differential Interference Contrast (DIC) microscopy, provides researchers in the optical fibre field with a powerful tool for the study of the optical fibre as a transparent object. There are several advantages to using light microscopy when studying optical fibres. The use of a light microscope allows direct observation of the fibre by exploiting the optical sectioning property of some techniques in transmission light microscopy.

In studying an optical fibre, Differential Interference Contrast (DIC) microscopy was employed based mainly on two reasons. Firstly for its ability to obtain both phase and amplitude information from the object by displaying this information in the characteristic DIC fashion, and secondly for its ability to extract information from a narrow depth of focus in the object and display it in the image with a reasonably high contrast. This thesis provides both qualitative and quantitative data to demonstrate the performance of the method proposed.

1.5 The Objectives of the Research

The aim of this thesis cannot be achieved out of context, and it is therefore necessary to bring together the ideas, which surround the research. To this point this thesis aims to review the current state of optical fibre characterisation research, with an emphasis on state-of the art technology existent to date.

The core of the thesis aims to investigate the relevant theoretical and experimental basis for implementing the Differential Interference Contrast microscopy method as a research tool in the quantitative investigation of optical fibres.

In addition it aims to use the above-mentioned method for studying the structure of fibre Bragg gratings and to provide the necessary groundwork and results for continuation of this work after this thesis is written.

1.6 The Structure of the Thesis

In an attempt to provide a suitable logical presentation of the information gathered in this thesis, the beginning of each chapter contains a summary of the subject matter to be covered and, where necessary, a brief review of the background needed to fully understand it.

So far this chapter has outlined the research objectives and method, pointing out the significance of the research. In the following a preview of the remaining chapters is provided.

It is appropriate to address some background material that is directly related to this study. In this vein, Chapter 2 – *A review on refractive index profiling of optical fibres*, firstly describes optical fibres for readers unfamiliar with this notion; outlining the operational characteristics together with their use as sensors. Next it is explained why it is important to objectively measure an optical fibre. Finally the chapter presents an overview of current techniques used to retrieve refractive index profile of optical fibres emphasising aspects like the type of measurement: destructive/non-destructive, direct/indirect, attainable resolution, computational difficulty and cost where known.

A detailed description of the research methodology emphasising the DIC microscope operation and the common environment in which all of the experiments were conducted is presented in Chapter 3 – *Aspects of the research method*. In doing so, this chapter provides a cursory view of the calibration of various elements of the microscope and the sensitivity of DIC imaging of an optical fibre to the refractive index of the immersion fluid and to fibre orientation.

Chapter 4 – *Estimation of the refractive index* introduces the methodology suitable for reconstructing the refractive index of an optical fibre presenting the advantages and limitations of this approach. It includes a theoretical model used to simulate the DIC image of the central region of an optical fibre, having known its refractive index distribution retrieved from other methodologies, and presents computer simulated images of it. Application of the technique to pertinent areas such as annealed fibres and new fibres such as a Bragg fibre, are presented. A comparison of the presented method and other methods available for the refractive index profiles for particular optical fibres is also examined.

The application of DIC imaging to optical fibre Bragg gratings is a novel approach to a complicated and demanding problem. Chapter 5 - *Fibre Bragg characterization* extends the analysis elaborated in Chapter 4 and focuses upon imaging of the Type I optical fibre Bragg gratings. Specific attention is paid to the formation of the Bragg structure in the optical fibre core, the difference between the ultraviolet (UV) induced effective refractive index and the induced refractive index of the fibre core material. The chapter also addresses modelling of the interference pattern behind a diffraction grating used to write fibre Bragg gratings and compares theoretical model predictions with experimental data. In particular the influence of different percentage contributions of the diffraction

orders on the observed structure in the fibre Bragg grating is investigated. This chapter ties together the results and lays the groundwork for future studies.

Finally, Chapter 6 – *Concluding Remarks,* concludes the thesis by bringing together the preceding chapters and examining the extent to which the objectives have been achieved, presenting some directions for future development and other related work.

2 A Review of Refractive Index Profiling of Optical Fibres

2.1 Overview

This chapter begins with a brief description of the optical fibre outlining its operational characteristics. This is followed by a review of the most current techniques used to retrieve refractive index profile of an optical fibre.

2.2 The Optical Fibre: General

The term "fibre optic" was first coined by Narinder Kapany[i] (Meyers 1992), and is used to distinguish the technology of transmitting information optically. In general an optical fibre can be defined as a thread of a dielectric material which uses total internal reflection to confine, guide and transport light enormous distances with great accuracy. One fibre is thinner than a human hair and stronger than a steel fibre of similar thickness and for long distances can carry many thousands of times more information than a copper wire (Hecht

[i] Narinder Kapany is considered the father of fibre optics: http:www.silicon-indiacom/digital-profiles/articledisplay.asp?article-id=916&imagedisplay=ent

1999). Optical fibres as information carriers in communication systems have been justified by their performance over the past two decades. They are immune to electromagnetic interference (from lightning, nearby electric motors, and similar resources) making them especially useful where interference may render other types of cable useless, inaccurate or hazardous.

An optical fibre is made of extremely pure silica comprising two slightly different optical materials. In a cylindrical arrangement, the centre cylinder, representing the core of the fibre carries the optical information; while the outer layer, called the cladding, serves to provide an optical boundary guiding light back into the core. The ability to guide is accomplished by the core having a slightly higher index of refraction than the cladding; the difference is sometimes as low as *0.1%* (Luc 1990). The cladding is generally made from silica glass, while the core, is composed of mostly silica with the addition of some special materials such as germanium. For practical applications, another layer of polymer coating and cable provides the fibre with mechanical strength and protects it from damage or moisture absorption, see Figure 2.1

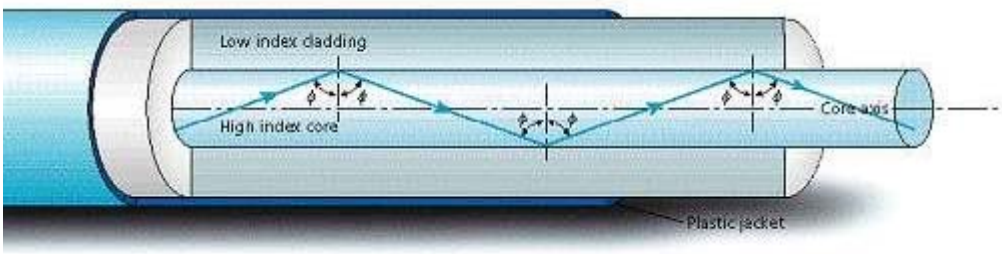

Figure 2.1. Schematic diagram of a typical optical fibre in cross-section. (Figure after Future Fibre Technologies Pty.Ltd. http://www.fft.com/backgrnd.html).

Although optical fibres are a key element in light wave communications they can be more than mere signal carriers; and also form the basis of optical fibre sensing systems (Grattan and Meggitt 1995b).

2.2.1 The Operational Characteristics of Optical Fibres

The phenomenon accountable for the guidance of the light through the optical fibre is known as total internal reflection, and is made possible by the existence of at least two transparent optical media having different indices of refraction representing the core and the cladding, n_1 and n_2 where $n_1 > n_2$ (Grattan and Meggitt 1995b).

The refractive index, n, characterizes the degree of refraction of light by a transparent material; it is linked to the speed of light in a material, v, by:

$$n = \frac{c}{v} \tag{2.1}$$

showing that the speed of light in a material is less than the speed of light in vacuum, c.

In general, four parameters affect the ability of an optical fibre to accept light into its core: the physical core size, the refractive indices of the core and the cladding and the wavelength (frequency) of light.

Guided light waves and their propagation through the core of an optical fibre are fully described by electromagnetic theory using a set of specific Maxwell equations. The solutions of these equations, satisfying conditions related to fibre geometry through boundary conditions and material properties, allow the description of a set of waveforms, called modes, that can propagate through the fibre (Grattan and Meggitt 1995b). Fibres that carry many modes are referred as "multimode fibres" and the ones carrying only one mode are termed "single mode fibres". The electromagnetic theory related to this topic is beyond the scope of this thesis. The focus in the next few sections is on the understanding of the material properties of the optical fibre as a waveguide and its interaction

with light signals, as a central step in describing optical fibres in their transmission or sensing function.

As mentioned above, the refractive indices of the core and cladding are two of the most important parameters of an optical fibre. They determine the numerical aperture (NA) of the fibre for signal propagation and the radial intensity distribution. The NA is a basic descriptive attribute of specific fibres and governs the degree of confinement of propagating radiation. Following Snell's law of light propagating within an optical fibre, and without taking into account surface irregularities or surface roughness, it can be shown that NA is a function of the indices of refraction of the core, n_1, and the cladding, n_2 (Marcuse 1981):

$$NA = \sqrt{n_1^2 - n_2^2}. \tag{2.2}$$

Another important fibre parameter dependent on the refractive index and also related to the NA is the normalized frequency, also called the V-parameter. This is given by the following expression (Snyder 1969):

$$\mathrm{V} = n_1 k\rho\sqrt{2\Delta} = k\rho NA, \tag{2.3}$$

where the wave number is given by $k = 2\pi/\lambda$, λ is the wavelength of the lightwave being carried by the fibre core, ρ is the core radius and Δ is a parameter that measures the relative difference between the maximum core refractive index n_1 and its cladding value n_2. Mathematically, the relative core-cladding index difference is expressed as:

$$\Delta = \frac{n_1^2 - n_2^2}{2n_1^2} \quad \text{or} \quad \Delta \approx \frac{\mathrm{n}_1 - n_2}{n_1} \text{ for } \Delta << 1. \tag{2.4}$$

The V-parameter determines the number of modes supported by the fibre. For $V < 2.405$, the fibre can support only one propagating mode and is said to be single moded. For larger values of V the fibre supports multiple modes.

Furthermore the refractive index plays an important role in determining the total intrinsic loss of a fibre. The total intrinsic loss, light loss inside the fibre or attenuation, is due almost entirely to Rayleigh scattering[ii] which is proportional to the eighth power of the refractive index (Lines 1984):

$$\alpha_R = \frac{8}{3}\left(\pi^3/\lambda^4\right)\left(n^4 p\right)^2 (kT)\beta_T \tag{2.5}$$

where α_R is the Rayleigh scattering coefficient, λ is the wavelength, n is the refractive index of the medium, p is the average photoelastic coefficient, β_T is the isothermal compressibility at an absolute temperature T and k is Boltzman's constant.

Manufacturing optical fibre requires some basic needs to be addressed: firstly, the chosen material to be transparent at particular wavelengths, so that the signals may be transmitted efficiently; secondly, a certain composition of this material is needed such that long, flexible, thin strands of fibres may be drawn; and thirdly, the material's optical properties should be easily modifiable (i.e. to have slightly different index of refraction).

The majority of optical fibres are made from silica glass, SiO_2 or silicate, even though some types of plastics can also be used (Allen 1983). Plastic fibres are used less due to their higher attenuation, but on the other hand, in certain harsh conditions requiring a certain mechanical strength, they have advantage over all silica fibres (Keiser 1991). For example in medical applications and sensors,

[ii] Rayleigh scattering is scattering by refractive index fluctuations (inhomogeneities in material density or composition) that are small with respect to wavelength. The scattered field is inversely proportional to the fourth power of the wavelength.

where a short length of OF is used, usually less then few meters, fibre loss and fibre dispersion are not primary areas of concern. Instead mechanical strength and flexibility make the polymer OF the preferred candidates.

Silica glass is a highly purified glass, made by Modified Chemical Vapor Deposition (MCVD) process, having an index of refraction of *1.458* at *850* nm (Keiser 1991). During this process a highly controlled mixture of chemicals, primarily silicon tetrachloride ($SiCl_4$) and germanium tetrachloride ($GeCl_4$) are converted into glass during preform manufacturing. Light travelling through silica glass has very low loss and silica is highly transparent in the visible and infrared regions of the spectra. In order to produce two materials having slightly different indices of refraction, for use as the core and cladding of the fibre, germanium, phosphorous, fluorine or various oxides, referred to as material dopants are added to the silica glass in the fabrication process. This process has the effect of changing the index of refraction or optical density of the material for the desired effect. Some dopants increase the silica glass's index of refraction while some others lower it. In any case, generally speaking, when manufacturing optical fibre for light transmission, the core material is made to have a slightly higher index of refraction than that of the cladding (Callister 1997). A commonly used combination is GeO_2-SiO_2 (signifying a germanium doped silica glass) core with a SiO_2 cladding. There are exceptions to this rule, like the Bragg fibre, which will be discussed in Chapter 4.

Over the last two decades great effort has been devoted to the development of an optimum method for measuring the refractive index distribution of an optical fibre which can be widely and universally applied to the variety of fibres being developed. Such a method would ideally be applicable to a fibre with an

arbitrary profile, highly accurate, having high spatial resolution, non-destructive and, if possible, simple to collect and process data. So far many methods have been proposed: Refracted Near-Field (RNF) method, Atomic Force Microscopy (AFM), Quantitative phase microscopy (QPM), Near Field Scanning Optical Microscopy (NSOM), and interferometric methods. In the following sections a synopsis of the commonly used techniques on refractive index profiling is presented with an emphasis on the merits of each method.

2.3 Refracted Near Field Technique

Originally developed for optical fibres, the Refracted Near Field (RNF), sometimes called refracted near field ray method or refracted near-field scanning method, (Stewart 1977; White 1979; Gisin, Passy and Perny 1993; Fontaine and Young 1999), derives the refractive index profile from the intensity of light refracted, but not guided by the fibre. The RNF method was originally proposed and demonstrated by Stewart (1977), and further developed by White (1979) and Young (1981).

The setup for the RNF technique is shown in Figure 2.2 (the notation in the figure is consistent with those presented by Fontaine and Young (1999). Stewart proposed that the fibre be illuminated with a focused beam whose vertex angle greatly exceeded the acceptance angle of the fibre such that the rays are not trapped by the fibre but are refracted at the core-cladding interface (Stewart 1977). An opaque circular stop, centred on the optical axis behind the fibre, blocks the leaky rays and guided light within the inner cone from reaching the detector (Young 1981).

It has been shown that for a uniform unclad fibre whose index variation is only radial not axial, the index of refraction *n(r)* at radius *r* is related implicitly to the angle of refraction θ_7 from the rear surface by the equation (Young 1981)

$$n^2(r) = n_3 + \sin^2\theta_1 - \sin^2\theta_7, \tag{2.6}$$

where $n_3 = n_5$ is the index of the liquid in the cell, and sin θ_1 is the numerical aperture of the incident cone, refer to Figure 2.2. The method has been further developed by reducing the uncertainty in the index at the reference point based on the observation that the dominant source of uncertainties was the index of the fluid (Fontaine and Young 1999). Consequently an index-matching block, fused silica, having the index of refraction $n_6 = 1.4570$, was used as a reference point, see Figure 2.2. The refractive index $n_4(x, y)$ at the point (x, y) on the specimen was related to the angle of incidence θ_3 and the final angle of refraction θ_7 by (Fontaine and Young 1999):

$$n_4^2(x,y) = n_6^2 + n_3^2\sin^2\theta_3 - n_7^2\sin^2\theta_7. \tag{2.7}$$

This relation also holds if the block is removed and the immersion fluid forms the 90° corner and n_6 is equal to n_3. The spatial resolution of the refracted-ray method is diffraction limited[iii].

The total power of refracted light transmitted past the stop is detected by a large area detector and is almost linearly related to the index difference when a Lambertian or point source is used (Young 1981). In the case when a Gaussian source is used, corrections must be considered to ensure the validity of the resulting profiles (Gisin and Raine 1991).

[iii] Diffraction limit is a consequence of the wave nature of light; it has been investigated by Abbe and it refers to the fact that the resolution is limited by the wavelength of the radiation used. Born, M. and E. Wolf, *Principles of Optics: Electromagnetic Theory of Propagation, Interference and Diffraction of Light*. 7th Ed., Cambridge University Press, Cambridge, 1999.

Although the refractive index resolution achieved by this method is of the order of 10^{-5} the method is destructive, as the end of the fibre must be used, and relies on the quality of the end face of the optical fibre and as such poor polishing may affect the quality of the results. In addition it is sensitive to the alignment of the fibre to the focal plane of the objective.

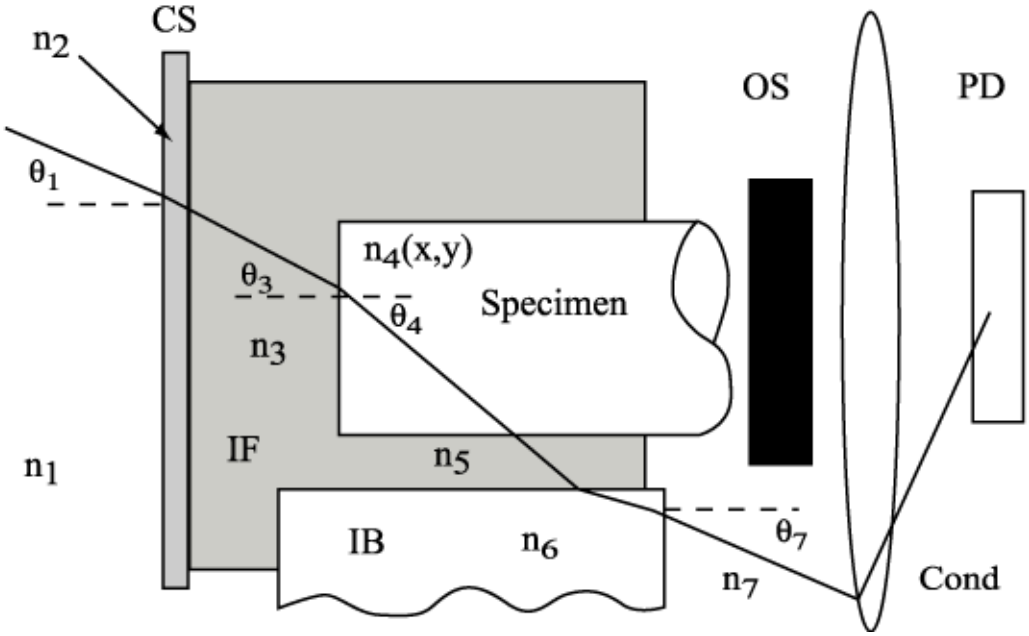

Figure 2.2. Ray trace of the light propagating in a refracted ray scanner. The basic components are the photodetector (PD), condensing lens (Cond), opaque stop (OS), index matching block (IB) with index n_6, specimen with index $n_4(x, y)$, index matching fluid (IF) with index $n_3 = n_5$ and coverslip (CS) with index n_2.

The RNF method has been calibrated to produce quantitative profiles of the refractive index (Young 1980), and has also been considered as the reference method of the Telecommunications Industry Association (1992). Despite having gained acceptance as the industry standard the RNF technique is frequently criticised for its strong reliance on the accuracy of the calibration

procedure. An alternative to the RNF method is the cladding-mode near field technique (Hatton, Buckland and Nishimura 1987). This method is very similar to the RNF method and derives the index profile from the cladding modes that propagate along the fibre.

2.4 Atomic Force Microscopy

Atomic Force Microscopy, (AFM), (Zhong and Innis 1995), used in conjunction with chemical etching of the fibre, (Burrus and Standley 1974), has been proved to be a powerful method for qualitative high resolution refractive index profiling, due to its nanometer spatial resolution, (Innis, Zhong *et al.* 1994; Tsai, Chung and Othonos 1996; Huntington, Mulvaney *et al.* 1997).

Although the data from AFM does not provide a direct measure of the refractive index distribution, the high spatial resolution of the technique is particularly useful for identifying structural and index changes within the small core of a fibre. It also provides a surface topography of the etched end, useful in identifying anisotropy in the index change or structure.

The cleaved end-face of the fibre is etched in either hydrofluoric (HF) acid diluted to different concentration levels or buffered oxide (BOE) solution diluted with a saturated citric acid solution. The two etchants have proved to reveal the core (germanium doped) and the cladding structure (silica) respectively. Zhong, (Zhong and Innis 1995) showed a correlation between the etch depth of the core and the index of refraction of the fibre for germanosilicate fibres. It is also known that the etch rate depends on the residual stress of the fibre. Recently this technique has been applied to an elliptical core fibre, (Butler, Horsfall *et al.* 1995), to measure the profile and compare it with the preform index measurements, (Huntington 1998).

2.5 Near Field Scanning Optical Microscopy

The lateral spatial resolution of an optical imaging system, given by the Rayleigh-Abbe criterion[iv] and imposed by conventional optics, was circumvented by the advent of Near-Field Scanning Optical Microscopy (NSOM)[v] (Betzig, Trautman *et al.* 1991). In NSOM a tapered single mode optical fibre is used as a sub-wavelength aperture tip, as shown in Figure 2.3, for the detection of evanescent components of the light scattered by the structure being analysed.

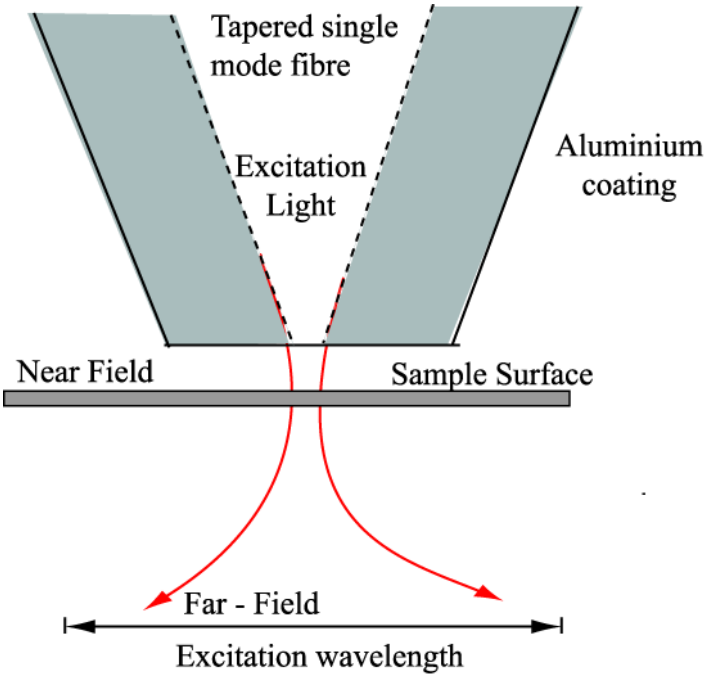

Figure 2.3. Schematic representation of the sub-wavelength aperture used in near-field scanning optical microscopy.

[iv] A number of definitions for the resolution of an imaging system can be found in the literature. In any conventional optical imaging system, the image of a point object is a finite-spot, called the Airy disk, rather than a point. If two points are very close together, their Airy discs will overlap. The Rayleigh-Abbe criterion states that two images are considered resolved when the centre of one Airy disc falls on the first minimum of the second Airy pattern; this is approximately half the optical wavelength of the radiation being used for imaging.

[v] NSOM is also known in the literature as SNOM Scanning Near-field Optical Microscopy (Heinzelmann and Pohl, 1994).

The resolution in NSOM is a function of physical size of the aperture and the distance between that aperture and the sample surface and not by the wavelength employed. NSOM studies of the end face of a fibre, have demonstrated that high spatial resolution measurements of the mode field profile of the fibre are possible (Butler, Horsfall *et al.* 1995; Huntington, Mulvaney *et al.* 1997). The method was developed by (Butler, Horsfall *et al.* 1995) and details regarding the near-field microscope constructed for mode field measurements of an optical fibre can be found in Shane Huntington's PhD Thesis (Huntington 1998) and in references therein.

Compared to AFM, the main advantage NSOM is of providing optical contrast images in addition to topographic images (Betzig and Trautman, 1992). A modified AFM using a tapered near-field optical fibre probe has also been developed for the determination of the mode profiles within an optical fibre (Ampem-Lassen 2000). Although the spatial resolution of an AFM is superior to that of a NSOM, optical information has proven to be of value for cases where material properties are not closely related to the surface morphology. Overall, the method offers the possibility of having an optical image with sub-wavelength resolution depending on the size of the aperture and the distance of the probe from the cleaved surface of the fibre. However, the method is destructive, which is a serious disadvantage in that it is based on studying the end face of the fibre.

2.6 Quantitative Phase Microscopy

Quantitative phase microscopy (QPM) (Barty, Nugent *et al.* 1998; Nugent 2001), a method developed at the University of Melbourne, proposes to

estimate the phase change of light passing through a specimen[vi] from bright field transmission images via computational algorithms (Gureyev and Nugent 1996; Paganin 1999).

The basis of the phase-retrieval scheme in the QPM technique is the transport of intensity equation (TIE) (Teague 1983; Gureyev, Roberts and Nugent 1995). This equation directly relates the longitudinal propagation of the energy distribution to the intensity $I(\mathbf{r}_\perp)$ and phase distribution $\phi(\mathbf{r}_\perp)$ in a plane perpendicular to the propagation direction and is expressed in the form:

$$\frac{2\pi}{\lambda}\frac{\partial I(\mathbf{r}_\perp)}{\partial z} = -\nabla_\perp \times \left[I(\mathbf{r}_\perp)\nabla_\perp \phi(\mathbf{r}_\perp)\right] \tag{2.8}$$

where the wave is described by $\sqrt{I(\mathbf{r}_\perp)}\exp(i\phi(\mathbf{r}_\perp))$. $\nabla_\perp$ and $\mathbf{r}_\perp$ are respectively the gradient operator and position vector in the plane perpendicular to the longitudinal optic axis z , λ is the wavelength, and $\frac{\partial I(\mathbf{r}_\perp)}{\partial z}$ is the longitudinal intensity derivative.

The method was applied in optical microscopy under partially coherent illumination for the two-dimensional and tomographic reconstruction of the refractive index distribution of fibres displaying rotational symmetry and also for twin-core optical fibres (Barty, Nugent *et al.* 2000).

The optical fibres have been imaged by means of bright-field microscopy, after being stripped of the plastic jacket, side-on (or transversely) so as to obtain a projection of the refractive index through all layers of the fibre structure. The fibre has been placed on a microscope slide, immersed in a pool of index

[vi] An object with differences in refractive index or optical path but not in absorbance. A pure phase object is characterised by a complex transmission function of the form: $g(x) = exp(i\ \phi(x))$; often weak phase objects are defined by a transmission function derived from a Taylor's expansion of a pure phase object, i.e. $g(x) = 1 + i\ \phi(x)$, where $\phi(x)$ is the phase change introduced by the object.

matching fluid and covered with a coverslip for which the imaging lens was corrected. A flat focal plane has been achieved by using two sections of fibres of similar diameter to the studied sample fibre as spacers as shown in Figure 2.4.

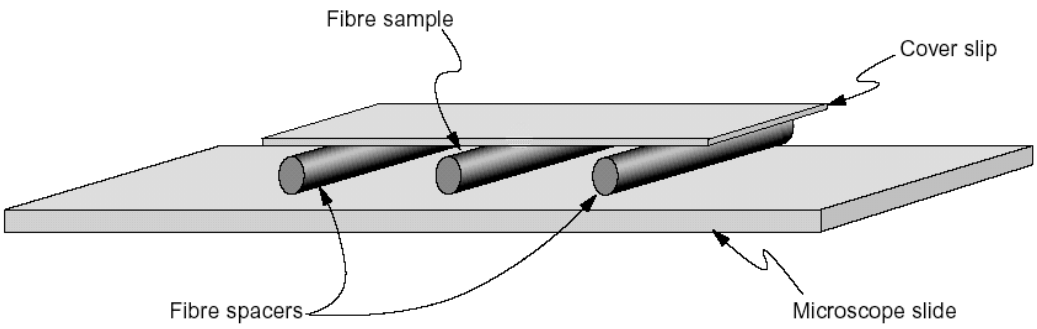

Figure 2.4. The mounting system used in the TIE imaging technique of an optical fibre (after (Barty 2000)) . The fibre sample has been placed in a pool of matching index fluid formed between two other identical fibres located on either side to ensure the parallelism between the cover slip and the microscope slide.

In practice the intensity derivative $\frac{\partial I(\mathbf{r}_\perp)}{\partial z}$ in Equation 2.8 cannot be directly measured but can be computed via a small known defocus of the imaging system. Thus equation 2.8 has been solved for phase via a deterministic algorithm (Paganin 1999) which numerically inverts the TIE by following a Fourier-transform based algorithm. Hence, the phase has been recovered by using a set of three images one in the plane of best focus and the other two at $\pm$ *2* μm either side. Using this information and the fact that the fibre is circularly symmetric, an Abel transform is applied to determine the refractive index distribution.

The researchers concluded that the resolution and the capability of the QPM technique is comparable to DIC imaging.

QPM has also been used to perform a three dimensional reconstruction of the refractive index distribution through the use of a computed tomography technique by means of an inverse Radon transform from the projection data (Barrett and Swindell 1981). The reconstruction has been performed for circularly symmetric optical fibres as well as non-symmetric fibres, such as the twin-core fibre. For a more detailed description of the tomographic technique the readers are referred to Anton Barty's Ph.D thesis (2000). QPM method has also been applied to measure stress birefringence[vii] by use of polarized light (Roberts, Thorn *et al.* 2002). Quantification of the refractive index of axially symmetric optical fibres has also been achieved by application of the inverse Abel transform to a single phase image obtained from QPM (Roberts, Ampem-Lassen *et al.* 2002).

QPM is an extraordinary technique for recovering the phase change of light passing through an object. It provides a cost effective solution for studying the structural changes within an optical fibre. In particular the internal structure of an optical fibre contains features that cannot be distinguished using the RNF method but are confirmed by the AFM method. However, QPM represents a digital image processing technique, which requires the acquisition of three bright-field images. Known source of errors such as the translation of the microscope stage during the acquisition of the defocused images is under continual development. It has been reported that for commercial QPM[viii] systems there have been developed a number of ways for reducing this type of errors including the translating of a relay lens in the microscope phototube

[vii] This is also called mechanical birefringence and is a phenomenon that occurs when certain transparent materials (eg. a fibre) are subjected to external stress. This stress is known to cause local changes in the refractive index of the material.

[viii] QPM is commercialised through Iatia, Ltd., http://www.iatia.com.au.

rather than the microscope stage and most recently by introducing a piezo controller.

2.7 Interference Microscopy - Axial Interferometry

An interference microscope (Burrus and Standley 1974), has been used for measuring core-cladding refractive index differences and approximating the index profiles of solid multimode fibres and enhancing the visibility of smaller-scale inhomogeneities in these fibres. The difference in the refractive index between fibre core and cladding was measured quantitatively on very short lengths of multimode fibres (< *1 mm*) using a Leitz interference microscope with a mercury spectral lamp (*546.1 nm* line) (Mach-Zehnder system). The fibre samples were prepared by embedding a short length of fibre (~ *1 cm*) in a glass capillary tube filled with an epoxy resin (≈ *1.48* refractive index), curing the epoxy and cutting slabs of approximately *1 mm* thick from the composite rod. The slabs were lapped and polished in order to provide very short lengths of fibre. The difference in refractive index, Δn, between two areas of a sample of thickness t as measured by the interference microscope, was given by (Burrus and Standley 1974):

$$\Delta n = \frac{\lambda q}{t}, \tag{2.9}$$

where q is the number of the fringe displacements and λ is the illuminating wavelength. The technique could not be applied to obtain profiles of many optical fibres, i.e., those with graded index profiles; also some detailed fibre properties, such as the germania-deficient centre of a germania doped optical fibre, could not be measured accurately (Presby, Standley *et al.* 1975).

Closely related to the Mach-Zehnder interference technique, is a technique developed by Stone who used a standard reflected-light microscope of equal quality with a monochromatic illuminator for obtaining fibre refractive index profiles (Stone and Earl 1978). In this case the transverse slice of fibre was placed between two flat glass or silica plates with a partially transmitting mirror coating on one face of each plate Figure 2.5.

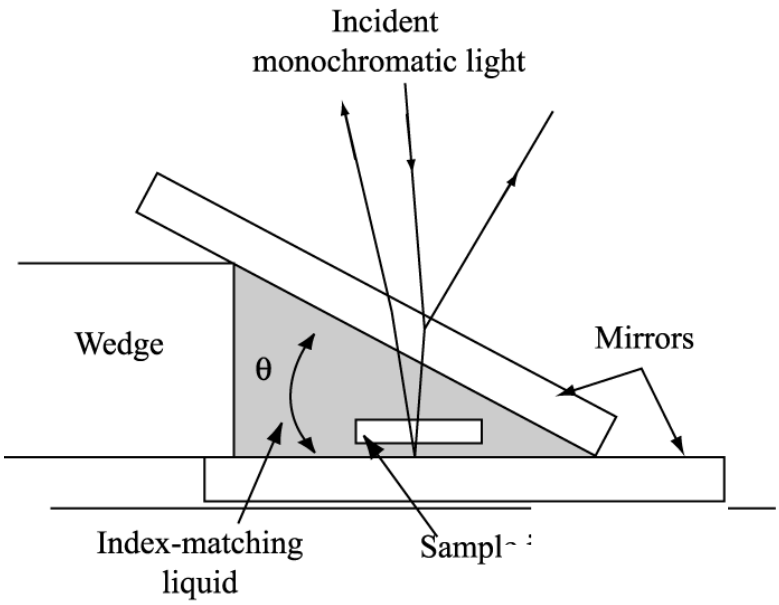

Figure 2.5. Sample arrangement used to observe tilted fringes in a reflected microscope with monochromatic light. Fringes are formed by reflection from the top mirror bottom surface and the bottom mirror top surface. The resultant interference pattern is that of a wedge, modified by the refractive index variation of the optical fibre.

The refractive index profile was obtained from the interference pattern by measuring the position of the fringes along its symmetry axis, expressed as a function of the angle, θ, and the index matching liquid (Stone & Earl 1978).

The advantage of using interference microscopy (axial interferometry) is that direct measurements in a fibre with many refractive index levels are possible ensuring equal geometrical distances in each region of refractive index.

However, the technique is highly destructive and limited to study of a small transversal slice of a fibre, (at National Physical Laboratory (NPL), a *250 μm* thick slice is commonly used; it is known that a *100 μm* thick slice provides the optimum trade-off between the requirements for maximum phase sensitivity and acceptable spatial resolution (2000)). The technique has relatively poor spatial resolution, is strongly dependent on the quality of the fibre surfaces and thickness variation, (Raine, Baines and Putland 1989) (a variation in thickness of *25 nm* is equivalent to a refractive index difference of *0.0001* in a slice of *100 μm* (Raine, Baines and Putland 1989) and is also dependent on stress relief induced by polishing (Scherer 1980; Chu and Whitbread 1982; Bachmann, Hermann *et al.* 1987). The method is not suitable for routine measurements and sample slice preparation is resource intensive as both the sample and reference must be optically flat, as stated in a technical report at the National Physical Laboratory UK (2000).

2.8 Transverse Interferometric Methods

The simplest of the transverse interferometric methods is the method based on the assumption that light rays passing transversely through an axisymmetric disturbance are changed in phase but do not deviate from their initial directions as they traverse the index-variation area; (see for example (Kahl and Mylin 1965; Kokubun and Iga 1977; Glantschnig 1985) and the references therein). A variety of analytical solutions to solve the problem of reconstructing the

refractive index profile of optical fibres, include cumbersome integral equations for the refractive index by either considering the contribution of the refraction of rays and defocusing effects, (Kahl and Mylin 1965), or the calculated optical paths inside the region of the index variation at the expense of neglecting refraction-related effects (Hunter and Schreiber 1975; Kokubun and Iga 1977). However, these solutions of the interferometric data reduction problem were based on the assumption that the test objects are weakly refracting media. Considering the case of strongly refracting objects, such as fibres, a method was described under the validity of geometrical ray optics and perfect cylindrical symmetry (Sochacki 1986). The refractive index, *n(u)*, of a transparent, optically inhomogeneous rodlike medium, (see Figure 2.6) with a cylindrically symmetric refractive index distribution immersed in a homogeneous environment of uniform refractive index was analytically reconstructed with the help of a

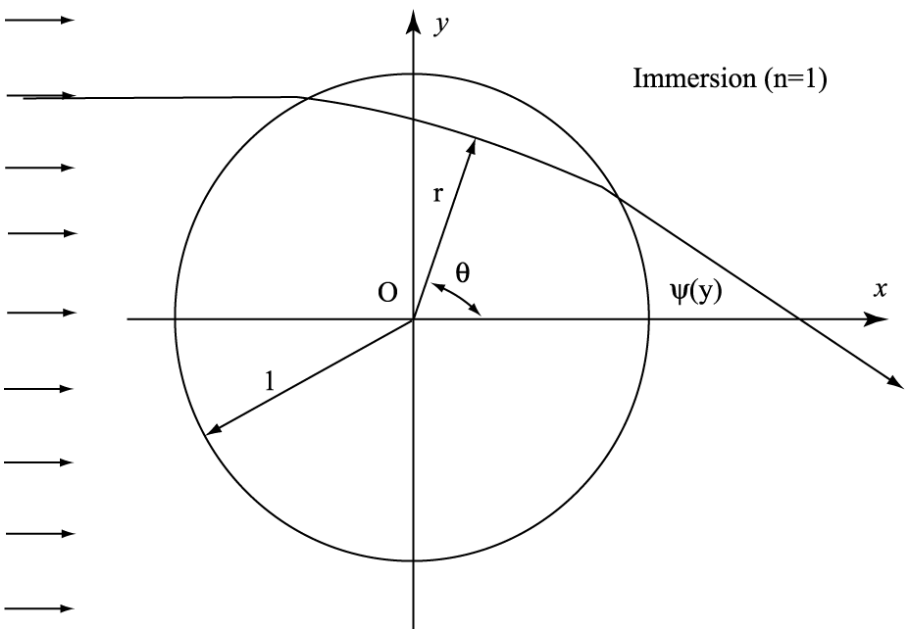

Figure 2.6. Transverse ray tracing through the inhomogeneous rod-like medium of unit radius. The test object is characterized by a radially symmetric index profile *n(r)* related to the function $u(r) = n(r) \times r$.

deflection function $\Psi(y)$, (Sochacki 1986):

$$n(u) = \exp\left[\frac{1}{\pi}\int_u^1 \frac{\Psi(y)dy}{\left(y^2 - u^2\right)^{1/2}}\right], \quad 0 \le u \le 1 \tag{2.10}$$

$$r = \frac{u}{n(u)}, \quad 0 \le u \le 1,$$

where the index profile $n(r)$ is related to $u(r)$.

2.8.1 The Phase Stepping Technique

The four-phase-stepping interferometry, (Brunning, Herriott *et al.* 1974), was introduced as a method for surface profiling, recognition of shape and deformation of optical elements. The four phase-step interferometry has proven to be an efficient method in index profiling of optical fibres and waveguides (Linares and Lopez-Lago 1996); many modifications of the original algorithm have also been made and the reader is guided to the reference (Creath 1988) and the extensive bibliography therein. The basis of the method consists of retrieving phase data from four intensity distributions in the interference pattern with consecutive phase shifts of $\pi/2$ between the interfering beams (Brunning, Herriott *et al.* 1974). Later the method was proposed for the refractive index profiling of optical fibres by representing the intensity distribution, as observed in the exit plane of an interferometer by a Fourier series in terms of the phase difference between the interfering wave fronts, $\Delta\theta$ (Sochacka 1994). This way the phase change introduced by the object, $\Delta\phi$ *(x, y)* is given by:

$$\Delta\phi(x,y) = \arctan\left[\frac{I_2(x,y) - I_4(x,y)}{I_1(x,y) - I_3(x,y)}\right], \tag{2.11}$$

where I_k *(k=1,2,3,4)* are the intensity distributions as observed with $\Delta\theta = (k-1)\frac{\pi}{2}$, *(k=1,2,3,4).*

It has been shown that in the case of differential interference contrast, the derivative of the optical path length through the fibre is expressed by (Pluta 1989):

$$\frac{d\delta(y)}{dy} = \frac{1}{s}\frac{\lambda}{2\pi}\Delta\phi(y), \tag{2.12}$$

where s is the shear wavefront. Using this expression of the derivative of the optical path length, the refractive index profile was given by Eq. 2.10, where the deflection function $\Psi(y) = -\arcsin\left[\frac{d\delta(y)}{dy}\right]$, (Sochacki 1986).

In addition a Carré algorithm has the advantage of suppressing systematic errors (Carré, 1966). This is a four-step algorithm, introduced in the 60's. However, the algorithm is seldom used because small amounts of phase shifting nonlinearity can introduce large error in the measurements (Kemao *et. al*, 2000).

2.8.2 Variable-Wavefront Interferometry

Transverse interferometry, applied for refractive index profiling of optical fibres, in the form of two-beam interferometry (Pluta 1972; Marhic, Ho and Epstein 1975; Pluta 1996), multiple-beam interferometry and variable-

wavefront interferometry (VAWI) (Pluta 1985) have been reviewed in a recent study (Hamza, Sokkar *et al.* 1999).

The VAWI technique was developed by Pluta in the early 1980s; an overview of all the versions derived from the initial method is described in (Pluta 1992) and reference therein. The method was based on the use of monochromatic light of continuously variable wavelength, extracted from a white light source (tungsten or halogen lamp) by means of a linear variable interference filter or continuous-wavelength interference filter, known as a wedge interference filter. A double refracting wavefront shear interferometric system, referred to in microscopy literature as the "*Pluta interference microscope*". This interference microscope, shown in Figure 2.7, is a complex system designed using four modified Nomarski Wollaston prisms. A short description of the main components of the microscope follows.

The Wollaston prisms, W_1 and Q_1, are rotatable around the objective, (Ob), and the condenser (C) axis, respectively, ensuring a change in the wavefront shear. The Wollaston prism, W_2, is placed in the microscope tube such that it can be translated in two directions: transverse and parallel to the objective axis, introducing a variable bias retardation. The compensator prism, Q_2, is fixed and orientated in such a manner as to cancel out the optical path difference between light wave components sheared by the sliding prism, W_2. The half-wave plate, H_2, is rotated in such a manner as to align the vibration directions of sheared light waves leaving the compensator, Q_2, parallel to the principal sections of the compensator, Q_1. Similarly the half-wave plate, H_1, enables the vibrations of light waves issuing from the birefringent prism, W_1, to be aligned parallel to the principal sections of the prism, W_2.

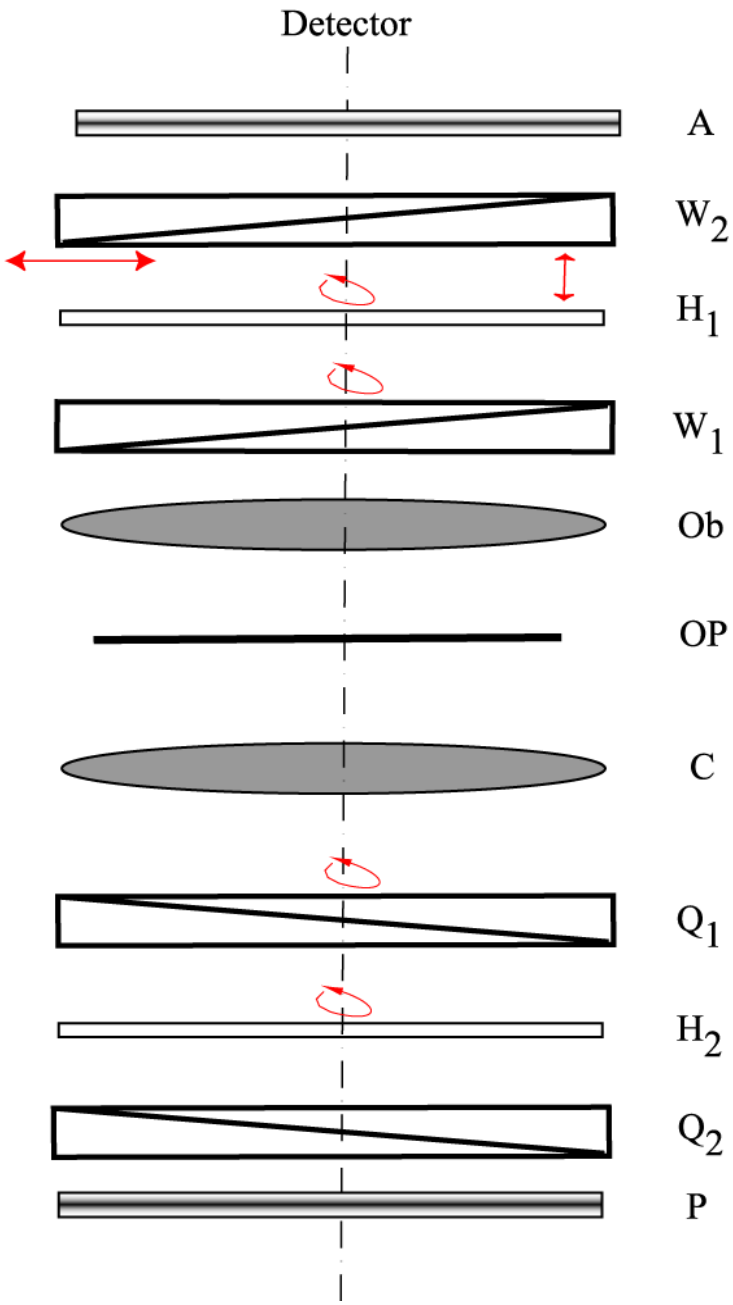

Figure 2.7. Optical System of the Pluta interference microscope with continuous variable wavefront shear. Notations are as follows: polarisers P, A; half-waveplates H_1, H_2; Wollaston prisms W_1, W_2; compensator Wollaston prisms Q_1, Q_2; Objective Ob; condenser C and object plane OP.

In the VAWI method, the interfringe spacing was directly measured from an interferogram, shown in Figure 2.8. Versions of the method have been developed for a variety of objects: objects with abrupt edges, cylindrical objects

(Pluta 1987b), objects that produce small optical path differences (Pluta 1987a) and birefringent objects (Pluta 1988).

In general, multiple beam interferometry utilizes a wedge interferometer, as shown in Figure 2.8, consisting of two silver-coated optical flats inserted in a special jig to form a wedge angle ε. This is the key element in either of the two transverse interferometric methods presented above.

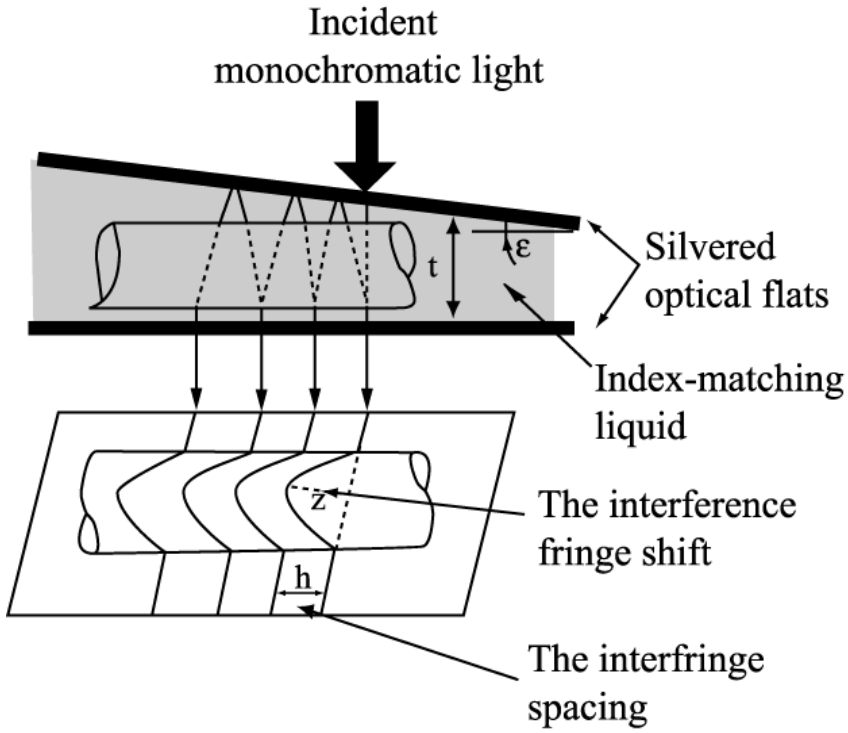

Figure 2.8. The liquid wedge interferometer used in multiple-beam Fizeau fringe in transmission and the produced interference fringe shift. Both the wedge angle ε and the interferometric gap thickness t are adjustable in order to produce sharp parallel fringe perpendicular to the fibre axis.

The fibre under study is immersed in an index-matching liquid of known refractive index. Adjusting the wedge angle, ε, and the interferometric gap thickness, t, sharp parallel fringes perpendicular to the fibre axis are produced. The refractive index profile, in both two and multiple beam interference, was analytically derived using either the interference fringe shift (Hamza, Sokkar *et*

al. 1995) or the area enclosed under it (Mabrouk and El-Bawab 1997; Sokkar, Mabrouk and El-Bawab 1999). Although non-destructive, accurate and applicable to large diameter fibres (300 μm), the techniques strongly rely on the refractive index of the matching fluid (Hamza and Mabrouk 1998) and a special preparation of the interferometer for each experiment (Hamza, Sokkar *et al.* 1999).

All these profiling techniques are linked in some ways but can also differ dramatically in their microscopic detail. The field remains an active area of research.

2.9 Summary

The methods of refractive index profiling presented in this chapter provide a comprehensive set of measurements for determining the refractive index profile of optical fibres. As one can see from the Table 2.1 any particular method will have some advantages and some disadvantages and one can easily conclude that there is no one method that does everything: cost effective, high resolution, applicable to any type of fibre, or user friendly. The motivation to explore the DIC imaging method arises from a desire to determine the absolute refractive index profile not only at the end surface of a fibre but also non-destructive ly along its length. As is evident in Table 2.1 only the QPM method (which was developed at the same time as the work of this Thesis) can make this claim.

In this chapter a brief description of the operational characteristics of an optical fibre has been presented. Efforts by others to obtain refractive index information from an optical fibre were also summarised.

Table 2.1. Summary of methods used for refractive index profiling of optical fibres

Method	Brief characteristics	Strengths	Weaknesses
Refracted Near Field	Method requiring the study of the end-face of the fibre; Refractive index profile of an optical fibre is obtained from the end face of the fibre.	a. Currently considered the standard method for refractive index profiling of optical fibres; b. Easily available commercially; c. Fully automatic; d. User friendly; e. Good spatial resolution varying from 380 to 500 nm.	a. Spatial resolution depends on the instrument being used; b. Some profilers may be used for only standard 125 μm diameter fibres; c. Criticised for its strong reliance on the accuracy of the calibration procedure; d. Can not provide information regarding the structure along the fibre; e. A minimum length of fibre is required; this length varies from 12 cm to 2 m.
Atomic Force Microscopy	Destructive method studying the end-face of the fibre; The end-face of the fibre is etched with an acid.	a. Very high resolution less then 10 nm; b. Provides information useful for identifying structural changes and index changes within the fibre core.	a. The data from the AFM does not provide a direct measure of the refractive index distribution; b. Requires skills for operation the AFM microscope and sample preparation.

Method	Brief characteristics	Strengths	Weaknesses
Near Scanning Optical Microscopy	Studies the end-face of the fibre in the near field region;	a. High resolution given by the probe tip size: 50 to 100 nm;	a. The refractive index profile is reconstructed indirectly from the mode field profile of the optical fibre; b. The method is sensitive to the quality of the end face of the fibre (the end-face surface must be polished, flat and parallel to the measuring instrument).
Quantitative Phase Microscopy	a. Non-destructive imaging method requiring the acquisition of bright-field images of the optical fibre 'side-on'	a. Detailed fibre properties, are easily observable and interpretable; a. It offers the capability to perform three dimensional reconstruction of the refractive index distribution; b. It is the most cost effective.	a. Newly developed technique.

Method	Brief characteristics	Strengths	Weaknesses
Interferometric Methods	**a. Axial interferometry: Destructive** A small slice of the fibre is required to reconstruct the refractive index of the fibre	Currently considered the standard calibration method for refractive index profiling of optical fibres.	a. Refractive index obtained is strongly dependent on the sample preparation, in particular on the quality flatness and parallelism of the two surfaces; b. Sample preparation is resource intensive and requires advanced skills from the operator.
	b. Transverse interferometry: Non-destructive	a. Sample preparation is straightforward and does not require considerable care when handling the fibre	a. Can not provide information regarding the three dimensional distribution of the refractive index within the fibre; b. It has been mostly applied to fibre having a large core area; has not been applied to small core diameter fibres; c. Spatial resolution given by conventional optics.

3 Aspects of the Research Method

3.1 Overview

The purpose of this chapter is to provide information about the basic operation of a Differential Interference Contrast (DIC) or Nomarski microscope and the common environment in which the experiments in this thesis were conducted. In doing so this chapter provides a cursory view of the calibration of the sliding Wollaston prism position and measurement of the point spread function. The measurement hardware includes the microscope, equipped with high resolution Nomarski optics and infinity corrected optics, photomultiplier tube and stepper motors that allow control of the microscope by the computer.

3.2 Data Acquisition

A good place to begin the overview of the experimental hardware is with the light source, which imposes restrictions on the resolution of the recorded images. Hence an argon-ion laser source has been chosen for its emission wavelength in the blue-green region satisfying the resolution condition.[ix] The argon ion air-cooled laser, single line at a wavelength of *488* nm Melles

[ix] This is related to the Rayleigh-Abbe limit of resolution mentioned in chapter 2. Generally for a microscope this can be determined using the expression $0.61\ (\lambda/NA)$, where λ is the free space wavelength of the illumination and NA is the numerical aperture of the imaging lens. For example if the microscope operates in air having an objective with $NA = 0.85$ and the operating wavelength is $\lambda = 488$ nm, the best resolution that can be achieved is ~ 350 nm.

Griot (model number 35 IMA 410) has a continuous wave (CW) with a total output power of *10* mW.

The beam expanded laser light is directed into the microscope via galvanometer-driven x-y mirrors; the synchronization between the scanner and the master data acquisition is part of the scanning unit controlled by a Pentium II processor under a Microsoft Windows NT station. The z-position of the objective is also controlled by the computer, which drives a geared stepper motor coupled to the standard manual height adjustment mechanism of the microscope along its optical axis. The control system is designed to have a position resolution of *0.1* μm over a total range of *600* μm. A photomultiplier tube (PMT) (model R3896, Hamamatsu) is used for the detection of light collected from the objective's focal plane. The analog output of the PMT is demodulated and digitised by the data acquisition of the computer to produce the digital image of the sample in *12*-bit numerical format.

Figure 3.1 illustrates a schematic diagram of a scanning DIC microscope employed for imaging the optical fibres studied in this thesis.

The objective lens is considered by some authors the most important component of any light microscope (Keller 1995; Piston 1998). The objective lens used in this work was a dry Olympus UplanApo $40 \times /0.85\ NA$, which is flat field and infinity-corrected. In addition it is corrected for chromatic and spherical aberrations. The numerical aperture, NA, of the objective is defined by the half-angle of the objective's collection cone (α) and the index of refraction of the immersion medium (n), and is expressed by $NA = n \sin(\alpha)$ (Inoue and Spring 1997, p.32). Using this objective a diffraction limited resolution (R_{diff}), can be achieved.

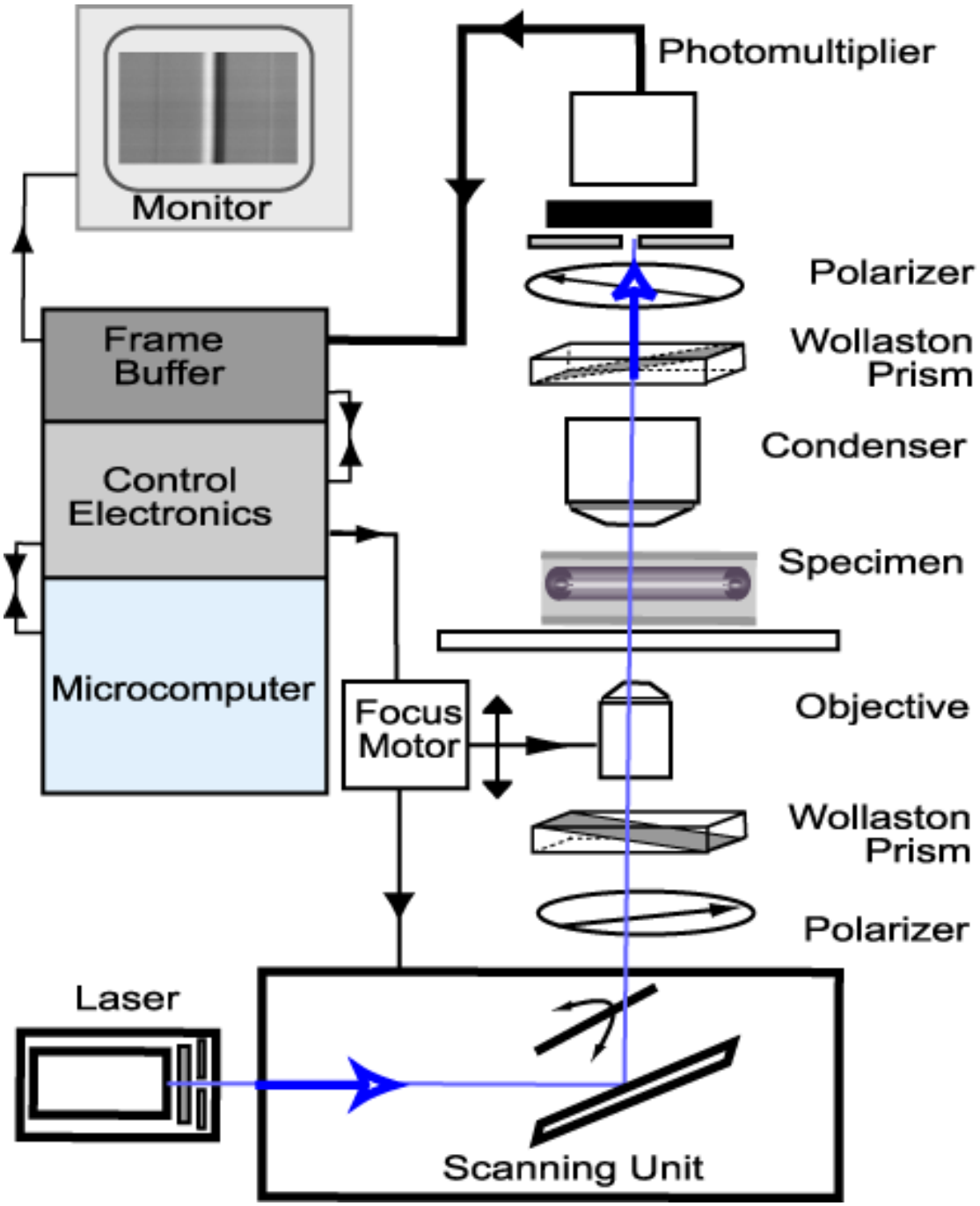

Figure 3.1. The measurement system. The microscope is an inverted Olympus FluoView IX Infinity Corrected Optical System, equipped with high resolution Nomarski optics. The photomultiplier tube is coupled to the microscope via a fibre bundle. The image output is converted to numerical format and recorded on a computer NT workstation. The computer controls the fine focus of the microscope in the *z*-direction via a piezo-stepper motor. The stepper motor translates the objective of the microscope in *0.1* μ*m* increments along the optical axis.

A long working distance condenser (27 mm) having a NA of 0.55 was used in conjunction with the objective specified above. This condenser ensured the separating power[x] of the optical system was optimal, i.e. 0.348 μm.

Further making use of the scanning laser system, the collecting of images was such that to maximize the information content in other words the Nyquist criterion was satisfied. The Nyquist criterion basically says that one should collect two points per resolution size (Inoue and Spring 1997), p.513. This was possible by varying the field over which the laser scanned the sample; this procedure is usually called "zoom" or more appropriately "electronic zoom". This is analogous to using an optical zoom lens such that the sampling resolution can be easily achieved. To summarize, in laser scanning microscopy, a *40* × magnification lens with a zoom factor of *2.5* is equivalent to a *100* × magnification lens with no extra zoom. The *40* × magnification lens has been chosen because it offered a larger field of view and therefore applicable to imaging an optical fibre.

3.3 Differential Interference Contrast Microscope Operation

Since its conception in the 1950s (Nomarski 1952, 1955) the differential interference contrast (DIC) imaging technique has experienced tremendous development. A detailed description of DIC microscopy can be found in the literature (Dana 1992; Preza, Snyder and Conchello 1996) and in references therein, and thus, only a summary of the basic operation of the DIC microscope is given in this section.

[x] The separating power is the smallest distance, d, between two elements that are seen as separated and it is given by $d = \lambda/(NA_{obj} + NA_{cond})$, *where* λ *is* the illumination wavelength, NA_{obj} and NA_{cond} is the numerical of the objective and the condenser respectively.

3.3.1 Principle of Differential Interference Contrast Imaging

The DIC microscope operation is based on the interference of two light beams. When two coherent light beams having the same wavelength and intensity are superimposed, the resultant light intensity is dependent on the phase difference ($\Delta\phi$) between the two waves. If the light beams are in phase ($\Delta\phi=0$) constructive interference occurs causing the intensity to quadruple; if the light beams are out of phase ($\Delta\phi=\pi$) destructive interference occurs causing the amplitude of the resulting intensity to be zero, as shown in Figure 3.2.

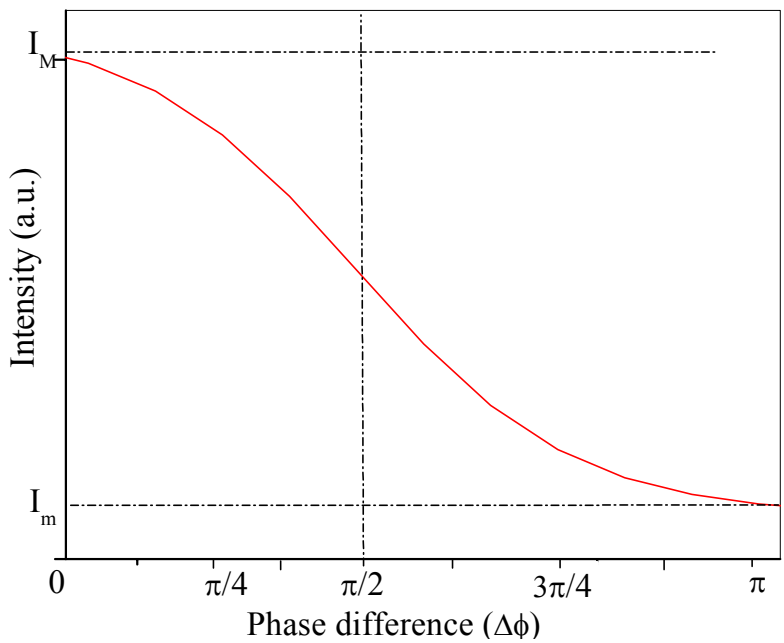

Figure 3.2. Interference between two monochromatic coherent light waves. The resultant intensity, as measured by the detector, reaches a maximum amplitude (I_M) when the two waves are in phase ($\Delta\phi=0$), and a minimum (I_m) when the waves are π out of phase due to the detector dark current.

A small object observed through a DIC microscope appears as a double image which is often referred to as a "typical shadow-cast". This is due to the phase difference between the two interfering beams. The largest phase difference between the two beams is formed when one of the beams falls just within, and

the other beam just outside, the object. This happens at the edges of the objects, perpendicular to the lateral shift. Opposite sides of the object will give rise to opposite phase differences resulting in to a bright edge on one side and a dark edge on the other side; this has also described as a so called bas-relief appearance in other words a false impression that the object is observed in relief.

Explanation of the double image origin is illustrated in Figure 3.3 with a simple example taken from literature (Van Munster, Vanvliet and Aten 1997).

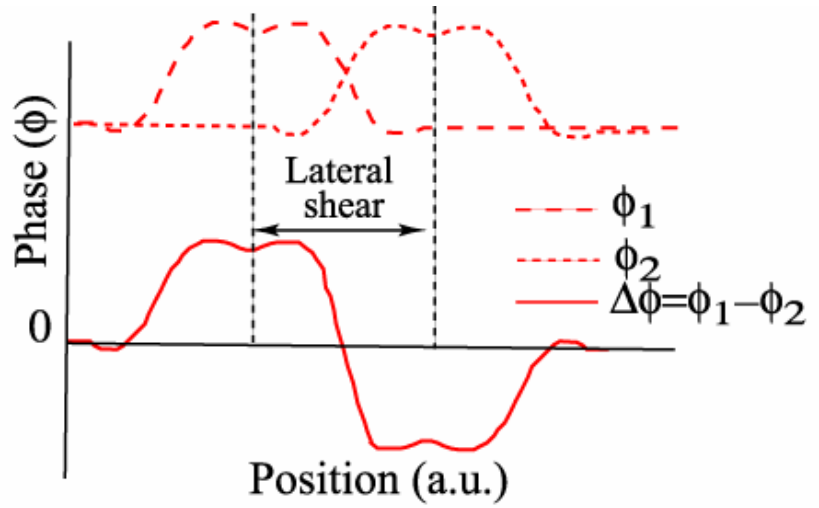

Figure 3.3. An example of imaging of a simple object through a DIC microscope. ϕ_1 and ϕ_2 represent the two wavefronts resulting from the object shifted with respect to each other as a result of the lateral shear introduced by the microscope. The intensity as seen in the DIC image is dependent on the phase difference between these two wavefronts.

When the two light beams pass through an object the resulting wavefronts ϕ_1 and ϕ_2 are shifted with respect to each other as a consequence of the lateral shift introduced by the microscope, this is represented schematically in Figure 3.3. By appropriate selection of optics (see 3.4.1) The intensity resulting from the interference is dependent on the phase difference between these two

wavefronts; by subtracting these two phase profiles in order to obtain this difference, a positive and a negative peak will be seen. At $\Delta\phi = \pi/2$ this will give rise to a lower and a higher intensity for the two peaks. The same conclusion can be drawn from Figure 3.2

3.3.2 Optical Components of a Differential Interference Contrast Microscope

The key optical components of a DIC microscope are a polariser, an analyser and two Wollaston[xi] prisms arranged as shown in Figure 3.4.

These optical components have certain properties that are fundamental to the operation of the DIC microscope. First, a polariser (or an analyser), which is an optical element with a single plane of vibration, has the property of letting only light with its electric field parallel to a single plane passs through it. Second, a Wollaston prism is used as a beam splitter, and consists of two prisms (wedges) made of birefringent, uniaxial[xii] material cemented together so that the optical axis of the upper prism is at 90° with respect to the optical axis of the lower prism.

When light emanating from a source passes through the polariser it becomes plane (linearly) polarised. The polariser's orientation is set such that its direction of light vibration is at 45° with respect to the optical axis of the sliding Wollaston prism and is 90° with respect to the analyser's direction of vibration. The polarised beam of light entering the sliding Wollaston prism splits it into

---

[xi] A Wollaston prism is made from positive uniaxial birefringent glasses: two triangular pieces of birefringent material are cemented together with their optical axes (o.a.) orthogonal to each other The Wollaston prism splits a linearly polarised incident beam into two orthogonally polarised beams: one whose electric field is perpendicular to the o.a. of the uniaxial medium (called the ordinary ray) and one whose magnetic field is perpendicular to the o.a. of the uniaxial medium (called the extraordinary ray). G. Nomarski invented a modified Wollaston (1952) prism which is used nowadays with both lower and high power objective lenses. In contrast to conventional Wollaston prisms, the o.a. of a modified Wollaston prism is inclined relative to the entrance and exit faces of the prism. As a consequence the splitting plane of the latter lies outside the prism.

[xii] A uniaxial crystal has only a single optical axis that indicates the direction in which the crystal behaves like an isotropic material, i.e. not birefringent. A birefringent material has the property of exhibiting two different refractive indices with different directions of orientation to waves that enter it with different polarisations.

two orthogonal components. As they leave the prism a very small distance shifts them laterally.

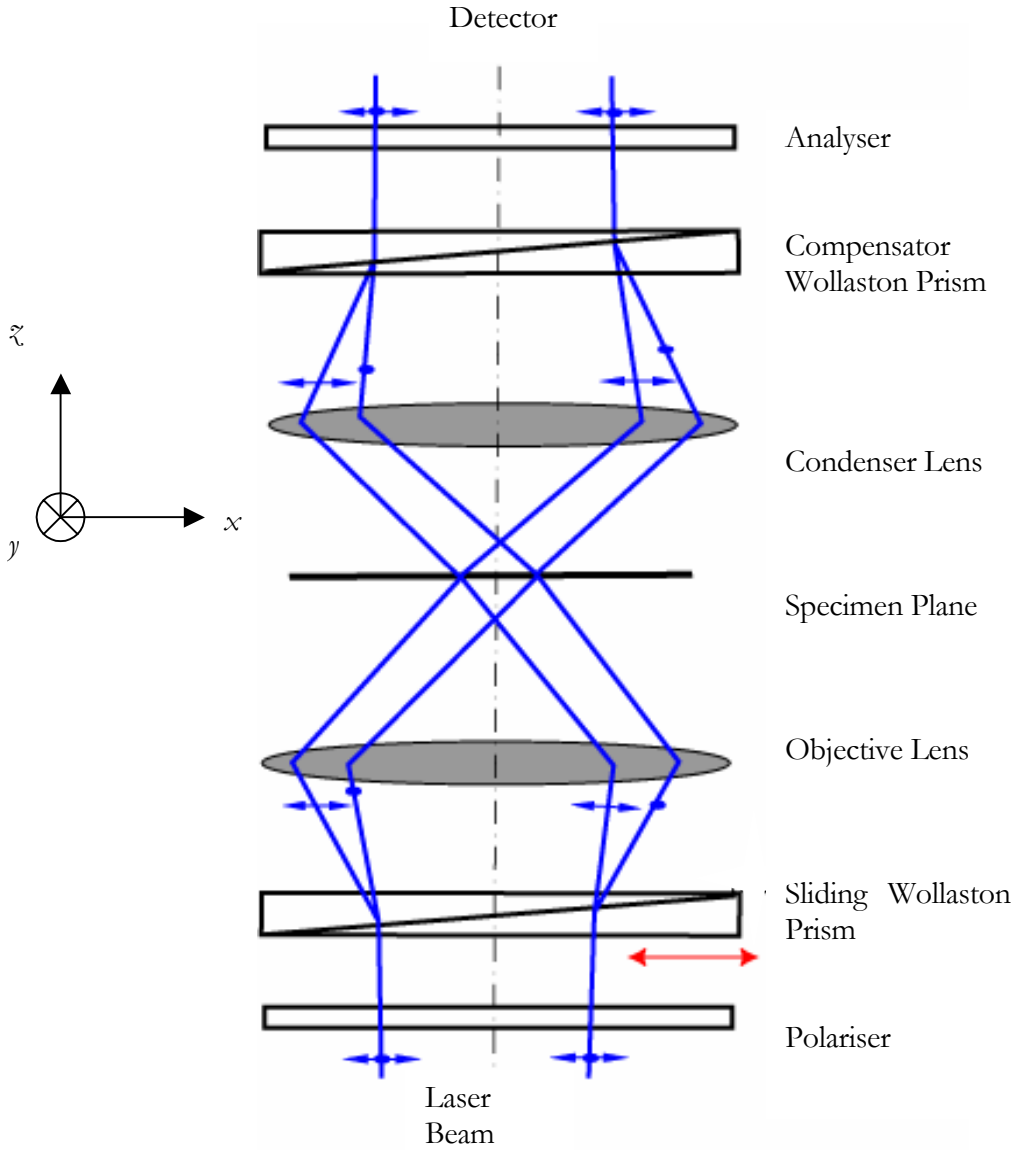

Figure 3.4. Schematic of DIC configuration in the Olympus IX inverted microscope. The DIC microscope is equipped with special optics that convert phase differences to amplitude differences: the polariser and analyser that create the necessary conditions for interference, and two Wollaston prisms that split and then recombine the illuminating beam into two components separated at the specimen's plane by a very small lateral shear. The orientation of the analyser is set such that its direction of light vibration is at 90° with respect to the polariser's direction of vibration, in other words the polars are crossed. The sliding Wollaston prism is placed such that its fringes are in the front focal plane of the objective lens. When the two prisms are perfectly aligned, as illustrated here, then the bias retardation between the two components of the sheared beam is zero. A translation of the sliding Wollaston prism (illustrated by the red arrow) along the direction of the shear produces a nonzero bias value.

The lateral separation distance between these two beam components is called the shear and is usually of the order of the resolution limit of the objective lens (Preza 2000a). After passing through the specimen's plane, where each is either phase advanced or retarded depending on its refractive index and thickness, the two beam components are collected by the condenser and recombined by the second Wollaston prism which is oriented opposite to the first one.

Figure 3.4 represents a particular case when the two Wollaston prisms are perfectly aligned with one another; in such a case the second one cancels the phase difference introduced by the first prism. Consequently, any remaining phase difference is due to the specimen only. From this one can easily deduce the importance of well-matched prisms and lenses for using DIC imaging as a quantitative tool. An additional phase difference, called bias retardation, can be introduced by sliding the first Wollaston prism perpendicular to the optical axis of the microscope. When a bias of $\pi/2$ is given by sliding the Wollaston prism, a small change in the phase difference $\Delta\phi$ will cause the largest variation in intensity and therefore a maximum use of the dynamic range of the system takes place (refer to Figure 3.2). As one can also see from Figure 3.2, a positive difference between the two interfering beams will result in a lower intensity, and a negative difference will give a higher intensity.

3.4 Calibration of the Microscope

Characterisation of the optical system is the first step to be considered in any image analysis sequence. The characterization process involves calibration measurements of the Wollaston prism slider followed by determination of the lateral shear for the objective lenses used in this work.

3.4.1 Sliding Wollaston Prism Calibration

For the calibration of the slider prism position in terms of bias, θ_b, the intensity for the entire range of possible prism positions, in the absence of a specimen was measured. In this case the measured light intensity, *I(x)*, is a simple function of the phase bias, θ_b:

$$I(x) = (1 - \cos\theta_b). \tag{3.1}$$

The microscope lens (Olympus Uplan Apo *40* × */0.85*-NA) was set up to image an apparently empty volume of the specimen consisting of a *176* μ*m* thick cell -containing index matching oil (*n = 1.460*).

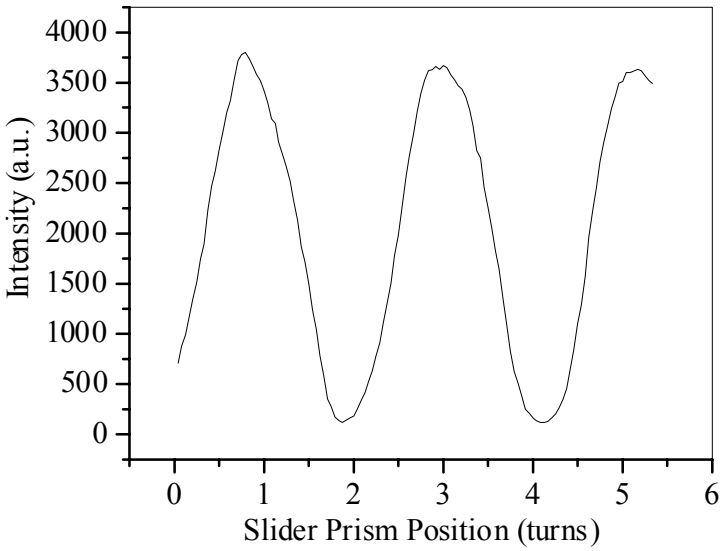

Figure 3.5. Effect of the slider prism position on intensity. The microscope was set up to image an apparently empty volume of the specimen with crossed polarisers. Intensities were measured as a function of slider prism position and averaged over a *512* × *512* (*0.28* μm pixel size) region. The slider has been advanced 20 steps per turn.

Figure 3.5 shows the measured intensity as a function of the number of the screw turns for the full range of possible prism positions. The measured

intensities were an average over a 512×512 pixel region. As the data shown in Figure 3.5 covers more than a complete period, one can calibrate the relationship between θ_b and the slider prism position. Considering that the zero point for θ_b corresponds to the slider position with minimum output intensity and each turn of the slider away from the zero point corresponds to $\theta_b = 2\pi$ radians divided by the number of points in a period (52), one step of the slider prism adjustment screw corresponds to $6 \pm 1°$ for θ_b. The range of θ_b was found to be $-360° < \theta_b < 540°$. In theory, under coherent illumination, the minimum intensity is zero when the phase due to the specimen is zero and the DIC bias is set to zero radians.

3.4.2 Wavefront Shear Characterisation

The magnitude of the wavefront shear is established by the manufacturer of the Wollaston prism and is usually of the order of the objective lens Rayleigh resolution. Each objective lens has a prism specifically designed for it. Knowledge of the lateral shear introduced by the Wollaston prism is crucial to quantitative interpretation of DIC images. The objective lens used in this work was $40 \times /0.85\text{-}NA$. The direction of the shear in this microscope is expected to be at 135 degrees with respect to the horizontal axis (x) of the microscope. The next two sections present two ways of measuring the lateral shear: one, an empirical approach, which is considered in the literature the standard method, and the second one, is a new approach developed by the author employing methods from near field optical microscopy.

3.4.2.1.1 The Empirical Approach

The lateral shift introduced by the DIC microscope can be seen when imaging a small object. For the *40* × */0.85-NA* lens, the shear value was empirically determined from the DIC image of a small bead using a method similar to the one described by Van Munster *et al.* (1997).

An image of a transparent small polystyrene microsphere, (Polysciences, Inc. $n = 1.59$), having a diameter of 0.365 ± 0.014 μm was recorded in order to measure the lateral shift produced by the microscope (see Figure 3.6.). The image was recorded with bias retardation set to $\pi/2$. The double image, one dark and one light, of the microsphere is formed as a result of the lateral shift.

Prior to the measurements several beads were attached to the inner glass surface of a glass cell by evaporation of the suspension in water. Once several beads were attached, the cell was filled with index matching gel (TMT 5097, AFC Group Pty, Ltd., $n = 1.4812$ at *488* nm). The lateral shear is approximately equal to the distance between the centre of the bright spot and the centre of the dark spot 0.58 ± 0.01 μm, as shown in Figure 3.6b. As expected one can conclude that the direction of the shear is approximately along the *135*-degree angle with respect to the horizontal axis.

This method, although considered important (Preza 2000a) and relatively quick, if one does not consider the time spent in finding the *0.3* μm bead in a field of view of *140* × *140* μm and without mentioning the slide preparation time, is indirect and insufficient as it does not reflect the properties of the lens. The pattern of the interference signal depends not only on the properties of the lens but also on the intensity of each interfering beam. It is thus, justifiable to consider alternative ways of determining this important parameter of the DIC

microscope. For this purpose a new method has been proposed and is discussed in the next section.

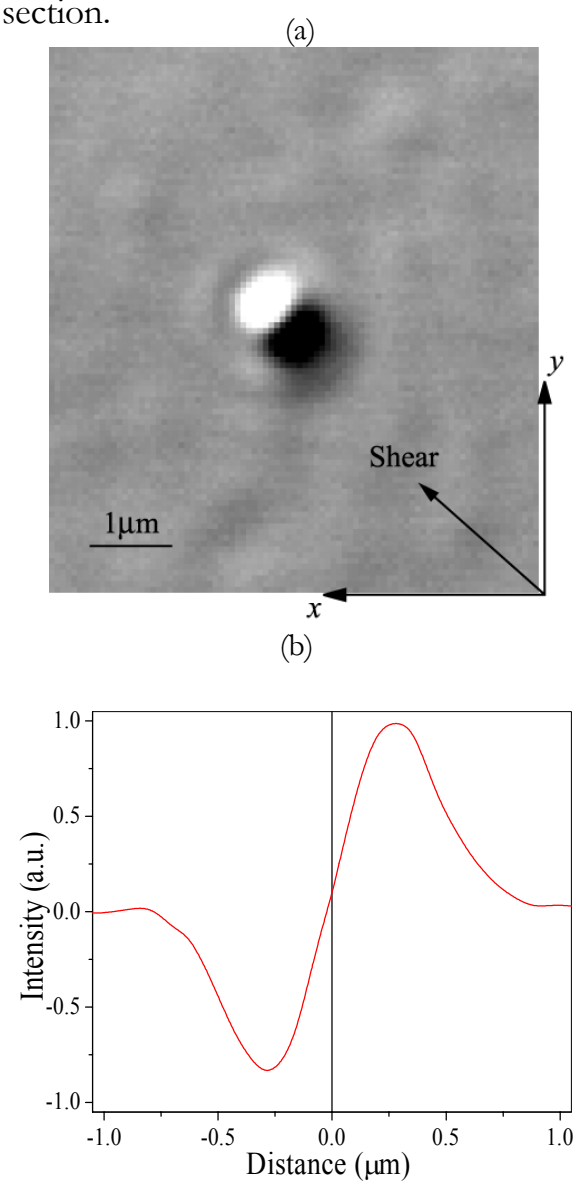

Figure 3.6. Determination of shear of the *40 × /0.85 - NA* lens. (a) An enlargement of a DIC image of a polystyrene microsphere (*365 nm* in diameter) in monochromatic light of *488 nm* with bias setting equal to $\pi/2$ radians. The DIC image was enlarged using linear interpolation for display purposes and shows a bright and dark spot at the edges of the bead. The direction of the shear is along the *135* degree angle. (b) Line profile along the shear direction. The lateral shift (shear) introduced by the microscope is determined by measuring the distance between the centre of the bright spot and the centre of the dark spot.

For comparison the lateral shear was also determined, (Dragomir, Baxter *et al.* 2002) using techniques borrowed from scanning near-field optical microscopy (SNOM). The idea of using a near-field probe (a tapered optical fibre with a sub-wavelength tip) to map the focal plane of an objective is not new. It was first demonstrated for quantitatively mapping the focal distribution of a glass aspheric lens with a numerical aperture of *0.4* (Rhodes, Barty *et al.* 1998). As stated by the authors this method is a high precision experimental technique for characterizing the focal region of a lens which has been compared to theoretical data, obtained from the mathematical formulation of the Fresnel-Fraunhoher diffraction (Born and Wolf 1999).

Experimentally the light describing the separation of polarisation states after the propagation of the laser beam through a polariser and a Wollaston prism at the focal plane of an objective (Olympus Uplan Apo *40* × */0.85-NA*) has been collected using a tapered Cr-coated optical fibre probe tip (Nanonics), with a *100* (± *10%*) nm diameter aperture, fabricated from a fibre that was single-moded at *488* nm. The experimental arrangement for this measurement is presented in Figure 3.7.

The optical fibre tip was mounted on a specially designed three-dimensional fibre positioner used for coarse positioning. This positioner allowed the aligning and centring of the fibre probe perpendicular to the field of view of the objective along the optical axis of the microscope. This was necessary to obtain the laterally symmetric results. Once the probe tip was mounted, it remained fixed and the axial and lateral translation of the objective was controlled via a stepper motor installed on the microscope. The light coupled into the optical fibre was detected by a photomultiplier tube, and the signal amplified and read into the computer.

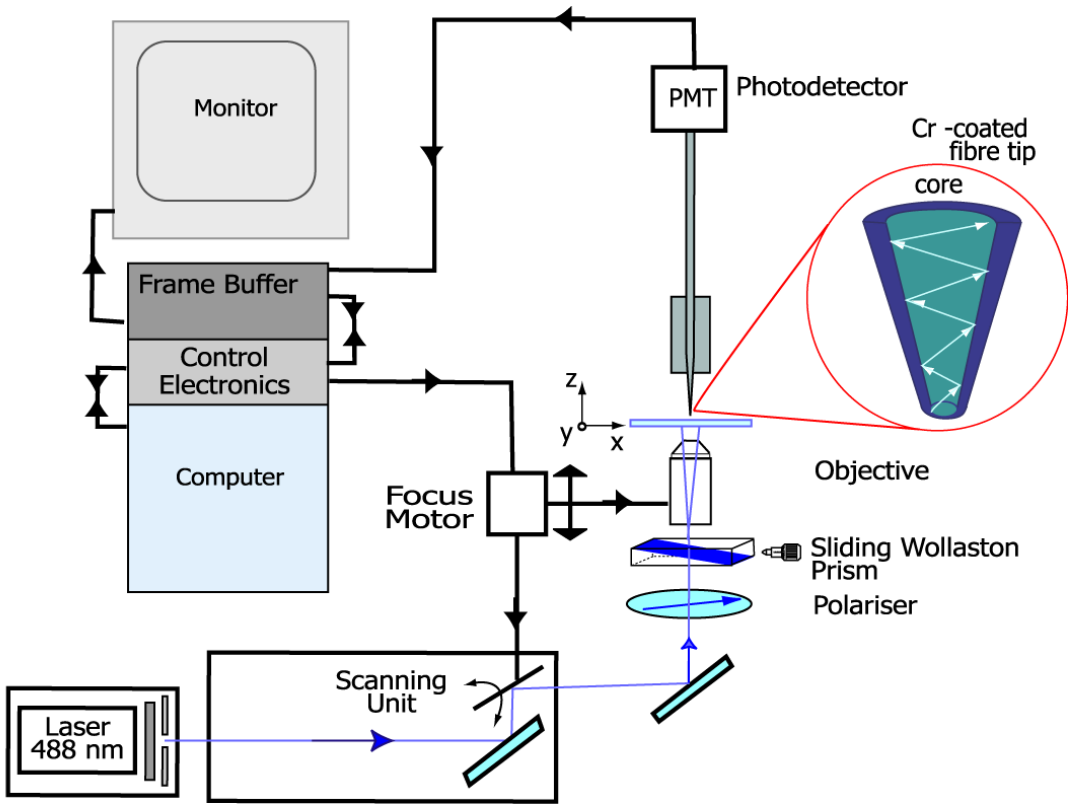

Figure 3.7. The experimental arrangement for the collection mode NSOM utilizing a stepper motor for controlling the objective probe separation. No cover slip was present in the focal region of the objective.

The lateral shear has been directly measured from a line scan along the shear direction in the image, Figure 3.8(a). After fitting with a Gaussian function, the dotted line in Figure 3.8 (b), the shear value was determined to be the distance between the two peaks. The value of the shear in this case was found to be *0.565* ± *0.02* μm. The beam spot diameter of each of the two beams was evaluated as the width of one peak at half the height, and its value *0.59* ± *0.01* μm is in excellent agreement with the theory *0.57* ± *0.01* μm.

Although, the value obtained above shows that the shear was underestimated with 2%, it has been considered negligible as this percentage is actually correctly related to the real error in the measurement.

(a) (b)

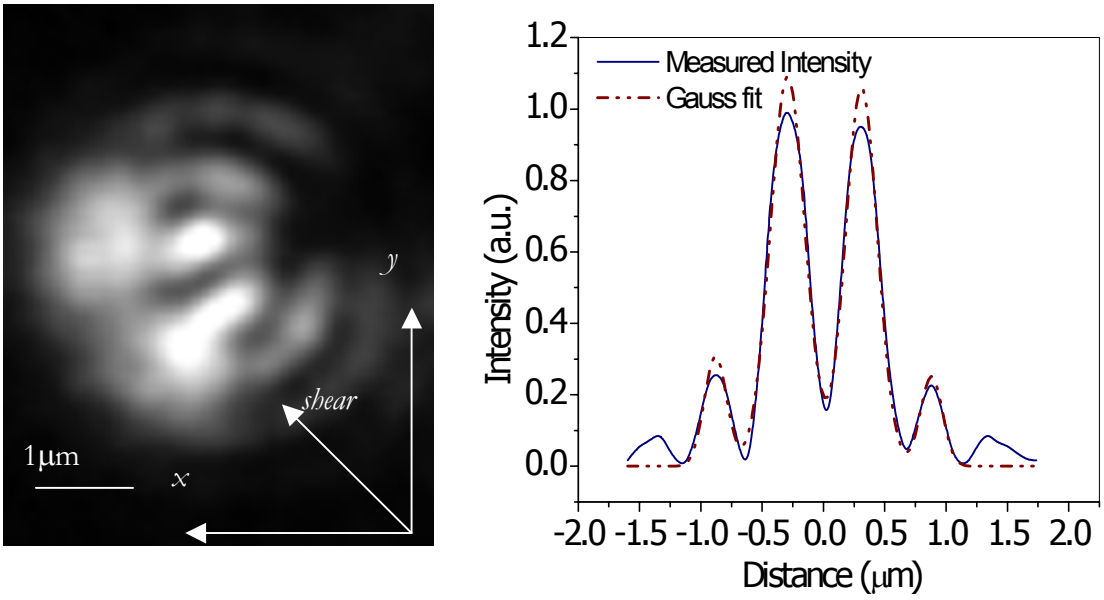

Figure 3.8. (a) Separation of the polarisation states after propagation of a Gaussian beam through the polariser, the Wollaston prism and the objective; measured optical intensity from scans in the axial plane using a near field probe. (b) Cross sectional profile along the shear direction; solid line plots the measured intensity profile; dashed line plots the Gaussian fit.

The focal field produced by a lens has been extensively studied in the past by many researchers. One of the most common ways of describing the focal field when one illuminates a lens, in the paraxial limit, is the so-called Airy pattern: a pattern of concentric dark and bright rings. This section argues that the fibre probe tip scans in a slightly defocused plane situated a distance $z = z_s$ from the

focal plane. Due to this reason, the well-known Airy disk cannot mathematically describe the measured pattern.

A schematic representation of a collection near-field optical microscope is presented in Figure 3.9.

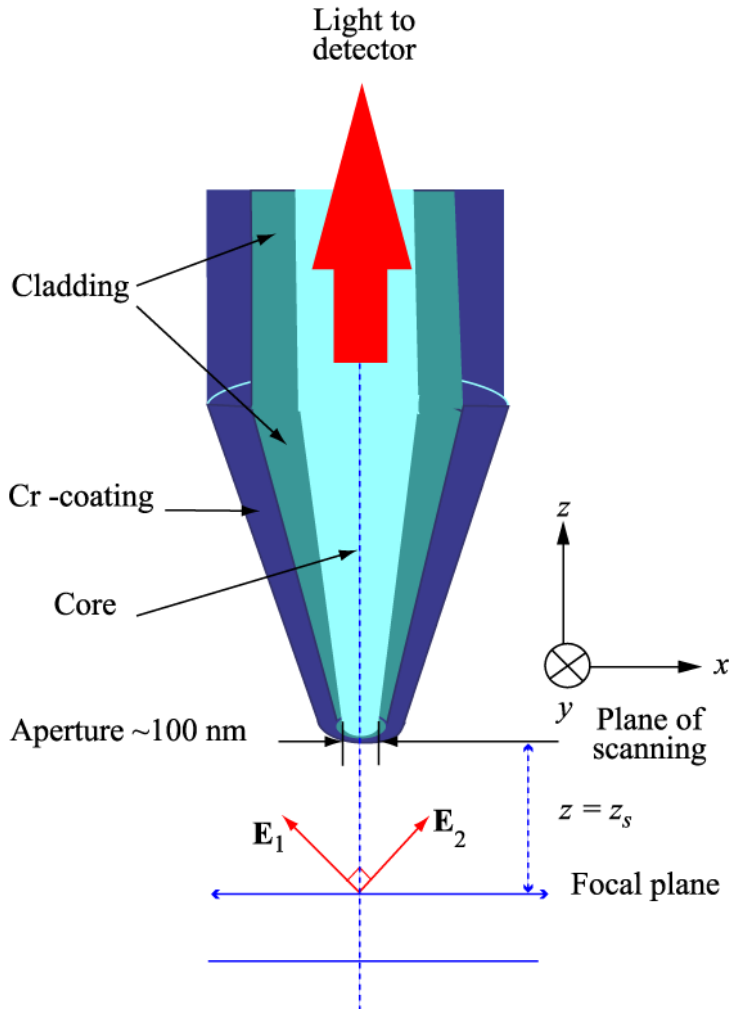

Figure 3.9. Schematic representation illustrating the geometry of the collection near-field optical setup. The plane of scanning is represented by the dashed arrow and is situated at a height z_s from the focal plane. The two propagating fields, orthogonal to each other, are represented by $\mathbf{E}_1$ and $\mathbf{E}_2$ respectively.

The light collected by a near-field probe propagates, toward a detector, in the form of guided fibre modes. A few considerations need to be noted, namely it is assumed that the probe fibre is single moded, possesses axial symmetry with

respect to the fibre axis, is oriented perpendicularly to the plane of scanning and to the electric field, in the absence of the probe. By the nature of the electric field that originates from the polariser this field is linearly polarised. The Wollaston prism splits this linearly polarised field into two orthogonal components $\mathbf{E}_1$ and $\mathbf{E}_2$ respectively. These two polarised waves are to be imaged.

Generally the electric field, $\mathbf{E}(x, y, z = z_s)$, at the point of scanning, can be represented by a plane wave expansion (Clemmow 1966; Greffet and Carminati 1997):

$$\mathbf{E}(\mathbf{r}_T, z_s) = \int \mathbf{E}_0(\mathbf{k}_T)\exp(i\gamma z)\exp(i\mathbf{k}_T \cdot \mathbf{r}_T)d\mathbf{k}_T, \tag{3.2}$$

where $\mathbf{r}_T \equiv x\,\hat{\mathbf{x}} + y\hat{\mathbf{y}}$ is the transverse position vector and $\left(\hat{\mathbf{x}}, \hat{\mathbf{y}}\right)$ the transverse unit vectors of the rectangular coordinate system (x, y, z); $\mathbf{k}_T \equiv k_x\,\hat{\mathbf{x}} + k_y\hat{\mathbf{y}}$ is the transverse wave vector; $\gamma^2 = k_0^2 - k_T^2$ with $k_0 = 2\pi/\lambda = \omega/c$ the vacuum wave number and ω the angular frequency and c is the vacuum speed of light. This expression of the field is established in Appendix B: Plane-Wave Expansion; it is based on a paraxial scalar theory[xiii]. Thus the field is represented as a superposition of plane waves, each of them having complex amplitude $\mathbf{E}_0(\mathbf{k}_T)$ and a wave vector $\mathbf{k} = (\mathbf{k}_T, \gamma)$.

Now, assuming that the probe is illuminated by a sharply focused laser beam whose orientation is collinear to the axis of the fibre probe the electric field from the spot that impinges on the tip consists of the two components $\mathbf{E}_1$ and

[xiii] A vectorial theory (Richards and Wolf, 1959) would have been able to explain better the complicated form of Fig. 3.8 (a). According to this theory, the focal spot is not cylindrically symmetric and cross-components of field may interfere in the superposition.

$\mathbf{E_2}$ separated by the shear, *s*, such that the total electric field at the point of scanning is expressed as:

$$\mathbf{E}(x, y, z = z_s) = \mathbf{E}_1(x, y, z = z_s) + \mathbf{E}_2(x, y, z = z_s). \tag{3.3}$$

Let $I\ (x, y, z = z_s)$ be the optical signal that is detected when the tip is located at the point $(x, y, z = z_s)$ representing the focal point of interest. It is thus clear that the optical signal detected when the fibre tip is located at the point of scanning $z = z_s$ is governed by the propagation of these two fields $\mathbf{E_1}$ and $\mathbf{E_2}$. Assuming the fibre probe is a point-like detector[xiv] and does not modify the near-field distribution at the scanning plane, the signal $I\ (x, y, z = z_s)$ is proportional to the local near-field intensity, defined as the squared modulus of the electric field $|\mathbf{E}(x, y, z = z_s)|^2$.

The experimental conditions were such that the distance between the focal plane and the plane of scanning could not be measured, therefore the z position was considered to be at least $\lambda/2$ from the focal plane such that improved resolution in the measurement was achieved (Williamson, Brereton *et al*, 1998).

It was also considered that the two fields produce Airy disks at the geometrical focal plane being separated by the shear *s*. The Fresnel diffraction pattern has been modelled for two situations: namely at the focal plane and out of focus. The in-focus intensity is the modulus squared of the light field satisfying condition (3.2) and (3.3) and it has been considered of the form:

$$I_{focus}(x, y) = (\pi N)^2 \left[\left[2\frac{J_1(\nu_1)}{(\nu_1)} \right]^2 + \left[2\frac{J_1(\nu_2)}{(\nu_2)} \right]^2 \right], \tag{3.4}$$

[xiv] The size of the probe is significantly smaller than the laser beam size

where $N = \frac{d^2}{\lambda f}$ is the Fresnel number, $2d$ represents the diameter of the objective lens, f is the focal distance, λ is the wavelengths of the incident light, $J_1(v)$ is the first-order Bessel function (Goodman 1996) and v is a dimensionless parameter representing the radial optical coordinate expressed as a function of the radial coordinated r, for the two fields separated by the shear s, along the 135 degree-angle in the xy-plane:

$$v_1(r_1) = \frac{2\pi d}{\lambda f} r_1, \qquad r_1 = \sqrt{(x + s/2)^2 + (y - s/2)^2} \tag{3.5}$$

$$v_2(r_2) = \frac{2\pi d}{\lambda f} r_2, \qquad r_2 = \sqrt{(x - s/2)^2 + (y + s/2)^2}.$$

The Fresnel diffraction in a defocus plane, generally has a much more complicated form and has been modeled starting from the Fresnel diffraction formula (Gu 1996):

$$I_{defocus}(v,u) = \left| 2\pi i N \exp(-ikf) \exp\left(-\frac{iv^2}{4\pi N}\right) \int_0^1 \exp\left(\frac{iu\rho}{2}\right) J_0(v\rho)\rho d\rho \right|^2 \tag{3.6}$$

where $\rho = \frac{r}{d}$ is the normalised radial coordinate over the lens aperture, $u = 4kzNA^2$ [xv] is a dimensionless parameter representing the axial optical coordinate introduced here to characterize the defocus Δz and $J_0(v)$ is a Bessel function of the first kind of order zero (Goodman 1996). This field can be evaluated by numerical integration and the full derivation is presented in

[xv] The term u is usually defined in the literature in the conventional manner, paraxial approximation, as [illegible], (Hamilton and Sheppard, 1982). The coordinate u defined as [illegible] accommodate systems having numerical apertures higher than 0.7. This definition of the axial coordinate, also termed, pseudoparaxial approximation, provides a 1% better description of the depth of focus of a high NA system compared to the conventional one (Sheppard and Matthews, 1987).

Appendix C: Diffraction Pattern in a Defocused Plane. The expression for the intensity of the image at an arbitrary defocus position due to the two orthogonal fields expressed by (3.2) is:

$$
\begin{aligned}
&I_{defocus}(v,u) \\
&\cong \left| 2\frac{J(v_1)}{v_1} + \frac{iu}{2}\left[2\frac{J_0(v_1)}{2} + \frac{2\left(1/2v_1^2 - 2\right)}{v_1^2}\frac{J_1(v_1)}{v_1} \right] + \frac{iu^2}{2!}\left[\frac{8}{3}v_1^2\left(-12 + \frac{3}{2}v_1^2\right)J_0(v_2) + \frac{16}{3}v_1\left(-3v_1^2 + 12 + \frac{3}{16}v_1^4\right)J_1(v1) \right] \right|^2 \\
&+ \left| 2\frac{J(v_2)}{v_2} + \frac{iu}{2}\left[2\frac{J_0(v_2)}{2} + \frac{2\left(1/2v_2^2 - 2\right)}{v_2^2}\frac{J_1(v_2)}{v_2} \right] + \frac{iu^2}{2!}\left[\frac{8}{3}v_2^2\left(-12 + \frac{3}{2}v_2^2\right)J_0(v_2) + \frac{16}{3}v_2\left(-3v_2^2 + 12 + \frac{3}{16}v_2^4\right)J_1(v_2) \right] \right|^2 .
\end{aligned}
\tag{3.7}
$$

Simulations presented in this section are in the horizontal *xy*- plane (i.e. parallel to the stage of the microscope) for two situations namely; in focus and out of focus. The vertical direction represents the intensity, and the other two directions are perpendicular to the optical axis of the microscope.

Figure 3.10a illustrates the intensity at the focal plane where one can see that the diffraction rings have a low visibility. The images have been normalised to the primary maximum such that the diffraction rings are also visible in the image. On defocusing, Figure 3.10 b, more energy is present in the diffraction rings and less in the primary maximum. Figure 3.10 c and d show a surface plot of the two situations represented in Figure 3.10 a and b for the case of equal strength beams; where the shear *s* has been taken to be *0.5* μm along the *135* degree angle. Hence, if there is an error in the choice of the *z* positioning for the in-focus plane it affects the diffraction pattern at this point. Comparing this situation with the measurements presented in Figure 3.8, it may be considered that the actual measurement may have been taken place at a distance approximately equal with the wavelength from the focal point.

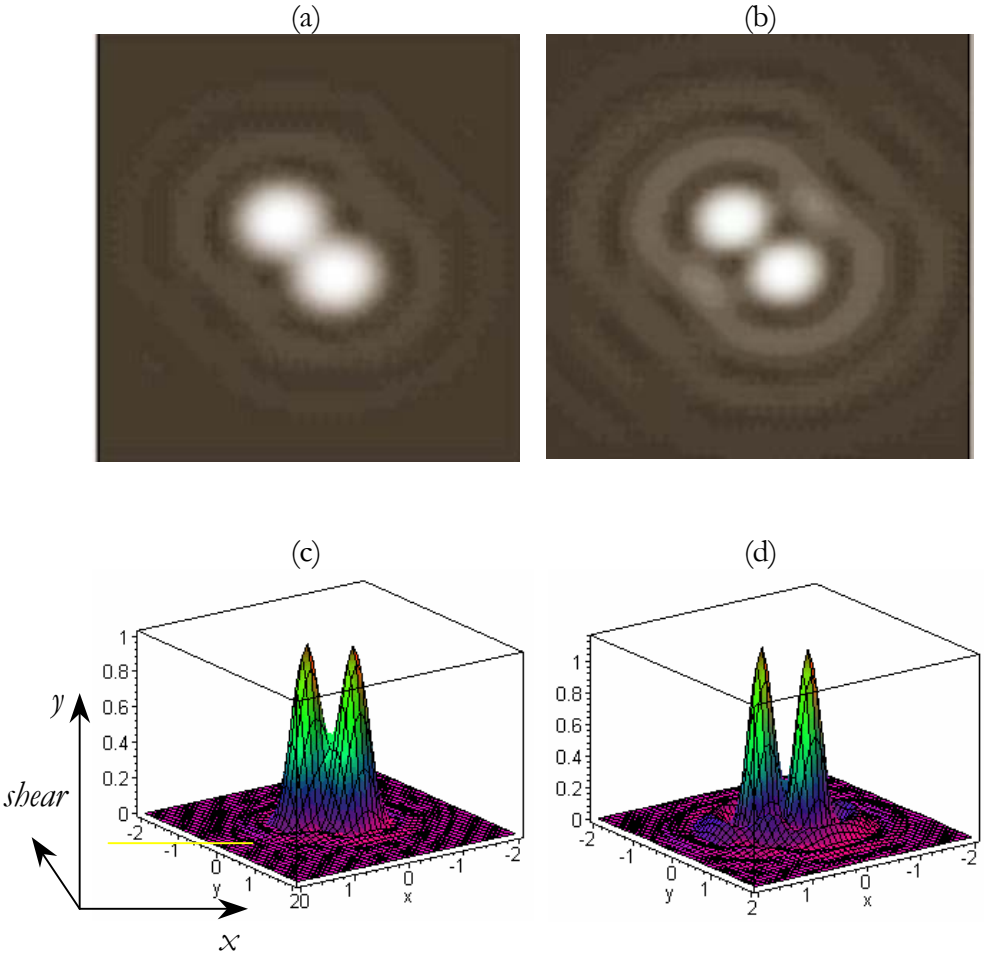

Figure 3.10. Calculated light field intensity in a differential intensity microscope: (a) in focus; (b) out of focus at a distance ~*0.6* μ*m* from the focal plane. (c) and (d) intensity plot contours of the diffraction pattern displayed in (a) and (b) respectively, showing equal strength beams. The distance between the centres of the two bright spots, in each case, is equal to the lateral shear s. The direction of the shear was considered to be along the *135*-degree angle. The scale bar is approximately *1* μ*m*.

3.5 Sensitivity Measurements in a Differential Interference Contrast Imaging System

In the previous section characteristics of the lateral shear were determined while this section discusses the sensitivity of DIC imaging to the refractive index of the immersion fluid and to the magnitude of lateral shear.

3.5.1 Sensitivity of DIC Imaging to Refractive Index of the Immersion Fluid

The refractive index of the embedding agent has been measured using an Abbe refractometer having as a light source the *488 nm* line of an argon ion laser, the same light source as used for imaging the optical fibre throughout this thesis; details of the refractive indices of the various matching fluids used in this section are presented in Table 3.1.

The Er^{3+} doped fibre[xvi] was chosen for its specific fine structure surrounding the core to test the sensitivity of DIC imaging of optical fibres to the refractive index of the embedding fluids shown in Table 3.1.

Table 3.1. Characteristics of immersion fluids used as embedding agent measured at 25 °C.

Immersion fluid	Manufacturer	Label	Refractive index
Coupling gel[xvii] Dorran 05 - 00097	3M Fiber Optic Products	G_1	1.4674 ± 0.0002
Index matching gel TMT 5097	AFC Group Pty. Ltd.	G_2	1.4812 ± 0.0002
Index matching oil	Cargille Laboratories Inc.	O_1	1.4635 ± 0.0002
Index matching oil	Cargille Laboratories Inc.	O_2	1.4576 ± 0.0002

In order to reduce the noise in the images and because it has been shown that theoretical DIC modelling of small transparent test objects are in good agreement with measurements for small apertures (Preza 2000a), the fibre has been imaged with the condenser aperture partially closed. The condenser aperture iris can be opened and closed with an uncalibrated slider. For

[xvi] The Er^{3+} doped fibre having a *2500* ppm ion concentration has been provided by Laboratoire de Physique de la Matière Condensé (Université de Nice, Sophia- Antipolis , France).

[xvii] This coupling gel together with the index matching gel are standard matching fluids used in the Telecommunication Industry.

simplicity only two-dimensional section images are shown. Each two-dimensional image is a cut through the middle of a three-dimensional volume.

The effect of the change in refractive index of the embedding fluid on the image is clearly seen in Figure 3.11. The images present the phase variations converted to intensity variations; differences in refractive index of the neighbouring points along the shear direction are visualised as intensity variations. Hence the fibre is perceived as gradients of its refractive index (or optical path length); steep slopes are emphasized and appear in sharp contrast to the image background level.

When the fibre is immersed in a fluid having a refractive index $n_{G2} = 1.4812$ which is (greater than the fibre's clad refractive index) the inaccuracy starts at the outer layer, (the clad-oil boundary) and is propagating inside it, Figure 3.11a, b. In this situation as the difference in refractive index of cladding and fluid is relatively high, as presented in Figure 3.11a,b, it is evident that reflection from the oil fibre interface takes place. Moreover, the reflection coefficient from a cylindrical surface is position dependent such that it affects the intensity distribution of the transmitted light across the fibre.

In addition internal reflection becomes significant as the fibre-oil refractive index difference increases. Furthermore, the fibre acts like a lens and focuses light. The focal length, f, of such a cylindrical surface depends on the fibre radius, r and the cladding–oil refractive index difference $(n_{cladding} - n_{oil})$ and from the thick-lens formula:

$$\frac{1}{f} = (n - n')\left(\frac{1}{r_1} - \frac{1}{r_2}\right) + \frac{(n - n')^2 t}{n r_1 r_2} \tag{3.8}$$

where n is the refractive index of the lens, r_1 and r_2 are its radii , t is the lens thickness and n' is the refractive index of the medium surrounding the lens.

Therefore for a cylindrical fibre of diameter $2r$, the radius $r_1 = r$ and $r_2 = -r$ (where the minus sign is due to the sign convention in geometric optics), $t = 2r$, the focal length f may be expressed as:

$$f = \frac{n_{cladding} r}{\left(n_{cladding} - n_{oil}\right)} \tag{3.9}$$

It is not difficult to see that as the refractive index of the oil increases the focal point becomes closer to the fibre output surface such that the optical rays traversing the fibre suffer from deflection from their parallel propagation, which in turn affects the intensity distribution of the light inside the fibre as shown in Figure 3.11a and b.

On the other hand when a good matching occurs, the focal length is far greater than the fibre diameter, meaning that the lensing effect of the fibre is significantly reduced and the optical rays are practically parallel inside the fibre. This situation is encountered in Figure 3.11 c, d. As can be seen the highest spatial resolution is obtained when the refractive index is close to $n_{O2} = 1.4576$. Note how the images of the fibre edges become increasingly larger as the refractive index increases and the core of the fibre is poorly resolved as the refractive index of the embedding fluid is increased to $n_{G2} = 1.4812$. The horizontal axis of the line profiles in Figure 3.11 is measured in μm units with the intensity on the vertical axis measured in arbitrary units.

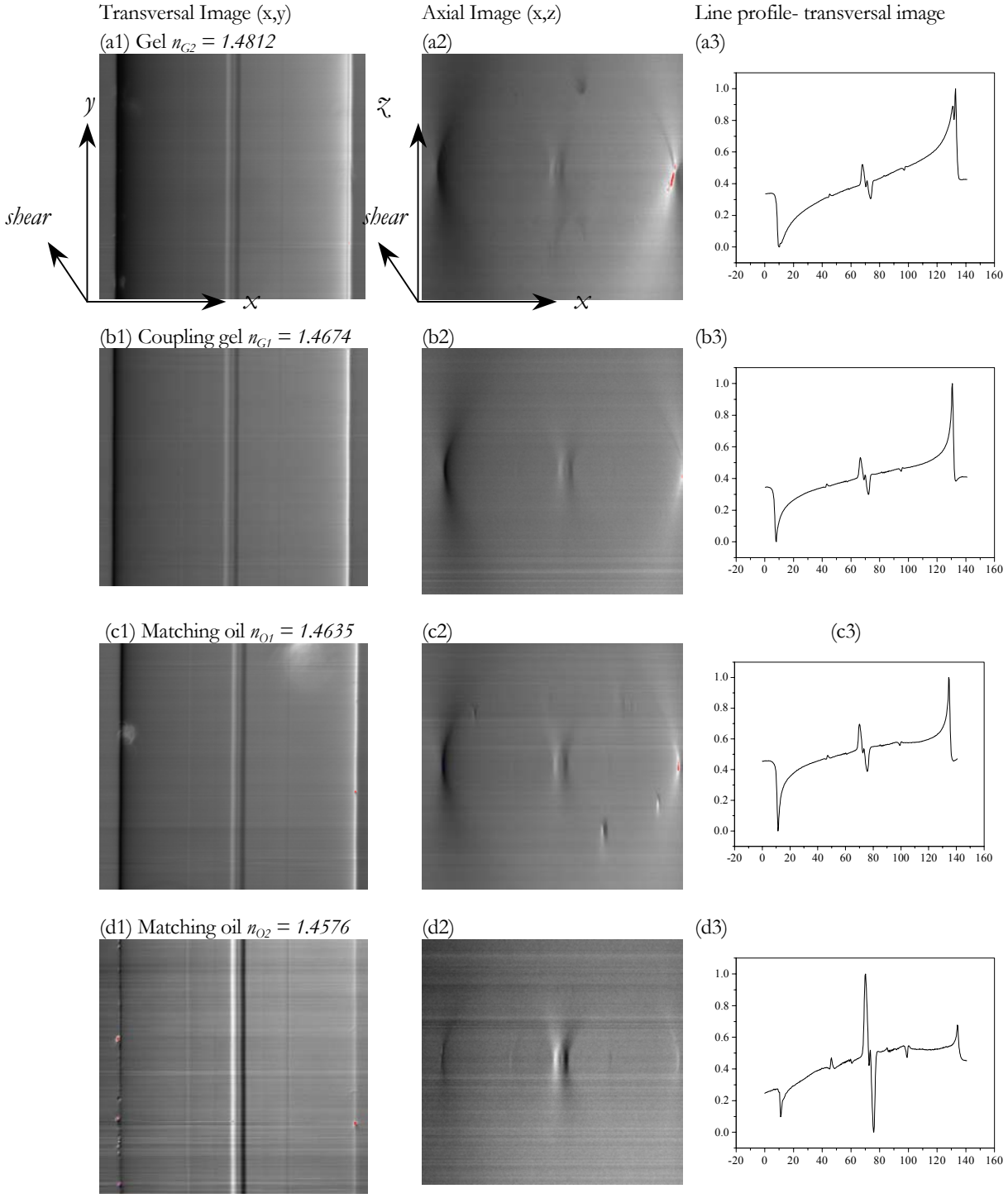

Figure 3.11. Effect of refractive index of the embedding fluid in the measured DIC image of an optical fibre. The far right column shows a line profile through the middle of the images on the far left. The images presented here are raw, uncorrected for the characteristic non-uniform illumination of DIC imaging therefore in the intensity line profile one can easily observe a linear intensity component near the axis of the fibre.

When the immersion liquid has a refractive index $n_{O2} = 1.4576$, which is near the fibre cladding refractive index, the optical difference between the cladding and the liquid is very small, thus the beam that traverses the liquid to the fibre has angles of incidence and refraction nearly equal. Hence, feature details in the core region, including the deposition layers surrounding it, are well resolved.

It is well known that a change in temperature will cause a change in the refractive index both in the immersion liquid and fibre. A temperature increase will induce a decrease in the refractive index for $n_{O2} = 1.4576$. This change causes little variation in the DIC image, especially in the region of interest: i.e. the core of the fibre, as shown in Figure 3.12 due to the different values of the temperature coefficient for silica and the oil correspondingly[xviii]. Figure 3.12a and b present two DIC images of the same central section of a single mode fibre (SMF-28 Corning®), measured at temperatures of *24.10* °C and *29.40* °C[xix]. The two images are almost identical in the core region with significant change occurring only at the cladding/oil interface as can be appreciated in Figure 3.12 c where a comparison of the two normalised intensity profiles is shown.

[xviii] $dn/dt)_{silica} = + 11.9 \times 10^{-6}/°C$; $(dn/dt)_{oil} = - 38 \times 10^{-5}/°C$

[xix] This was the room temperature and not only the temperature of the embedding oil.

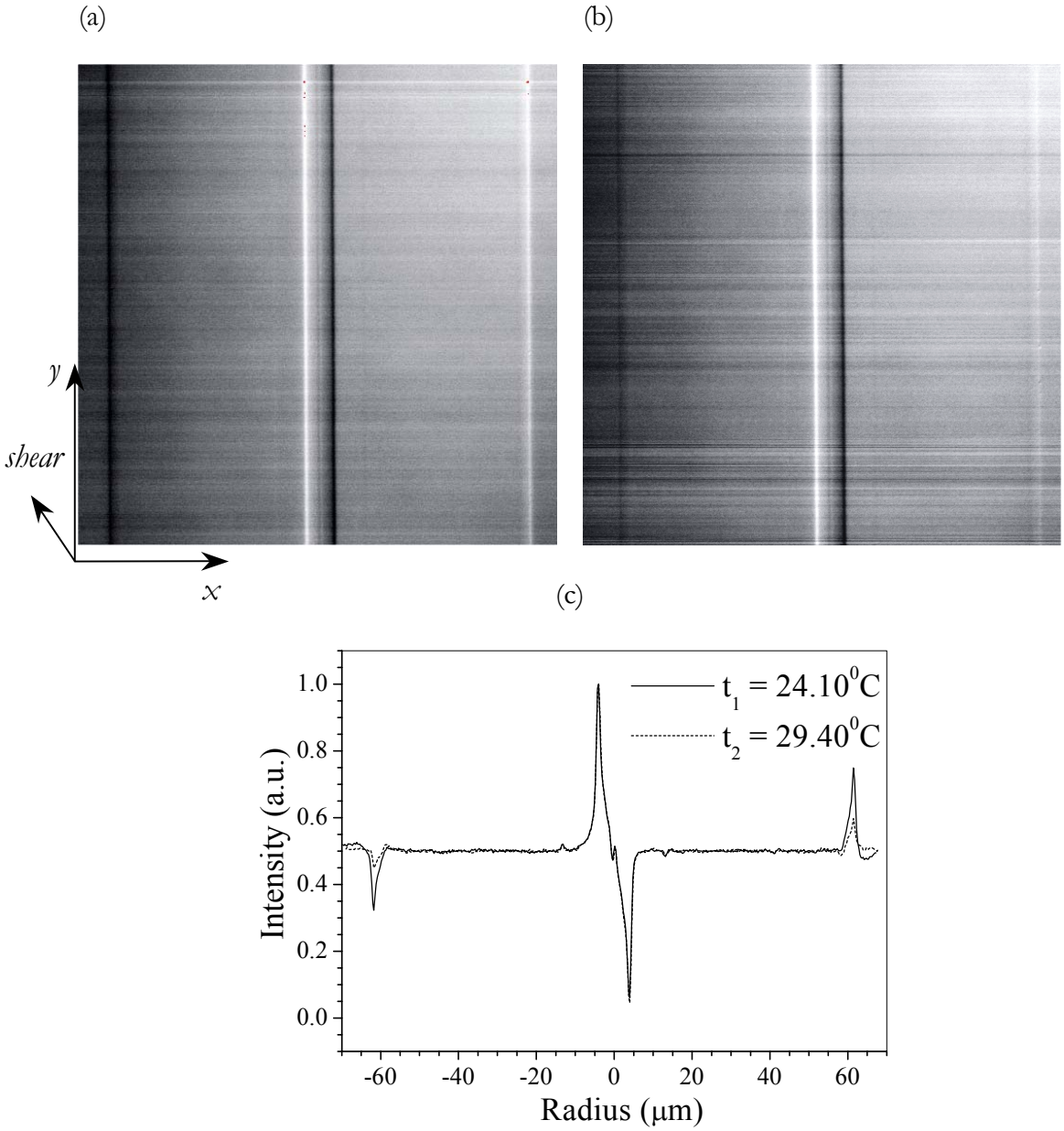

Figure 3.12. Effect of temperature change on the DIC image of an optical fibre in the case of very well index matched situation. The measurements were taken at *24.10* ºC and at *29.40* ºC in figure (a) and (b) respectively with the fibre immersed in index matching oil $n_{O2} = 1.4576$. A plot profile of the normalised intensity shows little difference for the two measurements. Here the presence of some horizontal lines degrades the quality of the images, it is believed that they are caused by the aliasing of the scan period with periodic fluctuations in the laser.

3.5.2 Sensitivity of DIC Imaging to the Orientation of the Fibre

To test for the direction sensitivity of DIC imaging, we measured images of the optical fibre acquired at different orientations. The imaging conditions were as described in the preceding section. Due to the lack of a rotational stage, the optical fibre was rotated by hand.

During the actual imaging process all precautions necessary for acquiring high quality DIC images ((Inoue 1994) pages 405 – 412)[xx] with thin optical sections have been taken.

At the first orientation of the fibre (shown in Figure 3.13) the shear direction makes a *45* degree angle with the edges of the fibre. As the fibre is rotated clockwise, the phase-gradient information of the optical fibre diminishes when the fibre is oriented along the direction of the shear. For this reason, all the other images presented in this Thesis have been acquired with the fibre orientated as in Figure 3.13a. It is evident that Figure 3.13 gives information about the symmetry of the fibre, as the width of the optical fibre edges is the same, suggesting that the imaged fibre has a cylindrical symmetry making easier the quantitative analysis with respect to the refractive index distribution.

[xx] Insuring that (a) well-corrected high-NA objective and condenser lenses are used with the condenser properly focused; (b) the full-aperture illumination of the condenser and uniform field of illumination of the object to be images is achieved; (c) the stray light is minimised; (d) the motion of the condenser and objective lenses is coordinated to maintain the parfocal illumination of both lenses. Although careful settings of specific parameters have been accordingly accomplished, the latter condition was not fully satisfied; this led to some blurring seen in the optical sections of fibre Bragg gratings presented in Chapter 5.

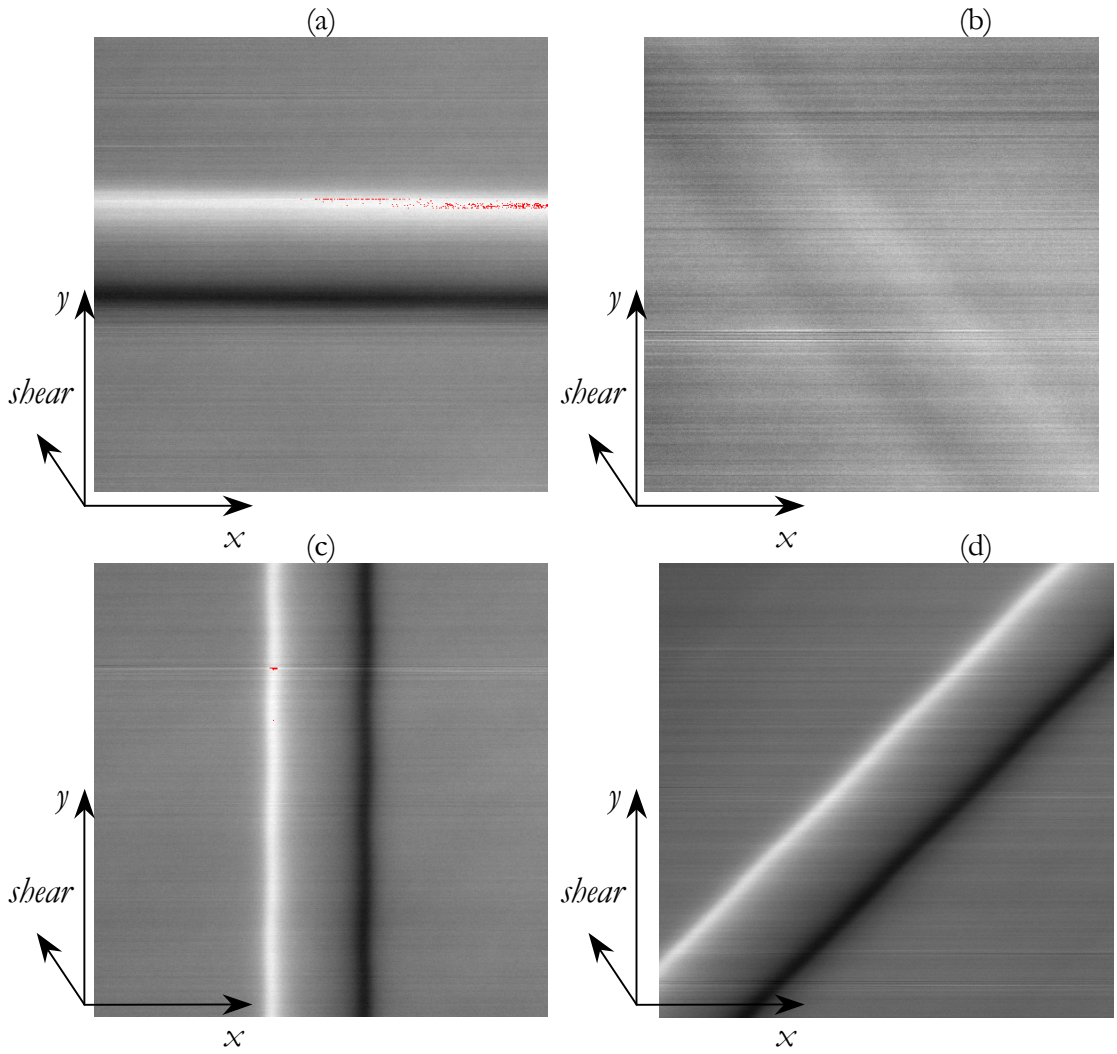

Figure 3.13. Measured DIC images of an optical fibre. Images were acquired with a *40 × /0.85 – NA* and a *0.55 NA* condenser with the aperture partially closed at different orientations of the fibre. (b) the fibre is rotated by *45* degrees clockwise from position (a); (c) the fibre is rotated by *45* degrees clockwise from position (b); (d) the fibre is rotated by *45* degrees clockwise from position (c). The section images are cuts through the three-dimensional images and are at the best focus of the objective lens. The horizontal lines are possible due to aliasing of the scan with the periodic fluctuations in the laser; they disappeared after the laser has been changed.

3.6 Summary

A brief description of the operation of a DIC microscope has been presented and illustrated. Calibration of essential parts of the microscope, namely the Wollaston prism and lateral shear, used in Nomarski DIC microscope setup has been described.

Firstly the calibration of the sliding Wollaston prism was performed by acquiring images from an empty slide at different positions of the prism. This is an important aspect of the imaging system as it provides the microscope's bias retardation setting, which is needed for computational DIC.

Secondly, two methods for quantifying the lateral shear of the microscope using a *40* × objective have been compared. One was an empirical method for measuring the lateral shear by imaging a latex microsphere. The other one was a high precision experimental technique for the measurement of the intensity distribution in the focal region also employed for determining the lateral shear. The latter was achieved by employing a near field probe (a tapered optical fibre with a sub-wavelength tip), which was scanned through the region of interest. A mathematical explanation and a modelling of the measured intensity, believed not to be in the focal plane, have also been presented.

Thirdly the sensitivity of DIC imaging of an optical fibre to the refractive index of the immersion fluid and to the direction of imaging has been examined. It was observed that the DIC image of an optical fibre is perceived as gradients in its refractive index with steep slopes being emphasized and presented in sharp contrast to the image background level. It was also found that the refractive index of the embedding fluid, though not critical, plays an important role in resolving fine structure of an optical fibre.

In Chapter 4 the mathematical framework needed for a theoretical understanding of the imaging model used throughout this work will be presented.

4 Estimation of the Refractive Index

4.1 Overview

This chapter introduces the methodology suitable for reconstructing the refractive index of an optical fibre using a differential interference contrast (DIC) microscope, presenting the advantages and limitations of this approach. It includes a mathematical framework needed for a theoretical understanding of the imaging model used throughout this work with emphasis on its relationship to the refractive index of an optical fibre. Relevant application to areas such as annealed fibres, new fibres such as the Bragg fibre are then considered to test the applicability of the method. A comparison of the present method with other available methods for obtaining the refractive index profiles of optical fibres is presented.

4.2 The Imaging Model

The general image formation model for transmitted-light in Nomarski DIC microscopy, under partially coherent illumination has been considered in this work. The imaging model on which we based our calculations was derived from the frequency theory of partially coherent illumination (Cogswell and

Sheppard 1992; Preza, Snyder and Conchello 1996). This has been achieved by propagating the intensity of the light through the optical system based on the theory of image formation in partially coherent light for transmission optics (Born and Wolf 1980).

In what follows, the characteristics of the imaging model are presented.

As mentioned in Section 3.3, in a DIC microscope the interference is achieved by splitting the incoming light into two components that are phase shifted relative to each other and are separated by a very small lateral shear (in the order of the wavelength of the light used). The phase difference between the two waves is due to the fact that the waves travel through different regions of the object. Also, the sliding Wollaston prism introduces an additional uniform phase difference between the two waves, called the bias retardation (usually expressed in radians).

In the assumption of coherent illumination, perfect polarising components and no instrumental stray light (i.e. the extinction factor[xxi] is at infinity), in the case of a zero phase difference (i.e. no object), the amplitude difference between the two waves is represented by the complex valued function (Preza, Snyder and Conchello 1999) also called the point spread function (PSF) of the DIC microscope or the DIC PSF:

$$h(x,y) = (1-R)e^{-i\Delta\theta}\, k(x-s,y) - R \cdot e^{i\Delta\theta}\, k(x+s,y) \tag{4.1}$$

where the shear parameter s is considered to be along the x axis, R is the amplitude ratio, defined as the amplitude of one wave divided by the sum of amplitudes of the two wave fields, $\Delta\theta$ represents the bias retardation, $k\ (x,y)$ is

[xxi] The extinction factor describes the degradation due to instrumental stray light; is defined as the ratio of the maximum and minimum light intensities transmitted by the DIC microscope at a bias equal to π and 0 radians respectively. In practice it places a limit on the weakest phase object that can be observed.

the amplitude PSF for transmission optics under coherent illumination; the amplitude PSF being defined by the Fourier transform of the pupil function (Goodman, 1996 p. 111). The amplitude ratio, *R*, is determined by the orientation of the polariser and the analyser; for crossed polars $R = 0.5$, yielding equal-strength illuminating beams.

It can be shown that under coherent illumination, which corresponds to closing the condenser aperture down to a single point, the intensity in the image at a point (x, y) is expressed as an integral (Preza 2000a):

$$I(x,y) = \frac{a}{(\lambda f_{con})^2} \left| \int_{-\infty}^{+\infty}\int_{-\infty}^{+\infty} f(x_0, y_0) h(x - x_0, y - y_0) dx_0 dy_0 \right|^2, \tag{4.2}$$

where a is the intensity of the light source at points that lie inside the circular aperture of the condenser lens, λ is the wavelength of the illumination light, f_{con} is the focal length of the condenser lens, $f(x_0, y_0)$ is the complex-amplitude transmission-function of the specimen. For a phase object having its transmission function of the form:

$$f(x_0, y_0) = \exp(-j\phi(x_0, y_0)), \tag{4.3}$$

and assuming $R = 0.5$, the intensity measured in the image plane for a wavefront shear, s, (very small relative to the size of the specimen) can be approximately related to the gradient of the specimen's phase function $\phi(x,y)$ along the direction of the shear (perpendicular to the optical axis):

$$I(x,y) = I_0 \sin^2\left(s\frac{\partial\phi(x,y)}{\partial x} + \Delta\theta \right), \tag{4.4}$$

where I_0, is the maximum intensity transmitted by the optical system, $\phi(x,y)$ is the object phase change as a result of refractive index variation and thickness,

and $\Delta\theta$ is the bias retardation, an additional phase shift introduced by the first Wollaston prism.

Notably, if the specimen has a small phase gradient and the bias is set to $\pi/2$ radians, the intensity expressed in Equation 4.4, can be approximated as a linear function of the gradient $\phi(x,y)$:

$$I(x,y) \approx \frac{I_0}{2}\left(1 + 2s\frac{\partial\phi(x,y)}{\partial x}\right). \tag{4.5}$$

In this thesis bias retardation introduced by the sliding Wollaston prism is considered fixed at $\pi/2$ for all calculations, consistent with the experimental methodology adopted.

4.3 Recovering Refractive Index from DIC Images of Optical Fibres

The purpose of this section is to establish the formalism for retrieving the refractive index of an optical fibre from its DIC image.

Let us consider a cylindrically symmetric optical fibre of radius R with the z-axis taken perpendicular to the axis of the fibre coinciding with the optical axis of the microscope.

Figure 4.1 represents a cross section in a step index fibre with the refractive index profile $n(r)$, where $r = \sqrt{x^2 + z^2}$ and the y- axis being along the axis of the fibre. The optical path length provides the distortion of the wavefront, $\delta(x,z)$, and is expressed as follows taking into consideration the circular geometry of the fibre:

$$\delta(x,y) = \int_{\Gamma(z)=\overline{AB}} n(x,y,u)du = 2\int_0^{\sqrt{R^2-x^2}} n(x,y,u)du \tag{4.6}$$

where R represents the fibre radius, $\Gamma(z) = \overline{AB}$ is the total length of the medium, see Figure 4.1.

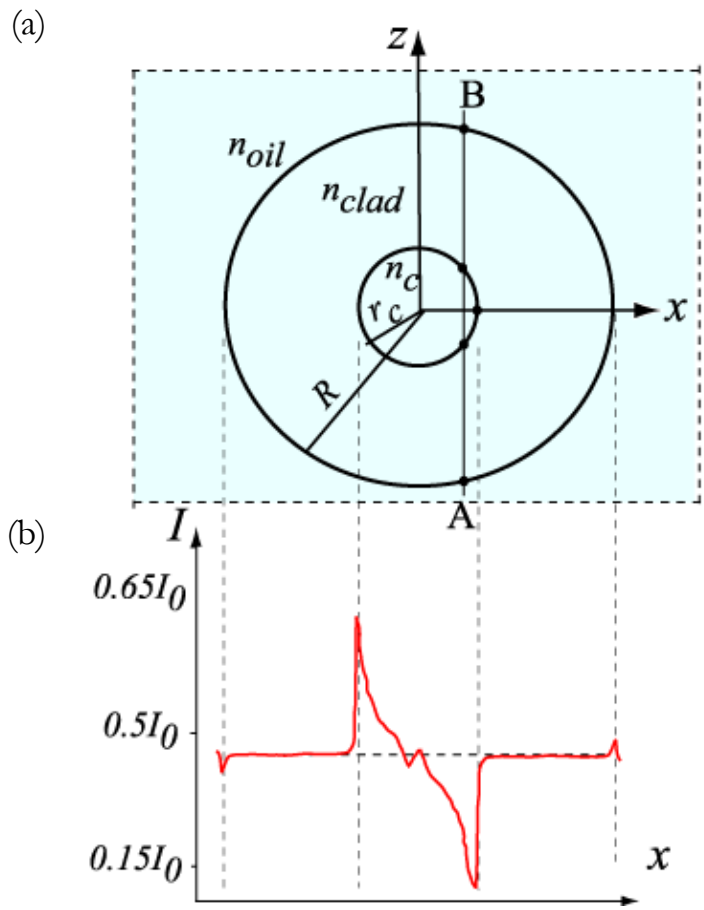

Figure 4.1. (a) Diagram of the cross sectional area of a uniform cylindrically symmetric optical fibre in oil and (b) the DIC image intensity when focussed in the plane containing the fibre centre; r_c represents the core radius, R represents the fibre radius. The refractive index of the oil is temperature controlled and matches the refractive index of the clad. A and B are defined in the text.

Accordingly the phase difference is given by:

$$\phi(x,y)=\frac{2\pi}{\lambda}\delta(x,y)=\frac{4\pi}{\lambda}\int_0^{\sqrt{R^2-x^2}} n(x,y,u)du. \tag{4.7}$$

In order to reconstruct the function describing the refractive index of the fibre, Leibniz theorem[xxii] is used for expressing the phase difference given by (Abramowitz and Stegun 1970):

$$\begin{aligned}\frac{\partial\phi(x,y)}{\partial x}&=\frac{d}{dx}\left[\frac{4\pi}{\lambda}\int_0^{\sqrt{R^2-x^2}} n(x,y,u)du\right]\\ &=\frac{4\pi}{\lambda}n\left(x,y,\sqrt{R^2-x^2}\right)\int_0^{\sqrt{R^2-x^2}} n(x,y,u)du\end{aligned} \tag{4.8}$$

It follows that Equation (4.4) and Equation (4.8) lead to an equation that has to be solved for *n(x,y)* :

$$\pm\frac{1}{s}\left[\arcsin\left(\sqrt{\frac{I(x,y)}{I_0}}\right)-\Delta\theta\right]=\frac{4\pi}{\lambda}\left[n\left(x,y,\sqrt{R^2-x^2}\right)\frac{-x}{\sqrt{R^2-x^2}}+\int_0^{\sqrt{R^2-x^2}}\frac{\partial n(x,y,u)}{\partial x}du\right] \tag{4.9}$$

Performing a numerical integration of Equation (4.9) leads to the refractive index *n(r)* of the fibre.

As can be seen the spatial distribution of the refractive index[xxiii] may be determined by exploiting information about the wavefront passing through the optical fibre. For this purpose the following assumptions must be made: the core and the cladding are cylindrically symmetric and are concentric, the refractive index in the core is a function of the radius only, the refractive index

[xxii] If $d/dx\left(\int_{uu}^{v} f(x,t)dt\right)=\int_u^v(\partial f/\partial x)dt+f(x,v)(dv/dx)-f(x,u)(du/dx)$ then for $\Phi(x,z)=\int_{\alpha(x)}^{\beta(x)}n(x,z)dz$,
$\Phi(x)/dx=n(x,\beta(x))\cdot(d\beta(x)/dx)-n(x,\alpha(x))\cdot(d\alpha(x)/dx)+\int(\partial n(x,z)/\partial x)dz$ is true.

[xxiii] Abel transform (Kalal and Nugent 1988) may also be used in a similar way to retreive the refractive index of circularly symmetric fibres (Kalal and Nugent 1988).

in the core is a continuous function, a suitable matching fluid, whose refractive index is as close as possible to the one of the outer cladding, surrounds the object. Also, knowledge of the working parameters of the microscope such as the bias introduced by the Wollaston prism and the shear must be known.

4.3.1 Sample Selection

The optical fibre can be generally considered to be a weak[xxiv] non-absorbing phase object. Measurements of phase for a diverse number of fibres has shown that their phase gradients are very small. For illustration the refractive index profile for a fibre (3M F-Sn-3224) together with the phase profile is presented in Figure 4.2.

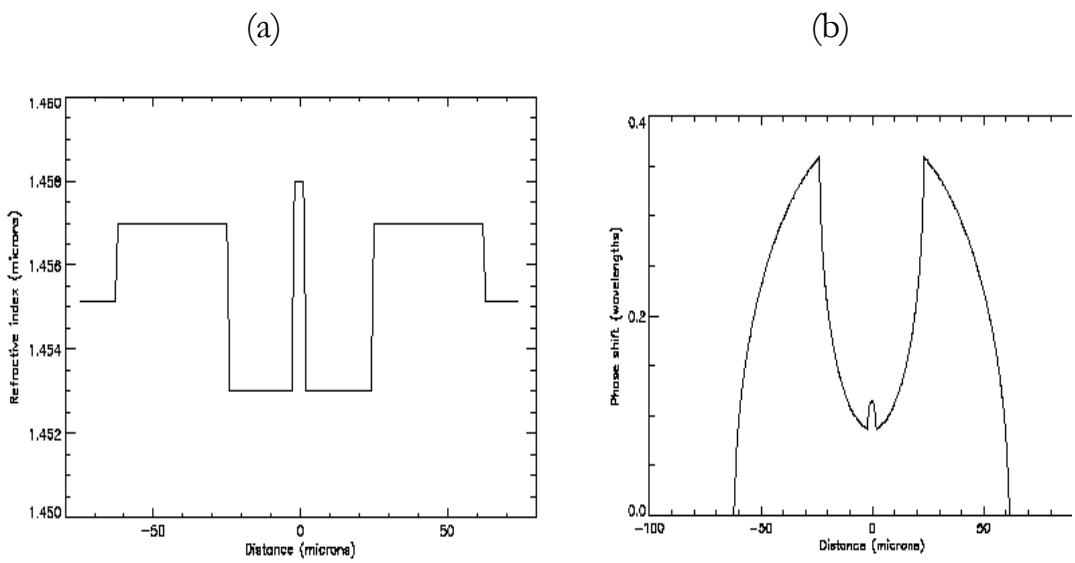

Figure 4.2. (a) The refractive index profile of 3M-FSN -3224; (b) Phase profile recovered by QPM phase imaging technique (after (Barty 2000)).

Several simple fibres were considered for refractive-index determination. Table 4.1 summarizes some of the properties of these fibres (also see Appendix A:

Sample Preparation and Mounting). These fibres were imaged with Nomarski DIC method described in Chapter 3.

Table 4.1. Several optical fibres imaged using DIC. Refractive indices n_1 and n_2 of the surrounding medium and the fibre structure respectively, maximum optical path length (Max.OPL), and maximum phase (Max. Phase) of the fibre core were studied under monochromatic light of λ = 488 nm wavelength. The OPL was computed from $(n_2 - n_1)t$ where t is the maximum thickness of the fibre, which is across its core diameter. The phase was computed from $(2\pi/\lambda)\cdot OPL$.

Fibre Name	Core Diameter [μm]	n_1	n_2	Max. OPL [μm]	Max. Phase [rads]
SMF 28	8.2	1.464	1469	0.081 λ	0.515
Er doped	3.5	1.464	1.4659	0.013 λ	0.085
Yb doped	4.6	1.464	1.4982	0.323 λ	0.645 π
Nd doped	3	1.464	1.498	0.209	0.418 π
FSS - 1300	7.457	1.464	1.468	0.073 λ	0.458
GF1	8	1.499	1.514	0.81 λ	1.6 π

4.3.2 Experimental DIC Images of Optical Fibres

The image in Figure 4.3 shows the intensity distribution recorded in a regular array of *512* × *512* points by beam scanning an area of *36* × *36* μ*m* along the fibre. The effective pixel size in the recorded image was *0.069* × *0.069* μ*m*. The image presents a strong differential edge response made up of light and dark

[xxiv] A phase object is considered to have a weak phase when the small phase approximation condition is valid, i.e. $e^{i\varphi(x)} \approx 1 + i\,\varphi(x)$.

regions, showing that gradients of phase difference of opposite signs produce shadows in opposite directions. The image reveals the known depression of the refractive index in the centre of the core due to the depletion in germanium concentration caused by the collapsing process in the fabrication of the fibre using the Chemical Vapour Deposition Technique. Also notable is the fact that the phase resolution in the image is sufficient so that the cladding deposition layer is visible in the region outside the core and it is distinguishable in the intensity distribution profile shown in Figure 4.3 b.

(a)

(b)

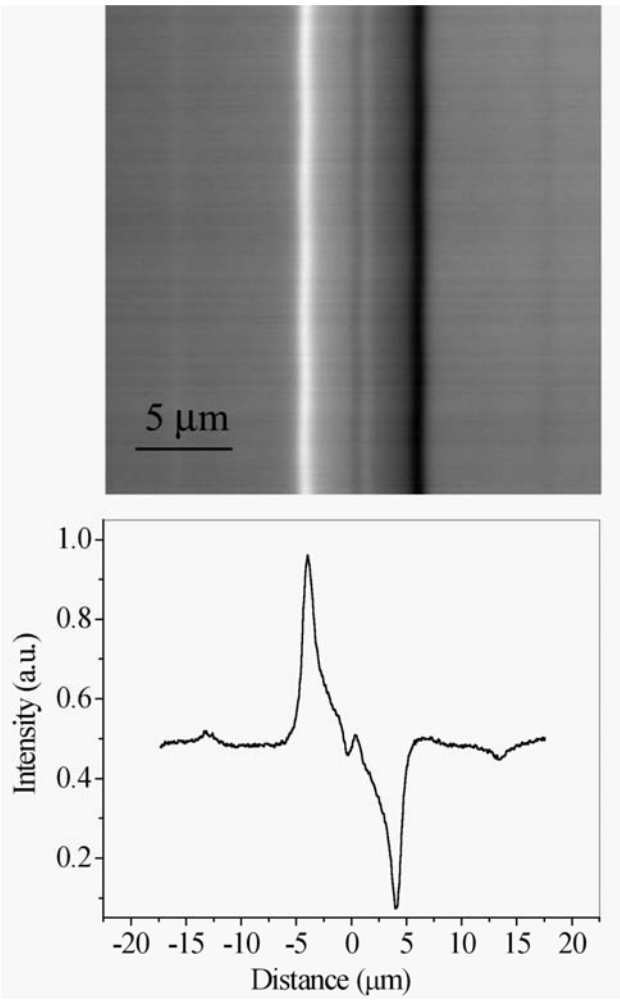

Figure 4.3. Panel (a) shows the measured DIC image of the central region of the SMF-28 optical fibre acquired with an Olympus UplanApo *40 × /0.85 - NA* dry lens. The scan area is *36 × 36* µ*m*. The minimum and maximum intensity in the image is mapped to black and white respectively. Panel (b) shows a horizontal line-profile through the above image.

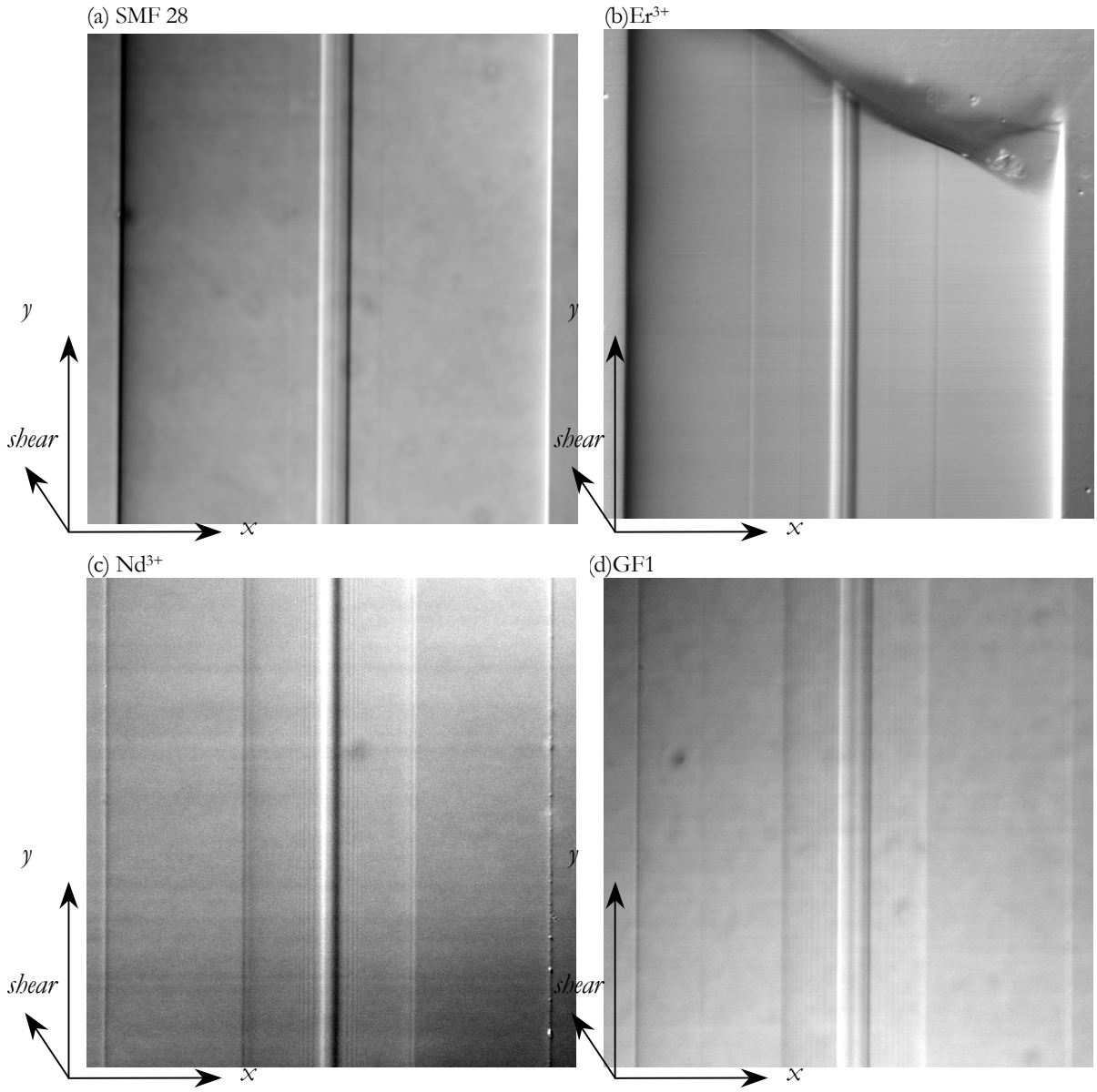

Figure 4.4. A collection of four measured DIC images of optical fibres. The name of each fibre is indicated above its image. The images in each figure cover an area of *140* × *140* μ*m* along the fibre with an effective pixel size of *0.28* × *0.28* μ*m*.

The images shown in Figure 4.4 were processes according to Equation (4.9) in order to obtain the refractive indices of the various fibres imaged.

4.3.3 Reconstructed Refractive Index of Optical Fibres

Figure 4.5 identifies the structure close to the centre of the fibre. The dip in the refractive index is consistent with the depletion of germanium in the centre of the core that occurs during the collapse stage of the fibre fabrication process.

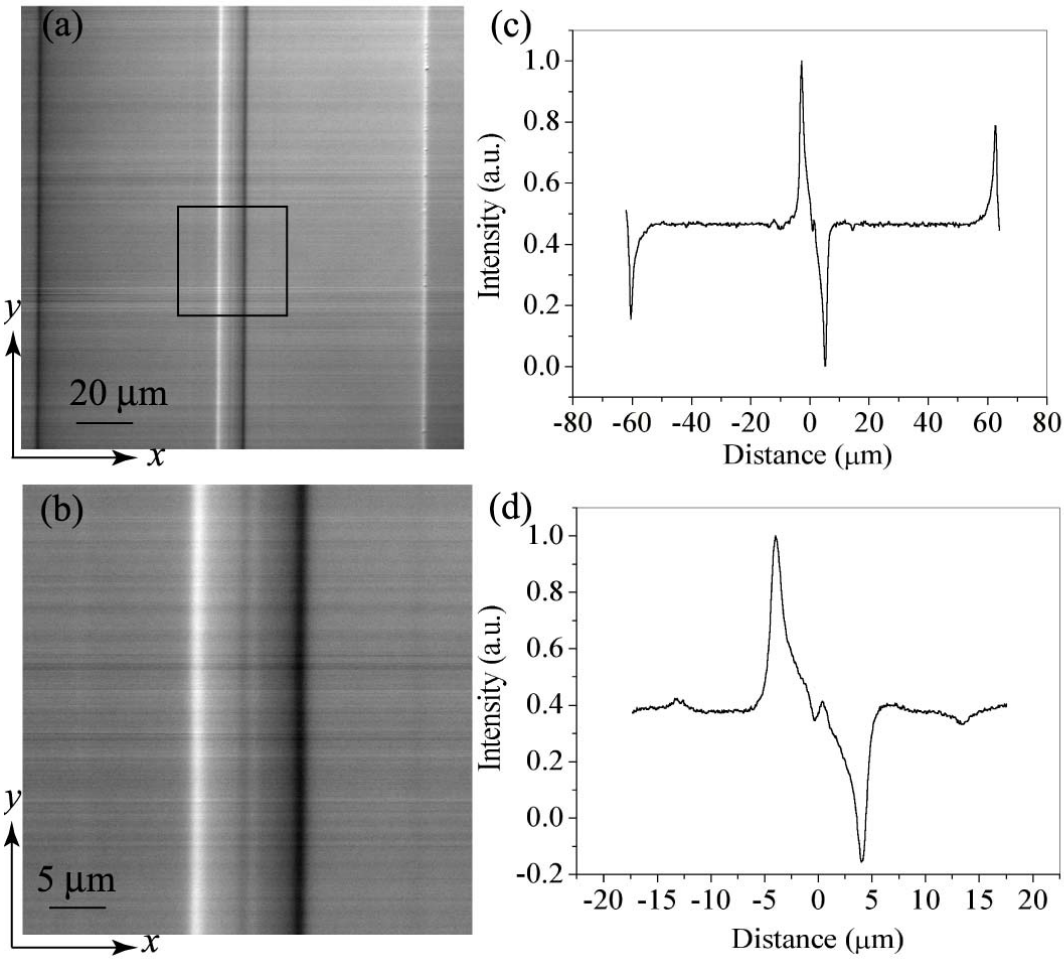

Figure 4.5. Measured differential interference contrast image of the central region of the SMF 28 optical fibre acquired with a *40 × /0.85 - NA* dry lens, 488 nm illumination wavelength. The scan area in (a) is *140 × 140* μ*m*; (b) represents the rectangular area outlined in (a); the dimension of the image is *36 × 36* μ*m*. The minimum and maximum intensity in each image is mapped to black and white respectively. Horizontal line-profiles through the images in (a) and (b) are plotted in (c) and (d) respectively. The horizontal lines evident in the image are possibly due to aliasing of the scan with the periodic fluctuations in the laser, they disappeared after the laser had been replaced.

The refractive index profile, Figure 4.6, of the fibre has been reconstructed from the DIC image presented in Figure 4.5 (d); a maximum index difference of *0.00372* ± *0.00015* was found. These values show a very good agreement with the specification provided by the vendor, i.e. core diameter of *8.2* μ*m*; refractive index difference *0.36%*.

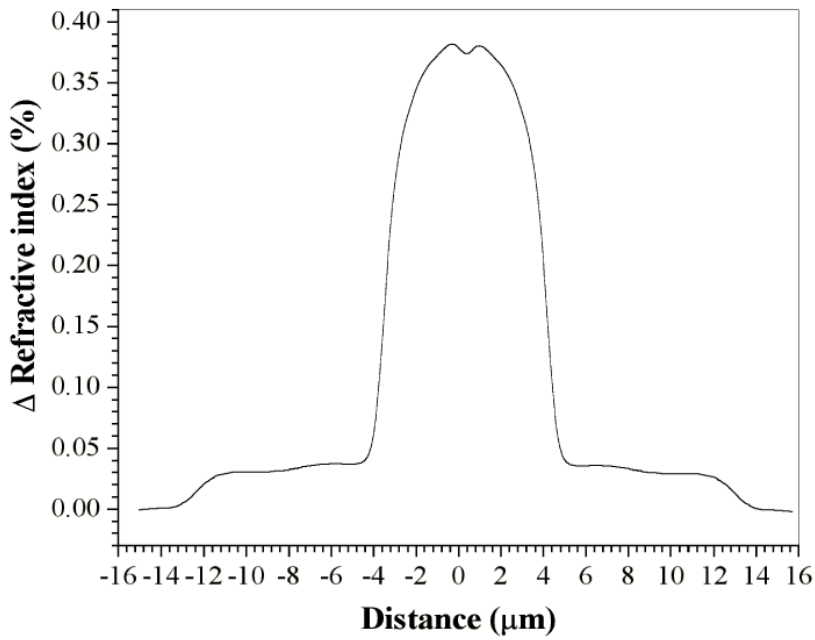

Figure 4.6. Refractive index profile of the SMF 28 optical fibre reconstructed from DIC image presented in Figure 4.5.

The refractive index profile of an FSS fibre was compared with the profile obtained from a commercial profiler[xxv] and using the phase retrieval algorithm (see Section 2.6) presented in Figure 4.7.The commercial profiler uses the refracted near field technique to measure fibre refractive index profiles, please refer for details on this technique to Section 2.2.1. What is immediately apparent in this figure is that the maximum values obtained with the commercial profiler are 20 % higher than the values obtained from either the phase retrieval algorithm or the DIC inversion at the centre of the fibre. One

[xxv] P101 analyser, York Technologies Chandlers Ford, UK. The profiling was conducted for us by the Optical Fibre Technology in Sydney.

possible explanation for such a large difference might be that the fibre being profiled using the commercial profiler might have been from a different spool yet the same type of fibre, or that the profiler had not been calibrated prior to the measurements being taken. It should be noted, however, that the spatial agreement between the three plots presented in Figure 4.7 is excellent. However, one can easily observe the fact that the profile shown does not reproduce the index profile found by the commercial profiler and the QPm. Another source of discrepancies may be introduced by the different wavelengths at which the measurements were obtained, namely *521 nm* for the phase retrieval, *633 nm* for the commercial profiler and *488 nm* for the DIC inversion.

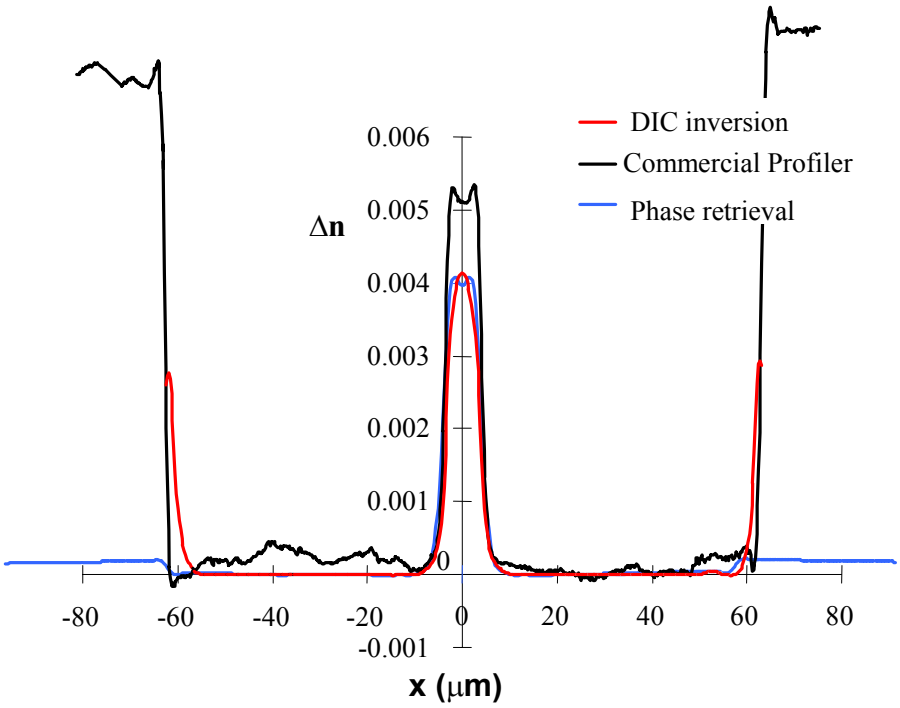

Figure 4.7. Comparison of refractive index profiles of the refractive index obtained for FSS fibre using three different techniques.

4.4 The Bragg Fibre

In this section an investigation of a complex fibre, so-called a Bragg fibre, was performed by means of DIC imaging. This fibre has been chosen for several reasons: firstly, the fibre is a multiple layer circularly symmetric structure containing regions with different refractive indices so that it is a challenge in itself to accurately image the fibre with such index variations and having such a complicated structure. Secondly, the fibre is difficult to characterise by means of most of the alternative techniques.

This fibre is a depressed-core-index photonic-band-gap fibre (DCI-PBG) which was manufactured by researchers at the Institute de Recherche en Communications Optiques et Microondes, Limoges, France by means of the classical Modified Chemical Vapour Deposition technique (Brechet, Auguste *et al.* 2000; Fevrier, Viale *et al.* 2003). Figure 4.8 represents a cross section of this fibre, highlighting the periodic structure of the fibre with its alternating regions of high and low refractive index, with respect with radius.

A schematic diagram showing the idealised refractive index profile of the fibre is presented in Figure 4.8. In this figure n_1, n_2 and n_3 refer to the refractive indices of the core, high inner cladding and outer cladding respectively. Optical fibres with this type of structure have some interesting properties that are very different from the properties of conventional two-layer fibres (i.e. fibres consisting with only a core and cladding). The properties listed below were described theoretically (Yeh, Yariv and Marom 1978) and achieved practically after more than two decades (Brechet, Auguste *et al.* 2000, Fevrier, Viale *et al.* 2003). Moreover the light guiding mechanism is achieved through what has been referred to in the literature as the Bragg reflection[xxvi]. Further the fibre can

[xxvi] The guiding of light in a fibre with a core refractive index lower than that of the substrate was first proposed by Yeh, P., A. Yariv and E. Marom, "Theory of Bragg Fiber". *Journal of the Optical Society of America,* **68** (9): 1196-1201, 1978.

be designed to have zero dispersion at virtually any desired wavelength in the single-mode region particularly at short wavelengths, and single-mode operation can be maintained for a relatively large core size (the radius of the core is ~*6.7* μ*m* in this case).

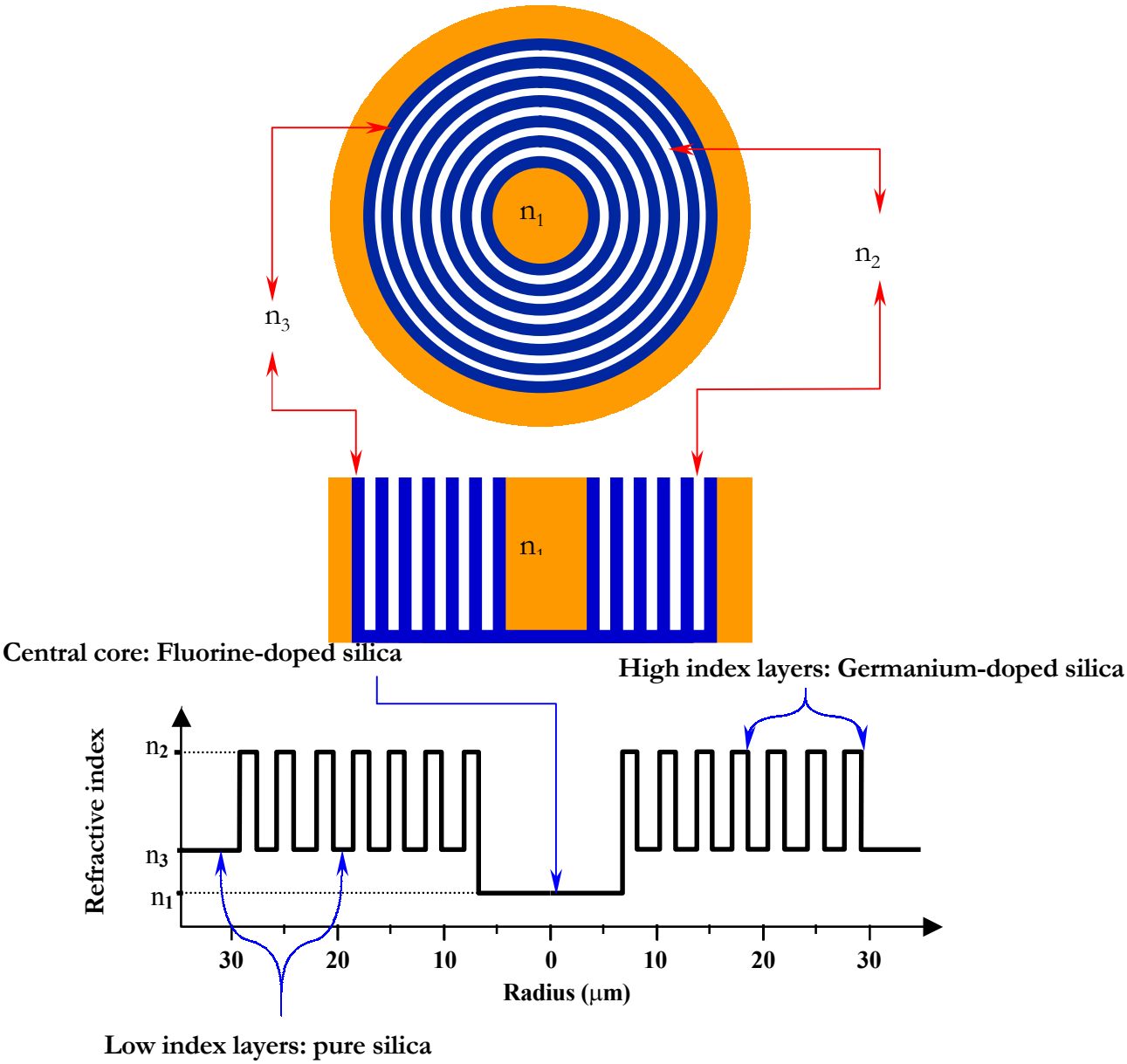

Figure 4.8. (a) Cross-sectional view of a Bragg fibre. The fibre consists of a low-index core surrounded by a cladding formed by seven alternating layers of dielectric media of high and low refractive indices. (b) Refractive index profile of an ideal DCI-PBG fibre.

A quantitative comparison has been made between a refractive index profile obtained from DIC measurements and that obtained of the profile of the relevant preform using a commercial profiler base on the RNF technique.

Prior to drawing, the fibre preform was profiled using a York Technology P101 preform analyser[xxvii]. The spatial resolution of the analyser is about *5* μ*m*. By scaling the preform data to the fibre dimensions one can compare the two profiles directly. In order to compare the spatial characteristics of refractive index profiles with those from the preform analyser, the maximum and minimum values obtained from the DIC measurements were equated with the maximum and minimum refractive indices of the preform.

In order to be analysed, the fibre has been prepared in the following way: a 5 mm length of uncoated fibre was placed in a cuvette filled with index matching agent and a DIC image of the fibre was acquired (please see also the Appendix A: Sample Preparation and Mounting). A typical image of the core region of the DCI-PBG fibre is shown in Figure 4.9a. The image shows the periodic structure of this fibre presenting its seven layers with alternating high and low indices. A computed DIC image of the central part of this fibre (Figure 4.9 panel (b)) has been obtained using the information on refractive index profile of the fibre preform data scaled down to match fibre diameter. Figure 4.9 panel (c) compares the measured and computed DIC profiles. As can be seen the two plots are in excellent spatial agreement. The slight shift between the two lines on the right hand side of the plot was attributed to the errors due to the averaging of preform data and also due to the fact that the fibre displayed a degree of ellipticity. Nonetheless, the fact that the measured DIC image

[xxvii] P101 preform analyser, York Technologies, Chandlers' Ford, UK. The profiling was conducted by Mr. Fabien Brechet of Guided and Integrated Optics Group, Limoges, France.

accurately represents the abrupt changes in the refractive index between the consecutive layers and provides a high spatial resolution is notable.

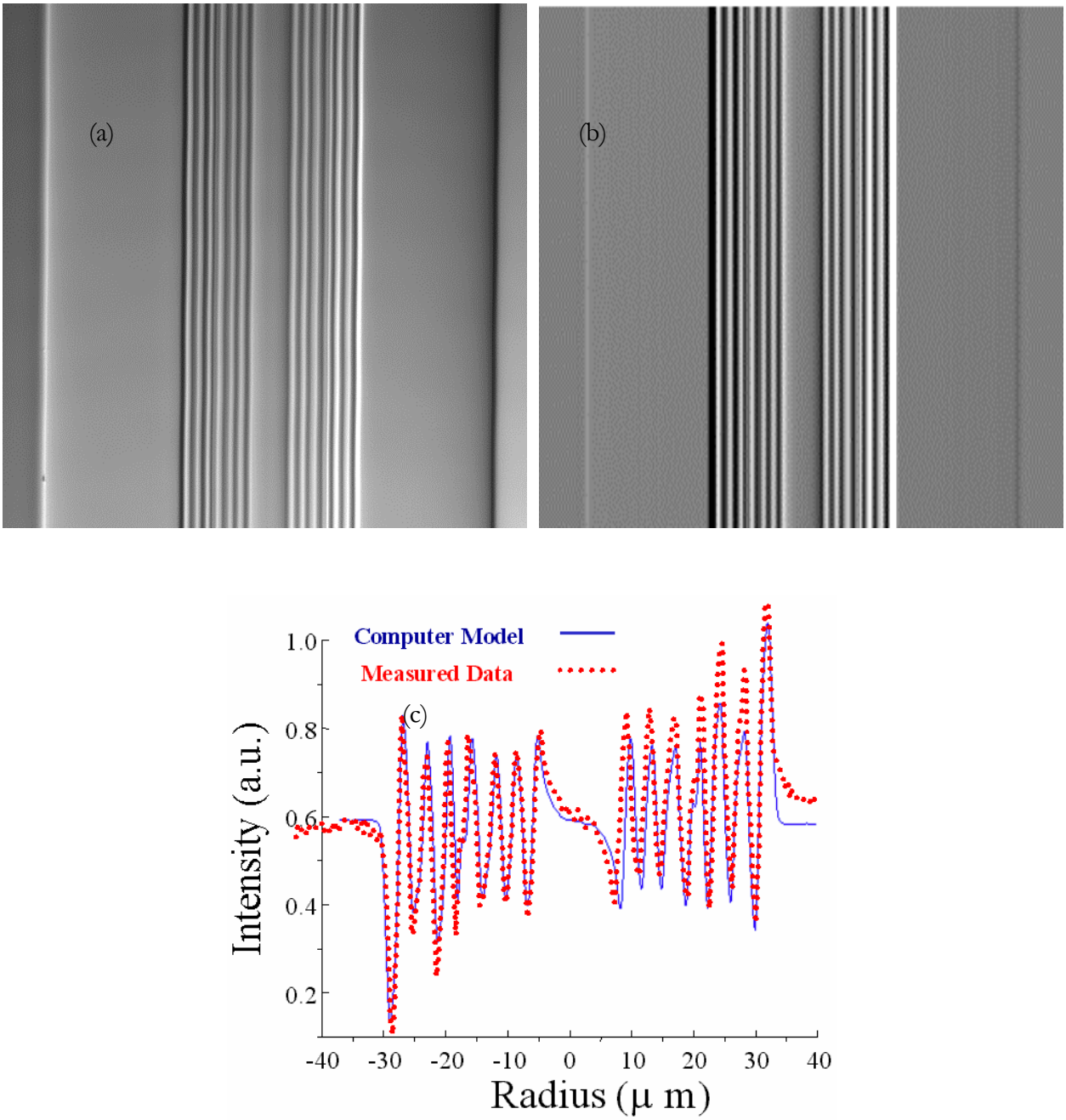

Figure 4.9 Quantitative comparison of the measured and computed DIC images of DCI-PBG fibre. (a) Measured DIC of the central region of the fibre representing a 140 μm × 140 μm transverse section of the fibre; (b) Modelled DIC image computed from the refractive index data of the preform from which the fibre has been drawn; (c) A comparison of profiles through the computed and real DIC images (continuous and dashed lines respectively). Note that the real and computed DIC images are indistinguishable by eye, and that the line profile through both the images shows an excellent agreement.

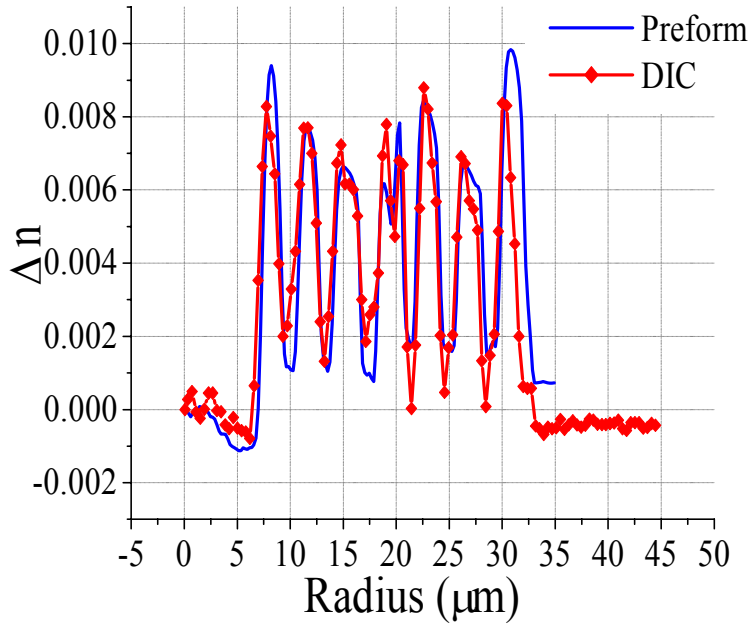

Figure 4.10. Extraction of refractive index profiles from DIC data. Known and reconstructed index profile (preform and DIC lines respectively) for the DCI-PBG fibre.

The reconstructed refractive index presented in Figure 4.10, is in good spatial agreement with that known from the preform data profile, with all layers appearing in the correct position for this structured fibre. Also notable is that the refractive index is in reasonable quantitative agreement with the known preform profile.

4.5 Annealing Effects in Optical Fibres

Heat treatment of optical fibre sensors, called annealing (Sun, Zhang *et al.* 1998), is a common treatment applied where an optical fibre is to be used as an optical sensing element in a particular application. The annealing process involves the fibre being heated to a known temperature after which it is stabilized for a number of hours. The annealing temperature and time required are dependent on the composition of the fibre being annealed. This procedure

leads to an increase in the reliability and repeatability of the measurement of the physical quantity under consideration as the sensor is cycled through the measurement range of interest. Various types of fibres are frequently used as sensor elements: standard fibres (Rose 1997), rare earth doped fibres (Zhang, Grattan *et al.* 1998) or fibres incorporating Bragg gratings (Erdogan, Mizrahi *et al.* 1994; Kersey, Davis *et al.* 1997).

Much of the work which investigates the thermal characteristics of optical fibre sensors is based on the use of either the fluorescence decay time technique (Grattan and Meggitt 1995a; Sun, Zhang *et al.* 1998) or the fluorescence intensity ratio technique (Collins, Baxter *et al.* 1998; Sidiroglou, Wade *et al.* 2003b; Wade, Collins and Baxter 2003). The first method utilizes the temperature dependence of the rate at which the intensity of fluorescence decreases after the source of fluorescence excitation is removed. The temperature, in the latter method, is determined from the ratio of the fluorescence intensities originating from two energy levels that are closely spaced, such that they are thermally coupled.

A series of experiments based on the use of the fluorescence decay technique have been performed on a range of sensor materials such as Nd^{3+} (Zhang, Gratan *et al.* 1998), Er^{3+} , Yb^{3+} , Tm^{3+} (Zhang, Gratan and Meggitt 2000) or Er/Yb (Sun, Zhang and Gratan 2000) co-doped fibres. Consequently, a diversity of thermal annealing procedures have been evaluated and compared in an attempt to stabilise the thermal characteristics.

In one particular study (Wade, Collins *et al.* 1999) the effect of annealing a Yb^{3+}-doped fibre was investigated by leaving the fibre at a temperature of 700ºC for approximately 100 hours whilst the fluorescence lifetime was monitored. Characteristically, an initial increase in the lifetime was observed,

followed by a stabilisation of the lifetime after a period of approximately 60 hours.

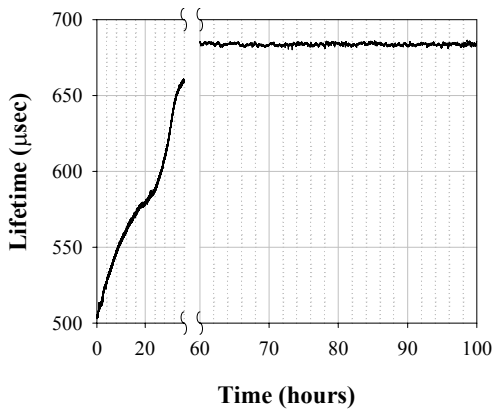

Figure 4.11. Annealing effects in Yb^{3+}-doped fibre, heated at 700°C (after Wade, Collins *et al.* 1999).

Recent investigations of the effect of annealing on the fluorescence intensity ratio method of temperature sensing, show that improved repeatability and reliability of measurements can be achieved using Nd^{3+}-doped fibre in the 18-700 ºC range – after the fibre has been annealed at 750 ºC for 100 hours (Wade, Dragomir *et al.* 2001; Sidiroglou, Wade *et al.* 2002; Sidiroglou, Wade *et al.* 2003a).

Apart from the aforementioned positive effect on stability little is known about the changes induced in fibres during the annealing process. One of the potential mechanisms responsible for the changes that occur during annealing is a change in the local environment for the rare earth ions in the glass lattice, which, in addition, may also result in changes in refractive index. Measurements of the refractive index profile of two different types of optical fibres used in

fluorescence-based temperature sensing, which have been subjected to annealing, are presented below.

The refractive index profiles of two optical fibres Corning® SMF-28™, often used as a lead to the sensor fibre, and an Yb^{3+}-doped fibre were obtained using the DIC imaging technique and are presented in Figure 4.12. The core of the second fibre had been doped with Yb^{3+} (~1800 ppm), Al and Ge. It had F and P_2O_5 deposited with an inner cladding (INO, Canada). The refractive index was derived using the formulation described in Section 4.3.3 considering the refractive index of the silica tube as a reference and exploiting the cylindrical symmetry of the optical fibre.

Fibres were annealed by placing samples in a Carbolite™ tube furnace, heated to the appropriate temperature, and then removed after it had been exposed for the appropriate period. Prior to imaging, the fibres were cleaned and then the samples (~5 cm long) were immersed in index matching fluid.

Figure 4.12a shows the refractive index analysis of three samples of Yb^{3+}-doped fibre prior to heat treatment and after annealing at *700°C* for *49* hours and *96* hours. Changes in refractive index are observed both in the core and in the inner cladding. The changes in refractive index for the core were approximately -7.1×10^{-4} and -7.7×10^{-4} after annealing for *49* and *96* hours respectively while changes for the inner cladding of approximately $+3.1 \times 10^{-4}$ and $+5.4 \times 10^{-4}$ were observed over the same annealing periods.

In Figure 4.12b the refractive index of two SMF-28™ fibre samples, one without heat treatment and with the other heated at 1000°C for 49 hours, are shown. For these conditions, a decrease in the refractive index was observed, for both the core ($\sim 0.3 \times 10^{-4}$) and for the inner cladding region ($\sim 0.7 \times 10^{-4}$).

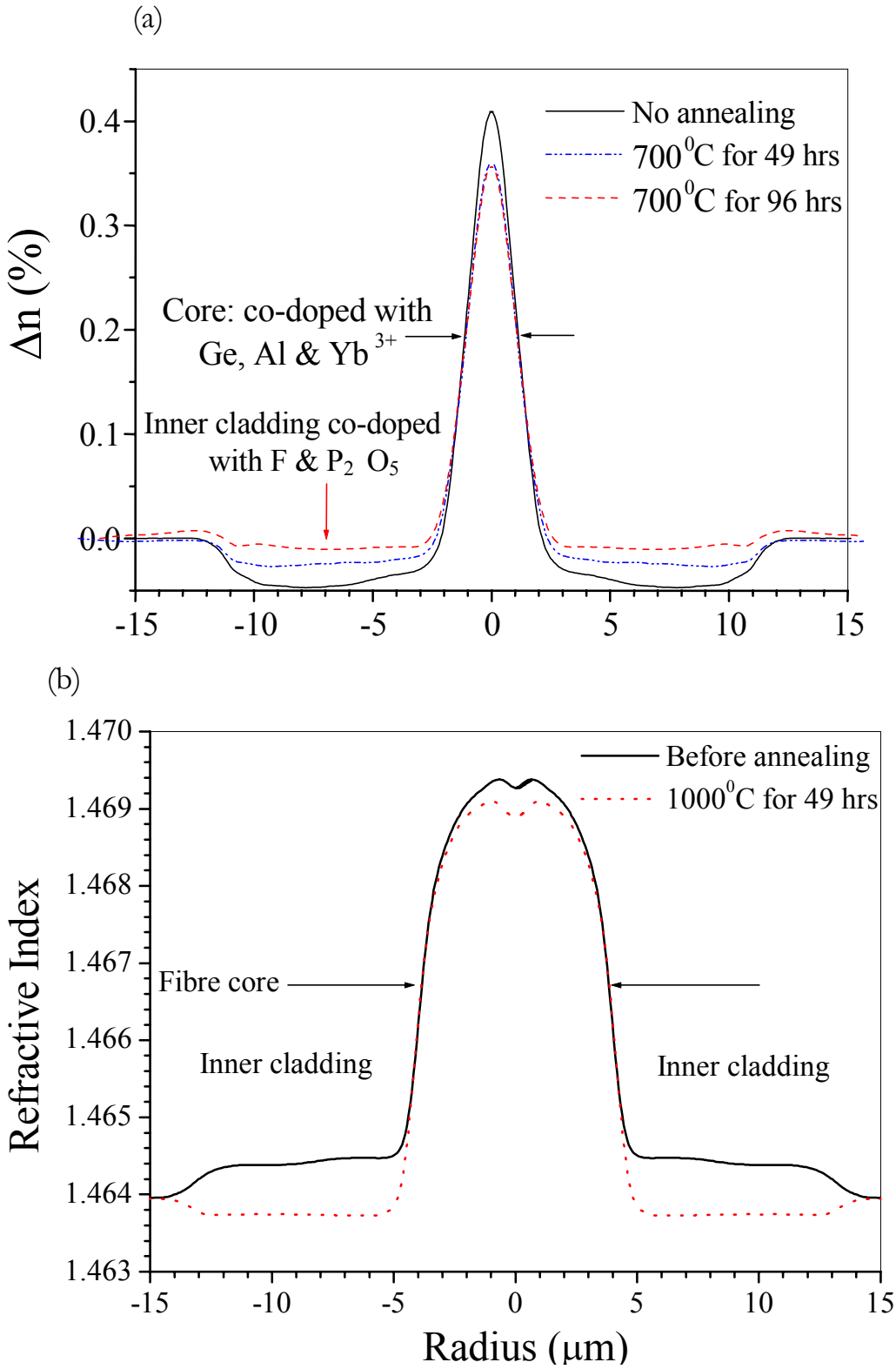

Figure 4.12. The effect of annealing on the refractive index profiles of (a) Yb^{3+}-doped fibre and (b) SMF-28™ fibre, obtained using DIC imaging.

Table 4.2 lists the change in the refractive index difference between the core and the cladding of the optical fibres tested and the core diameters (FWHM) for various stages in the annealing process and shows a comparison of the data with the specifications provided by the manufacturers[xxviii, xxix].

Table 4.2. Comparison of results obtained from DIC images and manufacturers' specifications.

Fibre	Data from this work		Manufacturers' Data xxviii' xxix	
	Δn (%)	d (μm)	Δn (%)	d (μm)
Yb^{3+} (0 hrs)	0.46	2.4 ± 0.1	0.6 → 1.1	3.4 ± 1
Yb^{3+} (49 hrs)	0.39	2.4 ± 0.1		
Yb^{3+} (96 hrs)	0.37	2.3 ± 0.1		
SMF-28™ (0 hrs)	0.34	7.82 ± 0.04	0.36	8.2
SMF-28™ (49 hrs)	0.37	7.9 ± 0.1		

For the Yb^{3+} fibre there is a reasonable difference between the results obtained with the use of the DIC images and from the manufacturers' specifications, which may be due to the different methodologies used for the measurement. Excellent agreement however is found for both the refractive index difference and the core dimensions for the SMF-28™ fibre. The refractive index resolution of the DIC imaging and analysis technique is of the order of 10^{-5} (Norman and Matt 1999). The uncertainties in estimating the absolute refractive index of the fibre arise predominantly from the reference materials. For a well-

[xxviii] Corning® SMF-28™ Optical Fiber – Product Information 2002 Corning Incorporated, www.corning.com/optical fibre

[xxix] Yb^{3+}-doped fibre data sheet and private communications with INO, www.ino.qc.ca

known solid such as silica, the uncertainty of the reference index lies between 5×10^{-5} and 7×10^{-4} (Raine, Baines and Putland 1989). Spatially, the resolution is near the diffraction limit.

It is well known that residual internal stress is generated in optical fibres both during the preform and drawing stages of manufacturing (Bachmann, Hermann *et al.* 1986, 1987; Kim, Park *et al.* 2001). Changes in the residual stress in fibres, due to CO_2 laser irradiation for example, have been shown additionally to affect the refractive index profile of the fibre (Kim, Park *et al.* 2001). The magnitude and sign of such changes are expected to be due to the type of dopant materials in the fibre and also to depend on the tension used at the fibre drawing stage. The changes in refractive index observed in this work are likely to be due to a thermal relaxation of the residual stress in the fibres tested.

4.6 Accuracy Considerations

The method outlined above, to reconstruct the refractive index from DIC images of the central region of an optical fibre, does not provide an estimate of the uncertainties. However, an estimate of these can be undertaken by considering the major contributing terms to the uncertainties. One factor is the accuracy with which one can match the refractive index of the immersion fluid with that of the cladding of the optical fibre.

Knowledge of the matching liquid and reference refractive indices are not of paramount importance. It is, however important that the refractive index of the immersion fluid is close to that of the fibre.

As far as the knowledge of the matching liquid refractive index is concerned, it is possible to measure its value by means of a commercially available

refractometer with an accuracy of $\pm\ 2 \times 10^{-4}$. The refractive index of the immersion fluid (series A, Cargille Laboratories, NJ USA) used in this work, $1.4639 \pm 2 \times 10^{-4}$, was measured at *25 °C* with an Abbe refractometer (ATAGO – model 302) for the *488* nm line, matching the wavelength at which the imaging of the fibres had been performed.

It is well known measurements of the refractive index in general are sensitive to various parameters such as the ambient temperature, humidity and pressure, which may change with time. Care has been taken to ensure a constant temperature, within the *0.12 °C* provided by the use of the temperature controlled stage (for more details see Appendix F: The Temperature Controlled Rotation Stage).

The phase measurement precision may be influenced by the interference image contrast according to the relation:

$$\delta = \frac{2\pi}{N} \tag{4.10}$$

where N is the image contrast expressed in grey levels of the digitising PMT. In the best case N is equal the whole range of the digitiser grey levels. High dynamic range of 12 bit for sample areas ensured a very small error in the measurement of phase. For a *12* bit image, *4096* grey levels images are processed. In this case the phase measurement precision of $\delta = 2\pi/4096 = 0.001$ *radians* is attained The phase measurement precision due to image contrast is smaller than the magnitude of errors due to phase shift error and for that reason a separate section on the calibration of the Wollaston prism phase bias (Section 3.4.1) has been included.

Another factor that may influence the accuracy of the reconstructed refractive index is the asymmetry factor. Preliminary measurements of the ellipticity of the

fibre confirmed they where consistent with the specifications provided by the manufacturer and they were sufficiently small and therefore have not been considered in this work.

4.7 Summary

Two main aspects associated with the estimation of the refractive index profile of optical fibres using DIC microscopy were presented in this chapter. The first was the mathematical formulation of the problem taking into account the geometry of the fibre and the characteristics of the imaging model. The second aspect was testing this formulation to reconstruct the refractive index of annealed optical fibres and a Bragg fibre.

Clearly, the information attainable from DIC images of optical fibres is strongly encouraging as one can obtain the refractive index of an optical fibre non-destructively along the length of the fibre.

Nonetheless, there are several aspects of this work, which warrant further development. First the validity of the formulation could be further examined using a calibrated test fibre. This would be particularly useful in calibrating and comparing the absolute refractive index against a known structure. Secondly, the formulation heavily relies on the geometry of the fibre having cylindrical symmetry. In addition, the imaging model presented considers only the case in which the fibre can be considered to be a purely refracting object and no scattering occurs for the light that passes through. Also the fibre acts like a lens and the larger the fibre fine-structure surrounding the fibre core is, the more refracted the light would be, causing inaccuracies in the refractive index inversion. Further, the work presented was a one-dimensional study, which means that when a two-dimensional analysis of the images will be involved, issues such as background correction and processing time need to be

considered due to the non-uniform illumination conditions that may occur during the image acquisition process.

A summary of the advantages and disadvantages of this methodology for reconstructing the refractive index profile of optical fibres from DIC images is presented in Table 4.3 below:

Table 4.3. Summary of advantages and disadvantages of refractive index profile reconstruction of optical fibres from differential interference contrast images.

Advantages	Disadvantages
The technique is non-destructive. Hence it can be used to study properties of fibres without breaking the fibre.	Some may argue that the data acquisition requires an expensive instrument – an Olympus microscope equipped with high resolution Nomarski optics. However this is less expensive compared to the commercially available RNF which often are designed for specific type of fibres.
Sample preparation is straightforward and does not require considerable care when handling the fibre.	Due to well-known non-uniform illumination of the specimen in DIC microscopy, correction of the acquired images may be necessary, especially for two dimensional data. This can be performed by subtraction of the background illumination, which would facilitate the quantitative interpretation of the DIC image of a fibre.

Advantages	Disadvantages
Detailed fibre properties, such as the germania-deficient centre of germania doped fibre is easily observable and interpretable.	In spite of the high spatial resolution achieved in the fibre images, they still contain out-of-focus information due to the fact that a conventional DIC microscope was employed. This can be overcome if a confocal DIC microscope is employed.
The data are obtained in a form that can be readily interpreted and understood.	
The analysis is straightforward and does not require complex nor detailed correction formulas.	
The analysis yields precise and potentially highly accurate data.	

5 Fibre Bragg Grating Characterisation

5.1 Overview

In the previous chapter, a technique for imaging optical fibres using differential interference contrast (DIC) microscopy was presented along with a method for estimating their refractive index profile based on assumptions about the fibre geometry. Toward this end, a series of tests were performed to determine how applicable the imaging technique is to various optical fibres. In order to further test the imaging technique, images of fibre Bragg gratings (FBGs) are presented and discussed in this chapter.

This chapter begins with an introduction to the fundamentals of FBGs, and summarises definitions and various relations among the physical quantities used. This serves the purpose of compiling a number of results scattered throughout the literature.

Further, in this chapter the current methods for assessing FBGs are reviewed. Next, the identification of a significant non-uniform refractive index structure is experimentally demonstrated.

At the time these experiments were conducted, the FBGs fabrication facilities within our laboratory were limited to the use of the phase mask technique, therefore only these types of gratings are presented and discussed in this chapter. To understand the complex structure observed in the FBG one needs to thoroughly investigate the diffraction field produced by a phase mask and the influence of the different diffraction orders present during FBG fabrication. The chapter closes with a set of simulated images describing the diffraction by a phase mask, which gives an indication of the non-uniform refractive index structure of a FBG.

5.2 The Optical Fibre Bragg Grating

Fibre Bragg gratings[xxx] made their debut in the field of telecommunications in the late 1970s when Hill and co-workers, of Communications Research Centre, Ottawa, Ont., Canada, reported the first observations of index of refraction changes in germanosilica fibres (Hill, Fujii *et al.* 1978). The first grating observed was described as having a very weak index modulation, which was estimated to be of the order of 10^{-6}.

Initially viewed as a scientific curiosity, FBGs are revolutionising telecommunications, laser and sensor technology due to their intrinsic integration into optical fibres and the large number of device functionalities that

[xxx] Bragg gratings are named after Sir (William) Lawrence Bragg (1890-1971), Australian-born British physicist and Nobel Prize winner (1915). The work that brought Bragg fame was on X-ray diffraction in crystals. He discovered that certain planes in a crystal reflect X rays according to the normal law of reflection.

they can facilitate. A recent review of the present applications of optical fibre sensors showed that FBGs are now the most widely studied topic (Lee, 2003). Figure 5.1 shows the technologies involved in the optical fibre sensors presented at one of the major conferences in the field of optical fibre sensors, the 15th Optical Fibre Sensors Conference held in Portland, Oregon, USA 2002.

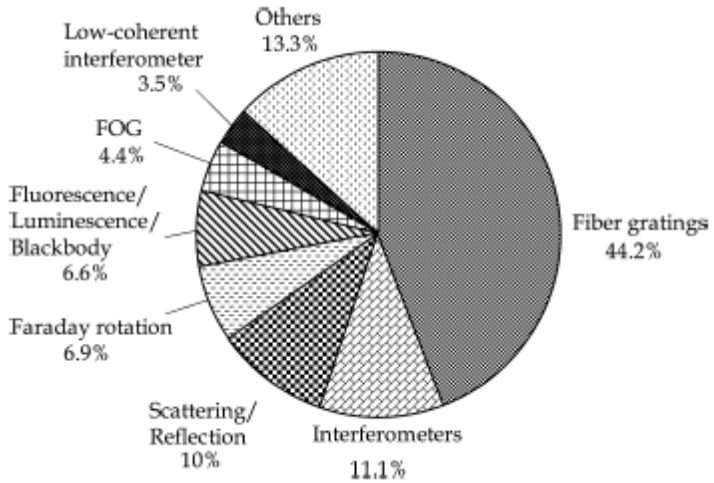

Figure 5.1. Statistics showing the fibre Bragg gratings technologies are the most widely studied topic in the field of optical fibre sensors (Source: Lee, 2003). FOG refers to fibre optic gyroscopes.

Moreover, they have been explored for use as channel selection in wavelength-division multiplexing networks and chromatic dispersion compensators (Eggleton, Krug *et al.* 1994a; Pastor, Capmany *et al.* 1996; Hinton 1998; Krug, Canning and Stepanov 1998; Zhu, Simova *et al.* 2000); gain flattening (Liaw and Chi 1999; Zhu, Simova *et al.* 2000); spectral filtering - as narrow-band reflection or transmission filters (Hill, Fujii *et al.* 1978; Hill, Malo *et al.* 1993a; Morey, Ball and Meltz 1994) or as laser components (Meltz, Morey and Glenn 1989). More recently, FBGs are being used as gain equalisers where their transmission spectra are used to smooth the gain ripple of an erbium doped fibre amplifier and as laser-diode pump stabilisers (Riant 2003).

A fibre Bragg grating is a wavelength selective reflective element formed by a periodic perturbation of the refractive index along the fibre length. It is created by exposing the core of the fibre to a spatially modulated intensity pattern of ultraviolet (UV) light. This exposure may permanently alter the refractive index of the fibre-glass material in the regions of high optical intensity by a photo-induced mechanism.

The characteristics of a FBG can be controlled during the fabrication process and this allows many important applications to be implemented in either telecommunications or sensing systems (Rao 1997, 1999). The advantages of FBGs over competing technologies include their all-fibre geometry, low insertion loss, high return loss, and the most distinguishing feature, their flexibility for obtaining desired spectral characteristics (Erdogan 1997) due to the broad range of possible variations in their structural parameters (Othonos and Kalli 1999b).

The increasing complexity and the ever more demanding specifications required of FBGs make it essential to consider methods for visualisation and analysis of these devices for the improvement of design and fabrication efficiency.

Before beginning the discussion of characterisation techniques for FBGs, it is important to provide a description of the major terms that relate to this work, so that the problem is well understood. This is done in order to allow the reader to understand the use of these terms in the following sections.

5.3 Refractive Index Change

The physical mechanisms responsible for the formation of FBGs are complex and depend on the optical fibre type, specifically the co-dopants in the core.

These have been extensively studied over the last two decades. Several models have been proposed to explain photorefractivity[xxxi]; among the most important are the "colour centres" model (Hand and Russel 1990) and structural transformation (Sceats, Atkins and Poole 1993). The latter led to the "photo-induced densification model" (Poumellec, Riant *et al.* 1995; Poumellec, Niay *et al.* 1996) .

The fundamental basis of the colour-centre model is that the refractive index change is considered to be the result of photo-ionisation of germanium oxygen deficient centres and has been associated with the induced absorption in the deep UV through the Kramers-Krönig relations (Hand and Russel 1990). Even though the model could explain refractive index modulations of the order of 10^{-4}, (Atkins, Mizrahi and Erdogan 1993) it fell short of explaining refractive index changes of the order of 10^{-3}, easily achievable in germanium doped fibres.

In contrast, the densification theory, based on the premise that the UV irradiation causes a structural rearrangement of the glass matrix causing the material to densify and thus change its refractive index, (Bernardin and Lawandy 1990; Cordier, Doukhan *et al.* 1994; Poumellec, Guenot *et al.* 1995), has been proposed to account for the so-called "macroscopic origin" (Poumellec, Niay *et al.* 1996) of large refractive index changes (Douay, Xie *et al.* 1997). The estimation of structural changes requires analysis of the elasticity problem and computation of the stress distribution induced by the grating

[xxxi] The refractive index change under irradiation is called the photorefractive effect. It occurs when the material is photosensitive. The photorefractive effect is permanent, although it has been demonstrated to age and may also be erased at very high temperatures, and it remains when the irradiating light is removed. It was originally considered that optical fibre photosensitivity is due to the presence of germanium in the core or in the cladding. However, the cause photosensitivity in optical fibres is not restricted to Ge alone, other dopants in the core, such as Ce, Eu, Er, Sn or Sb have also shown varying degrees of sensitivity (R. Kashiap, Photosensitive Optical Fibers: Devices and Applications, Optical Fiber Technology, **1**: 17-34, 1994).

inscription. Although, to date, this is the most accepted theory of photosensitivity in Ge-doped glasses, it cannot fully elucidate all aspects of this complex physical mechanism when a wide array of glass compositions and process conditions are considered.

5.3.1 Photosensitivity

Photosensitivity in optical fibres has been extensively studied over the last two decades and the physical and chemical mechanisms responsible for the changes in the refractive index still raises a great deal of interest. Studies show that the photosensitive response depends on a variety of factors including the fibre type, post-fabrication treatment of the fibre and UV laser writing power (Hill and Meltz 1997).

Standard telecommunications fibres[xxxii] normally have a low content of GeO_2 (~3%), thus exhibiting low photosensitivity and therefore leading to small refractive index changes when exposed to UV radiation. Consequently, a number of post-fabrication methods are used to increase their photosensitivity (Hill and Meltz 1997). Such methods include modifying the fibre drawing technique (Dong, Archambault *et al.* 1993), codoping (Williams, Ainslie *et al.* 1993), flame brushing (Hill, Bilodeau *et al.* 1993; Bilodeau, Malo *et al.* 1993), straining (Salik, Starodubov and Ffeinberg, 2000) and hydrogen loading (Bernardin and Lawandy, 1990; Lemaire, Atkins *et al.* 1993; Poumellec, Niay et al. 1996; Wei, Ye *et al.* 2002b). Table 5.1 presents the sensitivity of the photoinduced index change due to the various enhancement methods.

[xxxii] It is desirable to consider the fabrication of FBGs in standard telecommunications fibres for better compatibility with existing systems.

Hydrogen loading is one of the most common methods used to enhance the photosensitivity of optical fibres. A temporary sensitisation of the fibre occurs due to the fact that the fibre is placed in a high-pressure hydrogen atmosphere, which causes the hydrogen molecules to diffuse into the glass network.

Table 5.1. Sensitivity of the photoinduced index change for various enhancement methods.

Method of enhancement	Mechanism	Final refractive index change	Fibre type	Comments
Codoping[xxxiii]	Structural transformation dependent on the type of codopant introduced in the core structure of the fibre	$\sim 3 \times 10^{-3}$	Various germanosilicate and phosphosilicate optical fibres	Various codopants may be used: GeO_2, B_2O_3, SnO_2 or rare earths. Crystallization may occur during the doping process of certain optical fibres – e.g. tin silicate fibres[xxxiv].
Flame brushing[xxxv]	A combination of structural changes and creation of colour-centres takes place due to the in-diffusion of hydrogen and hydroxyl species into the glass network generating an increased defect absorption	$\sim 10^{-3}$	Various germanosilicate and phosphosilicate optical fibres	Mechanical degradation of the fibre occurs after prolonged processing.

[xxxiii] N. Chiodini, S. Ghidini and A. Paleari, "Photoinduced processes in Sn-doped silica fiber preforms". Applied Physics Letters, 77(23): 3701 – 3703, 2000.
G. Brambilla, V. Pruneri and L. Reekie, " Photorefractive index gratings in SnO_2:SiO_2 optical fibers". Applied Physics Letters, 76(7): 807 – 809, 2000.

[xxxiv] G. Brambilla, V. Pruneri and L. Reekie, " Photorefractive index gratings in SnO_2:SiO_2 optical fibers". Applied Physics Letters, 76(7): 807 – 809, 2000.

[xxxv] F.Bilodeau, B. Malo, J. Albert, D.C. Johnson, K.O. Hill, Y. Hibino, M. Abe and M. Kawachi, " Photosensitization of optical fiber and silica-on-silicon/silica waveguides". Optics Letters, **18**: 953-955 1993.

Method of enhancement	Mechanism	Final refractive index change	Fibre type	Comments
Straining[xxxvi]	Structural transformations dependent on the level of strain being applied and the type of fibre being tested	1.5×10^{-3}	SMF-28 (Corning)-Standard; telecommunication fibre Fibercore SM1500HG, AD270 - Fibres with high germanium concentration; Fibercore PS1500 - GeO_2-B_2O_3 codoped fibre.	The amount of enhancement varies for different fibres. Strain enhances the photosensitivity only if it is applied during the UV exposure. The resultant enhanced index change remains after the applied strain is released.
Method of enhancement	Mechanism	Final refractive index change	Fibre type	Comments
Hydrogen loadingxxxvii	Combined creation of colour centres and structural changes	10^{-3} - 10^{-2}	Standard telecom fibre	This method alters the physical properties of the optical fibre The hydrogen molecules diffuse out of the fibre after the fibre is removed from the high pressure environment.

It is known that, without hydrogen loading, germanium-doped glass becomes more compact when it is exposed to UV light (Bernardin J. P. 1990; Poumellec Niay *et al.* 1996), this is because the UV light excites germanium oxygen-deficient centres and the glass structure is rearranged becoming more compact. Since the early days of the telecoms fibres, it has been known that hydrogen is a good defect former in germania-doped fibres (Kashyap, 1994). As hydrogen

[xxxvi] E. Salik, D.S. Starodubov, J. Feinberg, "Increase of photosensitivity in Ge-doped fibers under strain", *Optics Letters*, **25** (16): 1147-1149, 2000.

[xxxvii] Bernardin, J. P. and N.M. Lawandy, "Dynamics of the formation of Bragg gratings in germanosilicate optical fibres". *Optics Communications*, **79** (3-4): 194 - 199, 1990.
Poumellec, B., P. Niay, M. Douay and J. F. Bayon, " The UV-induced refractive index Grating in Ge:SiO_2 preforms: Additional CW experiments and the Macroscopic Origin of the change in index". *Journal of Physics D: Applied Physics*, **29**:1842 – 1856, 1996.

remains chemically bonded within the material by hydrogen loading the optical fibres, it is thought that photoconversion of optically active defects occurs; i.e. it results in the formation of Ge-OH or GeH_2 from molecular hydrogen, leading to an enhancement of the fibre's photosensitivity by modifying its UV absorption (Kashyap, 1994). Although the microscopic picture is considered complex and the dynamics of the reactions are not fully understood, it is generally agreed that with the appropriate amount of hydrogen in the fibre, the Ge centres may contribute to the refractive index contrast of the core to the cladding. With increasing temperature, additional chemical reactions occur such as the formation of GeH and SiOH. Optical fibre sensitised by high-pressure hydrogen treatment (up to *800 bar*) remains photosensitive while hydrogen is still present, thus it needs to be stored at high pressures in a hydrogen atmosphere to stop the out diffusion of hydrogen.

Photosensitivity of optical fibres can be enhanced by up to two orders of magnitude by high-pressure hydrogen loading at either room temperature or at higher temperatures. Index variations between 10^{-3} *and* 10^{-2} have been obtained with such a procedure; this is a high value taking into account the fact that the refractive index of the core of a standard telecommunications fibre is around 5×10^{-3} (Hill and Meltz 1997).

In summary, for germanium doped fibres, the most relevant mechanisms that have been proposed and studied are the UV induced defect centres that result in modified absorption (Williams, Davey *et al.* 1991; Atkins, Mizrahi and Erdogan 1993) and material densification (Douay, Xie *et al.* 1997); either of which may be accompanied by stress changes (Sceats, Atkins and Poole 1993).

The work presented in this thesis mainly deals with FBGs written in germanium-doped fibres.

5.3.2 Classification of Fibre Bragg Gratings

In spite of the large number of fibre types, different UV radiation conditions and various laser powers available, it is generally accepted that FBGs are divided into two classification schemes: one based on the coupling characteristics and the other based on the growth dynamics of the grating during the fabrication process (Othonos and Kalli 1999a).

5.3.2.1 Classification by Coupling Characteristics

According to the coupling characteristics, fibre gratings are divided into two types: short-period (*0.25 - 0.5* μm) and long period-gratings (*100 - 500* μm). They are considered as being made out of planes across the fibre core, called the Bragg grating planes, which are distinguished only by their grating pitch[xxxviii] or the tilt[xxxix] as schematically represented in Figure 5.2. As such, their refractive index modulation is theoretically described only in the longitudinal axis of the fibre, as a quasi-sinusoidal expression.

In the case of short-period gratings, the light is coupled into the backward propagation direction by reflection. It is also possible to couple light out of the core into back propagating radiation modes by tilting the fringes of short-period gratings. These types of gratings are also referred to as slanted or tilted

[xxxviii] The word "pitch" is often used for the spacing between the planes. Generally FBGs are divided in short-period gratings (<5 μm) and long-period gratings (~100 - 500μm).

[xxxix] The grating fringes can be photo-imprinted perpendicular to the fibre axis or at an angle; the tilt is given by the angle between the grating planes and the fibre longitudinal axis, they are called slanted or blazed gratings.

gratings, see Figure 5.2b. In the case of long-period gratings, the light is coupled into forward propagating cladding modes.

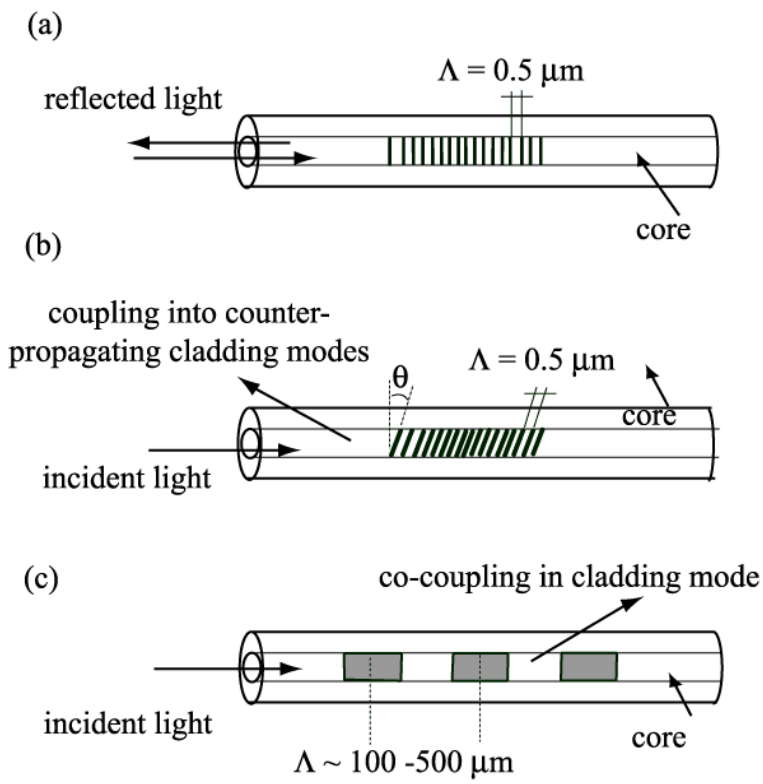

Figure 5.2. Schematic representation of a fibre Bragg grating. (a) a straight short-period grating; (b) a slanted short-period grating; and (c) a long-period grating. The period of the grating is Λ. For the slanted grating the planes of the grating form an angle θ with the normal to the fibre axis (after ((Riant 2003))**.**

5.3.2.2 Classification by Growth Dynamics

Several distinct formation regimes have been reported to account for the growth behaviour of the FBGs during fabrication. This classification is primarily used in describing short-period gratings.

The very first gratings called "Hill gratings" are also referred to as "type 0 gratings" and represent a special case. They are produced spontaneously within

the optical fibre and as such are called "self-organised" or "self-induced" gratings. These gratings are formed by launching light of 488 nm in the fibre, from which partial reflection at the cleaved end of the fibre, called Fresnel reflection, creates a weak interference pattern along the fibre (Hill, Fujii *et al.* 1978). As the grating is forming, this weak interference pattern, written along the fibre, gradually enhances the strength of the back-reflected light until the reflectivity of the grating reaches a saturated level.

Four other grating types with markedly different physical properties result from their fabrication conditions (Archambault, Reekie and Russel 1993a; Malo, Johnson *et al.* 1993). Firstly, categories entitled Type I and Type II FBGs have been proposed to distinguish the low- and high-fluence gratings, respectively (Archambault, Reekie and Russel 1993a).

Type I FBGs (Archambault, Reekie and Russel 1993b), also called conventional gratings, refer to gratings that are characterised by a monotonic increase in the amplitude of the refractive index modulation with writing time. There have been suggestions that their formation mechanism has been related to local electronic defects in the glass matrix.

Type I gratings can be written with continuous wave light or with many low-power UV pulses (Meltz, Morey and Glenn 1989), giving rise to a positive refractive index change, see Figure 5.3 (Salik 2001). The refractive index change achieved in the FBG depends on the type of fibre and writing conditions, i.e. whether the fibre is hydrogen-loaded; but generally its value varies from 4×10^{-5} to 10^{-3} in hydrogen loaded fibre (Culshaw and Dakin 1996).

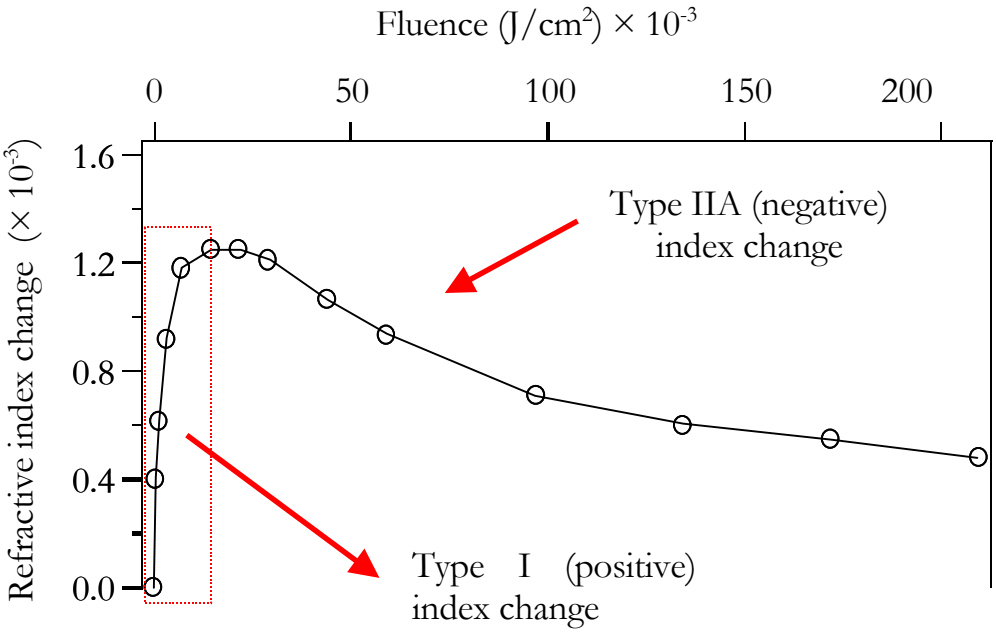

Figure 5.3. Refractive index dependence on UV fluence for Type I and Type IIA FBG written in high Ge-doped fibre. When the Ge-doped core is exposed to UV light the refractive index increases giving rise to, what is referenced in literature, a positive index change. With continued UV exposure the index change saturates and then starts decreasing. This later formation has been classified as Type IIA producing a so-called negative index change (after (Salik 2001)).

Another characteristic of a Type I FBG is that the reflection spectrum of the guiding mode is complementary to the transmission signal; a typical spectral response of a Type I FBG is presented in Figure 5.4.

The Type II FBGs category has been subdivided into Type IIA[xl], (Xie, Douay *et al.* 1993; Xie, Niay *et al.* 1993), and Type II gratings, (Archambault, Reekie and Russel 1993a) although they are clearly identified as different FBG types.

Type IIA FBGs evolve after continued exposure of particular Type I gratings, such that the refractive index change increases to saturation and then starts decreasing giving rise to a negative index change, which occurs after the

[xl] Some authors refer to these gratings as Type III (see Culshaw, B. and J. Dakin, *Optical Fibre Sensors*. Artech House, Boston, USA, Vol. 3: Components and Subsystems., 1996.).

positive index change (as shown in Figure 5.3). Usually they are formed in non-hydrogen-loaded fibres, (Xie, Niay *et al.* 1993), where the FBG is first partially erased and then rewritten into the fibre core.

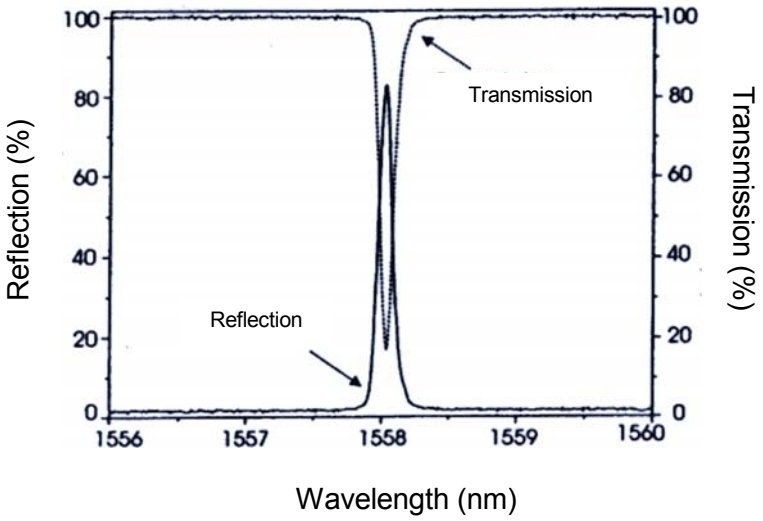

Figure 5.4. Spectral characteristics of a Type I Bragg grating (after (Othonos and Kalli 1999a)).

The formation mechanism behind these Type IIA gratings is not yet clear, but appears to be linked to the stress field caused by UV induced densification during fabrication (Kherbouche and Poumellec 2001).

Type II gratings are either formed by a single pulse from a high power UV laser of around *1* J/cm^2, with a pulse duration around *20* ns (Archambault, Reekie and Russel 1993a), or with a few shots of UV light at fluences of the order of *0.06* J/cm^2, (Hill, Atkins *et al.* 1995). These high energy pulses cause damage or fusion of the glass matrix resulting in large changes in the core refractive index, of the order of 5×10^{-3} up to 10^{-2} (Hill, Atkins *et al.* 1995). Type II grating characteristics include not only high refractive index changes but also very high

reflectivities, close to *100%*, together with broad and complex resonance peaks, refer to Figure 5.5, usually having a full width half maximum of between one and five nanometers (Malo, Johnson *et al.* 1993; Hill, Atkins *et al.* 1995).

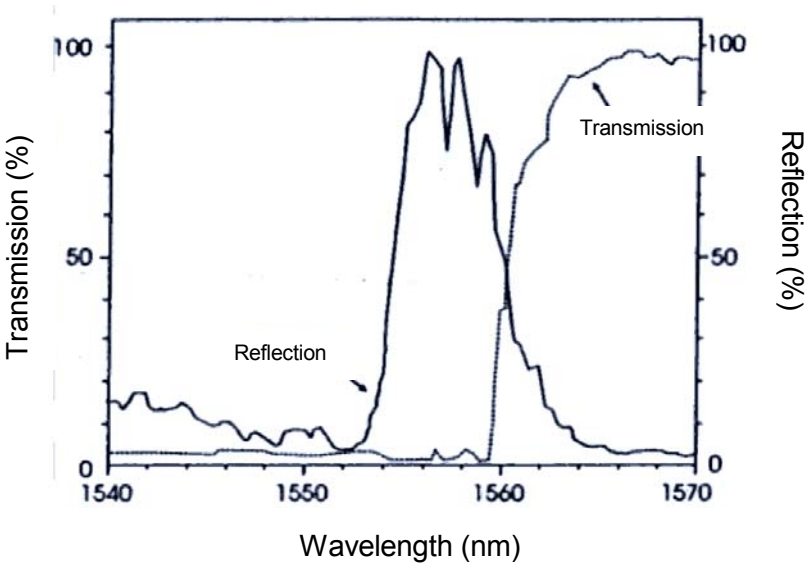

Figure 5.5. Spectral characteristics of a Type II Bragg grating (after (Archambault, Reekie and Russel 1993a)). The transmission spectrum shows that Type II gratings pass wavelengths longer than the Bragg wavelength, whilst shorter wavelengths are coupled into the cladding. The reflection spectrum is broad showing complex resonance peaks.

In Type II gratings, the fibre core appears to be fractured or damaged with a periodic structure. Images obtained with a scanning electron microscope have revealed gratings etched on the core/cladding interface after Type II grating formation; they suggested that the surface glass has melted, flowed and resolidified (Malo, Johnson *et al.* 1993; Mihailov and Gower 1994b, a; Hill, Atkins *et al.* 1995). However, the destructive nature involved in the scanning electron microscope imaging procedure, in which the fibre is polished to the core, may compromise the grating structure and in addition provides information on only surface morphology (Mihailov and Gower 1994a).

Recently a new type of FBG has been designated and is referred to as Type IA (Liu, Williams *et al.* 2002; Shu, Liu *et al.* 2002). It has been generally acknowledged that the evolution of a Type IIA FBG is formed in a non-hydrogenated fibre and starts from a Type I grating. After achieving a maximum reflectivity, the Bragg wavelength shifts towards larger values. Under continued UV exposure, the Type I grating arrives at the point of a partial or complete erasure after which the Bragg wavelength shifts to shorter values, referred in the literature as "blue shift". In contrast the newly designated FBG, Type IA, is formed in hydrogenated B/Ge-co-doped fibre and after the erasure of the Type I FBG, under continued UV exposure the grating regenerates such that the Bragg wavelength shifts towards larger values, giving rise to what the authors call a "red-shift". This red shift in the Type IA FBG is considered to be significant, as it is about 16 times larger than the blue shift accompanying the formation of a Type IIA FBG. Also the UV exposure time is significantly longer for the formation of a Type IA FBG; around *60* min. The refractive index modulation that can be achieved may be as large as 1.68×10^{-2}.

As mentioned above, the physical properties of these four Types of FBGs are markedly different. The spectral bandwidth of Type II gratings is generally broader than Type I gratings. In addition their transmission spectra is not symmetrical with respect to the Bragg wavelength. Moreover, Type II gratings are much more thermally stable than Type I gratings; being stable up to approximately *700 °C*. By contrast, Type IA gratings exhibit less temperature sensitivity but have a similar strain sensitivity to Type I gratings. Consequently Type IA gratings can be useful in dual-grating-based systems (Shu, Liu *et al.* 2002).

5.3.2.3 Fibre Bragg Grating Concepts

When light is launched into the fibre core containing a Bragg structure, some of the signal is reflected, some is refracted and some is transmitted. Following the diffraction theory of gratings, which requires that both energy and momentum be conserved, the Bragg grating condition is the result of a phase-matching condition. Energy conservation requires that the frequency of the incident light ω_I, and the diffracted light, ω_d, is the same (Othonos and Kalli 1999a):

$$\hbar\omega_i = \hbar\omega_d, \tag{5.1}$$

Momentum conservation requires that:

$$\mathbf{k}_i - \mathbf{k}_d = m\mathbf{K}_g, \tag{5.2}$$

where m is the diffracted order, $\mathbf{k}_i$ and $\mathbf{k}_d$ are the wave vectors associated with the incident and diffracted light respectively and the grating vector $\mathbf{K}_g = 2\pi / \Lambda$ points in the direction in which the refractive index of the medium is changing in a periodic manner. In the case of a single-mode fibre, the generally accepted representation of the grating is one of uniformly distanced planes (see Section 5.5.6), and these three vectors lie along the fibre axis. As a result:

$$\mathbf{k}_i - \mathbf{k}_d = -\mathbf{k}_i = \frac{2\pi n_{eff}}{\lambda_{Bragg}}, \tag{5.3}$$

and the diffracted light propagates backward. λ_{Bragg} is the free space center wavelength of the incident light that will be back-reflected from the Bragg grating and n_{eff} is the effective refractive index of the fibre core at the Bragg wavelength.

Hence, the momentum conservation condition becomes:

$$2\left(\frac{2\pi n_{eff}}{\lambda_{Bragg}}\right) = m\frac{2\pi}{\Lambda}. \tag{5.4}$$

If $m = 1$, then the periodic index modulation of the FBG structure reflects the wavelength that satisfies the condition expressed by Eq. 5.4 for the first-order Bragg condition. In the case of phase mask written FBGs, the Bragg wavelength, λ_{Bragg}, can also be expressed as a function of the periodicity of the phase mask corrugations, 2Λ, as (Morey, Meltz and Glenn 1989; Othonos and Kalli 1999a):

$$\lambda_{Bragg} = 2n_{eff}\Lambda, \tag{5.5}$$

where n_{eff} is the effective core index of refraction and Λ is the grating period.

The main parameters used to characterise a uniform fibre Bragg grating are refractive index modulation amplitude, $n(z)$, periodicity, Λ, Bragg wavelength, λ_{Bragg} and length, L. The refractive index modulation spatial profile, $n(z)$, taking the form of a phase and amplitude-modulated periodic waveform, has a direct implication in the spectral properties of the grating and may be represented by:

$$n(z) = n_0 + \Delta n \cos\left(\frac{2\pi}{\Lambda}z\right), \tag{5.6}$$

where n_0 is the average refractive index of the fibre core, Δn is the refractive index modulation amplitude, which practically determines the visibility of the UV fringe pattern, Λ is the periodicity of the grating refractive index modulation and z is the position along the axis of the fibre.

Note that (as with Eq. 5.6) it is assumed that the refractive index modulation amplitude, $n(z)$, depends only on z, an assumption that it shown in this work to be incorrect.

The back-reflected light with grating wavelength λ_{Bragg} is characterised by its reflectivity, expressed as:

$$R_B(L,\lambda) = \tanh^2\left(\frac{\pi L \Delta n \eta(V)}{\lambda_{Bragg}}\right), \tag{5.7}$$

where L is the length of the grating, $\eta(V) \approx 1 - 1/V^2$ is the fraction of the mode intensity in the core of the fibre which is normally close to unity and V is the normalised frequency of the fibre (as defined in Section 2.2.1).

Note that Eq. 5.7 represents the reflectivity for the first-order Bragg condition (i.e. $m = 1$). It can be easily seen that the reflectivity depends on the grating order; hence Eq. 5.7 can be re-expressed as:

$$R_B(L,\lambda) = \tanh^2\left(\frac{\pi L \Delta n \eta(V)}{m\lambda_{Bragg}}\right). \tag{5.8}$$

Consideration of the grating order is important because it must be known in order to use the measured grating reflectance to effectively evaluate the amplitude of the refractive index modulation.

5.3.2.4 UV-Induced Effective Refractive Index vs UV-Induced Refractive Index of the Fibre Material

Clear distinction should be made between the UV-induced change of the effective index as a characteristic of the fundamental mode and the UV-induced change of the refractive index of the fibre material.

The effective refractive index is the quantity that is usually accessible by various measurements methods (Kashyap 1999; Brinkmeyer, Johlen *et al.* 2000). The information inferred in relation to the refractive index of the fibre material, however does not reflect direct information on the actual UV-induced refractive index change of the fibre material. The latter is of interest for optimizing the photosensitivity of fibres. Additionally, the actual UV-induced peak refractive-index change in the fibre can be noticeably larger than the increase of the effective index of the fundamental fibre mode (Renner 2001). The quantitative relations between the UV-induced refractive index change and the propagation characteristics of the fundamental mode have been investigated theoretically.

The UV-induced refractive index is non-symmetric across the fibre core when the FBG is written from one side. Experimental measurements using atomic force microscopy (Inniss, Zhang *et al.* 1994) and refracted near-field measurements (Brinkmeyer, Johlen *et al.* 2000) have revealed that the UV-induced refractive index profiles have an exponential like-form with a $1/e$ width of only a few microns. This is a consequence of absorption.

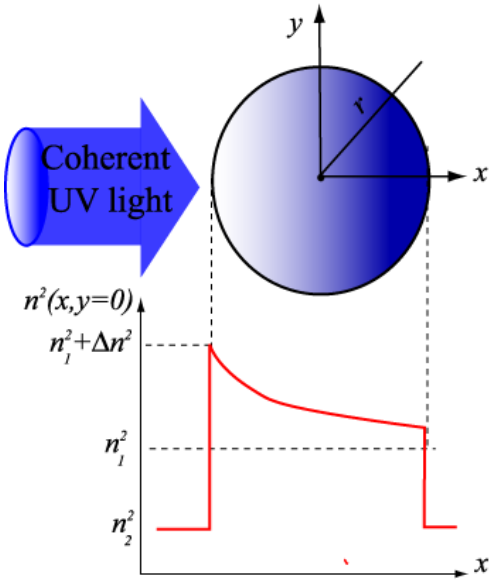

Figure 5.6. A non-symmetric UV-induced refractive index into the photosensitive fibre core resulting from a left side exposure of the fibre (Renner 2001).

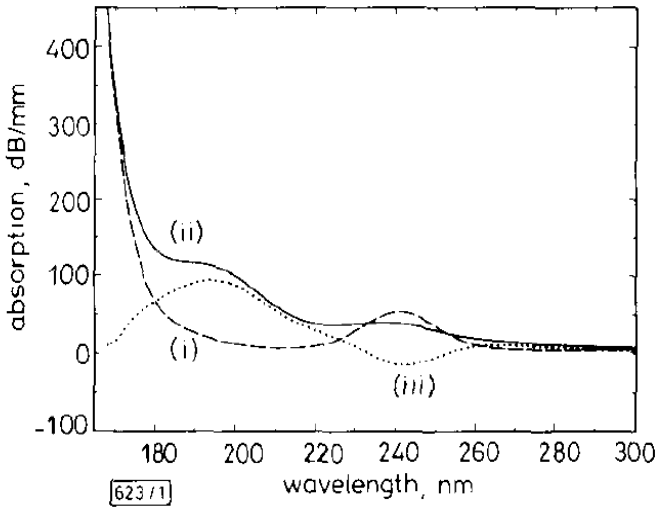

Figure 5.7. UV absorption spectra of a GeO_2:SiO_2 optical preform slice (~100 μm thick) before (Line (i) dashed) and after UV exposure line (iii) and (ii). Line (ii) and (iii) represent the absorption spectra around and after 30 min of UV exposure respectively (Atkins, Misrahi *et al.*, 1993).

Noteworthy is the different behaviour of germanosilicate glasses at various wavelengths in the ultraviolet regime, refer to Figure 5.7. It is well known that germanosilicate glasses show significant absorption peaks in the UV spectra between 170 to 300 nm. However, the UV-induced refractive index changes in the germanosilicate fibres were shown to be poorly dependent on the wavelength (Douay et al., 1997). Figure 5.7 compares the UV absorption spectra of a germanosilicate optical fibre preform before and after UV exposure.

5.4 Fabrication of Fibre Bragg Gratings

Fibre Bragg gratings can be produced by using either pulsed (Albert, Malo *et al.* 1995) or continuous wave ultraviolet irradiation (Williams, Ainslie *et al.* 1992); the magnitude of the photoinduced grating refractive index variation has been shown to be approximately linearly proportional to the optical intensity (Hill and Meltz 1997).

A number of fibre Bragg gratings fabrication schemes are known in the literature (Kashyap 1999). The most common techniques are: the internal writing techniques, traditionally known as "Hill's gratings" (Hill, Fujii *et al.* 1978); the holographic interferometer techniques (Meltz, Morey and Glenn 1989; Morey, Meltz and Glenn 1994); the prism interferometer techniques (Kashyap, Armitage *et al.* 1990; Zhang, Brown *et al.* 1994; Rizvi and Gower 1995; Garchev, Vasiliev and Booth 1997); the phase mask techniques

(Anderson, Mizrahi *et al.* 1993; Hill, Malo *et al.* 1993b) and point-by-point writing (Malo, Hill *et al.* 1993).

The phase mask writing technique provides a simple and robust method for the production of fibre Bragg gratings. In the following, a brief description of the phase mask method is given as this method has been used in the fabrication process of the Bragg gratings considered in this thesis.

The phase mask method (Hill, Malo *et al.* 1993b), is used for producing standard FBGs, employing a transmission diffraction grating which, ideally, generates two crossed beams to produce a laterally and spatially phase modulated interference pattern along the optical fibre, as is generally accepted in the literature, see Figure 5.8.

A phase mask is produced by etching a one dimensional surface relief structure on one side of a flat slab of fused quartz or silica glass using ion beam lithography or photolithography. The shape of the periodic pattern approximates a square wave in profile.

Normally a phase mask is designed so that most of the incident ultraviolet light is diffracted into the first-orders and diffraction into the zeroth-order is suppressed by controlling the depth of the corrugations to provide an effective π phase-shift from alternate striations. Therefore the incoming beam is split at the phase mask into two diffraction orders, +1 and -1, as shown in Figure 5.8, having equal power levels.

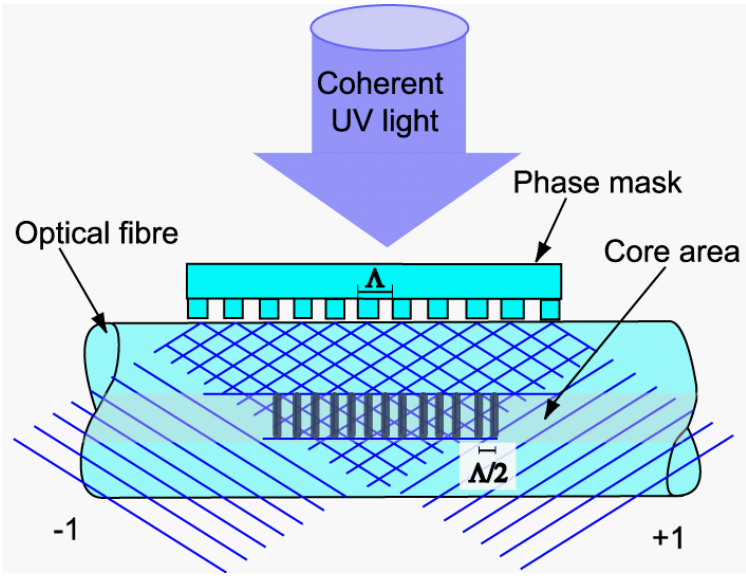

Figure 5.8. Schematic of the phase mask method used for the production of the fibre Bragg gratings. The coherent UV beam splits at a zeroth-order nulled phase mask (approx *3.5%*). The resulting beams, predominantly contained in the +1 and -1 diffracted orders, with approximately 38% of the total light intensity found divided in the two orders, interfere to produce the periodic pattern that photoimprints the gratings in the optical fibre. The phase mask period determines the grating period: if the period of the phase mask grating is Λ, the period of the photo-imprinted index grating is Λ/2.

Although in theory the amount of light in the zeroth-order is zero in such a designed phase mask, also called a nulled phase mask, in practice the level of the zeroth-order contribution can be guaranteed by the manufacturer to only a certain percentage varying from *3.5* to *1%*, with a specified percentage of *38* to *40%* in each of the two first-order diffracted beams. The effect of the zeroth-order contribution of a phase mask has been theoretically investigated in the past by various authors. Studies on this subject showed that a very small percentage in the zeroth-order, as low as *0.1%*, would have a substantial effect

on the structure of the fibre Bragg grating (Dyer, Farley and Giedl 1995;Xiong, Peng *et al.* 1999), which also affects the periodicity of the FBG.

In the phase mask writing technique, the optical fibre, stripped of its protective jacket, is placed almost in contact with the corrugations of the phase mask, such that the distance between the core of the fibre and the surface of the phase mask is around *60* to *65* μm. Different phase masks are required for different resonant wavelengths of FBGs. The resonant Bragg wavelength is determined by the periodicity of the phase mask corrugations.

The phase mask writing technique offers some advantages: it presents an easy way of controlling the alignment of the fibre for photoimprinting and has the capability to manufacture high performance gratings at a low unit cost. Furthermore, there is the possibility of manufacturing several gratings at once by irradiating parallel fibres through the phase mask (Hill and Meltz 1997). However, a drawback of this technique is the fact that that a separate phase mask is required for each Bragg wavelength, as previously mentioned. A further drawback of this technique is that all phase masks will direct some power into orders other than $+1$ or -1.

As this chapter argues, in practice not only the small percentage in the zeroth-order affects the structure of a Bragg grating but also the presence of a small relative intensity in the higher diffracted orders contributes significantly to a complex FBG structure.

5.5 Characterisation Methods

The characterisation of the microscopic properties of FBGs is problematic because of the diversity of the materials in which they are being written under a variety of fabrication conditions. It is widely appreciated that ideally, one would like to find an efficient combination of refractive index mapping at each point within a FBG using a non-destructive method. The quest for such a combination has long been one of the major challenges in the field of FBG characterisation.

Although FBGs have been in existence for a quarter of a century now, it has only been in the last few years that researchers have really begun to perform analysis and evaluation of the characterisation techniques, but a standard way to characterise FBGs is yet to be recognised. A recent round-robin among a group of telecom companies found that the state of fibre Bragg grating metrology in industry needs improvement (Rose, Wand and Dyer 2000).

Many methods for characterising FBGs have been proposed; some can be classified as direct methods and others as indirect methods. The direct methods used for characterisation, summarised in the following sections, have primarily focused on Type II FBGs. However research on Type I FBGs has, prior to this work, been carried out exclusively using indirect methods, i.e. these methods do not investigate the FBG structure itself but rather they examine the response due to the FBG structure, for example. Type I FBGs are difficult to study directly due to their low amplitude of refractive index modulation, which makes them difficult to detect and image by any technique.

In the following, different methods are critically reviewed with regard to their sensitivity, spatial resolution and their potential to obtain information routinely and non-destructively. The direct characterisation imaging methods reviewed here are: Confocal Microscopy, Scanning Electron Microscopy, Atomic Force Microscopy, Scanning Near-Field Optical Microscopy and the Half-Shade Polarising Technique. The next section reviews some of the indirect methods.

5.5.1 Direct Methods

5.5.1.1 Confocal Microscopy

Confocal microscopy has been used to non-invasively assess FBG morphology using light reflected from a fibre sample containing a FBG (Malo, Johnson *et al.* 1993; Hill, Atkins *et al.* 1995). The principle of confocal scanning optical microscopy, originally named "double focusing microscopy" (Minski 1957, 1988), has been described in the literature extensively and the theoretical analysis of confocal scanning optical microscopy has been researched by numerous authors (Wilson and Sheppard 1984; Wilson 1989; Gu 1996).

A confocal scanning optical microscope is, in essence, a conventional optical microscope equipped with a number of complex attachments to direct and process a beam of light. Confocal microscopes generally use intense laser light that illuminates and images one point on a sample through a pinhole, a small aperture (having a diameter of *50* to *250* μm) that acts as a spatial filter. The light passes through this pinhole and the out-of-focus haze, normally present in a conventional microscope, is removed producing a small depth of field. The capacity for a confocal microscope to image planes within a specimen is termed the optical sectioning property. This property is the key element in producing

three-dimensional (3-D) images of an object studied under confocal microscopy.

Confocal microscopy has been used for visualisation of a Type II FBG photoimprinted using the phase mask method (Malo, Johnson *et al.* 1993) and the holographic method (Hill, Atkins *et al.* 1995) in different types of fibre and using a high fluence laser. This visualisation was possible because of the large refractive index in the photoinduced grating; see Table 5.2.

It is well known that in confocal imaging of transparent specimens the refractive index changes are the greatest source of contrast[xli]. It has been shown that as the change in refractive index decreases to values around *0.05*, the image contrast approaches zero (Dunn, Smithpeter and Richards-Kortum 1996). As such, although confocal microscopy offers diffraction-limited resolution, it seems that it is only applicable to studying strong Type II FBGs where the refractive index modulation is high. The technique is inefficient in the evaluation of Type I FBGs where the refractive index modulation may be as low as 1.7×10^{-4}, for example; refer to Section 5.6.

5.5.2 Scanning Electron Microscopy

Scanning Electron Microscopy (SEM) uses a beam of highly energetic electrons to examine samples yielding information regarding their topography and

[xli] Contrast is defined as $(P_s - P_b)/(P_s + P_b)$, where P_s is the maximum value of the detected fraction of photons in the case in which the object layer has different optical properties than the other layers and P_b is the detected fraction of photons from the homogeneous background level, at the same focal plane depth as P_s.

morphology with a resolution[xlii] far beyond that of light microscopes. SEM was first used for examining FBGs by Mihailov and Gower (1994a).

The sample to be viewed using a SEM needs to be electrically conductive. When a nonconductive sample is directly illuminated with an electron beam, electrons collect locally and cause an abnormal contrast in the image. For this reason, the surface of a nonconductive material is coated with some conductive material prior to observation. As such, the fibre containing an FBG, being made of nonconductive material, needs to be covered with a thin layer of a conductive material after being polished close to the surface to be studied. After being polished and cleaned in an ultrasonic methanol bath, the FBG is sputter coated using a device called a sputter coater. This device coats the sample with gold atoms whereby presenting the potential for damaging the sample.

Type II FBGs written holographically in a Ge-doped fibre (BNR CA 2114), have had the exposed cladding surface of the fibre examined by SEM (Mihailov and Gower 1994a). The SEM images revealed evidence of the processes believed to be responsible for the formation of type II Bragg gratings, such as melting, flow and resolidification. The images also displayed a periodic modulation ~ *1* μm deep on the surface of the fibre cladding having a period of *0.53* μm. The authors concluded that, this grating, fabricated using a high power laser, led to the formation of the observed surface morphology on the cladding having an identical period to the Bragg refractive index grating created in the core. In providing this explanation the authors basically extrapolated the

[xlii] The resolution of a SEM microscope is 10 nm. Although theoretical values of 0.002nm are predicted, they can not be achieved due to limiting factors that depend on the particularities of the microscope and/or the environment being studied.

information seen on the surface of the cladding to the core of the fibre, and this represents a serious limitation of the SEM technique.

Although SEM is a reliable method for surface morphologies, serious drawbacks exist when it is applied to studying FBGs. Firstly, SEM is a destructive method for imaging an FBG and requires laborious sample preparation methods, such as metal evaporation onto the surface to be imaged. These processes can lead to image artefacts and the loss or change of detectable information about the structure and properties. In addition, SEM images provide information on surface morphology, and any attempt to polish the fibre to the core may compromise the grating structure. Moreover, the surface imaged does not necessarily fully characterise the FBG, since only a small arbitrary region of the FBG is actually imaged and this cannot be conclusive for characterising the FBG as a whole. To conclude, SEM is a destructive technique, which provides high spatial resolution and qualitative information regarding a single surface through a FBG or the cladding surface.

5.5.3 Atomic Force Microscopy

The Atomic Force Microscope (AFM) (Binning, Quate and Gerber 1986), also called the scanning force[xliii] microscope, utilises a sharp probe moving over the surface of a sample in a raster scan. An AFM was first used to observe surface modulations on planar slices of Ge:SiO_2 preforms following grating inscription (Poumellec, Guenot *et al.* 1995). Due to restrictions of the technique at that time, the investigations using AFM were made on planar slices of material

[xliii] A number of forces contribute to the image data obtained using an AFM; the main forces contributing to the cantilever deflection are electrostatic (Coulomb) repulsive forces and attractive van der Waals forces between the tip and the sample surface; other forces such as capillary forces may also contribute to the image. The reader is referred to Heinzelmann, H., E. Meyer, H. Rudin and H.-J. Guntherrodt, "Scanning Tunnelling Microscopy and Related Methods". R. J. Behm, N. Garcia and H. Rohrer (Ed.), NATO ASI Series Vol. 184, Kluwer Academic, Dordrecht. p. 449, 1990.

rather than on optical fibres. A surface corrugation pattern was observed following the inscription of FBGs in the slices, from which the densification mechanism was determined to be responsible for the photorefractivity.

More recently, the AFM has been employed in the investigation of optical fibres containing FBGs written using the phase mask method in two types of fibres, namely standard telecommunications fibres and germanium-boron co-doped fibres (Wei, Ye *et al.* 2002a).

The AFM technique examines the topography of an object through a fine ceramic or semiconductor probe scanning over a surface. A sharp AFM probe, called a tip, with a radius typically of *4* to *60* nm is attached to a flexible cantilever of a specified spring constant. The cantilever deflects in the *z*-direction due to surface topography whilst the tip scans over the sample surface in the *x-y* plane, therefore recording interactions between the tip and the surface. A photodiode detects the deflection of the cantilever through a laser beam focused on and reflected from the rear of the cantilever. A computer processes the electrical signal of the photodiode obtained from each point of the surface and generates a feedback signal for a piezoscanner to maintain a constant force on the tip. A plot of the laser deflection versus tip position on the sample provides the surface topography. The resolution of an AFM depends strongly on the shape of the tip. The smaller, i.e. sharper, the tip is, the smaller is the surface area sampled by the tip and the better the resolution.

The AFM images of FBGs revealed that the UV-exposure produced a spatially periodic relief pattern on the surface exposed to the UV light during fabrication.

Although this technique supplies resolution in the images of the order of nanometers, it is a destructive method for studying FBGs, requiring an experienced operator to avoid producing image artefacts and a thorough understanding of the AFM operation modes and tip-sample interactions. The fibre needs to be polished flat to a distance of a few micrometers (3-8 μm) due to the physical constraints of the scanner in the z-direction. Moreover, careful sample preparation is critical for producing quality images. In addition, due to the non-uniform transverse structure of the FBG, see Section 5.6, the application of the AFM method to studying FBGs is limited in that it can only provide information about one arbitrary surface of the FBG.

In comparison to SEM, the AFM method has the advantage of being relatively easy of use, at least requiring less sample preparation before examination on one hand, but on the other hand requiring a very small distance between the scanning probe and the surface to be imaged.

5.5.4 Scanning Near-Field Optical Microscopy

The sub-wavelength imaging (Betzig, Trautman *et al.* 1991) properties of scanning near-field optical microscopy (SNOM) (Pohl, Denk and Lanz 1984) attracted interest in examining FBG structure and its internal refractive index distribution (Mills, Hillman *et al.* 1999). The measurements are based on accessing the evanescent field (Huntington, Nugent *et al.* 1997) light propagating through the grating written in a fibre. SNOM overcomes the traditional diffraction limit and provides ultrahigh resolution of the structure and characteristics of the FBG. However all these advantages come at the cost of polishing the fibre within a few micrometers of the surface to be studied.

The principle of operation of a SNOM microscope has been described in Section 2.4 of this Thesis; more details can also be found in Shane Huntington's PhD Thesis (Huntington 1998).

In the work of Mills *et. al.* (1999), to access the evanescent field of a FBG, a D fibre has been first glued along a groove on a glass block of certain length (44 mm) and then has been polished down to a distance of *2* μm from its core (Mills, Hillman *et al.* 1999). Further, the fibre was then trimmed to the length of the *44* mm glass block and its ends were polished to ensure the coupling of the light into the grating. SNOM scanning of the grating section was performed using a 50 nm optical fibre tip after coupling light into the grating. The small size of the tip ensures the high spatial resolution of the SNOM images. The light coupled into the fibre was tuned to two wavelengths, one being equal to the second order resonance, called on resonance, and the other at a different wavelength, called off resonance. The authors concluded that fibre grating evanescent field images acquired at off resonance wavelengths revealed the refractive index contrast of the grating and that the evanescent field images acquired at on resonance display a standing wave distribution. The contrast in refractive index along the grating was not uniform and displayed a periodicity twice as large as the standing wave pattern period. The off resonance pattern was observed for two different wavelengths demonstrating the independence of the measurements of the wavelength of laser used.

As can be seen, this method is destructive and requires extensive sample preparation. Nevertheless it revealed a detailed structure of a FBG. Moreover the non-uniformities that were attributed to the errors in the refractive index may have been caused by irregularities on the polished surface.

The AFM and SNOM techniques are subject to similar limitations with regard to the quality of the probe used and as such artificial artefacts may be present in the acquired image (Hecht, Bielefeldt *et al.* 1996).

5.5.5 The Half-Shade Polarising Technique

A non-invasive study of FBGs has been performed using a microscope designed and constructed by K.W. Raine at the National Physical Laboratory (NPL), UK (Raine 1997; Raine, Feced *et al.* 1999), which allows the fibre to be viewed in polarised light. This system uses the half-shadow principle to compute the axial-stress profile of gratings by quantifying the birefringence profile along the fibre.

The NPL microscope consists of a polariser, the sample to be studied (which rotates the plane of polarisation), a quarter-wave plate orientated parallel to the polarizer, a half-shade device[xliv] (Koerster 1959) and a rotatable analyser. The key component of the instrument is the half-shade device, which divides the polarised light into two halves with the direction of polarization of the light in each separated by a very small angle. A schematic diagram of this microscope is shown in Figure 5.9.

A variety of half-shade devices are generally used in interference microscopes; some of the most familiar half-shade devices are the Laurent plate, the Lipich prism and the Soleil bi-quartz plate. A half-shade device is characterised by the so-called half-shade angle, *H*, that is, the angle through which the analyser has

[xliv] A device for forming at least two adjacent areas of polarised light. The angle between the directions of vibration of the light waves in the two areas is generally small (source http://www.photonics.com/dictionary/).

to be rotated to change from a minimum in one half of the field to a minimum in the other half.

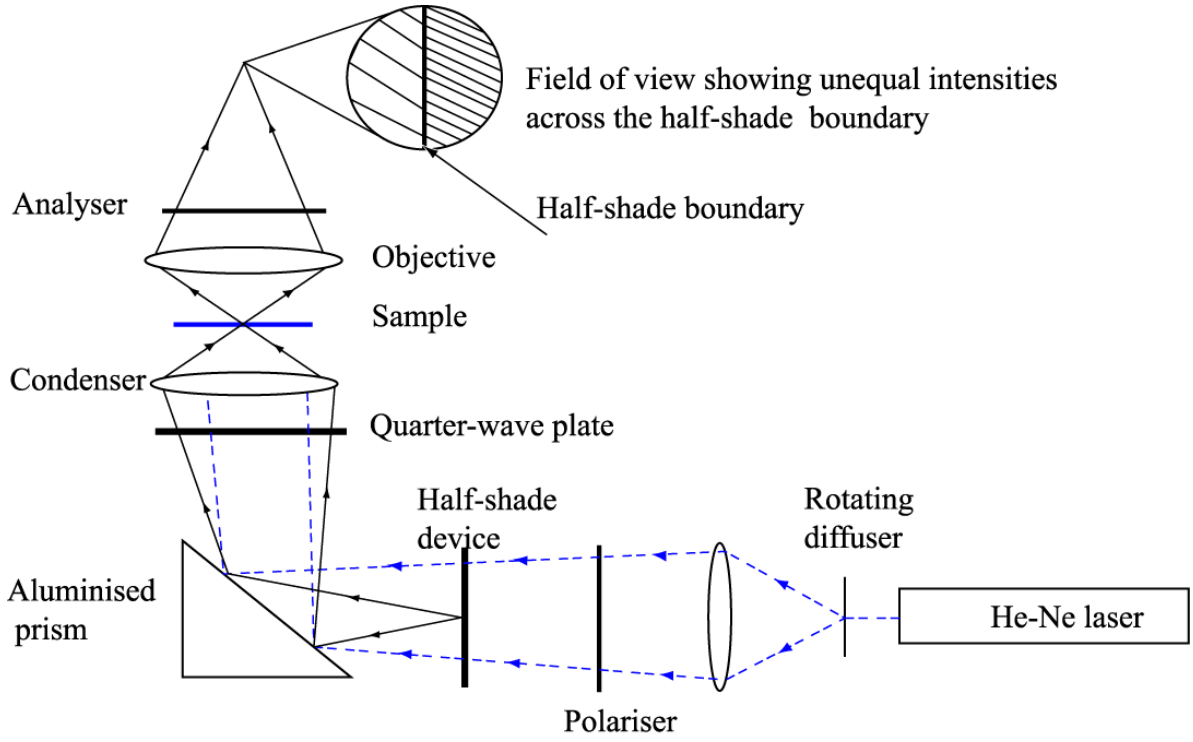

Figure 5.9. Schematic diagram illustrating the configuration in the NPL microscope for measuring birefringence. The circle at the top of the diagram represents the field of view as it appears to the observer; a small rotation, θ, of the quarter-wave plate produces unequal intensities into the hemispheres (after (Raine, Feced *et al.* 1999)).

The NPL microscope uses a mica half-wave plate as the half-shade device. By covering half of the light beam, the half-wave plate is used to rotate the plane of polarisation of the light beam with the transmission axis of the polariser in conjunction with the rotatable analyser in order to obtain the required half-shade angle. The edge of the half-wave plate is focused into the plane of the fibre through a microscope condenser. A CCD camera then records two complementary images of the fibre. By performing the difference between two

lines on each side of the half-shade boundary, the retardation profile[xlv] of the fibre is obtained.

Phase differences as small as *0.005°* are claimed to be detectable using this method. The intensity difference profile, ΔI, depends linearly on the half-shade angle, H, the retardation phase difference, δ, and the angular rotation of the quarter-wave plate, θ, (Raine 1997):

$$\Delta I \propto uH\delta + 2H\theta \tag{5.9}$$

where u is ± 1, depending on the orientation of the quarter-wave plate axes.

Type I FBGs, written in standard single-mode fibre, Corning SMF-28, using the phase mask method, have been studied using the NPL microscope. A non-uniform axial-stress along the grating was calculated with the modulation depth being greater on the side facing the incoming UV beam. In addition, the period of the grating was twice that of the expected value, being equal to that of the phase mask, leading to the conclusion that the FBGs were of second order but failed to provide a full explanation as to why the grating is of second order. The authors emphasised the importance of knowing the order of the grating in estimating the refractive index modulation from the measured grating reflectance (please refer to Section 5.3.2.3).

Although the microscope could resolve the grating structure, the limited depth of focus impeded a clear interpretation of the retardation profile.

As the microscope was used to map the birefringence profile parallel to the fibre axis, it can only be conclusive for providing information regarding the

[xlv] The authors defined the term "the retardation profile" as the phase difference introduced by the fibre.

axial-stress profiles and not for refractive index modulation, because the relationship between these two quantities is still to be quantified.

5.5.6 Indirect Methods

5.5.6.1 Coupled-Mode Theory

The most common theoretical tool for mathematically analysing FBGs is consideration of the wave propagation in gratings described by coupled-mode theory[xlvi] (Snyder and Love 1983; Marcuse 1991; Poladian 1996; Erdogan 1997). Coupled-mode theory, describes in a straightforward and intuitive way, the spectral dependence of a fibre grating and the corresponding grating structure. The grating is treated as a perturbation in the longitudinal axis of the fibre, with a z-dependent perturbation $n(x,y,z)$; the unperturbed fibre refractive index profile being described by $\bar{n}(x,y)$. The theory is developed around the weakly guiding condition, i.e. the differences in refractive indices in the core, n_{co}, and the cladding, n_{cl}, are very small, $\bar{n} \cong n \cong n_{eff} \cong n_{cl}$, where n_{eff} represents the effective index of the supported mode in the unperturbed fibre (Snyder and Love 1983).

Considering a forward and a backward propagating mode, the total electric field is obtained by the superposition of these two modes, described by their coefficients $b_{\pm 1}$:

$$E_x(x,y,z) = b_1(z)\psi(x,y) + b_{-1}(z)\psi(x,y). \tag{5.10}$$

[xlvi] The derivation of the coupled mode theory is given for the sake of completeness of discussion and follows Snyder, A. W. and J. D. Love, *Optical Waveguide Theory*. Chapman and Hall, London, 1983.

The transverse electromagnetic field, described by the function ψ, in the unperturbed fibre is described by the scalar wave equation (Snyder and Love 1983):

$$\left\{\nabla_t^2 + k^2 n^{-2}(x,y) - \beta^2\right\}\psi = 0 \tag{5.11}$$

where $\nabla_t^2 = \delta^2/\delta x^2 + \delta^2/\delta y^2$, $k = \omega/c$ is the vacuum wavenumber and $\beta = \beta(\omega) = n_{eff}\omega/c = n_{eff}k$ is the scalar propagation constant.

In the perturbed fibre, the total electric field must also satisfy the scalar wave equation, i.e.

$$\left\{\nabla_t^2 + k^2 n^2(x,y,z) + \frac{\delta^2}{\delta z^2}\right\}E_x = 0. \tag{5.12}$$

Now, taking into account the two modes represented by the coefficients $b_{\pm 1}$ and after performing the integration in the transverse *xy*-plane, Eq. 5.11 becomes:

$$\frac{d^2 b_1}{dz^2} + \frac{d^2 b_{-1}}{dz^2} + \left(\beta^2 + 2kn_{co}D_{11}(z)\right)\left(b_1 + b_{-1}\right) = 0 \tag{5.13}$$

where D_{11} is a coefficient defined as:

$$D_{11}(z)\frac{\frac{k}{2n_{co}}\int\left(n^2 - n^{-2}\right)\psi^2 dA}{\int\psi^2 dA}. \tag{5.14}$$

Further decomposition of Eq. 5.13, corresponding to separating the total electric field into its forward and backward-travelling waves, yields a set of first-order differential equations:

$$\frac{db_1}{dz} - i(\beta + D_{11})b_1 = iD_{11}b_{-1}$$
$$\frac{db_{-1}}{dz} + i(\beta + D_{11})b_{-1} = -iD_{11}b_1. \tag{5.15}$$

As it is generally agreed that the z-dependence of the index perturbation in a FBG is approximately quasi-sinusoidal, the coefficient D_{11} is consequently expressed as a quasi-sinusoidal function and can be written in the form of:

$$D_{11}(z) = \kappa(z)\exp\left(i\frac{2\pi}{\Lambda}z\right) + \kappa^*(z)\exp\left(-i\frac{2\pi}{\Lambda}z\right) + \sigma(z), \tag{5.16}$$

where $\kappa(z)$ is a complex, slowly varying function, called the coupling coefficient along the grating and $\sigma(z)$ accounts for the refractive index modulation.

Further, by defining the coefficients describing the forward and the backward propagating modes along the grating, and using new field amplitudes *u(z)* and *v(z)*, as follows:

$$b_1(z) = u(z)\exp\left(i\frac{\pi}{\Lambda}z\right)u(z)\exp\left(+i\int_0^z \sigma(z')dz'\right)$$
$$b_{-1}(z) = v(z)\exp\left(-i\frac{\pi}{\Lambda}z\right)u(z)\exp\left(-i\int_0^z \sigma(z')dz'\right), \tag{5.17}$$

the final expression for the coupled-mode equations is obtained:

$$\frac{du}{dz} = i\delta u + q(z)v$$
$$\frac{du}{dz}v = -i\delta v + q^*(z)u, \tag{5.18}$$

where $\delta = \beta - \frac{\pi}{\Lambda}$ represents the wavenumber detuning and the coupling coefficient of the grating is defined as:

$$q(z) = i\kappa(z)\exp\left(-2i\int_0^z \sigma(z')dz'\right). \tag{5.19}$$

Moreover, the refractive index change created by UV radiation during the fabrication process of FBGs is generally small and considered uniform in the core such that the index perturbation is often modelled as scalar perturbations and is composed of a constant and a fluctuating component denoted by "dc" and "ac" respectively:

$$n\text{-}\bar{n} = \Delta n_{ac}(z)\cos\left(\frac{2\pi}{\Lambda} + \theta(z)\right) + \Delta n_{dc}(z). \tag{5.20}$$

Note that (as with Eq. 5.16) it is assumed that Δn_{ac} depends only on z, an assumption that it confirmed in this work to be incorrect. Generally it is accepted that the following interpretation of the coupling coefficient, the modulus of the coupling coefficient $q(z)$, is proportional to the index modulation amplitude or the peak-to-peak modulation of the index variation and as such it determines the grating strength[xlvii]; its phase corresponds to the grating phase envelope (Skaar 2000).

Many indirect methods are available for characterising the spatial grating structure (i.e. the index modulation along the FBGs) obtaining a distributed measurement of the complex coupling coefficient, $\kappa(z)$. These methods include side scattering, interferometric and reflectometric.

[xlvii] It is worth noting that in the literature the term "weak grating" is often used and is referring to the influence that the grating has on the propagating waves.

5.5.6.2 Side-Diffraction Methods

The side scattering method (Krug, Stolte and Ulrich 1995) relies on the side-diffraction of a probe beam by the fibre grating. A laser beam is focused through the side of the fibre into its core, at an incident angle θ_i as shown in Figure 5.10.

The first-order Bragg diffraction of the probe beam by the grating occurs at the phase-matching Bragg condition:

$$\sin\theta_i = n\frac{\lambda}{\lambda_B}, \tag{5.21}$$

where θ_i is the incident angle onto the surface of the fibre (in air), λ is the wavelength of the probe laser, λ_B is the Bragg wavelength of the FBG and n is the effective refractive index of the fibre.

The diffracted signal, considered to have a quadratic variation with the core index modulation Δn, is recorded as the fibre is scanned under the probe beam yielding the refractive index variation along the grating.

Side-diffraction scattering relies on *a priori* knowledge of the grating distribution along the fibre, which is a limitation of the method. Furthermore it assumes a uniform axial distribution of the grating, it requires a perfect positioning of the fibre core during scanning to maintain the diffraction efficiency[xlviii] constant (Roussel, Magne *et al.* 1999) and yields information about the spatial distribution of amplitude but does not provide information about the spatial distribution of the period.

[xlviii] The diffraction efficiency of the grating for the first-order diffracted beam is $\eta=|S(2a)|^2/\ |R(0)|^2$ where R(0) is the incident field amplitude and S(2a) is the amplitude of the diffracted field emerging from the grating photoinduced in a fibre having a core diameter 2a.

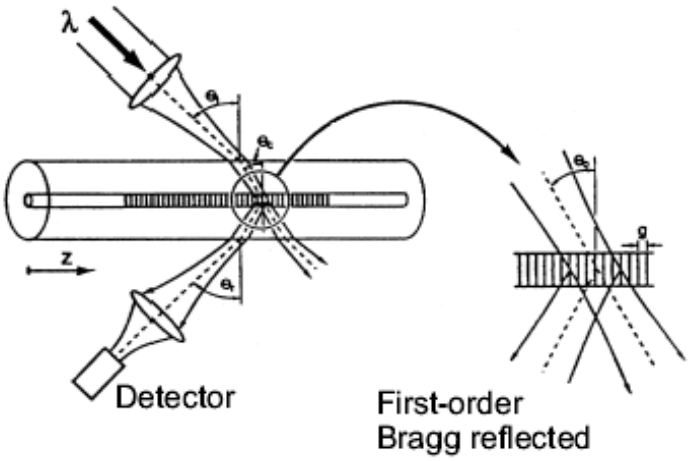

Figure 5.10 Schematic representation of the side-diffraction Bragg grating characterisation system (source (Krug, Stolte and Ulrich 1995)).

Recent measurements performed with a modified side-diffraction technique, such that the entire scattered beam is captured via a charged-coupled device, have concentrated on improving the sensitivity of the technique at the cost of reducing the spatial resolution from 10 μm (Krug, Stolte and Ulrich 1995) to about one millimetre and have demonstrated simultaneous measurement of FBGs refractive index modulation and its grating period (Baskin, Sumetski *et al.* 2003). Additionally, the authors have questioned for the first time the direct applicability of the coupled-wave theory based on a single-harmonic model[xlix] of the reflective index variation. Based on their measurements, they had reason to concede the presence of a grating having a double period alongside the main grating component.

An interferometric side-diffraction technique has been proposed as an extension of the work of Krug and co-workers (1995) (Fonjallaz and Borjel

[xlix] Coupled-mode theory considers a grating to be a quasi-periodic structure, which was referred to by Baskin, Summetski et al. as the single-harmonic model; i.e only the fundamental refractive index modulation.

1999, 2000). Here the fibre grating is illuminated from the side by a probe laser beam. The interferometric side-diffraction technique includes the measurement of the grating phase by detecting the interference pattern between the zeroth and first diffraction orders. Information about the refractive index distribution along the FBG, including its phase profile, is obtained with a spatial resolution of *15* μm (Fonjallaz and Borjel 2000). A recent theoretical quantitative investigation of this technique has revealed stringent requirements for the properties of the grating under test as well as its sensitivity to noise (Petermann, Helmfrid and Friberg 2002). Although it has been shown that the method is very useful for determining the phase distribution along a grating with modulation depths as low as $\Delta n \approx 10^{-3}$, the method is sensitive to optical noise originating from the fibre surface, distorting the amplitude of the detected signal, such that the phase for very weak[1] gratings would be difficult to retrieve.

Furthermore, another non-destructive analysis of a FBG, based on side-diffraction interference, has been recently reported (El-Diasty, Heaney and Erdogan 2001). This method relies on the interference of two side diffracted laser probe beams and it is used to measure the refractive index modulation along the fibre and the grating period. The fringe visibility and the spatial period of the interference pattern are a function of the refractive index modulation and the periodicity of the grating, respectively. Although sensitive and applicable to weak gratings, having an index modulation of 7×10^{-4}, the method cannot describe the FBG as a tridimensional (3D) structure. A drawback of the

[1] Note that there is some confusion in the literature over the uses of the term "weak" and "Type I grating" in relation to reflectance and refractive index modulation. Here "weak" is used to denote a low reflectance and "Type I" is defined in text. Some authors, however, refer to Type I gratings as "weak" or "extremely" weak gratings due to the fact that the FBGs investigated also have a low reflectance.

method is that it considers the FBG as being uniform across the core of the fibre, as described in Section 5.3.2.1.

5.5.6.3 Reflectometric Methods

Reflectometric methods, such as Optical Coherence Domain Reflectometry (OCDR) (Brinkmeyer 1995; Ingemar, Skaar *et al.* 1999) and Optical Low Coherence Reflectometry (OLCR) (Lambelet, Fonjallaz *et al.* 1993; Hui, Thomas *et al.* 2003) are designed to reveal the distribution of the so called "inner reflectivity's geometry" and are based on the reflection and transmission spectra measured with guided light.

Generally, OLCR is based on a Michelson interferometer with a cw light source characterized by a short coherence length combined with a coherent light detection method, see Figure 5.11. The interference signal is generated only when the time-of-flight of the light from the reference arm and from the sample arm differ by less than half the coherence length of the source. The output of the interferometer yields the response of the grating from which the reflection spectrum is calculated using a Fourier transform of the measured data. The refractive index modulation profile may be obtained using an inverse scattering method.

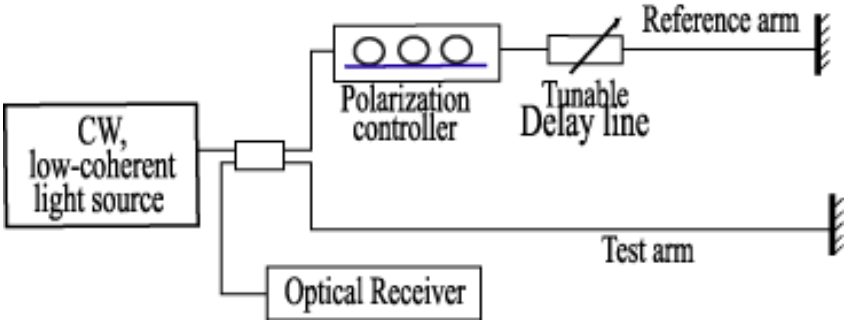

Figure 5.11. Schematic configuration of an OLCR Bragg grating characterization system (after (Hui, Thomas *et al.* 2003)). The setup is basically a Michelson interferometer with a movable reference mirror in the reference arm, and the device under test, i.e. the FBG, in the test arm.

Another reflectometric method is Optical Space Domain Reflectometry (OSDR). This is a non-interferometric technique used for spatial characterisation of fibre Bragg gratings and is based on a reflection measurement performed at an optical wavelength, λ, usually smaller than the Bragg wavelength λ_B, while a local phase perturbation is induced by exposing the grating to laser beam radiation (Brinkmeyer, Stolze and Johlen 1997).

The light from a tunable laser diode is launched into the fibre and the reflection spectra data is obtained while a He-Ne laser beam locally heats the grating, which is coated with an absorbing layer, in order to achieve a localized phase shift. Figure 5.12 presents a schematic view of the OSDR setup.

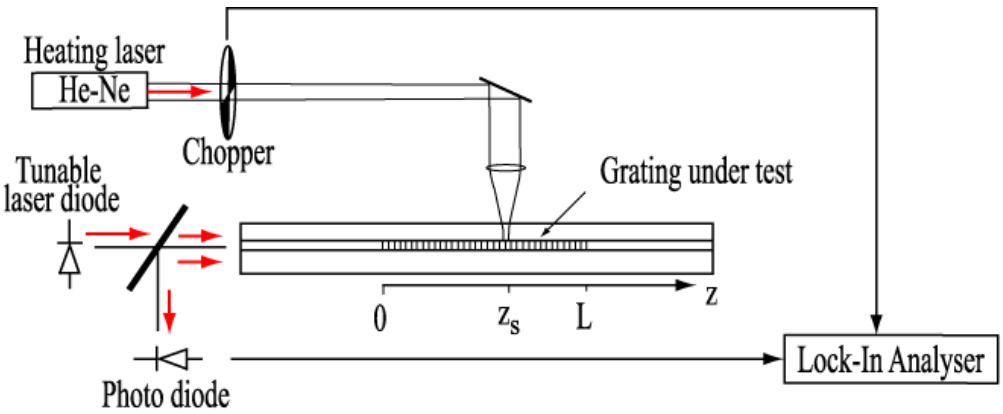

Figure 5.12. Schematic configuration of an OSDR Bragg grating characterisation system (after (Brinkmeyer, Stolze and Johlen 1997)). The light from a tunable laser diode is launched into the grating under test. A localised phase shift is produced at position z_s, by heating the grating with a focused He-Ne laser beam, which is also moved along the grating of length L. The He-Ne light is chopped at a certain frequency and the light from the grating is synchronously detected.

A characteristic of the reflectometric methods is the determination of the complex coupling coefficient from the complex reflection spectrum retrieved by various approaches.

As can be seen, the methods presented thus far, vary in complexity and their applicability to the various types of FBGs.

Reflectometric methods are designed to reveal the distribution of the "inner reflectivity's geometry" and are based on the reflection and transmission spectra measured with guided light. For complete technical details with regard to these methods, the reader is referred to the articles cited and references therein. Although such methods are, in principle, both powerful and relatively easy to implement, they suffer from severe limitations because of the *a priori* assumptions made with regard to the geometry of the grating, see Section 5.3.2.1. Furthermore, these methods are indeed heavily computational which increases the associated errors.

Common characteristics of all the indirect methods are the parameters used to describe the fibre grating structure. Without exception, the FBG is considered as being made out of planes across the fibre core, which are distinguished only by their grating pitch as schematically represented in Figure 5.2. As such their refractive index modulation is theoretically described only along the longitudinal axis of the fibre, as a quasi-sinusoidal expression. This assumption may not always accurately describe the grating structure, especially in the case of Type I gratings written using the phase mask technique and weak gratings (low reflectance).

Until now, it seems that none of the characterization and imaging methods reviewed have been able to meet all the requirements of sensitivity, spatial resolution and non-destructiveness with convincing results because each has its limitations. The reminder of this chapter demonstrates the application of DIC microscopy imaging in combination with rotation of the fibre. This new

method of measurement avoids *a priori* knowledge about the FBG structure, and aims to prove that the images taken for different orientations are dissimilar. The method has the advantage of avoiding time-consuming sample preparation as required in the case of SEM, AFM or SNOM, for example.

The utility and reliability of conclusions drawn from this study will depend on the applicability of the FBG models to which they are applied. The more flexible the model of the FBG, the more likely it will be that quantitative results can be obtained from computer simulation studies to help improve understanding of its structure. While many results can be insensitive to some details of the model, reliable quantitative information will require the development of more sophisticated models. For instance, it has often considered that FBGs are periodic planes across the fibre core, but the quantitative experiments presented in this thesis demonstrate the inaccuracy of this hypothesis, and show that the assumptions made are actually in error; moreover (Dragomir, Rollinson *et al.* 2003).

A summary of the methods used for direct characterisationof FBGs, highlighting features of the associated fabrication method including the laser energy and the type of FBG written, and giving the maximum refractive index achieved is presented in Table 5.2; all of these methods have been appropriately referenced in the sectioned above, the table contains no references due to space limitation. The table also outlines some critical remarks with respect to the method described. The objective of this table is to put in perspective the need for a non-destructive method for studying FBGs in general, and in particular, Type I FBGs, as this type of grating has not been previously imaged.

Table 5.2 Summary of direct techniques used for FBG characterisation.

Technique	Writing Method	FGB Writing Characteristics			FBG Characteristics				Spatial Resolution	Remarks
		Irradiating Wavelength	Laser Energy	Fibre Type	FBG Type	Reflection peak (nm)	Refractive Index Modulation (Δn)	Reflectance (%)		
Confocal Microscopy	Phase mask 1060 nm period	KrF excimer laser at 249 nm pulsed	A single pulse of 1J/ cm²	D-type polarisati-on-maintain-ing fibre	II	3.5 nm broad reflection peak at 1535 nm	Judging from the high contrast in the fringe pattern, the refractive index was called "large"	99.5	No specific details provided, assumed to be diffraction limited.	Photographic images of FBG confirmed the existence of a periodicity equal to that of the phase mask. A series of sharp transmission dips occurring at 1535, 1030, 770 and 620 nm have been measured, raising the issue of the FBG being a second order grating. The induced grating was localised on the core-cladding boundary and has not been observed to extend across the core.
Confocal Microscopy	Holographic	A 240 nm frequency – doubled dye laser pumped with a 308 nm XeCl excimer laser	0.06 J/cm²	Hi-Bi bow-tie fibre[li]	II[i]	5 nm broad and complex resonance peak around 1565.6 nm	5×10^{-3}	80	Depends on the light source used for imaging	Gratings are described as rodlike structures believed to be cracks running across the core. Gratings exhibited strong loss below the first-order Bragg reflection.

[li] Hi-Bi bow-tie fibre is a high birefringence fibre with a germanium-doped core (15 mol. % GeO_2) and boron-doped stress-induced sectors, having an elliptical core; the fibre has a high thermoelastic stress anisotropy which is believed to be responsible for the low threshold of the reported Type II grating.

Technique	Writing Method	FGB Writing Characteristics			FBG Characteristics				Spatial Resolution	Remarks
		Irradiating Wavelength	Laser Energy	Fibre Type	FBG Type	Reflection peak (nm)	Refractive Index Modulation (Δn)	Reflectance (%)		
Scanning Electron Microscopy	Holographic	KrF single excimer laser at 248 nm Pulsed	1.1 J/cm²	Ge-doped BNR CA2114	II	1559	3×10^{-4}	39	Practical 10nm	Surface structural changes to the cladding were observed. The grating period seen at ~1 μm deep on the surface of the fibre cladding had a periodicity of 0.53 μm, considered identical to the period of the Bragg refractive index grating created in the core.
Half-shade polarizing microscopic technique	Phase mask method ~1 μm period	193 nm Pulsed	0.4 kJ/cm²	Corning SFM-28	I[lii]	Not given	3.5×10^{-2}	Not given	Depends on the illuminating light and the NA of the objective used 0.35 μm	The grating pitch was twice the expected value, being equal to the pitch of the phase mask. Gratings extend across the full diameter of the core. The grating was named a second order grating.
		248 nm Pulsed	0.5 kJ/cm²				4.5×10^{-4}	96		
				Ge-B Co-doped fibre			2.2×10^{-4}	67		

[lii] It is questionable if the gratings written with such a high power were Type I gratings as it is known that for high germania fibres a distinct threshold between Type I and Type II is around 1J/cm², Malo, B., D. C. Johnson, F. Bilodeau, J. Albert and K. O. Hill, "Single-Excimer-Pulse Writing of Fiber Gratings by Use of a Zero-Order Nulled Phase Mask - Grating Spectral Response and Visualization of Index Perturbations". *Optics Letters,* **18** (15): 1277-1279, 1993.

Technique	Writing Method	FGB Writing Characteristics			FBG Characteristics				Spatial Resolution	Remarks
		Irradiating Wavelength	Laser Energy	Fibre Type	FBG Type	Reflection peak (nm)	Refractive Index Modulation (Δn)	Reflectance (%)		
Scanning Near Field Optical Microscopy	Phase mask	Excimer laser	Not given	D fibre	II[liii]	1540	10^{-2}	98	Depends on the tip size ~50 nm	An index profile having an average period of 522 nm has been identified. A non-uniform intensity distribution along the grating has been observed and explained by errors in the refractive index profile presumably caused by the low spatial coherence of the excimer writing laser.
Atomic Force Microscopy	Phase mask	A frequency quadrupled Nd: YAG pulsed laser 266 nm	2.0 W/cm² to 3.2 W/cm²	SM-1322/P3022-E Fibercore PSI 1250	Not given	Not given	Not given	60	Depending on the AFM tip size: 10 nm to 150 nm	The average period of the relief pattern, observed on the cladding surface exposed to the UV radiation in the AFM images, was 455 nm, which is equal to the period of the interference fringes generated by the phase mask. AFM images of the surface where the UV-irradiation had no influence, the rear surface of the FBG, presented no corrugation pattern.

[liii] Although the authors do not specifically state the type of the FBG it is assumed to be of Type II judging from the fairly large refractive index variation of the order of 10^{-2}.

5.6 Measurement of the Index Modulation along an Optical Fibre Bragg Grating

The material in this section is presented in chronological order in which the experimental measurements developed, giving the reader an opportunity to track the progress during the process of imaging the FBGs.

The fibre Bragg gratings used in these measurements were produced in the Optical Technology Research Laboratory at Victoria University. The FBGs considered in this work were Type I gratings photoimprinted in standard single mode communications grade optical fibre, (*9* μ*m* core diameter and *125* μ*m* outside diameter), using the phase mask technique, produced with both multiple pulse and continuous wave irradiation.

Standard telecommunications optical fibre is known to have poor photosensitivity, so prior to writing, the fibre was hydrogen loaded by soaking it in a high pressure atmosphere of industrial grade hydrogen gas (Lemaire, Atkins *et al.* 1993). This is a standard practice used to achieve ultrahigh photosensitivity in the fibre to UV exposure in order to maximize the refractive index change (Lemaire, Atkins *et al.* 1993; Erdogan and Mizrahi 1994). The fibre's polyacrylate coating is highly absorbing in the UV region of the spectrum, so once the fibre has been photosensitised, an approximately 20 mm long section of the coating was removed from the fibre surface before photoimprinting the FBG. It is well known that the process of removing the coating reduces the strength of the optical fibres to some extent (Wei, Ye *et al.* 2002b) depending on the stripping method used. A chemical–solvent stripping method has been employed since this is the least damaging method, maintaining 80% of the strength of the pristine optical fibre (Wei, Ye *et al.* 2002a). After being soaked in the chemical solvent for a few minutes, a lint-free tissue soaked with acetone

was used to remove any coating residue. The fabrication of the FBGs was accomplished by exposing the stripped section to UV radiation in a phase mask configuration. After photo-inscription of the grating, the fibre was annealed (Erdogan, Mizrahi *et al.* 1994) by baking it in a temperature controlled incubator in order to accelerate the out-gassing rate of residual hydrogen from the fibre and also to achieve long term stability of the fibre Bragg grating spectral properties .

The UV writing beam was provided by an Spectra Physics Innova internally frequency-doubled (FreD 300 model) Argon ion laser having a continuous-wave output operating with an optical power output power of approximately *106* mW with a wavelength of 244 nm Figure 5.13.

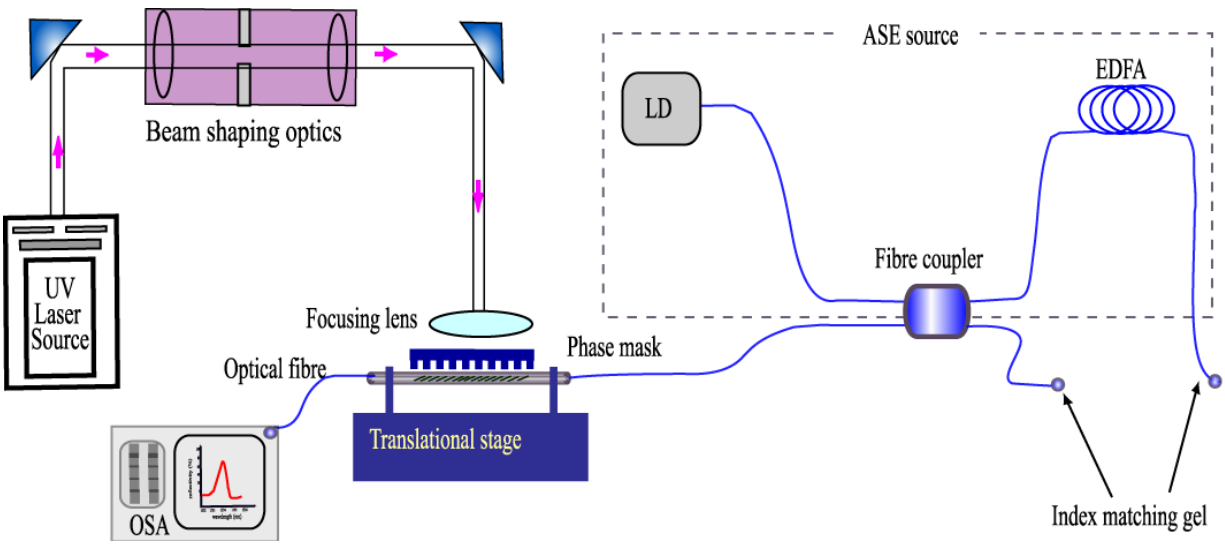

Figure 5.13. Schematic diagram of the phase mask system used to record and measure Bragg gratings. The optical source to illuminate the FBG was a Laser diode pumped Amplified Spontaneous Emission EDFA. Light transmitted through the grating is fed to the optical spectrum analyser through an optical coupler. The unused ports of the grating fibre and the optical coupler are index matched to avoid light reflected at the fibre-air interface.

In this work the power density, I_{eff}, of the writing beam at the fibre core in the absence of the mask is given by:

$$I_{eff} = \frac{w}{D}\frac{P_0}{f_l \Delta\phi x}. \tag{5.22}$$

where D is the fibre diameter, P_0 is the optical power, w is the beam waist diameter, $\Delta\phi$ is the divergence angle of the incident beam and f is and focal length of the lens used for focusing light. The estimated value for the power density was *40* W/cm^2.

The phase mask, manufactured by Lasiris™, was designed to suppress the zeroth order with a relative contribution, specified by the manufacturer, of approximately *3%* at *248* nm. The measured period was approximately *1.059* μ*m* (see Appendix E: Characterisation of the Phase Mask). During grating inscription, an Ando AQ-6310B optical spectrum analyser (OSA) having an erbium-doped fibre amplified (EDFA) spontaneous emission light source with a resolution bandwidth of *0.1 nm*, was used to monitor the transmission spectra (Figure 5.14).

A laser diode (*975* nm wavelength) was connected to the primary input of *2* × *2 50:50* single mode fibre coupler to pump the Er $^{3+}$-doped fibre connected to the primary output of the coupler. This Amplified Spontaneous Emission (ASE) source provided the light, having a centre wavelength of ~*1548 nm* and FWHM of *45* nm, to illuminate the FBG. The FBG was fusion spliced onto the secondary output port of the coupler, the pigtailed end was connected to the OSA in order to measure the transmission spectra during fabrication. The unused ports of the optical coupler and the ASE were dipped in index matching gel to prevent spurious back reflections.

Three FBGs have been produced using the phase mask technique and their parameters are listed in Table 5.3[liv].

Table 5.3. Parameters of the FBGs considered in this work. The values obtained for the refractive index modulation amplitude have been calculated using Eq. 5.7.

Grating label / FBG characteristic	FBG1-DG1	FBG2-DG2	FBG3-CR1
The estimated length of the grating (*L* in *mm*)	2.7	2.5	8
The refractive index modulation amplitude (Δn)	3.7×10^{-4}	2.2×10^{-4}	1.7×10^{-4}
The Bragg grating reflectance (R_B in %)	90	87	97
The full width at half maximum spectral bandwidth ($\Delta\lambda_B$ *in nm*)	0.5	0.5	0.55
UV exposure time (*minutes*)	20	20	22.7

The maximum Δn has been achieved after slightly different exposure times for each FBG studied due to the different hydrogen loading conditions.

Figure 5.14 illustrates the spectral transmittance of FBG1-DG1 as recorded at the point of maximum attenuation. The loss peak at λ_B = *1533.7 nm* was formed with an irradiance around 40 W/cm^2 at the fibre core. The transmission spectra shows some excess loss, called cladding-mode loss, below the Bragg resonance (λ_B=*1533.7 nm*), which is attributed to a low degree of blaze in the grating. The blazed Bragg grating is a common Bragg reflector; it has fronts tilted with respect to the fibre axis (refer to Figure 5.15). The tilt of the grating planes and strength of the index modulation usually determines the coupling efficiency and bandwidth of the light that is tapped out. Cladding-mode losses are related to the fibre structure as well as the fabrication of the FBG and are

[liv]Part of this Chapter related to Bragg gratings is the result of the collaborative work within the Optical Technology Research Laboratory. In particular I am grateful to Dr. Darol Garchev, Dr. Scott Wade and Ms. Claire Rollinson. Darol manufactured the first FBGs for imaging purposes ensuring that they had high reflectivity in spite of the reduced refractive index; Scott has continued to improve the writing process using the phase mask technique. This Chapter simply would not have been possible without the resources and experience contributed by each of these individuals.

wavelength dependent. The background loss, which is due to absorption in the fibre or scattering and is not wavelength dependent, may be observed on the higher side of the Bragg resonance it is very small in comparison to cladding-mode losses.

Particular characteristics of the grating have been inferred from the transmission spectrum and special attention was paid to estimating the refractive index modulation using Equation 5.7. This value, 3.7×10^{-4}, was obtained by also assuming that the grating is of the first-order, i.e. the grating periodicity is half the value of the phase mask used for writing.

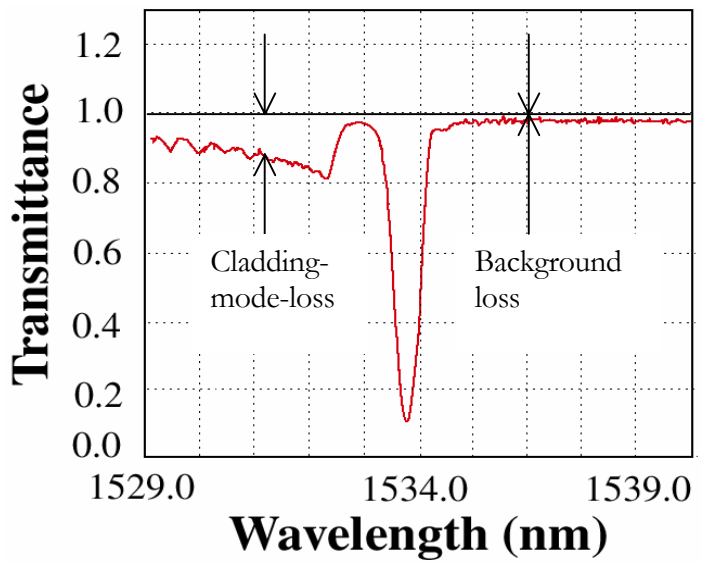

Figure 5.14. Spectral transmittance of a fibre Bragg grating (coded FBG1-DG1) fabricated in standard telecommunications fibre that was pre-soaked in hydrogen (~2.5 mol. %). The UV light source was a 244 nm CW laser and the phase mask had a 1.06 μm pitch. The transmission spectrum exhibits some loss on the low-wavelength side of the Bragg wavelength.

The fibre was imaged using the DIC microscope following the procedure set out in Chapter 3. The sample preparation is described in Appendix A: Sample Preparation and Mounting.

The gratings could be seen in the DIC image of the central region of the fibre containing the FBG, see Figure 5.15. The grating was seen to be blazed at an angle of a few degrees to the axis of the fibre, probably because of a slight misalignment of the writing beams.

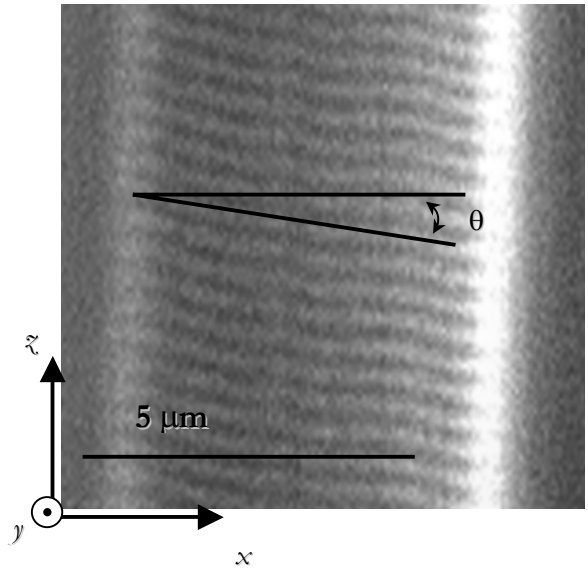

Figure 5.15. Measured DIC image of the fibre core with a blazed Bragg grating (FBG1-DG1). The tilt of the grating determine the coupling efficiency and the bandwidth of the light that is tapped out.

At the time these experiments were conducted, we concluded that the observed photoinduced perturbations are highly localized on the core-cladding boundary (Dragomir, Roberts *et al.* 2001; Dragomir, Roberts *et al.* 2002); this effect has also been observed by others (Malo, Johnson *et al.* 1993; Raine, Feced *et al.* 1999) as discussed in Section 5.5 of this thesis.

The refractive index modulation amplitude Δn, may be related to the fringe visibility by measuring the maximum and minimum fringe intensity values.

From the analysis of the DIC image, the measured period is twice that expected from simple ± 1 diffracted order interference, i.e. ~ 0.5 μm period would

generate a grating for a Bragg wavelength of *1.5* μ*m*. This lead to the conclusion, as prompted by other researchers (Raine, Feced *et al.* 1997), that the spectrally measured gratings are in fact higher order Fourier components of a grating whose main peak is closer to *3* μm. One explanation for such a period is that it can arise from Fresnel imaging that occurs when there is sufficient zeroth order present (Hegedus, Zelenka and Gardner 1993; Hegedus 1996). Despite these observations, the typical grating strength of phase mask written gratings is large, indicating that the index modulation is not large enough to generate strong higher order grating components. Furthermore, most commercial phase masks have very low zeroth order transmission, typically less than *3* to *4%* and most recent research shows that it can be further suppressed to less than 0.3 % (Laakkonnen, Kuittinen and Turunen 2001).

The grating period may be determined by extracting a line profile from four periods in the DIC image of the FBG (shown in Figure 5.16) and performing a Fourier transform on it. The grating period is then given by the change in the frequency of the interference fringes, which can be calculated from the location of the peak that results from the Fourier transform. It has thus been evaluated to be *0.510* ± *0.017* μm. It therefore appears that there is a contribution to the index modulation at the expected period. It is believed that this is a consequence of a Fresnel pattern produced by the phase mask with a contribution from the higher diffraction orders. This will be discussed further in Section 5.6.1.

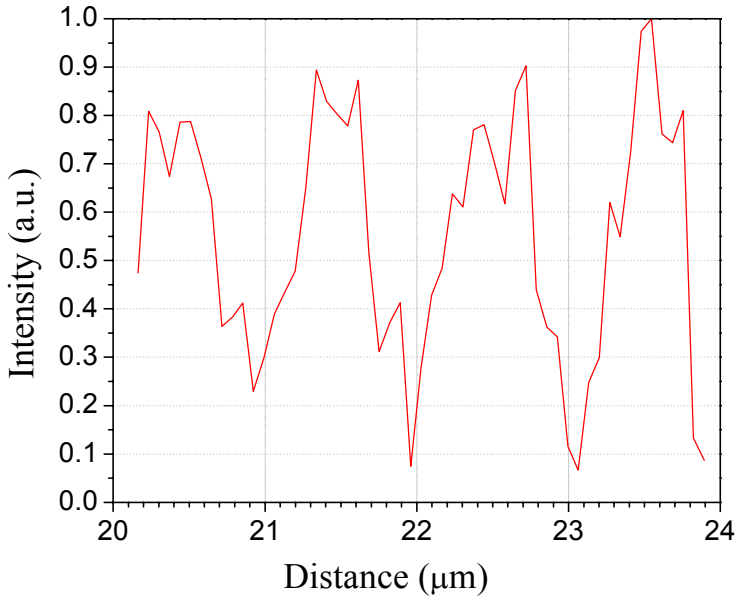

Figure 5.16. Line profile from four gratings imaged in Figure 5.11.

Judging by the image in Figure 5.15 and based on the generally accepted description of a FBG (Section 5.3.2.1 and Figure 5.2), one would expect these blazed gratings to fill the core of the fibre and if this is true they can therefore be imaged using the optical sectioning property of an imaging tool such as DIC imaging. Optical sectioning through a blazed FBG will be presented in the next section.

5.6.1 Optical Sectioning of a Fibre Bragg Grating

To investigate the above-mentioned hypothesis that the gratings would fill the core of the fibre as uniform planes, sequential optical sections were acquired using the DIC microscope.

Another FBG sample[lv], labelled FBG2-DG2, was imaged; it was written under the same conditions and had similar properties as FBG1-DG1 (refer to Table 5.3). This time the FBG was imaged by performing a series of axial images

[lv] Another was used here because the first FBG sample (FBG1-DG1) broke during cleaning.

starting with what appeared to be the blazed part of the FBG in the core of the fibre.

Figure 5.18 demonstrates the sectioning properties of the DIC imaging technique applied to this grating, FBG2-DG2. Illustrated is a stack of 12 consecutive sections through the core of the fibre into which the Bragg grating has been written. Each image is a horizontal section of the fibre containing the FBG; the sections are separated by *0.8* μ*m* representing a vertical scan across the diameter of the fibre core.

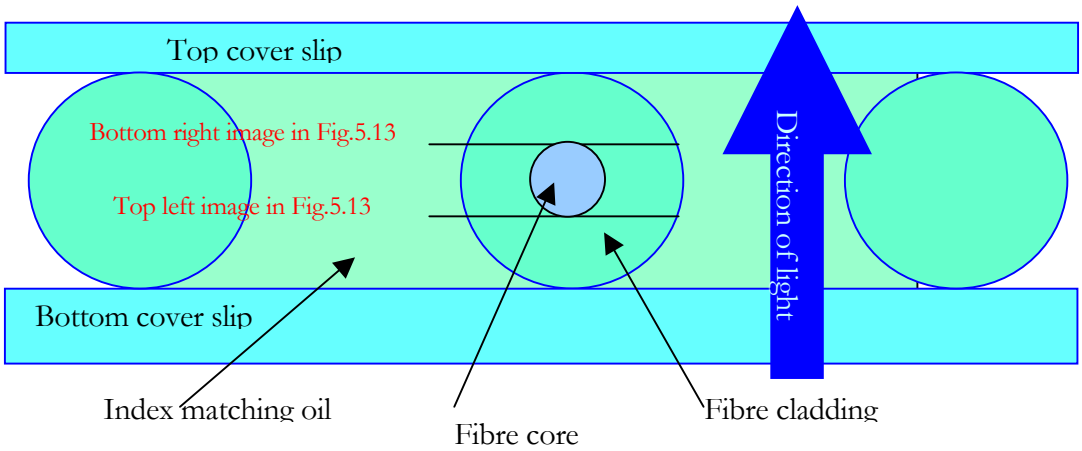

Figure 5.17. Schematic of the light path through sample in the DIC microscope used.

The top left section of the images in Figure 5.18 was taken from the bottom of the fibre; being closest to the bottom cover slip, refer to Figure 5.17. It is worth mentioning that in the DIC system used, the light travels from the bottom to the top. The series concludes at the inner surface of the core-cladding interface, closer to the second cover slip. The dimensions of each image are *35* × *35* μ*m*. The images are blurred due to the transmission features of the DIC imaging, where the condenser was at the optimum focus for the images of the central fibre section. It is pertinent to reiterate that these images are of raw data, that is,

they are intensity plots from the DIC system and no image processing has been performed. Nonetheless it can be clearly seen in these images that a significant change in the refractive index profile must exist throughout the core in the region where the grating has been written.

Whether this structure is of use in explaining the cause of the unwanted cladding-mode losses observed in the transmission spectrum, is a question that still needs further exploration. Nonetheless, it opens another avenue of enquiry and serves to illustrate the complexity of a FBG. As is readily observed these sequential acquisitions of many planes of focus can be used to build up a three-dimensional (3D) image of a FBG; but the 3D reconstruction of a FBG was not the object of this work at this stage. Rather, the attention was focused onto finding an explanation of what causes this structure.

From this set of images, one can conclude that the DIC imaging method provides structural information about the FBG where the refractive index changes have occurred. The apparent modulation in index change of the fibre may be influenced by: nonlinearities in the photosensitive response of the fibre, the less-than perfect nulling of the zeroth-order beam, the presence of higher order diffracted beams downstream from the phase mask and the low coherence of the UV laser source (Hill, Malo *et al.* 1993b). In particular the grating structure is not what would be expected from the simple explanation of grating formation and performance given in Section 5.3.2.

As seen in Figure 5.18, having observed such a non-uniform sophisticated structure and taking into account the cylindrical geometry of the optical fibre, an evident next step would be to rotate the fibre containing a FBG while imaging it. In addition to this, an explanation of what causes this structure is sought in the following sections.

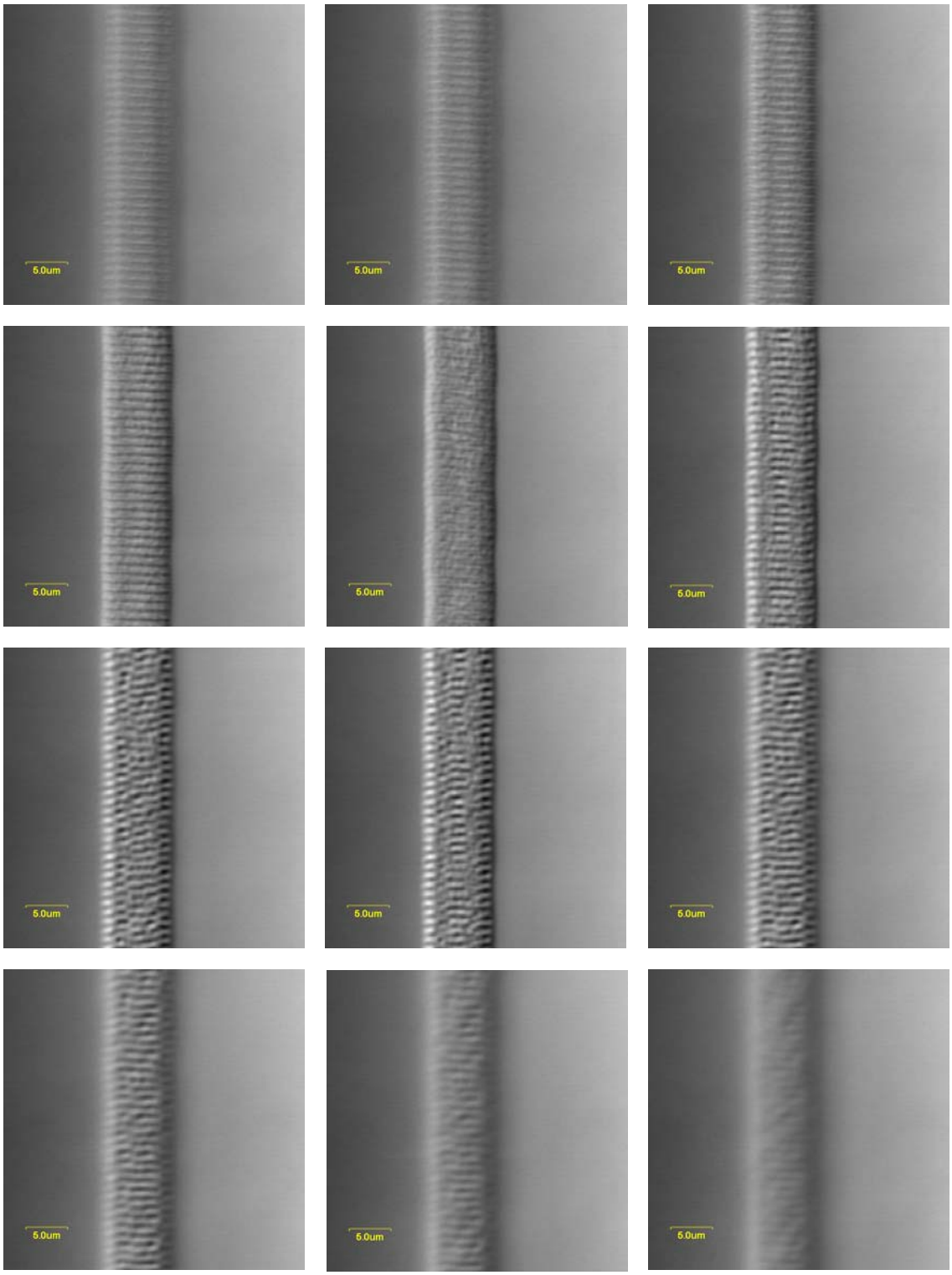

Figure 5.18. The sectioning property of DIC imaging containing a FBG is clearly evident in this stack of 12 consecutive horizontal sections through the fibre. The sections are separated by *0.8* μ*m* and represent a scanned area of *35* × *35* μ*m*. The top left section was taken from the bottom of the fibre while the bottom right image is from the top, as light travels from the bottom to the top. Note that all the images are raw data - no image processing has been performed (Dragomir, Roberts *et al.* 2002).

A complex model of the free space interference pattern formed behind a phase mask under UV illumination, considering the influence of higher diffracted orders has been performed (Mills, Hillman *et al.* 2000). This model predicted a 3D distribution of the diffracted intensity from the phase mask. Measurements of the free-space diffracted intensity behind the phase mask validated this model and revealed a periodic structure having periodicities both along the phase mask (parallel to the plane of the phase mask) and away from it, giving rise to a non-uniform pattern.

Writing a FBG in optical fibre, using a phase mask, produces not only an interference pattern laterally, called the Bragg grating pitch, but also a periodic pattern along the incident laser beam direction, known as the Talbot pitch (see Section 5.8). The Talbot diffraction pattern replicates the pattern of the original grating at periodic distances from its surface, subject to diffraction limits. This Talbot pitch can be observed by imaging optical sections through the fibre or just observing the image after the fibre is in the appropriate orientation. The structure would be a non-uniform tridimensional one having different periods that therefore should be observable using the DIC microscope.

Rotating[lvi] the fibre by *90°* revealed a different image, see Figure 5.19, leading to the conclusion that the modulation of the refractive index, for this grating, is greater on the side facing the incoming UV radiation; indicating that there is a significant UV absorption in the core during the writing process. This feature has been also observed by others (Raine, Feced *et al.* 1999). Also evident in the image is the presence of a transverse sequence of planes similar to a Talbot diffraction pattern (please refer to Section 5.7 & 5.8 for further details on this topic). This pattern is related to the diffraction properties of a grating. The

[lvi] The rotation of the fibre was done by hand as at this point of the experimental development because the rotational stage was not available.

diffraction properties of a real phase mask have been modelled and measured in free space, demonstrating that the Talbot diffraction pattern extends out from the phase mask to fill the region occupied by the fibre core during grating fabrication (Mills, Hillman *et al.* 2000).

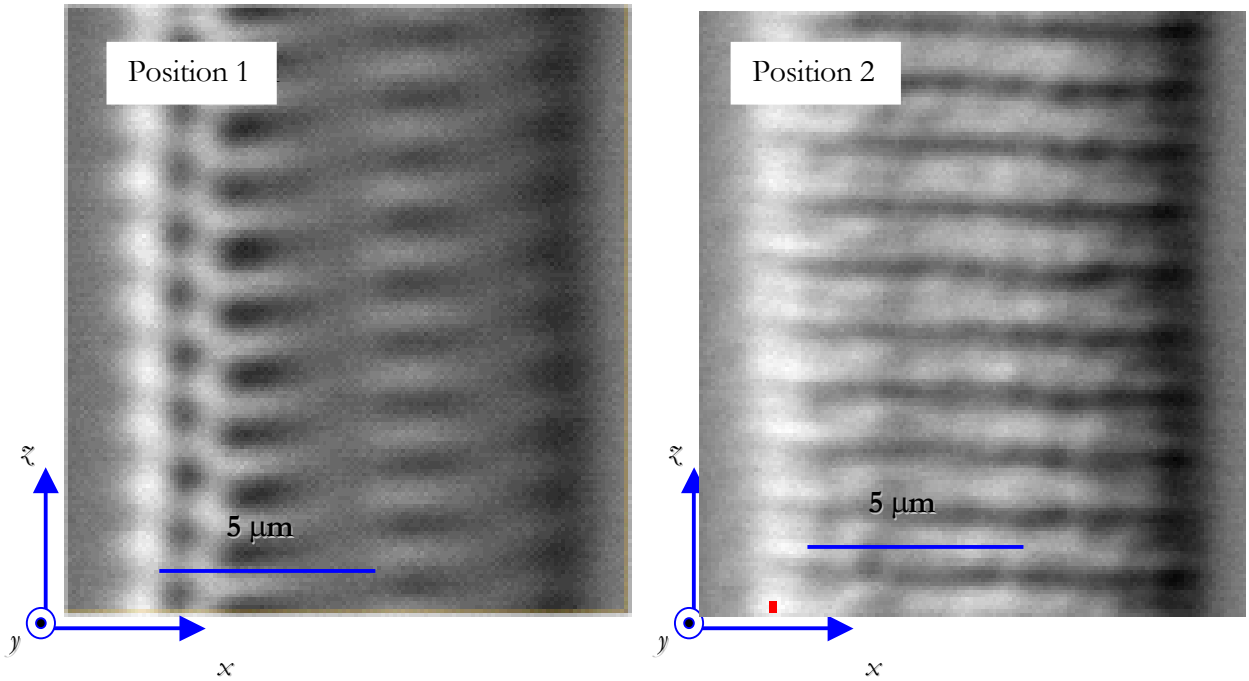

Figure 5.19. Measured DIC images of FBG2-DG2 with different axial orientation of the fibre. The images are *145* × *157* pixels and *140* × *150* pixels respectively with *0.069* µ*m* pixel size. The second image is obtained by rotating the fibre approximately *90* degrees from position 1.

In order to prove experimentally the presence of these planes inside the FBG, a temperature controlled rotational stage was designed and built to mount the FBG samples and control the embedding oil temperature to ensure the refractive index matching (for details please see Appendix E: Temperature Controlled Rotational Stage). Due to a very small region of contact, approximately *3 mm*, between the heating stage and the glass cell holding the fibre sample and the poor thermal conductivity of the glass cover slips, an experimental procedure was developed where all components were heated prior

to mounting the sample in order to match the refractive index of the oil with the silica cladding. The working temperature was 31 degrees Celsius.

A Type I FBG, labelled FBG3 - CR1, was manufactured using a standard phase mask technique (described in Section 5.4). The growth of the peak-loss as of the time of exposure for the period ~*1.5* min to ~*22.7* min is presented in Figure 5.20. It is important to have this writing history to clearly establish the FBG as Type I, i.e. its Bragg wavelength shifts towards longer wavelengths (the red-shift discussed in Section 5.2.1) correlated with the positive index change.

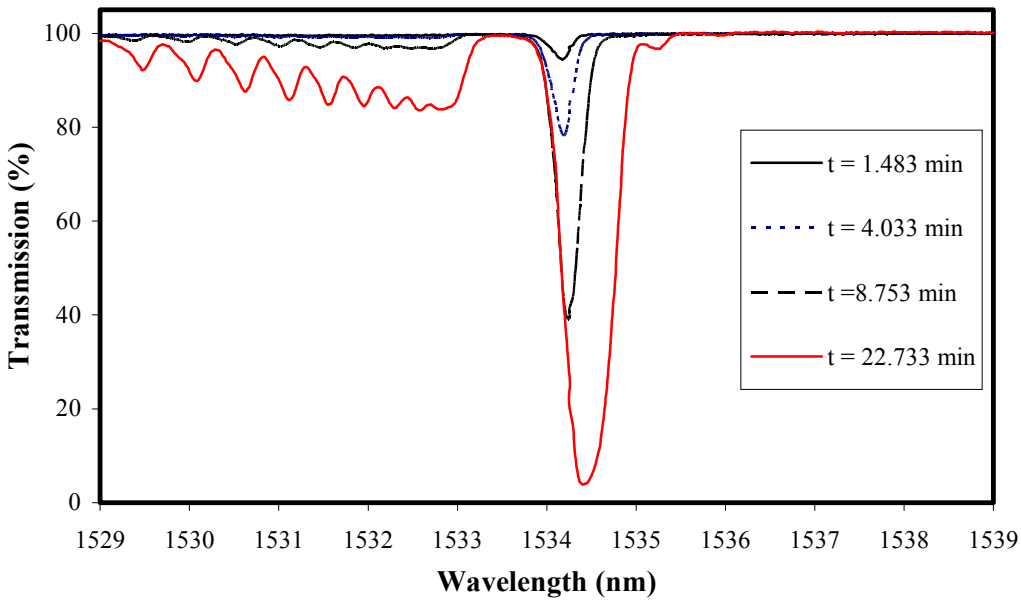

Figure 5.20. Evolution of the transmission spectra of Bragg grating labelled FBG-CR1 with exposure time. A noticeable change in transmission at around 1534.17 nm was observed after 1.48 min exposure, then the reflectance increases significantly with further exposure whilst the centre Bragg resonance shifts towards longer wavelengths. The peak reflectivity of approximately 97 % at 1534.46 nm has a spectral width of 0.5 nm.

The reflectance has been inferred from the depth of the transmittance spectrum, which as expected, shifted slightly to longer wavelengths during the writing process.

The refractive index modulation, of the FBG3-CR1 grating, of approximately 1.7×10^{-4} was estimated using coupled mode theory by considering it to have a uniform sinusoidal variation along the axis of the fibre and is presented in Table 5.3 together with other characteristics of this grating. Accordingly, Figure 5.21 shows the refractive index values corresponding to different exposure times demonstrating that this FBG is a Type I, i.e. its refractive index modulation increases linearly with the time of exposure to UV light.

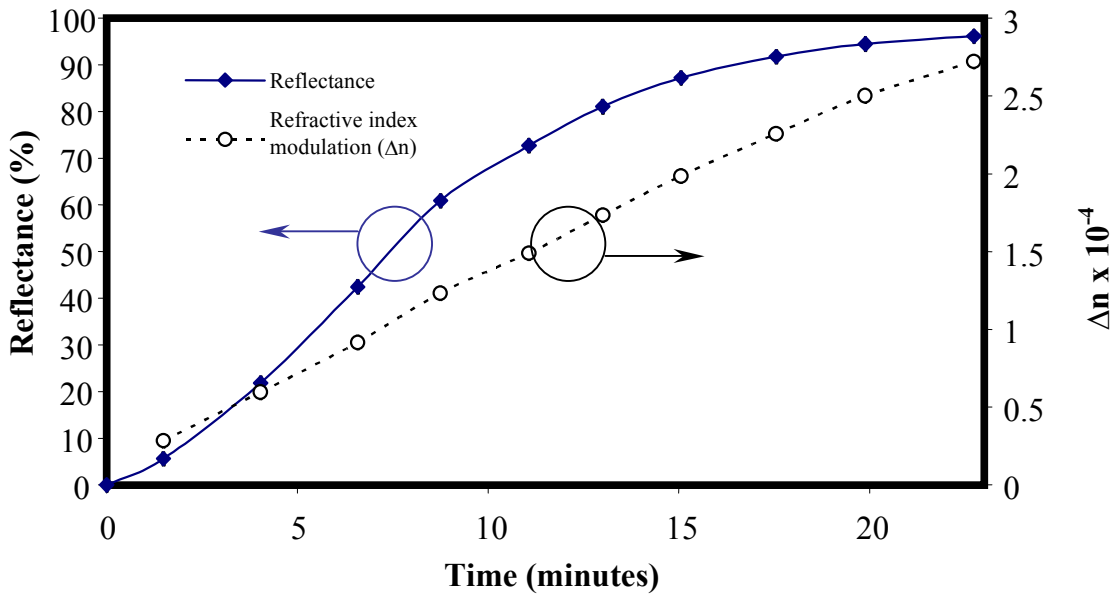

Figure 5.21. Reflectance and refractive index modulation of grating FBG3 - CR1 at different UV radiation time. The nearly linear response of the refractive index modulation with increasing exposure time is a characteristic of Type I gratings.

The fibre containing the FBG was rotated around its own axis and DIC images were recorded. A total of *70* images have been recorded in 2 ± 0.5 degrees

increment steps. This process permitted the identification of the principal measurement planes; parallel and perpendicular to the original FBG writing beam Figure 5.22.

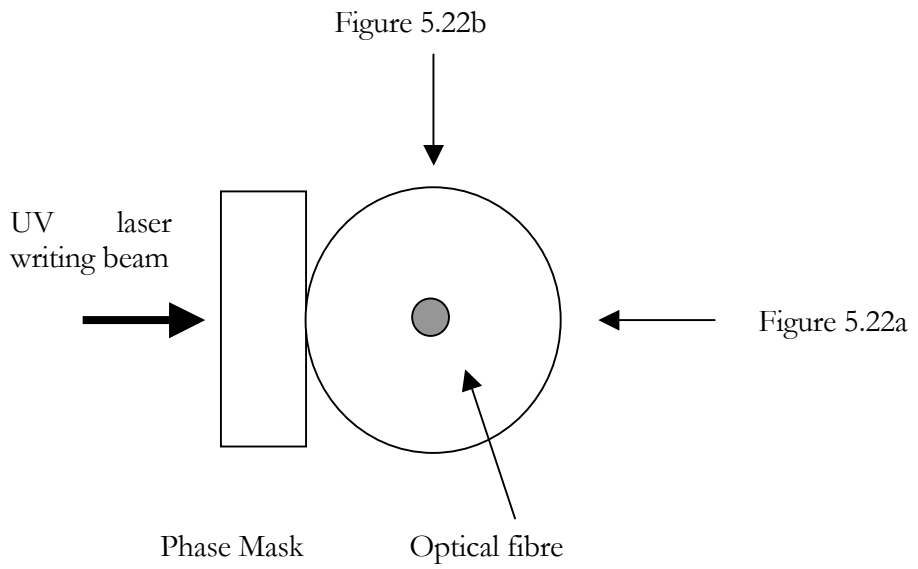

Figure 5.22. Schematic diagram identifying the direction of the microscope beam used for the images represented in Figure 5.22.

The two most significant images are presented in Figure 5.22, representing the image of the fibre taken from a direction parallel to that of the original writing beam, Figure 5.22a, while Figure 5.22b shows the image of the fibre after it had been rotated by *90* degrees about its axis from the position shown in Figure 5.22a.

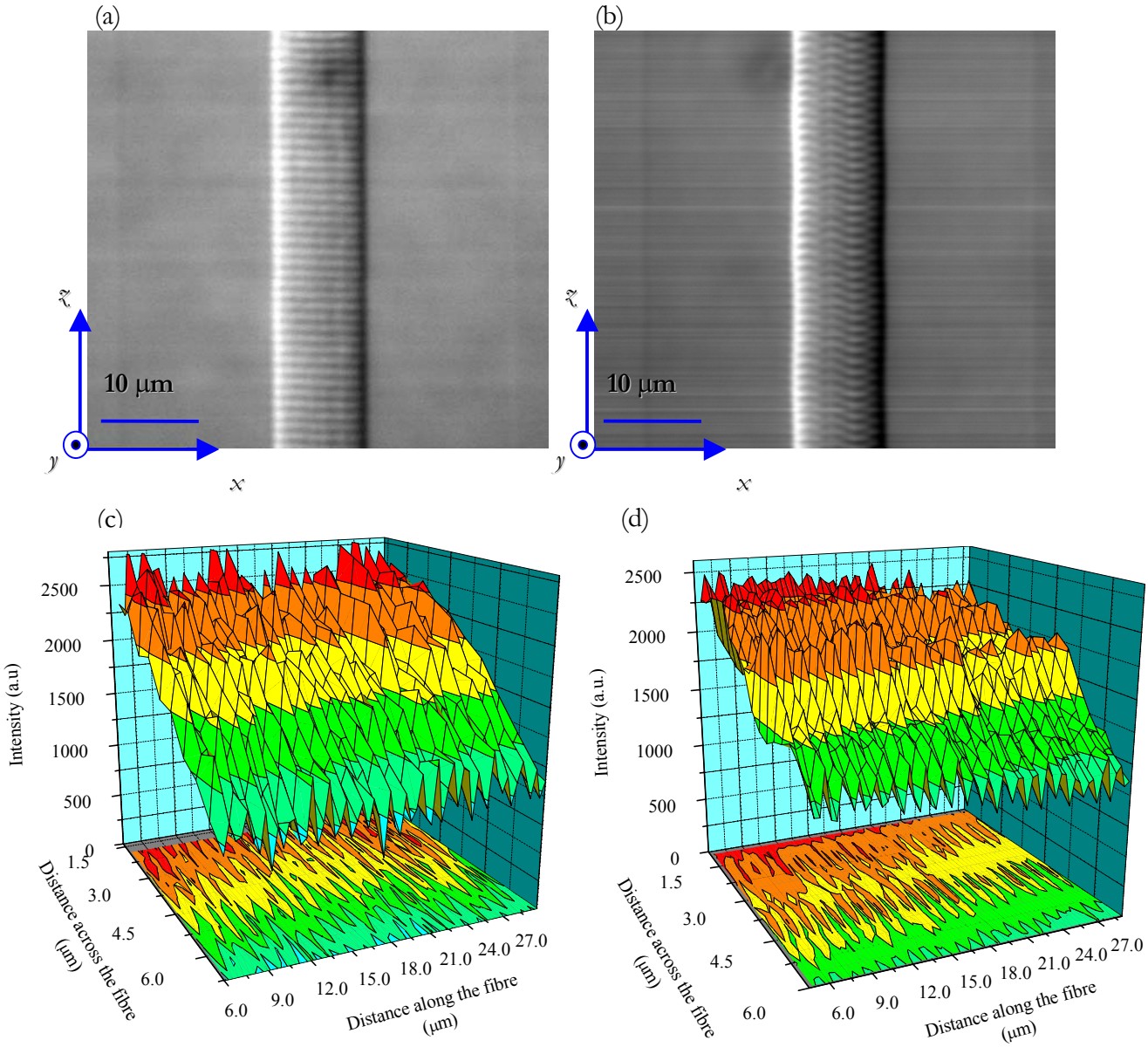

Figure 5.23. Measured DIC images of the core region containing the FBG 1 - CR1 Bragg grating, recorded for two different fibre orientations. (a) The fibre position has been selected so that the image is taken from a direction parallel to that of the writing UV laser beam.; (b) The same FBG as in (a) recorded after the fibre has been rotated by *90* degrees about its axis. The images' dimensions are *1024* × *1024* pixels covering *47* × *47* µ*m*; *x* and *z* represents distance across and along the fibre respectively. (c) and (d) The intensity distribution for a region of approximately 130 µm² within the core of the fibre represented in panels (a) and (b) respectively. The contour graph displayed on the bottom plane of both panels (c) and (d) clearly emphasises the different features observed in panels (a) and (b).

While Figure 5.22a represents what might be described as a standard type of image of a FBG having a spatial periodicity similar to that of the period of the phase mask. This feature was also observed using other type of imaging discussed in Section 5.5, i.e. *1.06* μ*m*. The impression given in Figure 5.22b is totally different and appears as an interleaved variation of the intensity. In addition, the surface intensity profile represented Figure 5.22c and d confirms the interleaved structure observed in Figure 5.22b. In the contour graph displayed on the bottom plane of Figure 5.22d there is a clear evidence of this feature. The image in Figure 5.22b was recorded from a direction perpendicular to the UV writing beam giving rise to a pattern that may be associated with the beating between diffraction orders of the writing beam associated with the self-imaging properties of the phase mask grating otherwise known as the Talbot effect (details regarding this topic are presented in Section 5.7 and 5.8 of this chapter). Comparisons of the periodicity of these planes with theoretical modelling are discussed in Section 5.8.

The variation in the refractive index within the core, as seen in Figure 5.22a appears as uniform rows having the periodicity equal to that of the phase mask, i.e. *1.06* μ*m*. A line profile through these gratings is presented in Figure 5.24. On the other hand the grating period as presented in Figure 5.22b shows a component of the index variation of half the period of the phase mask, i.e. half the value obtained in Figure 5.24, and would be 0.535 ± 0.005 μ*m*, a value which is consistent with that inferred from the measured transmission spectrum.

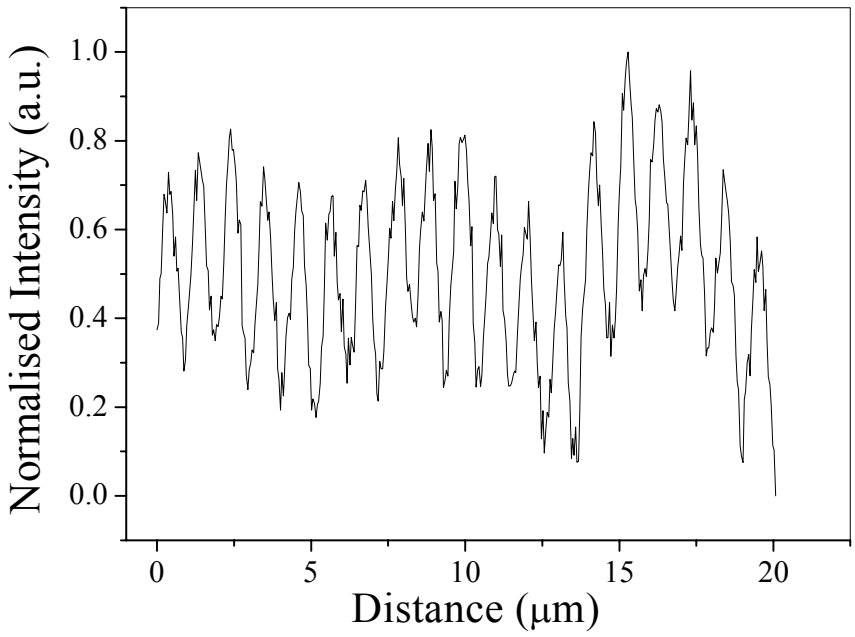

Figure 5.24. Line profile through grating represented in Figure 5.22a showing a period of the grating equal with that of the phase mask used for grating fabrication.

The complex structure observed in the FBG fabricated by the phase mask technique can be explained by investigating the interference pattern behind the phase mask. Theoretical investigations of this have been performed in the past by many authors. Next section presents some of the views found in the literature.

5.7 Diffracted Field Produced by a Phase Mask

An ideal phase mask used for fabricating a FBG is one which has a fully suppressed zero order, thus producing only ± 1 diffraction orders. In such a situation the fluence distribution in a plane parallel to the phase mask forms a system of fringes, as a result of the interference of the ± 1 orders, having half the period of the phase mask in the x direction (along the grating) (Dyer, Farley and Giedl 1995); the energy density distribution in free space is described by:

$$cU_k = 2I_1[\mathrm{sinc}(ky)\tan(\psi_1)(\Delta\phi)\cos(2kx)\sin(\psi_1)+1], \tag{5.23}$$

where c is the local velocity of light having the wavelength λ, $k = 2\pi/\lambda$ is the wave number describing the propagation direction vector, I_1 is the irradiance of the first diffraction order, $\Delta\phi$ is the incident beam divergence, and ψ_1 is the propagating angle of the first diffracted order satisfying $\sin(\psi_1) = \lambda/\Lambda$.

As an illustration the interference pattern of the ± 1 orders from a phase mask having a grating period of $d = 1.06\ \mu m$ is shown in Figure 5.25. The mask was assumed to be illuminated by a plane wave from a source with wavelength of $\lambda = 244\ nm$ and a line width of $\Delta\lambda = 1\ nm$. Both perfect and partial spatial coherence are considered (included by a non-zero beam divergence $\Delta\phi$).

As can be seen in Figure 5.25 panels a, b, c and d, fringe visibility in the case of partial spatial coherence is lost at a distance y away from the grating given by (Dyer, Farley and Giedl 1995):

$$y = \frac{\lambda}{2\tan(\psi_1)(\Delta\phi)} = \frac{\delta}{2\tan\psi_1}, \tag{5.24}$$

where $\delta = \lambda/\Delta\phi$ is the spatial coherence length at the mask.

In other words the first diffracted orders no longer overlap coherently beyond the distance given by Eq 5.24. Fringe visibility as a function of beam divergence is represented in Figure 5.26.

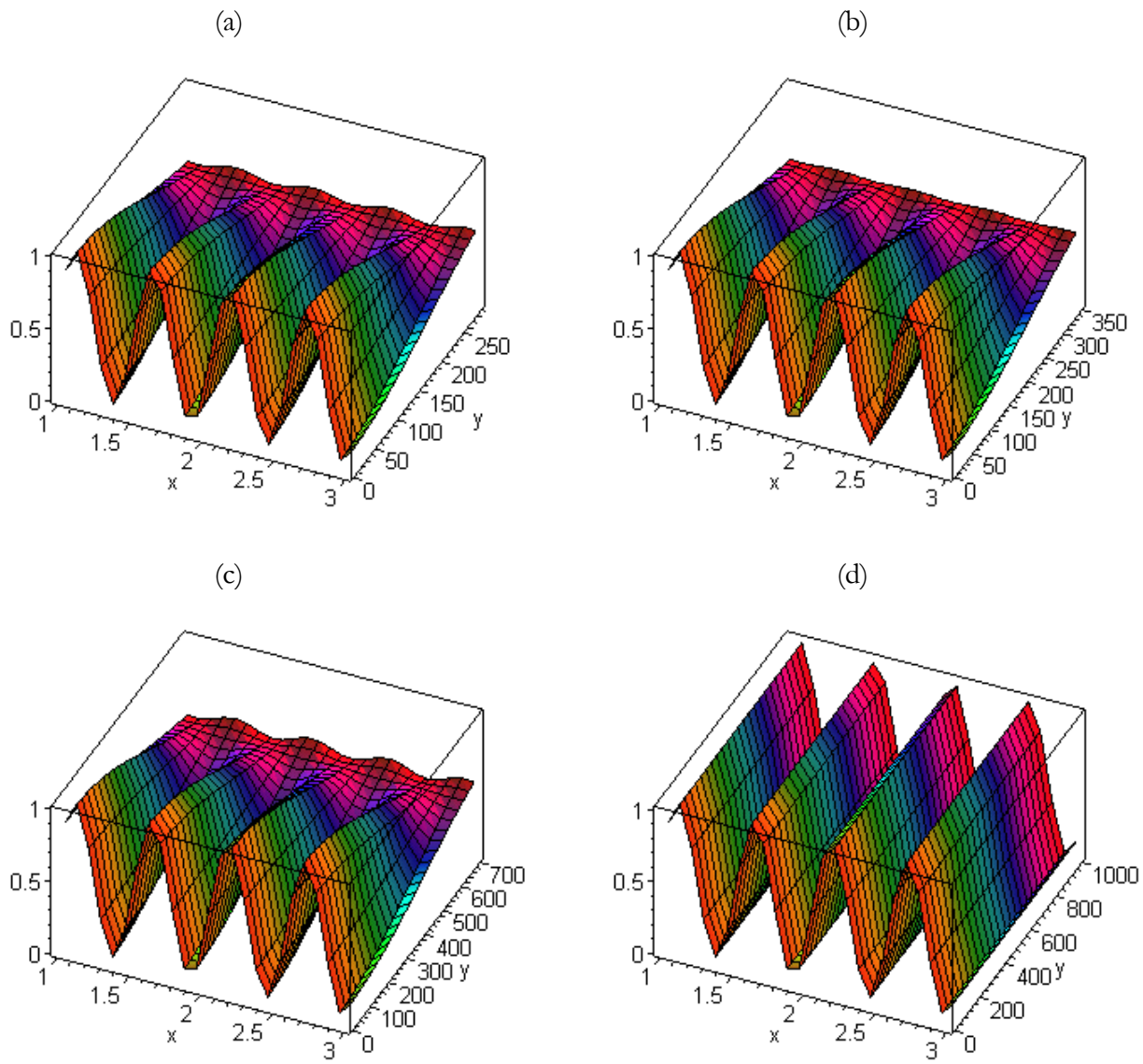

Figure 5.25. Diffracted field distribution in a plane parallel with an ideal phase mask (i.e. only the interference of the $\pm$ *1* orders is present) for an illumination wavelength of λ = *244 nm* having a line width of $\Delta\lambda$ = 1 nm. (a) and (b) are two examples of finite spatial coherence less then 300 μm having the beam incidence divergence of $\Delta\phi$ = *1.6* and *2 mrad* respectively. (c) Beam incidence divergence of $\Delta\phi$ = *0.85 mrad*, characteristic to our FBG writing conditions, in which case the spatial coherence length is approximately *606.97* μ*m*. (d) As the above but with perfect spatial coherence $\Delta\phi$ = 0. Distances *x* and *y* are measured in μm units while the intensity, normalized to unity is expressed in arbitrary units.

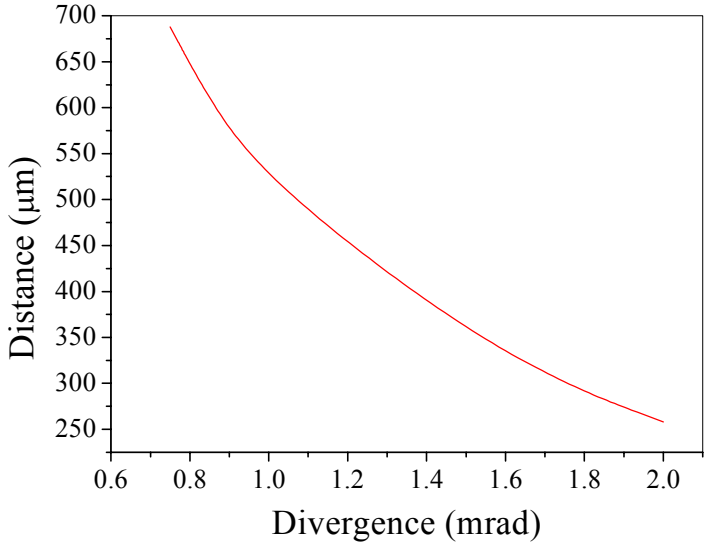

Figure 5.26. Fringe visibility as a function of the incident beam divergence. Evidently for a perfect spatial coherence at the mask, i.e. divergence → 0 the fringe visibility is the highest. A spatial coherence length of approx 600 μm characterized the illumination light used to write gratings for this work.

It is worth mentioning that when writing Bragg gratings at telecommunications wavelengths, typically up to four diffraction orders are present leading to very complicated interference patterns in the field behind the phase mask. Only the zeroth, ± 1, and ± 2 orders are considered in detail here. Figure 5.27 demonstrates the effect that varying the efficiencies of the various diffracted order contributions has on the diffracted field distribution at relatively short distances from the phase mask. The range of values was selected to correspond to the position where the core of a standard telecommunication fibre of diameter approximately six to nine μm would be situated during FBG fabrication.

An idealised intensity distribution would be made by excluding the zeroth order and considering only a first-order contribution of *48%* assuming the remainder is scattered (see Figure 5.27a); the fringes produced by the phase mask in this region have a frequency twice that of the phase mask corrugations. This would create a uniform refractive index across the fibre's core. However, in practice, parasitic diffracted waves arising from zero-order are always present. Numerous authors,(Dyer, Farley and Giedl 1995; Hegedus 1997) have analysed theoretically the contribution of the zeroth order and found that very small contributions in the zeroth order can produce intensity modulation not only along the core but also across the core. Figure 5.27b shows the influence of *0.05%* in the zeroth order plus a *1.5%* in the second order on the intensity distribution. With increasing the contribution of the second order the interference pattern becomes significantly more complex, as shown Figure 5.27 c and d. The intensity distribution of the phase mask used to write FBGs in this work is characterised as having a zeroth order nulled to approximately *5%,* with a *37%* first-order contribution and a second order of approximately *10%*, as presented in Figure 5.27d. The presence of higher diffracted orders has not been included in this modelling but their contribution is negligible.

It is a well known fact that when a grating is illuminated with light having a wavelength significantly smaller than the grating period, the phenomenon of self imaging occurs (Talbot 1836); this will be investigated in the next section.

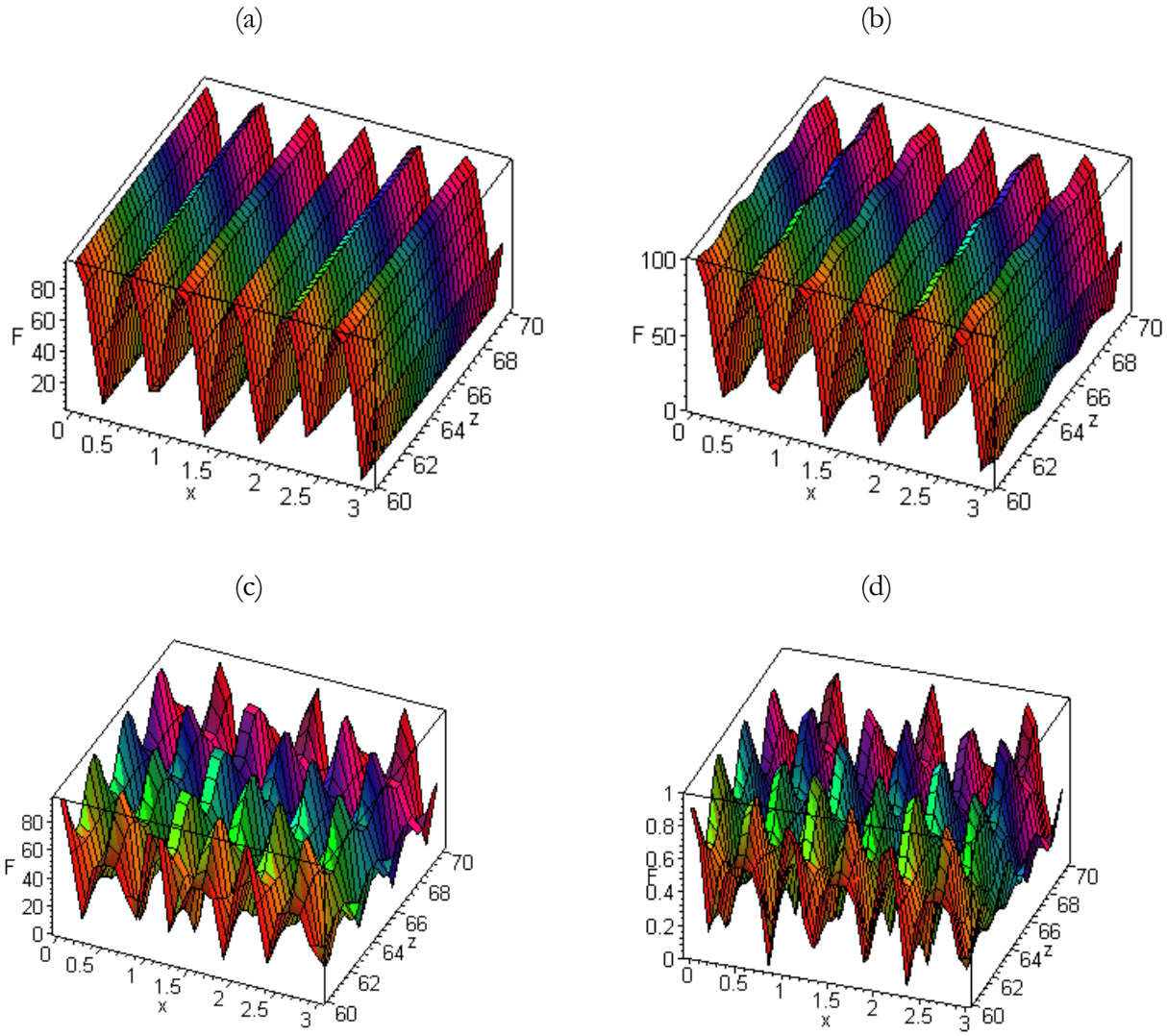

Figure 5.27. Fluence distribution in a plane parallel to the surface of a phase mask with various order efficiencies. (a) Excluding the zeroth order and having 48% in the first-order; (b) first-order as in (a) and including a very small zeroth order and second order of 0.05% and 1.5% respectively; (c) similar strength of the zeroth and second order contributions of 8% but having the first-order of 38%; (d) 5% in the zeroth order, 37% in the first and 10% in the second orders – characteristic to the phase mask used for FBG writing in this work. Units for x and z are expressed in μm.

5.8 The Talbot Effect – The Repeated Self-Imaging of a Diffraction Grating

The phase mask is an object of one-dimensional periodicity and an infinite aperture defined by its amplitude transmittance function, see Appendix D: Fresnel-Kirchhoff Formulation of Talbot Effect. When illuminated by a plane monochromatic wave of wavelength λ with a line width $\Delta\lambda$ and at normal incidence, the grating diffracts in a plane defined by the beam direction and the grating periodicity. The intensity pattern formed, replicates the grating intensity transmittance in a series of equally spaced planes parallel to the original grating subject to diffraction limits. Because the periodicity of these patterns is the same as that of the original grating, these patterns are called self-images.

The self-imaging property[lvii] of the gratings was first observed by Henry Fox Talbot, an inventor of photography, in the nineteenth century (Talbot 1836). This effect - the repeated self-imaging of a diffraction grating – has been through periods of being forgotten and then rediscovered. Yet it has proved to be considerably more than a mere optical oddity; it has been found to be one of a class of phenomena involving the extreme coherent interference of waves and also has profound and unexpected roots in classical number theory (Flores-Arias, Perez *et al.* 2001) illustrating that the research community is starting to appreciate more and more the rich and intricate structure of limits in physics (Berry, Marzoli and Schleich 2001).

Early explanations of the effect have existed since Lord Rayleigh (Rayleigh 1881) and have been described as the longitudinal periodicity exhibited by

[lvii] Henry Fox Talbot published the results of some experiments in optics that he had previously demonstrated at a British Association meeting in Bristol. He said, " On removing the lens a little further from the grating, the bands gradually changed their colours, and became alternately blue and yellow. When the lens was a little more removed, the bands again became red and green. And this change continued to take place for an indefinite number of times, as the distance between the lens and grating increased…".

lateral periodic objects under Fresnel propagation (Patorski 1989). The recent literature regarding theoretical expressions and experimental explanations give new interpretations for the key features of the Talbot effect (Winthorp and Worthington 1965; Bar-Ziv 1985; Latimer 1993; Mills, Hillman *et al.* 2000; Crespo, Alonso and Bernabeu 2002).

Throughout the literature one may find that the patterns in Talbot planes have been interpreted as Fourier images of the grating - a repetitive object is said to make repetitive images of itself (Rayleigh 1881; Winthorp and Worthington 1965; Prohaska, Snitzer and Winthorp 1994; Wang, Zhou *et al.* 2001) despite the fact that these images were not like the conventional ones; or as multiple-slit diffraction pattern diffraction (Chavel and Strand 1984) (Spagnolo and Ambrosini 2000). Also, the Talbot effect, as an important example of Fresnel diffraction, has been explained using a physical optics approach that involves conventional interference and diffraction effects by making use of Cornu's spiral (Latimer 1994), and based on Fresnel's integrals. This approach has been used to show, for example, that the interpretation of the Talbot effect in terms of array self-imaging (Chavel and Strand 1984; Patorski 1989; Latimer 1993) is physically unrealistic.

One of the most important features of the Talbot effect is the "self imaging" distance, which represents the repeat length of the pattern and was first deduced by Rayleigh (Rayleigh 1881) :

$$z = \frac{\lambda}{1 - \sqrt{1 - \lambda^2 / \Lambda^2}}, \tag{5.25}$$

whereby establishing the dependence of the grating period Λ and the wavelength of light λ. When the diffraction angle is small, $\lambda << \Lambda$ the spacing between the self-images reduces to the well-known Talbot length, Z_T (Rayleigh 1881):

$$Z_T = \frac{2\Lambda^2}{\lambda}, \tag{5.26}$$

where λ is the wavelength of the incident light and Λ is the period of the diffraction grating. Under these conditions, an image of the original grating can be replicated at repeat intervals above its surface. Equally spaced but interleaved are reversal images, in which the light and dark regions of the intensity field pattern are inverted.

The generation of these self-images can be explained by considering the various diffracted orders of the grating; each diffracted order contains a spatial frequency component of the grating. Self-images occur at locations where the diffraction orders add in phase, while reversal images occur at points where the diffraction orders from the grating are out of phase. There is a maximum distance z_{max} beyond which the diffracted orders from the grating no longer overlap (Edgar 1969):

$$z_{\max} = \frac{W}{2}\left[\frac{\Lambda^2}{\lambda^2} - 1\right]^{1/2} \approx \frac{W\Lambda}{2\lambda}, \tag{5.27}$$

where W is the beam waist diameter or the grating size, whichever is smaller. In this work the maximum distance beyond which the diffracted orders no longer overlap was about *10.86* mm as estimated by equation 5.27 for an incident beam with diameter ~*5* mm and a grating pitch of *1.06* μm illuminated by an UV light of 244 nm wavelength.

A geometrical representation of the region over which the Talbot effect occurs due to the coherent overlapping of the diffracted orders is illustrated in Figure 5.28.

The emerging field after the beam has passed through the grating is composed of a set of diffracted waves propagating at angles Ψ_n satisfying :

$$\sin \Psi_n = \frac{n\lambda}{\Lambda}, \qquad n = 0, \pm 1, \pm 2, \ldots, \pm m, \tag{5.28}$$

where λ is the wavelength in the medium and m is the largest integer value for which Ψ_n retains a real value.

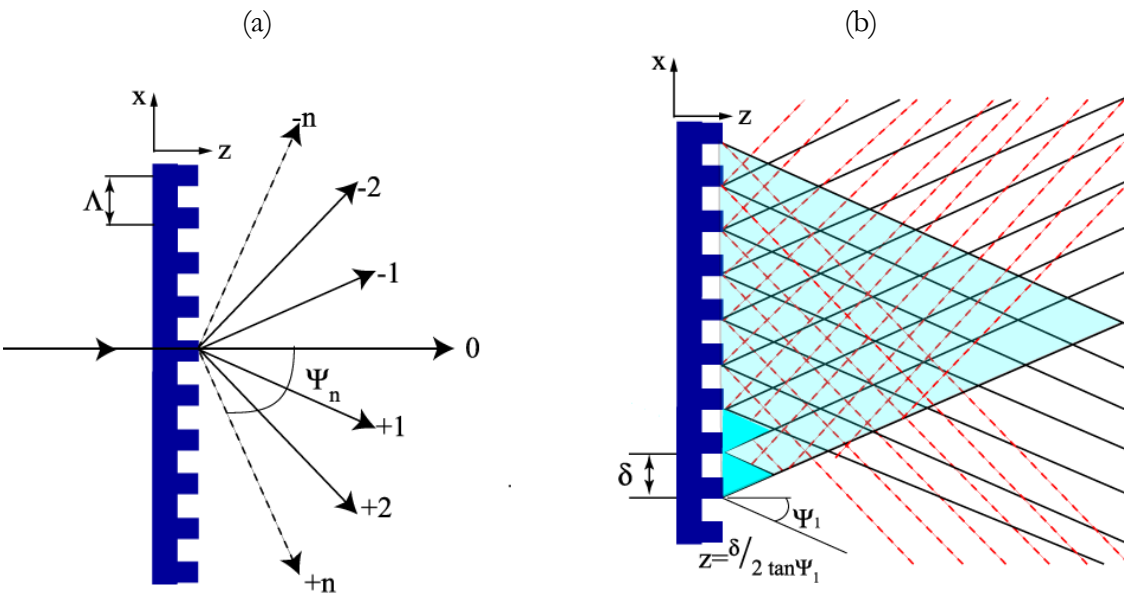

Figure 5.28. (a) Diffraction geometry from a grating. The Talbot effect occurs in the region where the diffracted orders overlap, the shaded region in (b). (b) Geometrical representation of the region over which the Talbot effect occurs due to the coherent overlapping of the diffracted orders illustrated in (a). $\delta = \lambda / \Delta\phi$ represents the spatial coherence length at the grating; $\Delta\phi$ is the incident beam divergence.

Theoretically, detailed information regarding the electric field distribution in the pattern, with regard to a phase mask have been calculated by various authors by either the finite element models (Wojcik, Mould *et al.* 1994) or scalar Fresnel-Kirchoff (Prohaska, Snitzer and Winthorp 1994).

Experimentally, the field distribution has been characterised using techniques involving exposures of photoresists (Dyer, Farley and Giedl 1995) and recently

techniques (Mills, Hillman *et al.* 2000) developed for scanning near-field optical microscopy (SNOM) (Hecht, Bielefeldt *et al.* 1996). The SNOM experiments were not performed in a typical near field region operation, i.e. where the tip-sample distance is required to be significantly smaller then the illumination wavelength. Moreover, Rayleigh's criterion for calculating the Talbot length has been found to be inaccurate and imprecise, as it did not take into account the influence of higher diffracted orders. As a consequence, it has been replaced by another theory. The complex patterns observed by the SNOM have been modelled in analogy with x-ray diffraction theory. Thus for a small number of diffracted orders the Talbot length, the periodicity of the pattern across the core, was estimated by (Mills, Hillman *et al.* 2000):

$$Z_T(m,n) = \frac{2\pi}{\left[\left(k^2 - m^2G^2\right)^{1/2} - \left(k^2 - n^2G^2\right)^{1/2}\right]}, \tag{5.29}$$

where $k = \frac{2\pi}{\lambda}$ is the wave number; $G = \frac{2\pi}{\Lambda}$ is the unit reciprocal lattice vector of the phase grating; m and n are integers representing diffracted orders and $Z_T(m.n)$ represents the Talbot length of a repeating pattern resulting from the interaction between two chosen orders. It is easy to see in equation 5.34 that the greatest repeat length is obtained for the zeroth and first diffracted orders, i.e. for $m = 0$ and $n = 1$.

Assuming that the diffracted orders are symmetrical such that their field amplitudes satisfy E_n=-E_{-n} and each diffracted component has the same phase at origin, the interference of these beams produces an electromagnetic energy density distribution $U_\lambda(x,z)$ described by (Dyer, Farley and Giedl 1995):

$$\begin{aligned} cU_\lambda(x,z) = I_0 + \sum_{j=1}^{m}\sum_{i=0}^{m} 4\sqrt{I_i I_j}\cos(kx\sin\Psi_i)\times \\ \cos(kx\sin\Psi_i)\cos(ky\cos\Psi i - ky\cos\Psi_j), \end{aligned} \tag{5.30}$$

where I_i is the irradiance of the ith order ($i = 0, 1, 2\ldots$) measured in a plane normal to its propagation direction, $k = 2\pi/\lambda$ is the wavenumber and c is the local velocity of light.

In Figure 5.28 (a) and (b), the intensity of the propagated wave is numerically calculated using Equation 5.35 and shown as grey levels. The familiar formation of self-images can be readily appreciated. The images illustrate theoretically predicted diffraction patterns in free space for various distances from the phase mask. The pattern is obtained using the same characteristics of the phase mask considered in this work i.e. a small contribution of the zeroth order, *5%*, and allowing the first *(37%)* and the second *(10%)* orders to be generated. It is easy to see that the periodicity of the pattern illustrated in Figure 5.30 is the same as of the phase mask, i.e. *1.06* μ*m*. The characteristic repetition rate of the Talbot pattern as a function of distance away from the grating is found to be *3.05* μ*m* in free space and *4.758* μ*m* in a medium with a refractive index of *1.56* representing the core of an optical fibre Figure 5.31. The latter value compares well with the experimentally measured value of *4.8* ± *0.2* μ*m* for the Talbot distance in the FBG (Dragomir, Rollinson *et al.* 2003). A calculation of the Talbot length using Equation 5.33 yields a Talbot distance of *4.65* μ*m* if only the first and second diffraction orders are considered, excluding the zeroth order, and *14.35* μ*m* for beating between the zeroth and the first-orders. If instead one would consider using, the Rayleigh's approximate expression, the Talbot length gives *9.2* μ*m* in free space and *14.367* μ*m* for a medium having a refractive index of *1.46* (equal to that of the fibre core) without considering the effects of beating between the individual diffracted orders. It is evident that this repeat length is dependent on both the refractive index of the medium and the diffracted orders involved and as such Eq. 5.29 provides a better explanation for the observed patterns in the FBGs.

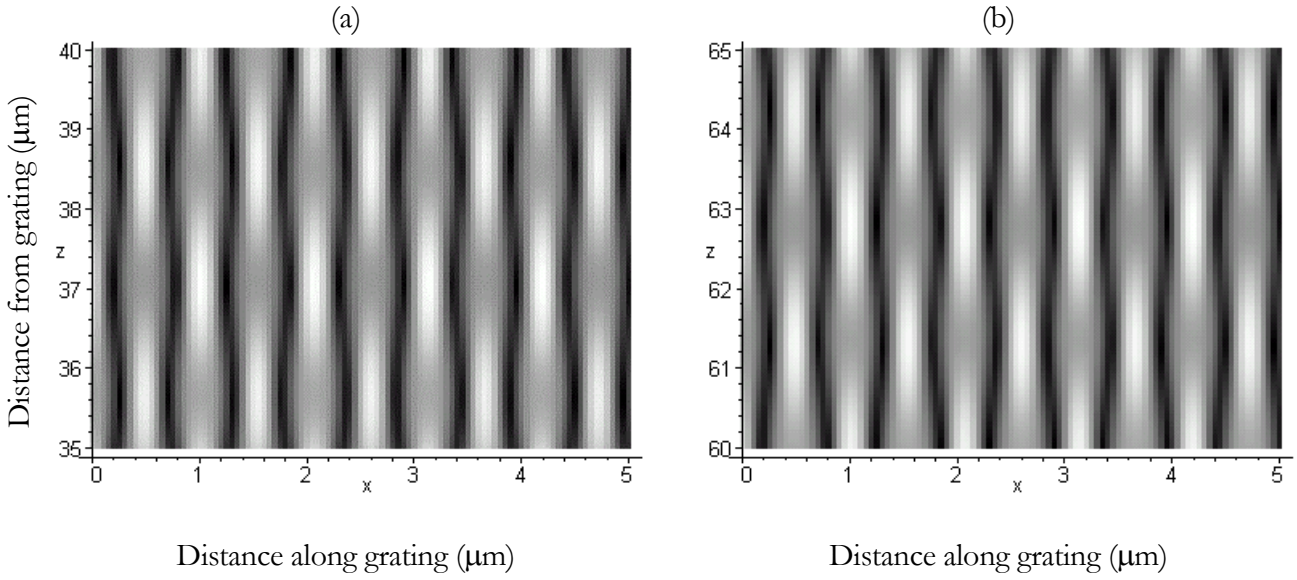

Figure 5.29. Numerically calculated intensity for the propagation of the optical field diffracted from a 1.06 μm period grating in free space. The images show a 5 × 5 μm free area space, representing the corresponding diffraction pattern for various distances from the grating, (a) z=35 to 40 μm, (b) z = 60 to 65 μm. The pattern's repeat distance is 3.05 μm. The phase mask is along the bottom of the image.

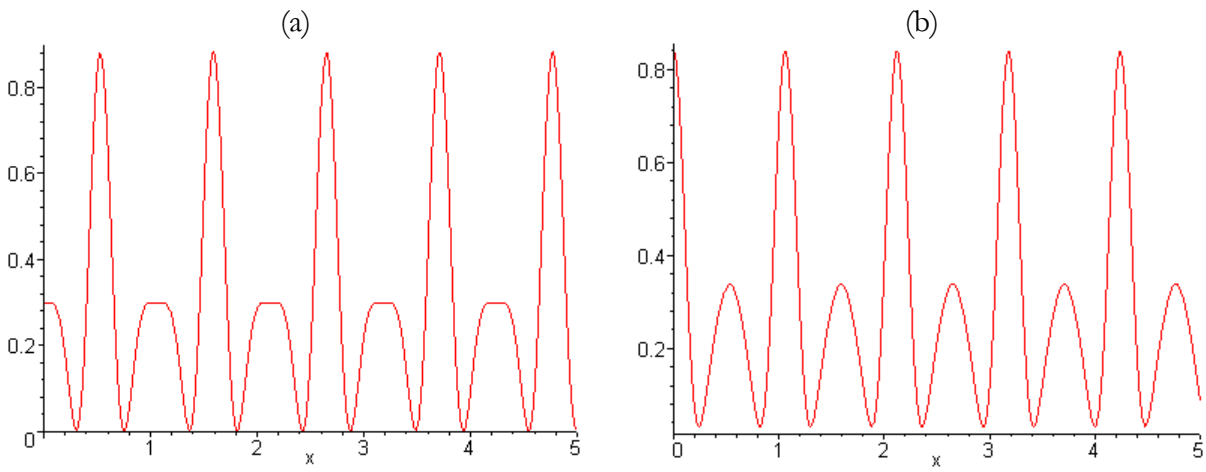

Figure 5.30. Cross-section of Figure 5.28b along the phase mask through fringes corresponding to (a) z = 61.2 μm and (b) z = 62.725 μm. The distance x is expressed in μm.

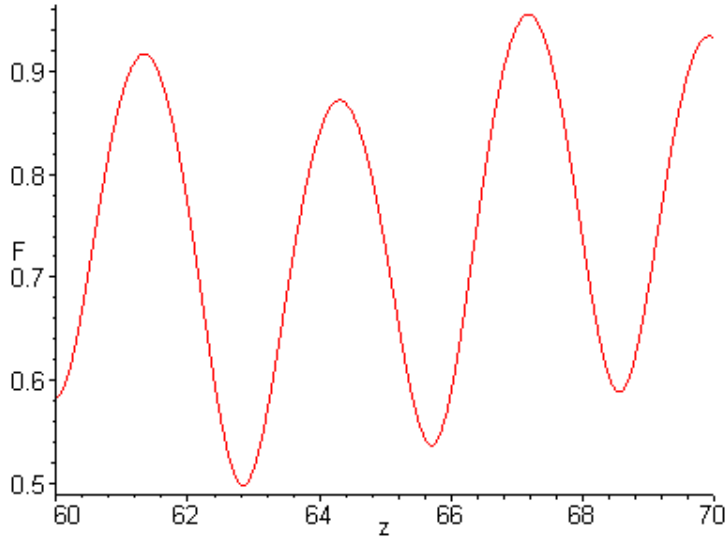

Figure 5.31. Cross-section of Figure 5.28b normal to the phase mask through two sets of Talbot peaks. The distance z is expressed in μm.

The sensitivity of the periodicity to the relative intensities of the different diffracted orders has not been the subject of this work.

5.9 Summary

In this chapter the phase structure of a Bragg grating written into the core of an optical fibre was successfully imaged using DIC microscopy. Figure 5.18 is a demonstration of the obvious fact that the gratings created by the phase mask technique do not have the characteristics predicted by simple two-beam interference theory. It was also observed that the gratings do not have a uniform distribution, commonly described in the literature as planes across the core of the fibre, but rather they are divided into interleaved layers across the core of the fibre with a contrast reversal between them. This gives rise to a

grating structure that can be explained by the diffraction theory. More over, the pattern was described using the self-imaging properties of a grating, where higher diffracted orders have been taken into consideration.

The presence of these layers, which can also be identified as the Talbot planes, in a Type I FBG was demonstrated by imaging the fibre whilst rotating it around its axis then carefully selecting two appropriate angles to identify the planes. Experimental measurements of the periodicity of these layers, the Talbot length, in Type I FBG's agree well with the theoretical values.

Simulations of the intensity distribution have been performed to support the case of the writing conditions for the FBG imaged in Figure 5.22. They incorporated not only the contribution of the zeroth-order diffraction but also the second order diffraction in addition to the prime contribution of the first-order. It was done so, because in the literature, the influence of the zeroth-order was believed to be the primary cause of the change in the gratings pitch (Xiong, Peng *et al.* 1999). The simulations show that the second diffracted orders interact with the first-orders and affect the period of the interference pattern. They also show that the second diffracted orders have at least the same importance as that of the zeroth order (Hegedus, 1997), and it is therefore essential that these orders are eliminated when high quality Bragg gratings are required.

The work presented in this Chapter provides insightful information about the detailed structure of the fibre Bragg grating. It has been shown previously that such a complicated structure exists by launching laser light into the grating and then tuning on and off resonance the evanescent distribution within the grating or the refractive index contrast along the grating being imaged (Mills, Hillman *et al.* 1999). However, the authors have attributed the observed irregularity of the intensity distribution of the scans covering several hundred microns along the

axis of the grating to errors in the refractive index profile which may have been caused by the generally low spatial coherence of the excimer writing laser. With the present explanation of the formation of the FBG one can easily see that such a non-uniformity can come from the grating itself in the case when the presence of a second diffracted order of as little as *6-7%* can influence the grating structure and the presence of the Talbot effect can not be neglected. In such a case, consideration of the grating geometry in the sample preparation for measuring the evanescent field coming from the grating is essential.

The technique presented in Chapter 3 of this thesis has the potential to be a powerful method for quantitative investigation of the UV induced refractive index in the optical fibre material during FBG fabrication. The use of this technique for reconstruction of the complex 3D phase structure of a FBG is the subject of another investigation and was outside the scope of this Thesis.

6 Concluding Remarks

This chapter concludes the thesis by summarising the main developments and results of this work and by indicating directions for further research.

The work presented in this thesis is part of ongoing research into addressing the problem of non-destructive characterisation of optical fibres and in particular fibre Bragg gratings.

6.1 Summary of Research Presented in this Thesis

One of the goals of the work presented in this thesis was to explore the applicability of developing a relatively low cost, non-destructive imaging technique to characterise the refractive index of optical fibres, with similar performance to commercially available techniques and using available apparatus. To achieve this goal the DIC imaging technique was employed to image optical fibres and then to reconstruct the refractive index of the fibre core. It is clear from the literature survey of Chapter 2 that a need for a reliable and non-destructive method for obtaining the refractive index profile of fibres remains despite the wide acceptance of the RNF method.

Refractive index profiling techniques have shifted from the standard methods, such as the refracted near field method, which is not only a destructive method,

but also expensive and sometimes not sufficiently reliable, especially for some of the new fibres coming into the telecommunications market, to newly developed methods. For example quantitative phase microscopy, is non-destructive and has the advantage of being less expensive, although it is not yet a widely used method for refractive index profiling of optical fibres. This evolution demonstrates that the field of refractive index profiling of optical fibres by means of direct optical imaging is an active area of research and as such there is still place to make improvements.

In Chapter 3 the basic operation of a DIC microscope was presented with the emphasis on the measurement of critical elements such as the calibration of the Wollaston prism and measurement of magnitude and orientation of the shear. A novel method for measuring the shear in the focal plane has been implemented and a theoretical framework to explain the findings was presented. Techniques taken from near field microscopy were used to collect the light from the focal plane of a lens. Although this is far from being the last word, it provided a favourable estimate of the lateral shear of the imaging system being used. Also presented in this chapter were the measurements that revealed the importance of matching the refractive index of the embedding medium to that of the fibre cladding, as was the sensitivity of the imaging method to fibre orientation.

The applicability of the imaging technique to reconstructing the refractive index of optical fibres was presented in the following chapter. Several optical fibres were presented. The reconstructed refractive index profiles of these fibres compared favourably with available commercial techniques.

Of particular interest was the measurement of the refractive index changes of fibres for use in fluorescence based temperature sensing which have been subjected to annealing. Notable was the fact that in spite of *a priori* knowledge

of the geometry of the fibre the reconstructed refractive index of the studied fibres provided a comprehensive understanding of the changes induced due to the annealing process.

In addition to the advantages/disadvantages of this methodology for reconstructing the refractive index profile of optical fibres from DIC images presented in Chapter 4, the author is aware of other limitations that have not been fully explored. They are as follows:

(i) the DIC images analysed are direction sensitive because of the preferred direction in which the fibre's information was captured (as shown in Chapter 3);

(ii) the images have a spatial resolution limited to the diffraction effects of the optical system;

(iii) the method is applicable for fibres having a cylindrical geometry and some *a priori* information about the object was necessary in the analysis;

(iv) the experimental data are discrete, given as fringe location information, which leads to sampling and positioning considerations in the error analysis, therefore introducing noise into the data set used in the refractive index reconstruction.

A major contribution of this work is the framework and methodology proposed and used in relation to non-destructive imaging of a fibre Bragg grating presented in Chapter 5. In addition, this tested the applicability of the imaging technique to FBGs. Also included in Chapter 5 was a brief review of relevant current characterisation techniques of FBGs. One of the biggest problems facing Bragg gratings characterisation is that it is generally based on the assumption that the gratings are uniformly distributed as planes across the fibre core and as such the refractive index modulation can be described by a

simple one dimensional model in the axial direction of the fibre. Focused on a FBGs fabricated using the phase mask technique, this chapter demonstrates that for these gratings this assumption is clearly not valid. Work on discovering their three-dimensional structure is ongoing.

Measurements of a fibre containing a FBG, axially rotated in a temperature controlled refractive index bay, has been performed for the first time non-destructively. It has revealed a detailed and complex three-dimensional structure of a Type I FBG fabricated using the phase mask technique. This structure can be explained using diffraction theory and the presence of Talbot planes produced by the phase mask replicated in the grating structure was shown. Details of modelling the diffraction patterns using this theory are in excellent agreement with the measured Talbot distance in the optical fibre. It was also found that the higher diffraction orders (particularly the second order), contribute not only to the formation of a three-dimensional structure of the FBG but also affect the transverse periodicity of the grating. This complex structure may have an impact on the reflectance spectrum of the studied FBG, proving a clear benefit of the above-mentioned technique in improving the understanding of FBG's formation. This topic has not been addressed and is the subject of an ongoing work.

6.2 Directions for Further Work

There are a number of ways in which further work may be carried out using this thesis as a basis.

For example, the evaluation of the refractive index reconstruction, presented in Chapter 4, could be carried out using a well calibrated optical fibre and the results compared with results from the RNF technique. In particular, results using the DIC imaging technique could be compared with other phase retrieval

algorithms such as QPM based on the transport of intensity equation, developed at Optics Group, University of Melbourne (Nugent 2001), or the rotational diversity phase estimation algorithm, developed at Washington University (Preza 2000b).

A direct extension of the work, as presented in Chapter 4 would involve the generalisation of the refractive index reconstruction from DIC images from the particular case of a fibre having a circular geometry to a more general one of elliptic geometry. This would employ a deeper theoretical modelling of DIC for phase objects of elliptical cross section, which automatically involves more work to simulate ray tracing through these types of objects. The ray tracing simulation would characterise the intensity distribution for various configurations of transversely illuminated optical fibres with circular or elliptical geometry and for various refractive index distributions. In addition the degree of elipticity of a given fibre may be determined using the rotation stage. This would simplify the analysis process.

6.2.1 Improving Quality of Images

In spite of the high spatial resolution achieved in the images presented throughout this thesis, an optical microscopic image is an optical section of an object at the focal plane and contains only a fraction of the total information content present in the actual object. Conventional DIC microscopes do not have the optical sectioning capabilities of confocal DIC microscopes, because they cannot exclude the out-of-focus, low-spatial-frequency component from an optical section image (Cogswell and Sheppard 1992; Cogswell 1997). It is worth further investigating the 3D structure of an optical fibre and that of an FBG (presented in Chapter 5), with such a microscope.

Recent research has shown that improved DIC images can be achieved by means of polarization modulation (Holzwarth, Hill and McLaughlin 2000). This is achieved by introducing a liquid crystal variable retarder (modulator) inserted into a differential-interference contrast microscope between the polariser and the sliding Wollaston prism (please refer to Chapter 3: Figure 3.3). The polarisation of the incident light beam can thus be switched in alternate video frames and controlled through a computer in order to increase the contrast signal of the specimen to be imaged. It has been reported that by subtracting alternate frames, a difference DIC image is created in which the contrast is doubled while other image defects including noise are cancelled (Holzwarth, Hill and McLaughlin 2000). This particular feature could prove to be useful particularly in imaging FBGs as it increases the contrast in the DIC image. In addition differential phase contrast (Hamilton and Sheppard, 1984; Hamilton et. al 1984) could prove useful for weak phase objects. Recently the work of Arnison *et al.* (2004) has opened a new avenue of improvements in the differential interference contrast imaging of weak phase objects.

6.2.2 Quantifying the Thermal Diffusion Processes: Fusion Splices

New optical fibres that come into the arena of the fibre technology require different splicing methods. Preliminary measurements of the fusion splice area between various fibres[lviii] were performed and revealed the thermal diffusion of the dopants into the cladding (Stevenson, Garchev *et al.* 2000). Thermal diffusion rates depend on the dopant and host species, for example fluorine diffuses much more rapidly in silica than germanium. The variety of new optical fibres that have become, and are becoming, available means that an understanding of the process involved in splicing is essential in order to develop new splice protocols. The work presented in Chapter 4 can be further

developed to study the process of dopant diffusion in optical fibres during the splicing procedure.

6.2.3 Quantify the Shear Modulus of Optical Fibres

The work presented in this thesis can be further extended to sensitive and analytic measurements of the shear modulus of the optical fibres, especially when low strain effects (Beltran 2002) need to be quantified. Recently multiple-beam Fizeau fringes in transmission crossing a bent single-mode fibre have been employed to obtain the shear modulus of the cladding material (El-Diasty 2002).

6.2.4 Periodicity of Light in Three Dimensions

The results in Chapter 5 related to the phenomenon known in the literature as "Talbot effect" or "self-imaging" has been demonstrated in the FBG. This has an impact on further determining the spatial distribution of the UV induced refractive index change within a fibre core. Further work should include the modelling and simulation of the phase mask pattern, with emphasis on the role of the efficiencies of the higher diffraction orders on the grating.

6.2.5 Bragg Grating Resonance

It has been shown that for a Bragg reflector a large refractive index modulation having the periodicity equal to that of the phase mask was present (Malo, Johnson et al. 1993). The contrast in the refractive index was high enough that a photographic image of the photoinduced perturbation has been presented. The authors concluded that as a consequence of the limited spatial resolution of the microscope, they could not observe the period of half the phase mask

[lviii] The fibres have been supplied by Dr. Adrian Carter from Redfern Fibres Inc. Eveleigh, New South Wales, Australia.

period. The authors also observed a sequence of transmission dips occurring at *1535*, *1030*, *770* and *620 nm* in the transmission spectrum over a large spectral range, (Figure 6.1). The light at these wavelengths was reflected by the grating structure and radiated since a grating with period Λ = *530 nm* cannot efficiently reflect light at wavelengths of *1030 nm* and *620 nm*, the authors concluded that all the reflections within this grating were a result of a grating period twice that expected, 2Λ, equal to that of phase mask.

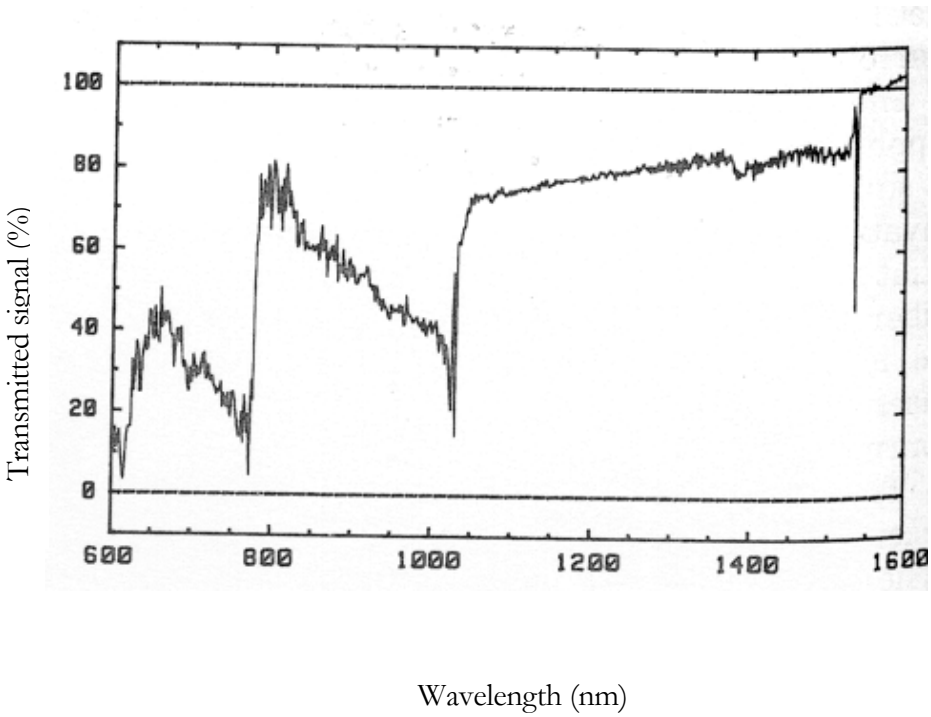

Figure 6.1. Transmission spectra of a Bragg reflector extended over the spectral range *600* nm to *1600* nm (after (Malo, Johnson et al. 1993)). The transmission dips that occur at *1535, 1030, 770* and *620* nm suggest a period of the grating equal to that of the phase mask.

The measurements performed on the FBGs, Type I, presented in Chapter 5 demonstrate that the grating has periodicity in both axial and transverse directions and that the axial direction has a periodicity equal with that of the phase mask whilst the transverse periodicity is related to the Talbot diffraction

pattern. As the instrument used has a spatial resolution close to the diffraction limit (approximately *0.3* μm), the grating period in the z direction found to be equal to that of the phase mask lead us to the conclusion that the observed grating, having the Bragg wavelength resonance of *1534.6 nm*, is a second order reflection grating and therefore is expected to have higher harmonics given by (Malo, Johnson et al. 1993):

$$m\lambda_{resonance} = 3070, \qquad m = 1,2,3,4,5..... \tag{6.1}$$

where *m* is the order of the reflection, in which case the *1534.6* nm was being considered as a second order reflection. As a consequence, it is expected that the transmission spectra to have dips of around *1023, 767.5* and *614* nm. This is the subject of a continuing work involving both accurate measurements of the reflectances at various harmonic wavelengths and modelling of the FBGs.

6.2.6 Fibre Bragg Gratings Birefringence

In this thesis it has been shown that FBGs are not symmetric and hence there should be intrinsic birefringence . Birefringence effects occur in both Type I and Type II FBGs. Birefringence is a serious disadvantage particularly in optical fibre communication lines, networks and certain optical fibre sensors.

In a FBG birefringence induces bifurcation and/or a split in the peak at the Bragg reflection wavelength (Wagreich, Atia et al. 1996) or to polarisation mode dispersion in chirped dispersion compensation Bragg gratings. Additionally this leads to a field mismatch and may cause transition losses of the order of 1 dB (Johlen, Knappe *et al.* 1999; Renner, Johlen and Brinkmeyer 2000).

The birefringence effects in FBG having high Bragg reflectivity have been reported (Gafsi and El-Sherif 2000). It was shown that for a traditional FBG,

having a uniform sinusoidal modulation of the refractive index, the Bragg reflection wavelength for the *x*-polarisation is larger than the *y*-polarisation for plane strain and plane stress. This was accredited to the photoelastic property of the optical fibre's material.

Further steps in modelling the three-dimensional distribution of the refractive index modulation of a Bragg grating, including the case of Bragg gratings fabricated by the phase mask writing technique, would offer information about the birefringence effects which are not accessible from the conventional approach.

6.2.7 Multipeaked FBG

Wavelength calibration references systems are a serious concern now days for optical telecommunications components and test equipment manufacturers. Currently, the National Institute of Standards and Technology, Colorado, USA offers wavelength references using gas-filled absorption cells, covering the *1510-1630* nm wavelength range (Gilbert and Swann 2001). Newly developed technologies, such as wideband optical amplifiers, active dispersion management, require wavelengths ranging from as low as *1300* nm to *1600* nm. Wavelength references for such a broad range can be acquired with, what is called in the literature, a multipeaked FBG (Eggleton, Krug *et al.* 1994b; Othonos, Lee and Measures 1994; Rabin, Swann and Gilbert 2002). This type of FBG has multiple reflection peaks over the *1300nm-1600 nm* range and can be manufactured by various means, using superimposed FBGs[lix] (Othonos, Lee

[lix] Superimposed FBGs are created by exposing a section of a photosensitive fibre to a series of ultraviolet interference patterns, each having a different period, resulting in an overlapping set of oscillations in the refractive-index profile of the fibre core. Thus separate refection peaks are produced for the different periods of the refractive-index.

and Measures 1994), sampled gratings[lx] (Eggleton, Krug *et al.* 1994b) or interleaved sampled grating FBGs[lxi] (Rabin, Swann and Gilbert 2002).

These types of FBGs are very complicated and studying them by using DIC imaging techniques would provide a means of understanding their structure, as it is known that the actual model used for predicting the shape of the reflectance peaks is still based on the uniform distribution of planes along the z-axis. These researchers are currently facing difficulties explaining a certain asymmetry of the envelope of the reflectance peaks, which cannot be explained using "simplistic model" (Rabin, Swann and Gilbert 2002).

6.3 Summary

This thesis has made a timely and substantial contribution to our understanding of complex optical fibres and in fibre optical devices. This chapter proposes a number of strategies to further develop this work to maximize its contribution to the future of our technology

[lx] The sampled gratings are created when a square-wave amplitude sampling (modulation) is imposed on the refractive-index profile of a standard grating. This results in a reflectance spectrum consisting of a central peak and a series of side peaks.

[lxi] The interleaved sampled gratings FBGs came in to the market overcome the too small bandwidth (300 nm) offered by the sampled gratings. They are produced by using an especially designed phase mask called a sampled phase mask, which enables the writing of a sampled FBG with one exposure Loh, W. H., F. Q. Zhou and J. J. Pan, "Novel Designs for Sampled Grating-Based Multiplexers-Demultiplexers". *Optics Letters,* **24** (21): 1457-1459, 1999, Gioannini, M. and I. Montrosset, "Novel Interleaved Sampled Grating Mirrors for Widely Tunable DBR Lasers". *IEE Proceedings Optoelectronics,* **148**: 13-18, 2001..

7 Appendices

7.1 Appendix A: Sample Preparation and Mounting

7.1.1 Choice of Optical Fibres

Optical fibres can be considered as phase objects[lxii] (Starodumov, Zenteno and Mendoza 1998); although they are made of clear glass they have regions of varying refractive index which contribute to a significant phase structure. Optical fibres have a number of properties that have been considered in the analysis such as a relatively well-characterised geometry and refractive index distribution. These parameters are essential to the fibre design and carefully controlled during fabrication. As a consequence of their commercial significance there are a number of commercial index profiling techniques, which can be used to independently verify the manufacturer's quoted profiles.

A number of optical fibres have been used in this work for various reasons; a list of the fibres imaged in this thesis is presented in Table 7.1.

[lxii] A fibre, which is immersed into index-matching oil introduces a maximum phase shift of $\phi = 2\,k\Delta n r_0 << 1$, where $k = 2\pi/\lambda$ is the wave number, Δn is the index-difference between core and cladding, r_0 is the core radius. The phase changes are very small so that no amplitude redistribution occurs inside the fibre, in other words an initial light amplitude distribution is presented in the plane after the light has passed through the fibre.

Table 7.1. Optical fibres used in imaging experiments in this thesis.

Name (symbol) of the optical fibre	Manufacturer	Independent measurement of the refractive index	Comments
SMF-28™	Corning®	Commercial profiling techniques[lxiii]	Commercial fibre used as a lead to the sensor fibre.
3M F-SN-3224	3M	Quantitative phase imaging[lxiv]	Study of bending in fibres[lxv].
DCI-PBG[lxvi]	Centre National De La Recherche Scientifique, France	Preform profiling and commercial profiling technique	The fibre has been designed to propagate a zero dispersion single mode at wavelengths as short as 1 μm and consists in a low-index cylindrical core surrounded by a cladding made of 7 layers with alternating high and low indices whose values are higher than that of the core.
Er^{3+} doped fibre (CD 497_01)[lxvii]	Redfern	Profile not available	This fibre had a depressed cladding region either side of the fibre core and has been used in fusion splice measurements.
Nd $^{3+}$doped fibre ()[lxviii]	Redfern	Profile not available	This fibre presented a depressed cladding region with alternating layers of slightly high/low-index in the depressed region.
Yb^{3+}- (~1800 ppm), Al and Ge doped fibre	INO, Canada	Preform profiling	This fibre had a F and P_2O_5 deposited inner cladding and is used in fluorescence based temperature sensing after being annealed.

[lxiii] P102 analyser, York Technologies, Chandlers' Ford, UK. This profiling was done for us by the Optical Fibre Technology Centre in Sydney.

[lxiv] Barty, A, K.A. Nugent, D. Paganin, A. Roberts (1998) Quantitative Optical Phase Microscopy, Optics Letters, 23(11):1-3; A. Barty,(2000) Quantitative Phase – Amplitude Microscopy, PhD thesis, University of Melbourne.

[lxv] Roberts, A., K. Thorn, M.L. Michna, N.M. Dragomir, P.M. Farrell and G. W. Baxter, Determination of bending in Optical Fibres using Quantitative Phase Imaging , Optics Letters, 27 (2): 86-88, 2002.

[lxvi] DCI-PBG = Depressed core index photonic band gap fibre, the fibre was provided by Dr. Gerard Monnom of Laboratôire de Physique de la Matière Condensé, Nice, France. (for detailed information concerning the DCI-PBG fibre see Brechet, F., J. L. Auguste, J. Marcou, P. Roy, D. Pagboux, J. M. Blondy, G. Monnom and B. Dussardier, "Very First Evidence of Propagation in Modified Chemical Vapour Deposition Photonic Band Gap Fibre (Bragg Type)". *European Conference on Optical Communications (ECOC' 2000)* Nice, France, paper CME1, 2000.

[lxvii] The fibre has been supplied by Dr. Adrian Carter of Redfern Fibres Inc. Eveleigh, New South Wales, Australia

[lxviii] [lxviii] The fibre has been supplied by Dr. Adrian Carter of Redfern Fibres Inc. Eveleigh, New South Wales, Australia

The depressed core index photonic band gap (DCI-PBG) optical fibre, is a research fibre for which we have independent measurements of the refractive index distribution obtained of the preform using commercial profiling techniques. This provided an additional test for the imaging system because it had to accurately image several transitions in refractive index rather than just two.

7.1.2 Stripping the Plastic Jacket

The polyacrylate coating of all fibres investigated in this thesis were removed using a chemical-solvent (acetone based) stripping method; this method has the least damaging effect, maintaining 80 % of the strength of the pristine optical fibre (Wei, James *et al.* 1999). The fibres were soaked in the chemical solvent, and a lint-free tissue soaked with acetone was used to remove any coating residue.

The optical fibres were imaged side-on so as to obtain a projection of the refractive index through all layers of the fibre structure. A small segment of fibre, typically one centimetre in length, was placed in a cell made up by a microscope slide having *170* μm thickness, covered with a *0.15* mm thick cover glass filled with index matching fluid. A special cell for imaging the FBG's has been made of only the microscope slide and the cover glass using as spacers two optical fibres of similar diameter placed parallel to and about half a centimetre either side of the studied fibre. This way any spurious tilt in the image is greatly reduced.

The refractive index of the oil (Cargille Laboratories) was measured using the same source light as that used for imaging with an Abbe refractometer.

In order to maximise the visibility of the fibre's internal structure the refractive index of the matching fluid was temperature controlled by firstly heating the oil to a certain temperature and then maintaining it using a temperature controlled stage (details regarding the temperature controlled stage may be found in Appendix F: The Temperature Controlled Rotation Stage). This method is particularly useful for fibres made from different material where the cladding is itself doped.

7.2 Appendix B: Plane-Wave Expansion

In this Appendix the plane wave expansion representation of a field propagating in a vacuum (which is also valid for any non-conducting, source-free, linear, spatially and temporally homogeneous, isotropic, and linear dielectric medium described by a constant refractive index n is presented. The derivation follows the angular spectrum approach, consisting of decomposition of the propagating field into monochromatic-wave fields, which is rigorous within scalar diffraction theory and is formally equivalent to electromagnetic field propagation. It follows closely the work of Greffet and Carminati (1997) and it is included here for the sake of completeness; no originality is claimed.

Let $\boldsymbol{E(r)}$ be a monochromatic field of wavelength λ. This electromagnetic field that propagates along the beam axis z satisfies Helmholtz propagation equation for $z > 0$ (omitting the temporal dependence $exp(-i\omega t)$):

$$\nabla^2 \mathbf{E}(\mathbf{r}) + k_0 \mathbf{E}(\mathbf{r}) = 0, \tag{7.1}$$

where $k_0 = 2\pi/\lambda = \omega/c$ is the vacuum wave number, ω is the angular frequency and c is the vacuum speed of light; and $\mathbf{r}$ is the position vector.

The field must have a finite energy for any $z \geq 0$:

$$\int \left|\mathbf{E}(\mathbf{r}_T, z)\right| d\mathbf{r}_T < \infty, \tag{7.2}$$

where $\mathbf{r}_T \equiv x\hat{\mathbf{x}} + y\hat{\mathbf{y}}$ is the transverse position vector and $\left(\hat{\mathbf{x}}, \hat{\mathbf{y}}\right)$ the unit vectors of the rectangular coordinate system *(x, y, z)*. Furthermore the electric field must also satisfy the vector form of Sommerfeld's radiation condition:

$$\lim_{r \to \infty} r \left(\nabla \times \mathbf{E} - ik_0 \frac{r}{|r|} \times \mathbf{E} \right) = 0. \tag{7.3}$$

The field ***E(r)***, has a two-dimensional Fourier transform in any plane *z* = *const*:

$$\mathbf{E}(\mathbf{r}_T, z) = \int \widetilde{\mathbf{E}}(\mathbf{k}_T, z) \exp(i\mathbf{k}_T \cdot \mathbf{r}_T) d\mathbf{k}_T, \tag{7.4}$$

where $\mathbf{k}_T \equiv k_x \hat{\mathbf{x}} + k_y \hat{\mathbf{y}}$ is the transverse wave vector.

Introducing (7.4) into (7.1) leads to:

$$\frac{\partial^2}{\partial z^2} \widetilde{\mathbf{E}}(\mathbf{k}_T, z) + \gamma^2 \widetilde{\mathbf{E}}(\mathbf{k}_T, z) = 0, \tag{7.5}$$

with $\gamma^2 = k_0^2 - k_T^2$.

The solution of (7.5), compatible with the condition expressed in (7.3), is:

$$\widetilde{\mathbf{E}}(\mathbf{k}_T, z) = \mathbf{E}_0(\mathbf{k}_T) \exp(i\gamma z), \tag{7.6}$$

Substituting (7.6) in (7.4) leads to the expression of the angular spectrum or plane-wave expansion of the field:

$$\mathbf{E}(\mathbf{r}_T, z) = \int \mathbf{E}_0(\mathbf{k}_T) \exp(i\gamma z) \exp(i\mathbf{k}_T \cdot \mathbf{r}_T) d\mathbf{k}_T. \tag{7.7}$$

Thus the angular spectrum representation decomposes an arbitrary propagating field into a continuous sum of homogeneous plane waves that propagate with an angular frequency ω (Greffet and Carminati 1997).

7.3 Appendix C: Diffraction Pattern in a Defocused Plane

In this Appendix the field distribution at an axial defocus position in a differential interference configuration is presented. The derivation follows the generalised Fresnel diffraction theory approach for describing the diffraction pattern when an observation plane is very close to a diffracting aperture.

First consider the field distribution, ***E****(v,u),* from a light wave of wavelength λ , passing through an optical lens of focal length *f*, at a defocus distance *dz* from the focal plane (Gu 1996):

$$\mathbf{E}(v,u) = 2\pi i N \exp(-ikf)\exp\left(-\frac{iv^2}{4\pi N}\right)\int_0^1 \exp\left(\frac{iu\rho^2}{2}\right)J_0(v\rho)\rho d\rho \,, \tag{7.8}$$

where $N \equiv \frac{d^2}{\lambda f}$ is the Fresnel number, *2d* is the radius of the objective's aperture, $k = 2\pi/\lambda$ the vacuum wave number, $\rho = \frac{r}{d}$ is the normalised radial coordinate over the lens aperture, $v = \frac{2\pi d}{\lambda f} r$ is the radial optical coordinate , $r = \sqrt{x^2 + y^2}$ is the radial coordinate at the diffraction plane, $u = \frac{2\pi}{\lambda} NA^2$ [lxix] is a

[lxix] The term u is usually defined in the literature in the conventional manner, paraxial approximation, as , (Hamilton and Sheppard, 1982). The coordinate u defined as accommodate systems having numericalapertures higher than 0.7. This definition of the axial coordinate, also termed, pseudoparaxial approximation, provides a 1% better description of the depth of focus of a high NA system compared to the conventional one (Sheppard and Matthews, 1987).

dimensionless parameter representing the axial optical coordinate introduced here to characterize the defocus Δz and $J_0\ (v)$ is a Bessel function of the first kind of order zero (Goodman 1996).

By denoting:

$$P_0(v) = 2\pi i N \exp(-ikf)\exp\left(-\frac{iv^2}{4\pi N}\right), \tag{7.9}$$

and

$$P(v,u) = \int_0^1 \exp\left(\frac{iu\rho^2}{2}\right) J_0(v\rho)\rho d\rho\ , \tag{7.10}$$

such that the absolute field represented in (7.8) becomes:

$$|\mathbf{E}(v,u)| = |P_0(v)| \cdot |P(v,u)| = 2\pi i N |P(v,u)|. \tag{7.11}$$

The integral in (7.10) can be evaluated by using the linear terms of the series expansion formula $\exp(z) = 1 + z + \frac{z^2}{2!} + \frac{z^3}{3!} + \ldots + \frac{z^n}{n!}, z \in C$:

$$P(v,u) = \int_0^1 \left(1 + \left(\frac{iu\rho^2}{2}\right) + \frac{1}{2!}\left(\frac{iu\rho^2}{2}\right)^2\right) J_0(v\rho)\rho d\rho\ . \tag{7.12}$$

The first term in (7.12) can be readily evaluated by using the first-order Bessel function:

$$\int_0^1 J_0(v\rho)\rho d\rho = 2\frac{J_1(v)}{v}, v \neq 0, \tag{7.13}$$

the second and the third term in (7.12) are obtained using Maple program:

$$\int_0^1 \rho^3 J_0(v,u)d\rho = 2\frac{J_0(v)}{v} + \frac{2(1/2v^2-2)}{v^2}\cdot\frac{J_1(v)}{v}. \tag{7.14}$$

$$\int_0^1 \rho^5 J_0(v,u)d\rho = \frac{8}{3}\nu^2\left(-12+\frac{3}{2}\nu^2\right)J_0(\nu)+\frac{16}{3}\nu\left(-3\nu^2+12+\frac{3}{16}\nu^4\right)J_1(\nu) \tag{7.14a}$$

Consequently, introducing (7.13), (7.14) and (7.14a) into (7.12) leads to:

$$P(v,u) \cong 2\frac{J_1(v)}{v} + \frac{iu}{2}\left[\frac{J_0(v)}{v} + \frac{2(1/2v^2-2)}{v^2}\cdot\frac{J_1(v)}{v}\right] + \frac{iu^2}{2!}\left[\frac{8}{3}\nu^2\left(-12+\frac{3}{2}\nu^2\right)J_0(\nu)+\frac{16}{3}\nu\left(-3\nu^2+12+\frac{3}{16}\nu^4\right)J_1(\nu)\right]. \tag{7.15}$$

Thus the field distribution $|\mathbf{E}(v,u)|$, at a defocus in the axial direction is evaluated as:

$$E(v,u) = 2\pi N \cdot |P(v,u)|. \tag{7.16}$$

This field is the superposition of two orthogonal electric fields, $\mathbf{E_1}$ and $\mathbf{E_2}$, separated by the shear *s*, along a known angle in the *xy*-plane. The irradiance of this field can be approximated as:

$$I(u) \approx (2\pi N)^2\left[|P(v_1,u)|^2 + |P(v_2,u)|^2\right]. \tag{7.17}$$

where the two radial optical coordinates, v_1 and v_2 are expressed as:

$$v_1(r_1) = \frac{2\pi d}{\lambda f} r_1, r_1 = \sqrt{(x+s/2)^2+(y-s/2)^2}$$
$$v_2(r_2) = \frac{2\pi d}{\lambda f} r_{21}, r_2 = \sqrt{(x-s/2)^2+(y+s/2)^2}. \tag{7.18}$$

7.4 Appendix D: Fresnel-Kirchhoff Formulation of Talbot Effect

The phase mask can be considered as being an object of one dimensional periodicity and of infinite aperture defined by the amplitude transmittance function *t(x,y)* with grooves parallel to *y* of period *d*.

If illuminated by a uniform plane monochromatic wave of wavelength λ at normal incidence and amplitude *a*, $f(x,y,z) = a\exp(2\pi i\nu z)$, the grating diffracts in a plane parallel to it at a distance z. For an infinite grating and illumination beam this wave is itself periodic in *x* having the same period as the grating and so its squared modulus $|I(x,y,z)|^2$, the diffracted intensity.

The complex amplitude at a distance z from the grating as:

$$f(x,y,z) = \frac{-ia}{\lambda z}\exp\left(\frac{2\pi iz}{\lambda}\right)\int_{-\infty}^{\infty}\int_{-\infty}^{\infty} T(x',y')\times\exp\left\{2i\pi\left[\frac{(x-x')^2+(y-y')^2+\nu x'}{2\lambda z}\right]\right\}dx'\,dy' \tag{7.19}$$

This diffracted amplitude at a distance *z* from the grating, can be expressed adopting the Fresnel-Kirkoff's scalar approximation of diffraction (Prohaska, Snitzer and Winthorp 1994):

$$I(x,z) = |a|^2\frac{|t_{z\nu}(x)|^2}{\lambda^2 z^2}, \tag{7.20}$$

where $t_{z,\nu}(x)$ is the transmission of the periodic grating in the *x* direction and can be expressed as:

$$\begin{aligned} t_{z,\nu}(x) &= \frac{1}{\lambda z}\int_{-\infty}^{\infty} t(u)\exp\left\{2i\pi\left[\frac{(x-u)^2}{2\lambda z}+\nu u\right]\right\}du \\ &= \frac{1}{\lambda z}\int_{-\infty}^{\infty} t(u)\cos\left\{2\pi\left[\frac{(x-u)^2}{2\lambda z}+\nu u\right]\right\}du + i\frac{1}{\lambda z}\int_{-\infty}^{\infty} t(u)\sin\left\{2\pi\left[\frac{(x-u)^2}{2\lambda z}+\nu u\right]\right\}du, \end{aligned} \tag{7.21}$$

with

$$At_{z,v}(x) = \mathrm{Re}(t_{z,v}(x)) = \frac{1}{\lambda z}\int_{-\infty}^{\infty} t(u)\cos\left\{2\pi\left[\frac{(x-u)^2}{2\lambda z} + vu\right]\right\}du$$
$$Bt_{z,v}(x) = \mathrm{Im}(t_{z,v}(x)) = \frac{1}{\lambda z}\int_{-\infty}^{\infty} t(u)\sin\left\{2\pi\left[\frac{(x-u)^2}{2\lambda z} + vu\right]\right\}du. \tag{7.22}$$

As the grating is still finite it can only be numerically evaluated on a finite interval *[a,b]* in the real space such that expression in (7.22) becomes

$$A_{z,v}(x)(a,b) = \frac{1}{\lambda z}\int_{a}^{b} \cos\left\{2\pi\left[\frac{(x-u)^2}{2\lambda z} + vu\right]\right\}du$$
$$B_{z,v}(x)(a,b) = \frac{1}{\lambda z}\int_{a}^{b} \sin\left\{2\pi\left[\frac{(x-u)^2}{2\lambda z} + vu\right]\right\}du. \tag{7.23}$$

For computing the coefficients in (7.23) the Maple program provides

$$A_{z,v}(x)(a,b) = \frac{-\frac{1}{2}\sqrt{2\pi}}{\lambda z\sqrt{\frac{\pi}{\lambda z}}}\left\{\cos[\pi\nu(2x-\nu\lambda z)]FresnelC\left(\frac{\sqrt{2\pi}(-b+x-\nu\lambda z)}{\lambda z\sqrt{\frac{\pi}{\lambda z}}}\right) + \sin[\pi\nu(2x-\nu\lambda z)]FresnelS\left(\frac{\sqrt{2\pi}(-b+x-\nu\lambda z)}{\lambda z\sqrt{\frac{\pi}{\lambda z}}}\right)\right.$$
$$\left. -\cos[\pi\nu(2x-\nu\lambda z)]FresnelC\left(\frac{\sqrt{2\pi}(-a+x-\nu\lambda z)}{\lambda z\sqrt{\frac{\pi}{\lambda z}}}\right) - \sin[\pi\nu(2x-\nu\lambda z)]FresnelS\left(\frac{\sqrt{2\pi}(-a+x-\nu\lambda z)}{\lambda z\sqrt{\frac{\pi}{\lambda z}}}\right)\right\},$$
$$B_{z,v}(x)(a,b) = \frac{-\frac{1}{2}\sqrt{2\pi}}{\lambda z\sqrt{\frac{\pi}{\lambda z}}}\left\{\cos[\pi\nu(2x-\nu\lambda z)]FresnelS\left(\frac{\sqrt{2\pi}(-b+x-\nu\lambda z)}{\lambda z\sqrt{\frac{\pi}{\lambda z}}}\right) + \sin[\pi\nu(2x-\nu\lambda z)]FresnelC\left(\frac{\sqrt{2\pi}(-b+x-\nu\lambda z)}{\lambda z\sqrt{\frac{\pi}{\lambda z}}}\right)\right.$$
$$\left. -\cos[\pi\nu(2x-\nu\lambda z)]FresnelS\left(\frac{\sqrt{2\pi}(-a+x-\nu\lambda z)}{\lambda z\sqrt{\frac{\pi}{\lambda z}}}\right) - \sin[\pi\nu(2x-\nu\lambda z)]FresnelC\left(\frac{\sqrt{2\pi}(-a+x-\nu\lambda z)}{\lambda z\sqrt{\frac{\pi}{\lambda z}}}\right)\right\}. \tag{7.24}$$

Accordingly the diffracted intensity at distance z from the grating in free space is:

$$I(x,z) = |a|^2 \frac{|a|^2}{\lambda^2 z^2}\left[\left(At_{zv}(x)\right)^2 + \left(Bt_{zv}(x)\right)^2\right] \tag{7.25}$$

Owing to this, the grating can create images of itself in coherent or incoherent monochromatic light in the *z*-direction.

7.5 Appendix E: Characterisation of the Phase Mask

The periodic grating structure of the simplest phase-mask design has the general shape of a rectangular wave pattern, with an amplitude of *h* and a spatial period, called pitch of 2Λ, consisting of the barrier width *2b* of the pattern and separation spacing $2(\Lambda\text{-}b)$.

A phase mask Lasiris™, having a specified period of *1.06* μ*m,* was imaged in both axial and transversal planes using an Olympus Laser Scanning Microscope (IX FL) operating in reflection with an Ar ion laser light source(*1 mW, 488 nm*) and a dry objective of a variable numerical aperture (Olympus UplanApo *100 × /0.2 – 0.9 NA*). The phase mask has been positioned horizontally to allow the laser light to pass through from below and emerge at the phase mask rulings above. Figures 7.1 and 7.2 show the transverse *(x - y)* and axial *(x - z)* images of the phase mask. The *(x - z)* image presented the well known self imaging effect such that the repeat pattern, of around *4.5 ± 0.03* μ*m*, for the imaging wavelength of *488* nm matched closely the calculated value of *4.605* μ*m.*

The measured phase mask period was found to be *1.057 ± 0.0052* μ*m* which is in good agreement with the manufacturer specified value of *1.06* μ*m.*

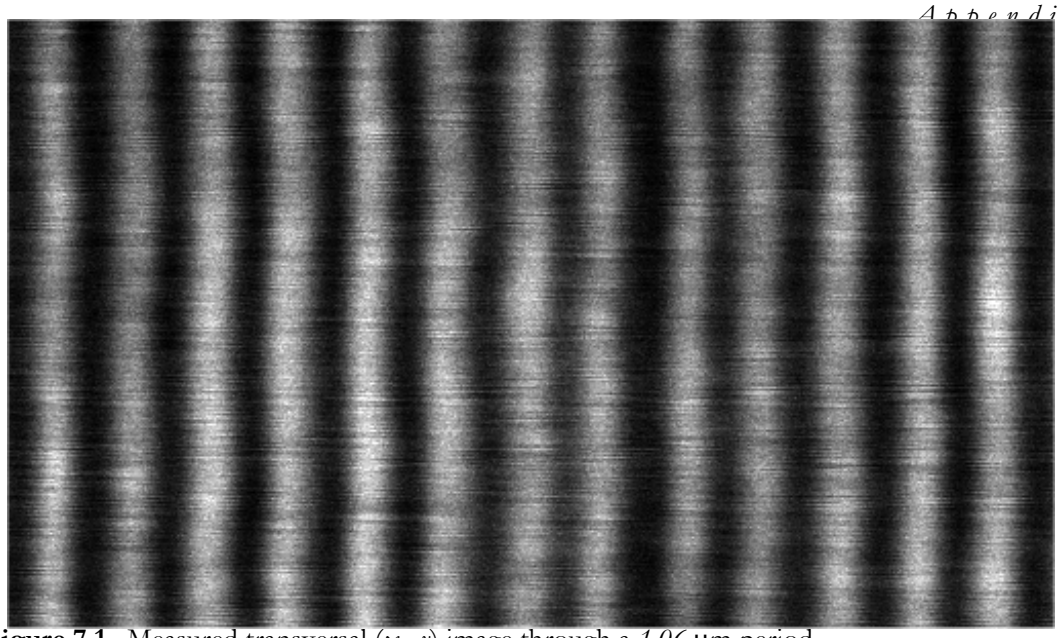

Figure 7.1 . Measured transversal (*x* - *y*) image through a *1.06* μm period.

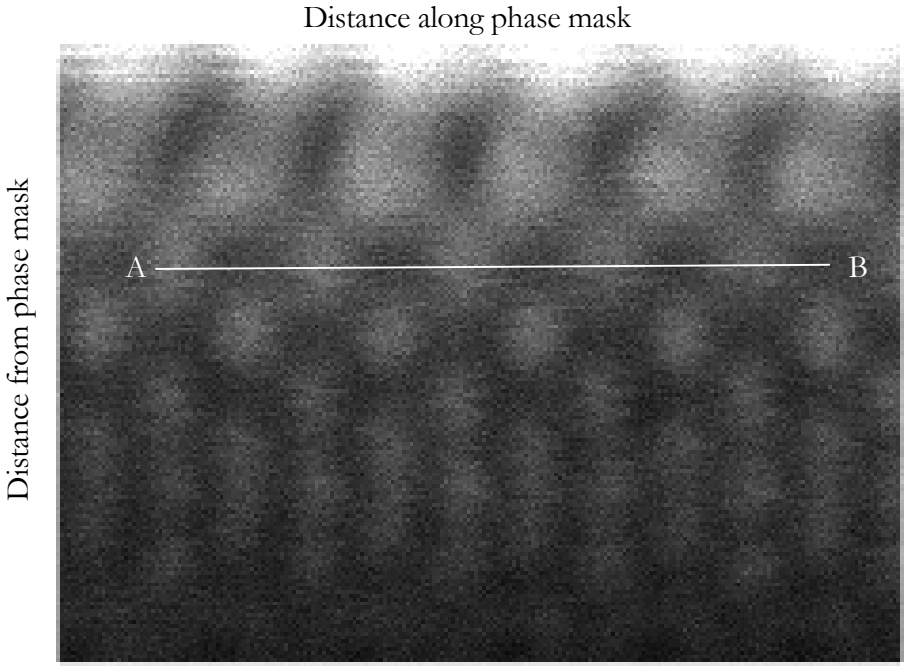

Figure 7.2. Measured axial *(x - z)* image through a 1.06 μm period phase mask demonstrating the Talbot diffraction pattern at 488 nm wavelength. The image represents an $x \times y$ section of *6.1 × 17.1* μ*m*. The phase mask is along the top of the picture and the propagation of light travels from top to bottom. The centres of the high elevations on the phase mask are positioned directly below of the lowest full row of maxima. The pattern repeat distance is *4.5 ± 0.03* μm, which matches the calculated value of *4.605* μm illustrating a strong zeroth order diffraction (for *488* nm).

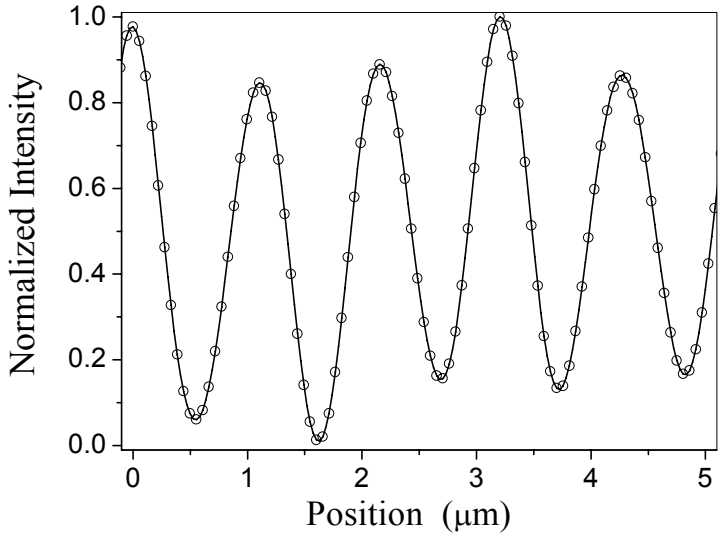

Figure 7.3. Cross section of Fig. 7.1 (along line AB) normal to the phase mask, through sets of Talbot maxima, showing the same period with the phase mask, i.e. ~*1.06* μm.

Defects in the ruled surface of the phase mask, shown in Figure 7.4 may generate distorted fields when used for writing FBGs. Figure 7.5 shows a distorted FBG probably due to defects in the ruled surface of the phase mask.

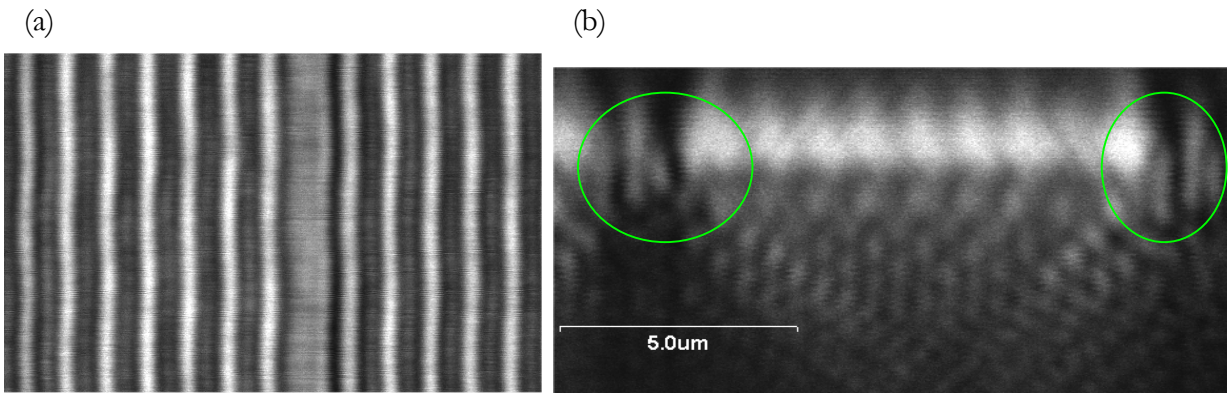

Figure 7.4 . Transverse (a) and axial (b) images of a region with defect in the phase mask. The axial image shows that in the distorted regions, marked by circles, a missing line in the grating limits the number of self-images. The disturbance is due to the fact that each diffracted order separates from the others at increasing distance, thus limiting the distance at which there still is interference.

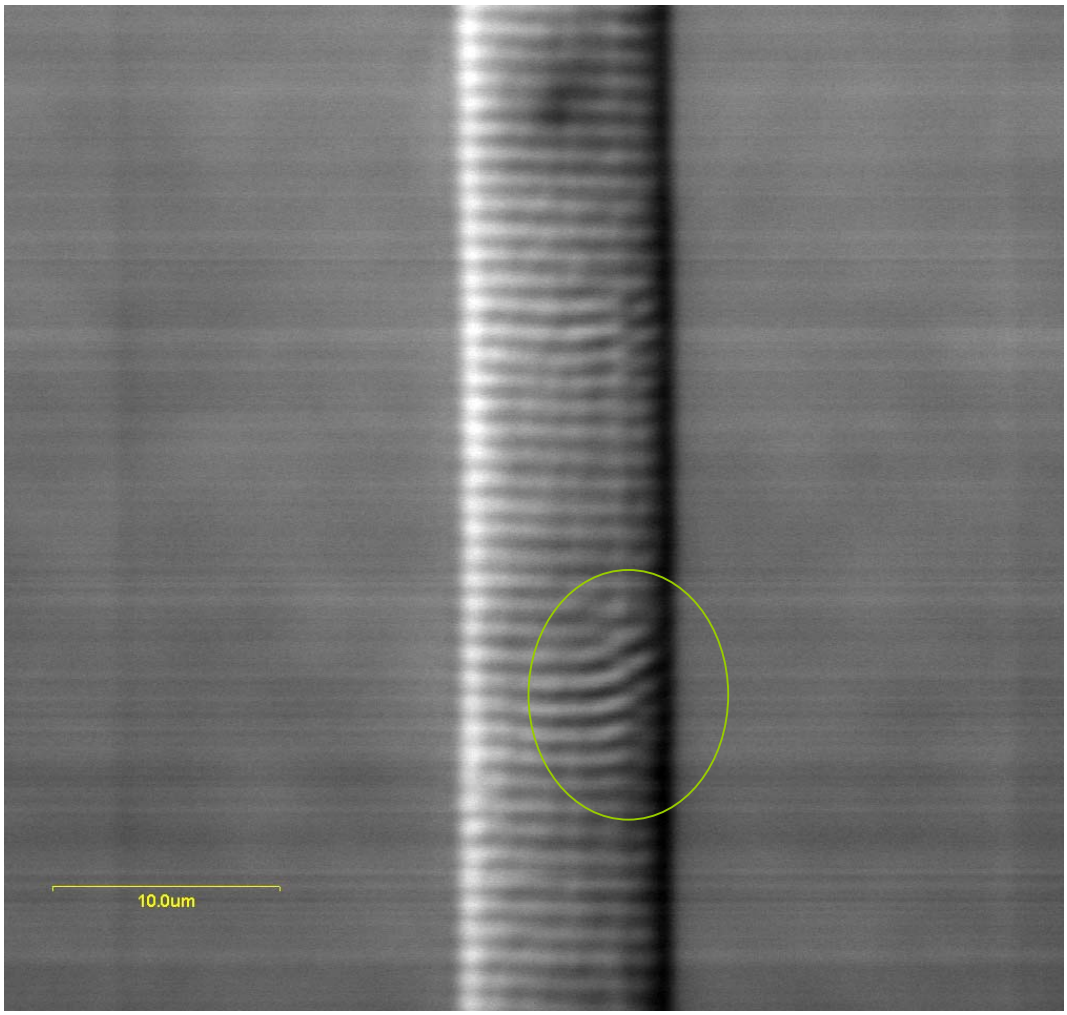

Figure 7.5. Measured image of an FBG presenting a defect. The unexpected structure may be due to defects of rulings surface in the phase mask, as shown, for example in Figure 7.4.

7.6 Appendix F: The Temperature Controlled Rotation Stage

There were two main concerns that needed to be addressed when imaging a fibre Bragg grating. Firstly the fibre should be placed in a cell such that the refractive index of the embedding medium can be controlled and kept constant for the duration of a scan. Secondly the fibre should be mounted such that it

can be rotated around its axial axis within the confines of the optical microscope imaging area in order to visualise the presence of the Talbot planes (discussed in Section 5.8). To this end a custom mounting plate combining both functions was designed and built in the Optical Technology Research Laboratory [lxx].

The technical requirements for this stage were quite challenging: it had to be able to rotate the sample through a full *360* degrees rotation about an axis perpendicular to the microscope optic axis while maintaining the sample within both the field of view and the depth of focus of the objectives, whilst at the same time the sample had to be immersed in a pool of index matching fluid, the fibre assumed to be perfectly cylindrical object was therefore positioned in the rotational stage in such a way that its longitudinal axis coincided with the axis of rotation of the fibre holder. In addition the mounting plate has also been designed to temperature control the cell containing the optical fibre sample.

The emphasis in this system was on low cost but with sufficient sensitivity for actual imaging requirements. The rotation stage illustrated in Figure 5.3 meets all of these requirements and was used to obtain the data presented in Chapter 5.

The fibre is clamped such that is concentric with the turntable's rotational axis. A standard fibre chuck has been modified and specially designed such that the radial centre of the fibre is in line with the centre of the fibre chuck centre, eliminating the precession when the fibre is rotated.

The fibre was placed on a V-groove, held onto the plate by using two cover slips and was mounted between two fibres used as spacers having the same diameter as the fibre studied. The V-groove continues on both sides of the

[lxx] This rotation stage was constructed by Mr. Donald Ermel.

glass cell in order to minimise the fibre's precession during rotation. A set of crossed-roller bearings inside the fibre chuck was used for clamping the fibre directly on the cladding surface. The use of cross rollers increases the positioning accuracy and stability. It is estimated that the Abbe error is less than 2.5 μm.

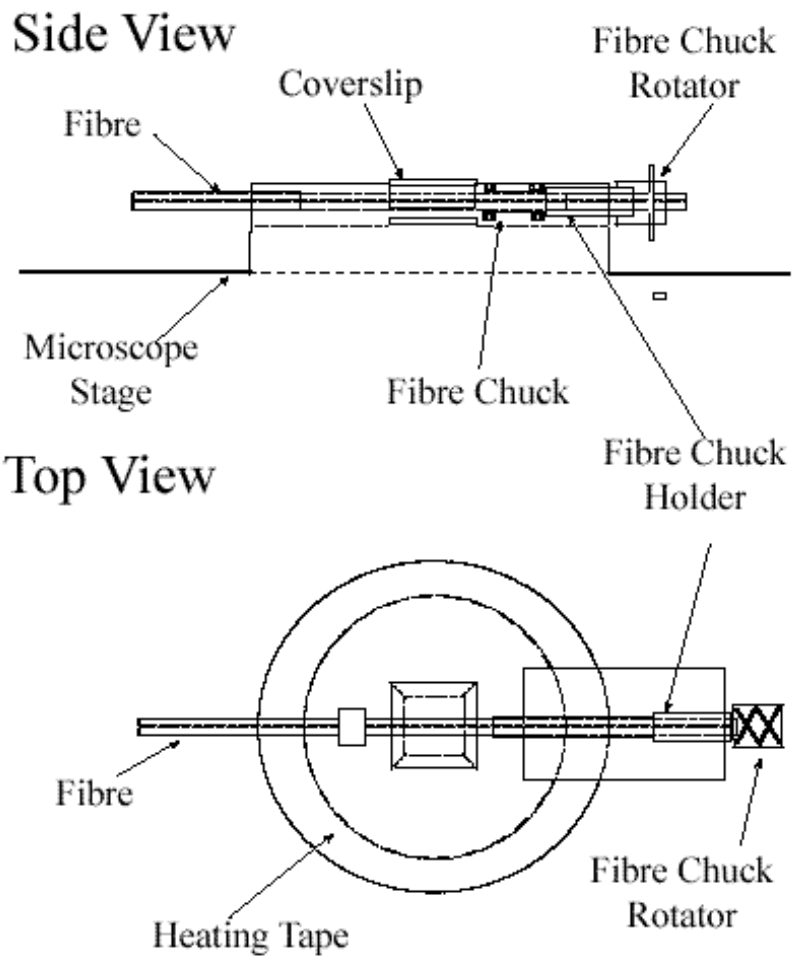

Figure 7.6. Schematic of the temperature controlled rotation stage. The smooth angular rotation of the fibre placed in matching oil between two cover slips has been achieved by combining a home made fibre chuck rotator with a fibre chuck. This way 360 degrees of initial fibre rotation have been provided whilst the optical fibre sample is kept within the working distance of the microscope objective (600 μm) and lateral constrained motion to within a 350 μm × 350 μm field of view of the objective. This combination is attached directly on top-side of the temperature controlled stage. A graduated knob and vernier scale allows initial setting of the rotation angle.

The heating of the stage was achieved by applying a current through a resistor thermally contacting the plate using a heat sink compound. An electronic temperature controller (BTC–9090) manufactured by Hotco® (http://www.hotco.com.au) monitored the stage temperature via a standard thermocouple, (iron – constantan, Type J) thermocouple. This thermocouple has been chosen due to its low temperature range (from -50 to 999° C), accuracy of ± 0.2° C and its fast response time (1 sec) achieved by using a very small size wire (0.005 inch).

The system is setup so that the heating is strongest under the source. Unfortunately the glass slide is known to have a poor thermal conductivity. This means that one needs either to apply a large heat flux through the heating element which is not desirable due to the short working distance of the objective lens or separately heating the elements used to building up the cell to the wanted temperature and then transfer them on the temperature controlled stage. The latter procedure was chosen because it also ensures that the glass elements are heated evenly and temperature gradients are minimised which in turn provides the conditions of a uniform background in the imaging plane.

7.7 Appendix G: Companion Publications

The following publications were produced in the course of this study and they are listed along with the chapters that they are relevant to:

2003: Toward a better understanding of optical fibre Bragg grating sensors, *The 12th Conference on Sensors and their Applications*, Limerick, IOP, Bristol), pp.435 - 441, 2003 (chapter 5).

2003: Nondestructive Imaging of a Type I Optical Fiber Bragg Grating, *Optics Letters* 28(10) 789 - 791 2003 (chapter5).

2003: Evaluation of optical fiber sensors using differential interference contrast imaging techniques, *The 16th International Conference on Optical Fiber Sensors (OFS-16)*, Nara, Japan (IEICE, Japan), pp. 230 – 233, 2003 (chapter5).

2003: Effects of high-temperature heat treatment on Nd^{3+}-doped optical fibres for use in fluorescence intensity ratio based temperature sensing, *Review of Scientific Instruments*, vol. 74, no. 7, pp.3524-3530, American Institute of Physics, USA, 2003, (chapter 4).

2003: Effect of phase mask writing technique on the higher order reflections of Type I and Type IIA fibre Bragg gratings, *Proceedings Conference on Optical Internet 2003 and 28th Australian Conference on Optical Fibre Technology*, Melbourne (ISBN 739 4), pp.411 – 414, 2003 (chapter 5).

2002: Annealing effects in optical fibres used in fluorescence base temperature sensing, Proceedings of the 27th Australian Conference on Optical Fibre Technology, co-located with 15th National Congress of the

Australian Institute of Physics, Sydney, (ISBN 0-9581182-0-5), pp.122-124.

2002: Phase imaging methods for optical fiber characterization, *Technical Digest: Symposium on Optical Fiber Measurements, NIST Special Publication* 988, pp. 109-112, 2002, (chapter 4).

2002: Near-field measurements of a Wollaston Prism shear displacement, 15th National Congress of the Australian Institute of Physics incorporating the Conference of the Australian Optical Society, Sydney, AIP, pp.331-333.2002, (chapter3).

2002: Non-destructive imaging and characterization of optical fiber Bragg gratings, *Photonics Prague*, *Proceedings of SPIE* **5036**, pp.182-186. 2002 (chapter 5).

2002: DIC imaging of an optical fibre Bragg grating, *Technical Digest Optical Fiber Communication Conference*, OFC 2002 (TOPS vol 70), 17-22 Mar 2002, Anaheim USA, Optical Society of America, pp.700, 2002, (chapter5).

2001: Investigating refractive index of photonic band gap fibres using DIC microscopy, *Conference proceedings OECC/IOOC 2001 Conference Incorporating ACOFT*, pp. 156 - 157, 2001, Sydney, Australia, (chapter 3).

2001: DIC Imaging of an Optical Fibre Bragg Grating, *Australasian Conference on Optics, Lasers & Spectroscopy (ACOLS)*, University of Queensland, 3-6 December 2001, (chapter5)

2001: Analysis of physical changes to optical fibre resulting from annealing processes, *Proceedings of the Eleventh Conference on Sensors and their Applications*, Institute of Physics Publishing, pp. 347-353, Bristol, UK, 2001 (chapter 4).

2000: Reconstructing Refractive Index From DIC Images of Optical Fibres and Waveguides, *The 14th National Congress of the Australian Institute of Physics*, Adelaide University, South Australia, December 10-15, 2000 (chapter4).

2000: Quantifying Dopant Diffusion Processes in Optical Fibre Splices, *Proceedings of Australian Optical Society Conference*, Adelaide University, 10-15 December 2000 (chapter 4).

2000: Estimation of the Refractive Index Profile of an Optical Fibre Using DIC Images, *Proceedings of The 25th Australian Conference on Optical Fibre Technology*, Australian National University, Canberra, 126-128, June 2000. (chapter4).

8 Glossary, Symbols and Acronyms

This section contains a glossary of terms including symbols and abbreviations used in relation to the themes of this thesis. It can not hope to replace the use of an Optical Dictionary. The terms are presented in alphabetical order.

8.1 Glossary of Terms

Quantity	Meaning
Abbé error	Term named after Dr. Ernest Abbé, 1800's, representing a positioning or linear displacement error, which results from parasitic rotations when there is a misalignment between the measurement axis and the point of interest. By reducing either parasitic rotations or the offset of misalignment, or both, the Abbé error and can be minimised.
Airy disk	Named after George Airy (1801 - 1892), the seventh "Astronomer Royal" to the British Crown. Airy disk consists of small concentric light and dark circles formed in an optical system due to diffraction of the light as it passes through a circular aperture, for example an imaging lens.
Annealing	The controlled process of slowly cooling an object modified by heat; the procedure is often used in optics to special optical elements in order to prevent cracking, stress-related irregularities, assuring strength, integrity and stability.
Annealing of an optical fibre	The process of heat treatment of an optical fibre commonly applied when the fibre is to be used as an optical sensing element for a particular application. This treatment involves raising the temperature of the fibre to a high point for a known period of time and slowly cooling back to room temperature. It is believed that the annealing process reduces stress in the glass structure and initiates a number of physical and chemical changes to the glass.
Atomic Force Microscope	One of the classes of scanning probe microscopes which uses a small cantilever with a pyramidal point to interact with the surface of a sample. The deflection of the cantilever at the tip as it is scanned across the sample surface is measured and used to indicate surface topography; the atomic force microscope utilises the attractive or repulsive forces between the tip and the sample to deflect the cantilever.
Bias retardation	Parameter characterising the phase shift between two orthogonal wavefronts

	produced by adjusting the position of a Wollaston prism in a differential interference contrast microscope. It is introduced by the operator of the microscope and controls the contrast of the image.
Birefringence	A medium is said to be birefringent when its refractive indices along two different directions in an appropriate coordinate system are different. Birefringence of materials can be exploited for sensing, but birefringence caused by undesired perturbances can also produce spurious effects on measurements. Birefringence in optical fibres may result from fibre geometry, stress, or a combination of both. Stress induced birefringence is called material birefringence; birefringence induced due to noncircular geometry of the fibre is usually referred as geometric birefringence.
Bragg fibre	A multilayer cylindrically symmetric fibre containing different refractive indices. The fibre consists of a core with a low refractive index surrounded by higher refractive index cladding.
Cantilever	An important structural part of an atomic force microscope, which is constrained from rotation and translation at one end, and is free at the other.
Charge-Coupled Device	Charge-coupled devices store information in the form of charge packets in an array of closely spaced capacitors; the packets can be transferred from one capacitor to the next sequentially by electronic manipulation, so that the information containing the array can be sequentially read electronically. In imaging microscopy, the charge packets are created by radiation and the devices are sensitive detectors for a range of wavelengths.
Confocal	Having the same focus or foci. In a microscope, the sample is at the common focus of the objective and the condenser optical systems; in a confocal microscope, either one or two apertures, called pinholes, define the measured area of the sample. These apertures are typically placed at the rear focal plane of the objective or the rear focal plane of the condenser. The best spatial definition of the sample can be achieved by placing an aperture at both positions.
Contrast	The number of shades, or grey levels, found in an image. It represents the ratio between the light and the dark levels illustrating of the light intensity of a specimen to the light intensity of the background.
Coupled-mode equations	A set of linear first order differential equations that describe how energy is transferred to and from different modes in an optical system. In particular for a grating structure in an optical fibre, the solutions of these equations establish the coupling coefficients of the grating, which serve as direct measure of its spectra. See "Coupled-mode theory".
Coupled-mode theory	Also known as "coupled-wave theory", is a well-known technique that pioneered the analysis of Bragg gratings in optical devices. This method is predicated upon the existence of weak periodic modulations of the effective refractive index of a guided –wave mode and assumes that mode coupling exists only between the fundamental forward and the reverse wave. See "Coupled-mode equations".
Cover glass	Also called coverslip; is an extremely thin flat glass cover for a specimen on a glass slide. It is available in various thickness; it may affect the optical performance of objectives of 40x and higher magnification. Certain objectives optimally perform with cover glasses of specific thickness.
Critical angle	The smallest angle t at which total internal reflection occurs within an optical fibre.

Depth of field	The range of depth that a specimen is in acceptable focus. It is dependent on the type of objective and its numerical aperture, the wavelength of light and the type of imaging used. The narrower the depth of field the higher the optical sectioning capacity of an optical system.
Differential Interference Contrast Microscopy	Imaging method that uses polarised light to produce contrast by transforming the phase shift of light, induced by a specimen refractive index, into detectable amplitude differences. A differential interference contrast microscope may be considered a microscope interferometer, i.e. it generates contrast within a specimen by exploiting phase differences between a specimen light ray and a reference ray. The two rays are created after the ray traverses the sample, being phase distorted one over the other and also being spatially separated due to a special optical element (See " Wollaston prism").
Diffraction	Formation of alternate dark and light fringes due to the passage of light through a small aperture.
Diffraction efficiency (of a grating)	The ratio of light passing the grating to the total amount of an energy of light illuminating the grating
Diffraction grating	Optical element causing diffraction of transmitted or reflected light. It consists of equidistant parallel lines on a glass plate.
Diffraction limited	Limit on the quality of an optical system due to diffraction.
D-shaped polarisation maintaining fibre	Specialty fibre having a cladding of semicircular cross-section and an eccentric core located few micrometers beneath the flat surface of the cladding. The core can have either circular or elliptical shape.
Evanescent field	Optical field that decreases monotonically, mathematically expressed by an exponential function, as a function of the transversal radial distance from the element or surface that it generated it.
Extraordinary ray	In uniaxial crystals the optic axis coincides with the symmetry axis. The refractive index of the crystal is the same in all directions perpendicular to the optic axis but is different along the optic axis. Consequently, electromagnetic rays or waves that do not travel along the optic axis experience different refractive indices in different directions perpendicular to their direction of propagation. Two waves result; one has its electric vector perpendicular to the optic axis and forms the ordinary wave (see "Ordinary ray"). The other has its electric vector oblique to the optic axis, and does not obey the normal laws of refraction. The latter wave is called the extraordinary wave or extraordinary ray.
Fibre Bragg grating	Photonic device based on periodic refractive index modulation providing a wavelength selective reflection. This device is produced via the phenomenon of photosensitivity in the core of a fibre. (See Photosensitivity").
Fibre-optic gyroscope.	An extremely sensitive optical fibre sensor, based on the Sagnac effect, for measuring rotation. The Sagnac effect is according to relativistic theory a problem of clock synchronisation, i.e. it does not rely on the interactions between light and the propagation medium
Gaussian beam	A beam of light whose electric field intensity has a Gaussian distribution.
Ge-B co-doped fibre	Optical fibre composed of a silica cladding and core doped with germanium and boron to enhance the fibre's photosensitivity.
Guided mode	In an optical fibre a guided mode is a mode that has the electromagnetic field strength or optical power density that decays monotonically in the transverse direction everywhere external to the core.
Half-shade device	A device for forming at least two adjacent areas of polarised light. The angle between the directions of vibration of the light waves in the two areas is generally small.

Hi-Bi bow-tie fibre	Hi-Bi bow-tie fibre is a high birefringence fibre with a germanium-doped core and boron-doped stress-induced sectors, having an elliptical core.
Irradiance	Power delivered per unit area of a laser beam, also known as power density; it applies to CW lasers. (See "Power density"). SI unit : W cm^{-2}.
Isotropic	Having properties that are the same in all directions.
Kramers-Kronig relations	General: Transforms based on the physical principle of causality that interconvert the real and imaginary parts of complex optical quantities when they are known over a sufficiently wide (strictly infinite) wave number range. Optical fibres: Mathematical expressions associated with the variations in the real and imaginary components of the refractive index of doped silica with the frequency.
Lateral resolution	See "Spatial Resolution"
Light amplifier	A device used to emit light of the same wavelength as the input light, only with an increased intensity.
Mode	When related to the optical fibres modes represent one of the various patterns of propagating or standing electromagnetic fields. The electromagnetic field pattern of a mode depends on the geometry of the fibre, the frequency and the refractive indices of the cladding and core.
Morphology	Internal or external structure of a solid structure.
Nomarski prism	Optical device used in a differential interference contrast microscope for the purpose of dividing a polarised light path into two states of polarisation. Characteristic to this beam splitter is its obliquely oriented optical axis to the flat face of the lower prism wedge element. The angle of the optical axis dictates where the interference plane of the prism is located: at some point on the exterior of the prism. (See " Wollaston prism").
Numerical Aperture (NA)	Microscopy: The NA of a microscope objective is a measure of its capacity to collect light and resolve fine details in a specimen at a fixed object distance. For a typical optical system the NA is the sine of the half-angle of the beam at an aperture. The higher the NA of an optical system the better the resolution. Fibres: The NA is equal to $n_0 sin\theta$, where n_0 is the refractive index of the exterior medium and θ is the maximum input half-angle that can support propagation.
Nyquist criterion	A result in information theory that a sine wave can be completely reconstructed if its ordinate is known at two or more points in a cycle. In microscopic imaging the Nyquist criterion states that one should collect two points per resolution size.
Optical fibre grating	An optical fibre with a periodic refractive index perturbation pattern inscribed in the core such that it diffracts the optical signal in the guided mode at specific wavelengths into other core-bounded modes, cladding modes, or radiation modes. (See "Fibre Bragg grating").
Optical path difference	The term is derived from phase retardation, which refers to the change in the phase of the electromagnetic radiation in an optical system. If the optical path difference is one quarter of the wavelength, then the system just meets the Rayleigh criteria and is diffraction limited. SI unit : m. Common unit : cm.
Optical path length	Term defined as the product of the optical path geometrical length and the refractive index in an homogeneous medium through which a wavefront

	traverses.
Optical sectioning	Capacity of an optical system to image planes within a specimen due to its small depth of field.
Ordinary ray	In a uniaxial crystal electromagnetic waves that have their electric vector perpendicular to the optic axis obey the normal laws of refraction and are called ordinary waves or ordinary rays. See also "Extraordinary wave".
Phase object	An object with differences in refractive index or optical path but not in absorbance. A pure phase object is characterised by a complex transmission function of the form: $g(x) = exp(i\ \phi(x))$; often weak phase objects are defined by a transmission function derived from a Taylor's expansion of a pure phase object, i.e. $g(x) = 1 + i\ \phi(x)$, where $\phi(x)$ is the phase change introduced by the object.
Phase retrieval	Technique used for extracting the phase of an optical wave field.
Photomultiplier Tube. (PMT)	Photomultiplier tubes are wavelength sensitive devices used to convert light into an electrical signal whose integrated are is proportional to the number of photons. They detect low intensity levels light in the form of photon counts. The photons strike a photoemissive cathode, which emits electrons due to the photoelectric effect. These electrons are then accelerated towards a series of additional electrodes called dynodes, which are maintained at a positive potential. This way, additional electrons are generated at each electrode through a cascading effect; depending on the number of the dynodes and the accelerating voltage a number of 10^5 to 10^7 electrons for each photon hitting the cathode may be generated. The amplified signal is finally collected at the anode where it can be measured.
Photorefractive	Light induced refractive index change.
Photorefractive effect	Non-linear optical effect, discovered in 1966, which consists of the ability of an optical material to change its refractive index under electromagnetic irradiation.
Photosensitivity	Property of a material indicating that will react when exposed to light.
Pitch	Term describing the distance between two successive grating elements, also referred as period. For a fibre Bragg grating, the pitch of the grating defines the reflected wavelength.
Pluta interference microscope	A double refracting wavefront shear interferometric imaging system based on continuous variable wavefront shear.
Polarisation maintaining fibres	Special fibres having the capacity to maintain the polarisation properties of light.
Power density	The amount of radiant energy concentrated on a surface. In the case of continuous wave lasers power density is also known as the irradiance. (See "Irradiance"). SI unit: Wcm^{-2}
Quantitative Phase Microscopy (QPM)	Image processing method used for estimating the phase of a specimen from transmission images acquired via a small defocus of the imaging system.
Rayleigh criterion	The Rayleigh criterion of resolution was proposed by Lord Rayleigh to define the resolution obtainable from diffraction-limited optical system. The criterion states that two separate sources of equal brightness are resolved when the center of diffraction pattern from one is superimposed with the first minimum of the other one. Under this condition for a microscope, a 26.5% dip in brightness appears between the two maxima.
Reflectance spectrum	The word "reflectance" is used for showing the fraction of the incident radiation that is reflected by a sample. Thus, the term "reflectance spectrum" is used when the intensity axis shows the reflectance.

Reflectometric methods	Techniques for measuring reflectance from a fibre Bragg grating.
Refractive index	The ratio of the velocity of light in the vacuum to that in another medium; it determines how much a ray of light will bend when it passes through the given medium.
Resolution	The finesse of an optical system offering details about a specimen. Usually it is considered to be the smallest distance that two objects can be apart and still be discerned as two separate objects. In transmission microscopy, where two lenses are involved, namely the objective and the condenser, the resolution may be calculated according to Rayleigh criterion as $R = 1.22 \times$ wavelength of light/($NA_{condenser} + NA_{objective}$). (See "Spatial resolution").
Scalar wave equation	A simplified version of the vector wave equation, written in the cartesian coordinate system, describing the axial components of the electric field of the bound modes in an optical fibre.
Scanning Electron Microscopy	Imaging method that uses a focused beam of electrons to scan and produce an image of the surface morphology. The image, having a lateral resolution below 10 nm, is constructed based on the detection of secondary electrons emitted by the sample surface. The surface to be studied must be coated with conductive material.
Shear	A key factor in a differential interference contrast (DIC) microscope. It refers to the difference in the distance within the specimen that two paths of light are made to travel by interference. This quantity determines the resolution and contrast in DIC images. Increasing the shear provides greater contrast but at the cost of resolution. Decreasing the shear provides greater resolution but contrast suffers.
Signal-to-noise ratio	The ratio of the size of the signal to the size of the noise, usually calculated as the average signal divided by the root-mean-square noise.
Single harmonic model	Model used in fibre Bragg grating modelling that considers that the FBG is made up single planes across the fibre core.
Spatial resolution	The smallest physical distance between measured positions on the sample in either single-point, mapping, or imaging. Also see "Resolution".
Talbot diffraction pattern	See "Talbot effect".
Talbot effect	Well-known effect in classical optics, named after Henry Fox Talbot, having many applications in image processing. It describes the reproduction of a periodic pattern at predictable distances from its surface subject to diffraction limit.
Talbot length	Distance at which the image of a periodic object reoccurs.
Tip	A sharp probe used in atomic force microscope and/or scanning near–field optical microscope to collect/transmit light from/to a surface in order retrieve to information of the surface structure.
Transport of intensity equation (TIE)	It represents a partial differential equation that relates the phase of an optical disturbance to its intensity and spatial intensity derivative.
Variable-Wavefront Interferometry (VAWI)	Imaging method based on the use of monochromatic light of continuously variable wavelength extracted from a white light source by means of a linear variable interference filter.
Wollaston prism	Optical device used in a differential interference contrast microscope for the purpose of dividing a polarised light path into two states of polarisation. (See "Nomarski prism").
Zero order	In interference pattern, the point where there is no difference between the optical paths of the interfering wavefronts.

optical paths of the interfering wavefronts.

8.2 Symbols

Symbol	Quantity	Meaning/Units
∇	Mathematical operator "del"	
d	Fibre diameter	
f	Focal length	
I	Intensity	The radiant power received per unit area. Intensity and irradiance are formally the same quantity; the term intensity is generally used for collimated beam of radiation. SI unit: $W \cdot m^{-2}$.
k	Wave number	The reciprocal of the wavelength of the radiation in a material of refraction index n.
k_0	Vacuum wavenumber	
L	Bragg grating length	
m	Indices representing the diffracted order	
$n(z)$	Refractive index modulation	
n_d	Refractive index un the cladding	
n_{co}	Refractive index of the core	
n_{eff}	Induced effective refractive index	Effective index of the mode
P_0	Optical Power	SI unit: W.
R_B	Bragg reflectance	
	Reflectance at the Bragg wavelength	
s	Shear wavefront	SI unit: m.
V	Normalised frequency of the fibre	
w	Beam waist diameter	SI unit: m.
z	Position along the axis of the fibre or	
	Propagation direction of light	
z_T	Talbot length	
Δ	Relative core-cladding refractive index difference	
$\Delta\phi$	Divergence angle	
$\Delta\lambda$	Full width at half maximum spectral bandwidth	
Λ	Grating period (pitch)	
β	Scalar propagation constant	

δ	Wavenumber detuning	$\delta = \beta - \frac{\pi}{\Lambda}$
$\kappa(z)$	Coupling coefficient	
λ	Wavelength	Distance travelled by the electromagnetic radiation in a non-absorbing medium of refractive index *n*, $\lambda = \frac{\lambda_0}{n}$. SI unit: m. Common unit nm or μm.
λ_{Bragg} *or* λ_B	Bragg wavelength	
ν	Frequency	The number of cycles of periodic motion in unit time. In spectroscopy the periodic motion is of the electric and magnetic vectors of electromagnetic radiation. SI unit: Hz.
$\sigma(z)$	Refractive index modulation	

8.3 Abbreviations

Abbreviation	Meaning
AFM	Atomic Force Microscopy
CCD	Charge-Coupled Device
DIC	Differential Interference Contrast
EDFA	Erbium doped fibre amplified
FBG	Fibre Bragg grating
Fibrecore PSI 1250	Optical fibre composed of a silica cladding and a core with germania phosphorus doped-silica to enhance the photosensitivity
FOG	Fibre-optic gyroscope
FWHH	Full width at half height
FWHM	Full width at half maximum, the full width of a band at half of the peak height.
GeO_2-SiO_2	Term signifying a germanium doped silica glass
GF1 fibre	Photosensitivity optimised germanosilicate fibre designed to provide ultra-high photosensitivity to UV radiation.
HF	Hydrofluoric acid
NA	Numerical Aperture
Nd:YAG laser	Laser in which Neodymium doped Yttrium Aluminium Garnet is used as a laser active medium to produce a wavelength having its centre at 1064 nm

	laser active medium to produce a wavelength having its centre at 1064 nm.
OCDR	Optical Coherence-Domain Reflectometry
OLCR	Optical Low Coherence Reflectometry
OPD	Optical Path Difference.
OSA	Optical Spectrum Analyser
PMT	Photomultiplier Tube
QPM	Quantitative Phase Microscopy
RNF	Refracted Near Field
SEM	Scanning Electron Microscope
SM-1322/P3022-E fibre	The SM-1322/P3022-E fibre is a standard telecommunications fibre fabricated by Optical Fibres, Deeside.
SMF-28	Single mode fibre. The most popular standard in single mode is SMF 28, product originally introduced by Corning
TIE	Transport of intensity equation
VAWI	Variable-Wavefront Interferometry.

9 References

"Refractive Index Profile, Refracted-Ray Method, Fiber Optic Test Procedure FOTP-44B, TIA/EIA-455-44b". *Technical Report*, Telecommunications Industry Association, 2500 Wilson Blvd., Suite 300, Arlington, VA. 22201-3384, 1992.

"Measurements and Calibration Services". *Technical Report*, National Physical Laboratory, Teddington, Middlesex, United Kingdom, TW11 0LW, 2000.

Abramowitz, M. and I. A. Stegun, Handbook of Mathematical Functions with Formulas, Graphs and Mathematical Tables. Dover Publications Inc., New York, 1970.

Albert, J., B. Malo, K. O. Hill, F. Bilodeau, D. C. Johnson and S. Theriault "Comparison of One-Photon and Two Photon Effects in Photosensitivity of Germanium Doped Silica Fibers Exposed to Intense ArF Excimer Laser Pulses". *Applied Physics Letters,* **67** (23): 3519 - 3521, 1995.

Allen, H. C., *An Introduction to Optical Fibers*. McGraw-Hill, 1983.

Ampem-Lassen, E. H., S.T. Roberts, A, "Optical Fibre Profiling Using Emission Mode Near Field Scanning Optical Microscopy". *25th Australian Conference on Optical Fibre Technology*, Information, Telecommunications & Electronics Engineering Society, Canberra, Australia, 129-131, 2000.

Anderson, D. Z., V. Mizrahi, T. Erdogan and A. E. White, "Production of In-Fiber Gratings Using a Diffractive Optical Element". *Electronics Letters,* **29** (6): 566 - 568, 1993.

Archambault, J. L., L. Reekie and P. S. J. Russel, "100% Reflectivity Bragg Reflectors Produced in Optical Fibres by Single Excimer Laser Pulses". *Electronics Letters,* **29** (5): 453 - 455, 1993a.

Arnison, M. R., K. G. Larkin, C. J. R. Sheppard, N. I. Smith, and C. J. Cogswell, "Linear Phase Imaging using Differential Interference Contrast Micrcoscopy", *Journal of Microscopy*, **214**, 7-12, 2004.

Archambault, J. L., L. Reekie and P. S. J. Russel, "Excimer Laser Production of Fiber Bragg Gratings". *Proceedings of SPIE - The International Society for Optical Engineering,* **2044**: 69 - 75, 1993b.

Atkins, G. R., V. Mizrahi and T. Erdogan, "248 nm Induced Vacuum UV Spectral Changes in Optical Fibre Preform Cores: Support for a Colour Centre Model of Photosensitivity". *Electronics Letters,* **29** (4): 385 - 387, 1993.

Bachmann, P. K., W. Hermann, H. Wehr and D. U. Wiechert, "Stress in Optical Waveguides. 1: Preforms". *Applied Optics,* **25** (7): 1093 - 1098, 1986.

Bachmann, P. K., W. Hermann, H. Wehr and D. U. Wiechert, "Stress in Optical Waveguides 2; Fibers". *Applied Optics,* **26** (7): 1175-1182, 1987.

Barrett, H. H. and W. Swindell, "Radiological Imaging - The Theory of Image Formation, Detection and Processing". (Ed.), Vol. 2, Academic Press, New York, 1981.

Barty, A., "Quantitative Phase - Amplitude Microscopy". PhD, The University of Melbourne, Melbourne, Australia, 2000.

Barty, A., K. A. Nugent, D. Paganin and A. Roberts, "Quantitative Optical Phase Microscopy". *Optics Letters,* **23** (11): 1 - 3, 1998.

Barty, A., K. A. Nugent, A. Roberts and D. Paganin, "Quantitative Phase Tomography". *Optics Communications,* **175**: 329 - 336, 2000.

Bar-Ziv, E., "Effect of Diffraction On The Moire Image. I. Theory". *Journal of the Optical of Society of America,* **2** (3): 371-379, 1985.

Baskin, L. M., M. Sumetski, P. S. Westbrook, P. I. Reyes and B. J. Eggleton, "Accurate Characterization of Fiber Bragg Grating Index Modulation by a Side-Diffraction Technique". *IEEE Photonics Technology Letters,* **15** (3): 449-451, 2003.

Beltran, G., "to be found". *Optics Communications,* **204**: 145-, 2002.

Bernardin, J. P. and N. M. Lawandy, "Dynamics of the Formation of Bragg Gratings in Germanosilicate Optical Fibers". *Optics Communications,* **79** (3-4): 194 - 199, 1990.

Berry, M., I. Marzoli and W. Schleich,*Quantum Carpets, Carpets of Light.* [Online, Internet]. physicsweb.org Available: http: physicsweb.org/article/worls/14/6/7/1/pw1406072, Accessed 4 March 2003.

Betzig, E., J. K. Trautman, T. D. Harris, J. S. Weiner and Kostelak, "Breaking the Diffraction Barrier: Optical Microscopy on Nanometric Scale". *Science,* **251**: 1468-1470, 1991.

Betzig, E. and J. K. Trautman,, "Near Field Optics: Microscopy, Spectroscopy and Surface Modifications beyond the Diffraction Limit". *Science,* **257**: 189-195, 1992.

Binning, G., C. F. Quate and C. Gerber, "Atomic Force Microscope". *Physical Review Letters,* **56** (9): 930-933, 1986.

Bilodeau, F., B. Malo, J. Albert, D.C. Hibino, M. Abe and M. Kawachhi, "Photosensitization of Optical Fiber and Silica-on Silicon/Silica Waveguides".*Optics Letters,* **18** : 953-955, 1993.

Born, M. and E. Wolf, *Principles of Optics.* Sixth ed., Pergamon Press, New York, 1980.

Born, M. and E. Wolf, *Principles of Optics: Electromagnetic Theory of Propagation, Interference and Diffraction of Light.* 7th Ed., Cambridge University Press, Cambridge, 1999.

Brechet, F., J. L. Auguste, J. Marcou, P. Roy, D. Pagboux, J. M. Blondy, G. Monnom and B. Dussardier, "Very First Evidence of Propagation in Modified Chemical Vapour Deposition Photonic Band Gap Fibre (Bragg Type)". *Lasers and Electro-Optics Europe,*

European Conference on Optical Communications (ECOC' 2000) Nice, France, paper CME1, 2000.

Brinkmeyer, E., "Simple Algorithm for Reconstructing Fiber Gratings from Reflectometric Data". *Optics Letters,* **20** (8): 810-812, 1995.

Brinkmeyer, E., D. Johlen, F. Knappe and H. Renner, "Methods for Experimental Characterization of UV-Induced Grating and Waveguides". In *Bragg Gratings, Photosensitivity and Poling in Glass Waveguides*, (Ed.), 33, OSA Trends in Optics and Photonics. 155 - 175, 2000.

Brinkmeyer, E., D. Stolze and D. Johlen, "Optical Space Domain Reflectometry (OSDR) for Determination of Strength and Chirp Distribution along Optical Fiber Gratings", *OSA Technical Digest Conference on Bragg Gratings, Photosensitivity and Poling in Glass Fibers and Waveguides: Applications and Fundamentals*, Williamsburg,Virginia, USA, Optical Society of America, Washington, DC, **17**: 33-35, 1997.

Brunning, J. H., D. R. Herriott, J. E. Gallagher, D. P. Rosenfeld, A. D. White and D. J. Brangaccio, "Digital Wavefront Measuring Interferometer for Testing Surfaces and Lenses". *Applied Optics,* **13**: 2693-2703, 1974.

Burrus, C. A. and R. D. Standley, "Viewing Refractive-Index Profiles and Small-Scale Inhomogeneities in Glass Optical Fibers: Some Techniques". *Applied Optics,* **13** (10): 2365-2369, 1974.

Butler, D. J., A. Horsfall, K. A. Nugent, A. Roberts, I. M. Bassett and K. M. Lo, "Measurement of an Elliptical Fiber Mode Field Using Near-Field Microscopy". *Journal of Applied Physics,* **77** (11): 5514-5517, 1995.

Callister, W. D. J., *Materials Science and Engineering: An Introduction*. Fourth Edition, John-Wiley and Sons, 1997.

Carré P., " Instalation et Utilisation du Comparateur Photoelectrique et Interferentiel du Bureau International des Poids de Measures" *Metrologia*, **2** 13-20, 1966.

Chavel, P. and T. C. Strand, "Range Measurement Using Talbot Diffraction Imaging of Gratings". *Applied Optics,* **23** (6): 862-871, 1984.

Chu, P. L. and T. Whitbread, "Measurements of Stress in Optical Fiber and Preform". *Applied Optics,* **21** (23): 4241-4245, 1982.

Cogswell, C. J. and C. J. R. Sheppard, "Confocal Differential Interference Contrast (DIC) Microscopy: Including a Theoretical Analysis of Conventional and Confocal Imaging". *Journal of Microscopy,* **165** (1): 81-101, 1992.

Cogswell, C. J., Smith N. I., Larkin K. G., Hariharan P, "Quantitative DIC Microscopy using a Geometric Phase Shifter", *Proceedings of SPIE* – The International Society for Optical Engineering, Proceedings of Three-Dimensional Microscopy: Image Acquisition and Processing IV: 12-13 Febraury 1997, San Jose, California/ Cogswell C. J., José-Angelo Conchello and Tony Wilson, Bellingham, Washington, USA **2984**: 72-81, 1997.

Clemmow P. C., *The Plane Wave Spectrum Representation of Electromagnetic Fields*. Pergamon Press Ltd., London, UK, 1966.

Collins, S. F., G. W. Baxter, S. A. Wade, T. Sun, K. T. V. Grattan, Z. Y. Zhang and A. W. Palmer, "Comparison of Fluorescence-Based Temperature Sensor Schemes:

Theoretical Analysis and Experimental Validation". *Journal of Applied Physics,* **84** (9): 4649 - 4654, 1998.

Cordier, P., J. C. Doukhan, E. Fertein, P. Bernage, P. Niay, J. F. Bayon and T. Georges, "TEM Characterization of Structural Changes in Glass Associated to Bragg Grating Inscription in a Germanosilicate Optical Fiber Preform". *Optics Communications,* **111** (3 -4): 269 -275, 1994.

Creath, K., "Phase-Measurement Interferometry Techniques". In *Progress in Optics*, E. Wolf (Ed.), XXVI, Elsevier Science Publishers, North-Holland Physics Publishing, Amsterdam, The Netherlands. 349 -393, 1988.

Crespo, D., J. Alonso and E. Bernabeu, "Experimental Measurements of Generalised Grating Images". *Applied Optics,* **41** (7): 1223-1228, 2002.

Culshaw, B. and J. Dakin, *Optical Fibre Sensors.* Artech House, Boston, USA, Vol. 3: Components and Subsystems., 1996.

Dana, K., "Three Dimensional Reconstruction of the Tectorial Membrane: An Image Processing Method Using Nomarski Differential Interference Contrast Microscopy". Master Thesis, Massachusetts Institute of Technology, Massachusetts, 1992.

Douay, M., W. X. Xie, T. Taunay, P. Bernage, P. Niay, P. Cordier, B. Poumellec, L. Dong, J. F. Bayon, H. Poignant and E. Delevaque, "Densification Involved in the UV-Based Photosensitivity of Silica Glasses and Optical Fibers". *Journal of Lightwave Technology,* **15** (8): 1329 - 1342, 1997.

Dragomir, N. M., G. W. Baxter, P. M. Farrell, E. Ampem-Lassen and A. Roberts "Near Field Measurements of a Wollaston Prism Shear Displacement". *The 15th Biennial Congress Australian Institute of Physics*, Australian Institute of Physics, Sydney, Australia, 331 - 333, 2002.

Dragomir, N. M., A. Roberts , G. W. Baxter , S. Collins, P. M. Farrell , A. J. Stevenson and D. D. Garchev "DIC Imaging of an Optical Fibre Bragg Grating". *Optical Fibre Communications, 2002* Anaheim, USA, TGG62, 2002.

Dragomir, N. M., A. Roberts , G. W. Baxter, P. M. Farrell and D. D. Garchev "DIC Imaging of an Optical Fibre Bragg Grating". *Australasian Conference on Optics, Lasers and Spectroscopy (ACOLS)* Brisbane, Australia, 57-59, 2001.

Dragomir, N. M., C. Rollinson, S. A. Wade, A. J. Stevenson, F. C. Collins, G. W. Baxter, P. M. Farrell and A. Roberts, "Nondestructive Imaging of a Type I Optical Fiber Bragg Grating". *Optics Letters*, **28** (10):789 – 791, 2003.

Dunn, A. K., A. J. Smithpeter and R. Richards-Kortum, "Sources of Contrast in Confocal Reflectance Imaging". *Applied Optics,* **35** (19): 3441-3446, 1996.

Dyer, P. E., R. J. Farley and R. Giedl, "Analysis of Grating Formation with Excimer Laser Irradiated Phase Masks". *Optics Communications,* **115** (3 - 4): 327 - 334, 1995.

Edgar, R. F., "The Fresnel Diffraction Images of Periodic Structures". *Optica Acta,* **16** (3): 281-287, 1969.

Eggleton, B. J., P. A. Krug, L. Poladian, K. A. Ahmed and H. F. Liu, "Experimental Demonstration of Dispersed Optical Pulses by Reflection From Self-Chirped Optical Fiber Bragg Gratings". *Optics Letters,* **19** (12): 877-879, 1994a.

Eggleton, B. J., P. A. Krug, L. Poladian and F. Ouellette, "Long Periodic Superstructure Bragg Gratings in Optical Fibres". *Electronics Letters,* **30** (19): 1620-1622, 1994b.

El-Diasty, F., "Application of Fizeau Fringes with Bending Technique to Determine the Shear Modulus of the Cladding Material of Single-Mode Optical Fibres through the Mechanically Induced Change of Refractive Index". *Optics Communications,* **212** (4-6): 267-274, 2002.

El-Diasty, F., A. Heaney and T. Erdogan, "Analysis of Fiber Bragg Gratings by a Side-Diffraction Interference Technique". *Applied Optics,* **40** (6): 890-896, 2001.

Erdogan, T., "Fiber Grating Spectra". *Journal of Lightwave Technology,* **15** (8): 1277-1294, 1997.

Erdogan, T., "Fibre Gratings Provide Keys to Future Optical Networks". *Photonics Spectra,* **32**: 96-97, 1998.

Erdogan, T. and V. Mizrahi, "Fiber Phase Gratings Reflect Advances in Lightwave Technology". *Laser Focus World,* **30** (2): 73, 1994.

Erdogan, T., V. Mizrahi, P. J. Lemaire and D. Monroe, "Decay of Ultraviolet-Induced Fiber Bragg Gratings". *Journal of Applied Physics,* **76** (1): 73-80, 1994.

Fernando G.F., D.J. Webb and P. Ferdinand, "Optical Fiber Sensors" *Materials Research Society Bulletin*, 27 (5): 359 – 364, 2002.

Ferdinand, P., S. Magne, V. Dewynter-Marty, S. Rougeault and L. Maurin, "Applications of Fiber Bragg Sensors in the Composite Industry" *Materials Research Society Bulletin*, 27 (5): 400 – 408, 2002.

Fevrier, S., P. Viale, F. Gerome, P. Leproux, P. Roy, J.M. Blondy, B. Dusardier and G. Monnom, "Very Large Effective Area Singlemode Photonic Bandgap Fibre" *Electronics Letters*, 39 (17): 1240 – 1242, 2003.

Flores-Arias, M. T., M. V. Perez, C. Gomez-Reino, C. Bao and C. R. Fernandez-Pousa, "Talbot Effect Interpreted by Number Theory". *Journal of the Optical Society of America A Optics & Image Science,* **18** (11): 2707 - 2716, 2001.

Fonjallaz, P. Y. and P. Borjel, "Bragg Gratings, Photosensitivity and Poling in Glass Waveguides", *OSA Technical Digest*, Washington DC, Optical Society of America, Washington DC: p. 230, 1999.

Fonjallaz, P. Y. and P. Borjel, "Interferometric Side-diffraction Technique for the Characterisation of Fibre Gratings". In *Bragg Gratings, Photosensitivity, and Poling in Glass Waveguides*, E. J. Friebele, R. Kashyap and T. Erdogan (Ed.), Vol. 33, Optical Society of America, Washington, DC, Washington, D.C. 179-181, 2000.

Fontaine, N. H. and M. Young, "Two-Dimensional Index Profiling of Fibers and Waveguides". *Applied Optics,* **38** (33): 6836-6844, 1999.

Gafsi, R. and M. A. El-Sherif, "Analysis of Induced-Birefringence Effects in Fiber Bragg Gratings". *Optical Fiber Technology,* **6**: 229 - 323, 2000.

Garchev, D. D., M. Vasiliev and D. J. Booth, "Wavelength-Tunable Chirped In-Fiber Bragg Gratings Produced with a Prism Interferometer". *Optics Communications,* **148** (4 - 6): 254-258, 1997.

Gilbert, S. L. and W. C. Swann, "Acetylene $^{12}C_2H_2$ Absorption Reference for 1510 to 1540 nm Wavelength Calibration-SRM 2517a". *NIST Special Publication 260-133*, National Institute of Standards and Technology, Gaithersburg, Md., 2001.

Gioannini, M. and I. Montrosset, "Novel Interleaved Sampled Grating Mirrors for Widely Tunable DBR Lasers". *IEE Proceedings Optoelectronics,* **148**: 13-18, 2001.

Gisin, N., R. Passy and B. Perny, "Optical Fiber Characterization by Simultaneous Measurement of the Transmitted and Refracted Near Field". *Journal of Lightwave Technology,* **11** (11): 1875-1883, 1993.

Gisin, N. and K. W. Raine, "Correcting Refracted Near-Field Refractive Index Profile Measurements for Gaussian Intensity Distributions". *Optics Communications,* **83** (3-6): 295-299, 1991.

Glantschnig, W. J., "How Accurately Can One Reconstruct an Index Profile from Transverse Measurement Data". *Journal of Lightwave Technology: a joint IEEE/OSA publication,* **LT - 3**: 678-680, 1985.

Goodman, J. W., *Introduction to Fourier Optics.* 2nd ed, Mc Graw-Hill, New York, 1996.

Grattan, K. T. V. and B. T. Meggitt, *Fiber Optic Fluorescence Thermometry.* Chapman and Hall, London, 1995a.

Grattan, K. T. V. and B. T. Meggitt, *Optical Fiber Sensor Technology.* Chapman and Hall, London, 1995b.

Greffet, J.-J. and R. Carminati, "Image Formation in Near-Field Optics". *Progress in Surface Science,* **56** (3): 133-237, 1997.

Gu, M., *Principles of Three-Dimensional Imaging in Confocal Microscopes.* World Scientific, Singapore, 1996.

Gureyev, T. E. and K. A. Nugent, "Phase Retrieval with the Transport of Intensity Equation II: Orthogonal Series Solution for Non-uniform Illumination". *Journal of the Optical Society of America A-Optics & Image Science,* **13**: 1670 - 1682, 1996.

Gureyev, T. E., A. Roberts and K. A. Nugent, "Phase Recovery with the Transport of Intensity Equation: Matrix Solution with Use of Zernike Polynomials". *Journal of the Optical Society of America A-Optics & Image Science,* **12** (9): 1932 - 1941, 1995.

Hamilton, D.K. and C.J. Sheppard, "A Confocal Interference Microscope" *Optica Acta*, **29**, 1573-1577, 1982.

Hamilton DK and Sheppard C.J. R, "Differential phase contrast in scanning optical microscopy", *Journal of Microscopy*, **133**, 27-39, 1984.

Hamilton DK, Sheppard CJR, Wilson T (1984) Improved imaging of phase gradients in scanning optical microscopy, *Journal of Microscopy* **153**, 275-286, 1984.

Hamza, A. A. and M. Mabrouk, "Interferometric Studies on Multi-Mode Step-Index Optical Fibres". *Pure and Applied Optics,* **7**: 449-456, 1998.

Hamza, A. A., T. Z. N. Sokkar, K. A. El-Farahaty and H. M. El-Dessouky, "Comparative Study on Interferometric Techniques for Measurements of the Optical Properties of a Fibre". *Journal of Optics A: Pure and Applied Optics,* **1**: 41-50, 1999.

Hamza, A. A., T. Z. N. Sokkar, A. M. Ghander, M. A. Mabrouk and W. A. Ramadan, "On the Determination of the Refractive Index of a Fibre: II. Graded Index Fibre". *Pure and Applied Optics,* **4**: 161-177, 1995.

Hand, D. P. and P. S. J. Russel, "Photoinduced Refractive Index Changes in Germanosilicate Fibers". *Optics Letters,* **15** (2): 102 - 104, 1990.

Hatton, W. H., E. L. Buckland and M. Nishimura, "Measuring the Refractive-Index Profile of Optical Fibers by the Cladding-Mode Near-Field Technique". *Optics Letters,* **12** (9): 738-740, 1987.

Hecht, B., H. Bielefeldt, Y. Inouye and D. W. Pohl, "Facts and Artifacts in Near-Field Optical Microscopy". *Journal of Applied Physics,* **81** (6): 2492-2498, 1996.

Hecht, J., *The Story of Fiber Optics*. Oxford University Press, New York, 1999.

Hegedus, Z. S., "Contact Printing in Optical Fibers: Rigorous Diffraction Analysis, *Applied Optics*, 36(1) 247-252, 1997.

Hegedus, Z. S., Z. Zelenka and G. Gardner, "Interference Patterns Generated by a Plane-Parallel Plate". *Applied Optics,* **32** (13): 2285-2291, 1993.

Heinzelmann, H., E. Meyer, H. Rudin and H.-J. Guntherrodt, "Scanning Tunnelling Microscopy and Related Methods". R. J. Behm, N. Garcia and H. Rohrer (Ed.), NATO ASI Series Vol. 184, Kluwer Academic, Dordrecht. p. 449, 1990.

Heinzelmann, H. and D.W. Pohl, "Sacnning Near-Field Optical Microscopy". *Applied Physics A,* **59**: 89-101, 1994.

Hill, K. O., Y. Fujii, D. C. Johnson and B. S. Kawasaki, "Photosensitivity in Optical Fibre Waveguides:Application to Reflection Filter Fabrication". *Applied Physics Letters,* **32**: 647-649, 1978.

Hill, K. O., B. Malo, F. Bilodeau and D. C. Johnson, "Photosensitivity in Optical Fibers [Review]". *Annual Review of Materials Science,* **23**: 125-157, 1993a.

Hill, K. O., B. Malo, F. Bilodeau, D. C. Johnson and J. Albert, "Bragg Gratings Fabricated in Monomode Photosensitive Optical Fiber by UV Exposure through a Phase Mask". *Applied Physics Letters,* **62** (10): 1035-1037, 1993b.

Hill, K. O. and G. Meltz, "Fiber Bragg Grating Technology Fundamentals and Overview". *Journal of Lightwave Technology,* **15** (8): 1263 - 1276, 1997.

Hill, P. C., G. R. Atkins, J. Canning, G. C. Cox and M. G. Sceats, "Writing and Visualization of Low-Threshold Type II Bragg Gratings in Stressed Optical Fibers". *Applied Optics,* **34** (33): 7689-7694, 1995.

Hinton, K., "Dispersion Compensation Using Apodized Bragg Fiber Gratings in Transmission". *Journal of Lightwave Technology,* **16** (12): 2336-2346, 1998.

Holzwarth, G., D. B. Hill and E. B. McLaughlin, "Polarization-Modulated Differential Interference Contrast Microscopy with a Variable Retarder". *Applied Optics,* **39** (34): 6268-6294, 2000.

Hui, R., J. Thomas, C. Allen, B. Fu and S. Gao, "Low-Coherence WDM Reflectometry for Accurate Fiber Monitoring". *IEEE Photonics Technology Letters,* **15** (1): 96-98, 2003.

Hunter, A. M. and P. W. Schreiber, "Mach-Zehnder Data Reduction Method for Refractively Inhomogeneous Test Objects". *Applied Optics,* **14** (3): 634-639, 1975.

Huntington, S. T., "Advances in Photonic Device Characterisation Using Scanning Probe Microscopy". Ph.D. Thesis., School of Physics, University of Melbourne, Australia, 1998.

Huntington, S. T., P. Mulvaney, A. Roberts, K. A. Nugent and M. Bazylenko, "Atomic Force Microscopy for the Determination of Refractive Index Profiles of Optical Fibres and Waveguides: A Quantitative Study". *Journal of Applied Physics,* **82** (6): 2730-2734, 1997.

Huntington, S. T., K. A. Nugent, A. Roberts, P. Mulvaney and K. M. Lo, "Field Characterization of a D-Shaped Optical Fiber Using Scanning Near-Field Optical Microscopy". *Journal of Applied Physics,* **82** (2): 510-513, 1997.

Kalal, K.A. Nugent, "Abel Transform using fast Fourier Transforms", *Applied Optics* **27**, 1356-1359, 1988

Ingemar, E. P., J. Skaar, B. E. Sahlgren, R. A. H. Stubbe and A. T. Friberg, "Characterization of Fiber Bragg Gratings by Use of Optical Coherence-Domain Reflectometry". *Journal of Lightwave Technology,* **17** (11): 2371-2378, 1999.

Inniss, D., Q. Zhang, A. M. Vengsarkar, W. A. Reed, S. G. Kosinski and P. J. Lemaire, "Atomic Force Microscopy Study of UV-Induced Anisotropy in Hydrogen-Loaded Germanosilicate Fibers". *Applied Physics Letters,* **65** (12): 1528 - 1630, 1994.

Inoue, E., "Ultrathin Optical Sectioning and Dynamic Volume Investigation with Conventional Light Microscopy". In *Three-Dimensional Confocal Microscopy: Volume Investigation of Biological Systems*, J. Stevens, L. Mills and J. Trogadis (Ed.), Academic Press, San Diego. 397-419, 1994.

Inoue, S. and K. R. Spring, *Video Microscopy: the Fundamentals*. 2nd Edition, Plenum, New York, 1997.

Johlen, D., F. Knappe, H. Renner and E. Brinkmeyer, "UV-Induced Absorption Scatering and Transition Losses in UV Side-Written Fibers". *Optical Fiber Communications* San Diego, California, USA, paper ThD1, 1999.

Kahl, G. D. and D. C. Mylin, "Refractive Deviation Errors of Interferograms". *Journal of the Optical Society of America A,* **55** (4): 364-372, 1965.

Kashyap R, "Photosensitive Optical Fibers: Devices and Applications, *Optical Fiber Technology* 1: 17-34, 1994.

Kashyap, R., *Fiber Bragg Gratings*. Academic Press, San Diego, London, ch.3, 1999.

Kashyap, R., J. R. Armitage, R. W. Wyatt, S. T. Davey and D. L. Williams, "All-Fibre Narrow-Band Reflection Gratings at 1500 nm". *Electronics Letters,* **26** (12): 730-731, 1990.

Keiser, G., *Optical Fiber Communications*. Second Edition, McGraw-Hill, 1991.

Keller, E. H., "Objective Lenses for Confocal Microscopy". In *Handbook of Biological Confocal Microscopy*, 2nd Edition, J. B. Pawley (Ed.), Plenum Press, New York. 111-126, 1995.

Kemao Q., S. Fangjun and W. Xiaoping, "Determination of the best phase step of the Carré algorithm in phase shifting interferometry" *Measurement Science and Technology,* **11**: 1220-1223, 2000.

Kersey, A. D., M. A. Davis, H. J. Patrick, M. LeBlanc, K. P. Koo, C. G. Askins, M. A. Putnam and E. J. Friebele, "Fiber Gratings Sensors". *Journal of Lightwave Technology,* **15** (8): 1442 - 1463, 1997.

Kherbouche, F. and B. Poumellec, "UV Induced Stress Field During Bragg Grating Inscription in Optical Fibers". *Journal of Optics A: Pure and Applied Optics,* **3** (6): 429-439, 2001.

Kim, B. H., Y. Park, T. J. Ahn, D. Y. Kim, B. H. Lee, Y. Chung, U. C. Paek and W. T. Han, "Residual Stress Relaxation in the Core of Optical Fiber by CO_2 Laser Radiation". *Optics Letters,* **26** (21): 1657 - 1659, 2001.

Kogelnik, H. and C. V. Shank, " Coupled-Wave Theory of Distributed Feedback Lasers" *Journal of Applied Physics,* **43** (5): 2327-2335, 1972.

Koerster, C. J., "Optimum Half-Shade Angle in Polarizing Instrument". *Journal of the Optical Society of America,* **49** (6): 556-559, 1959.

Kokubun, Y. and K. Iga, "Precise Measurement of the Refractive Index Profile of Optical Fibers by a Nondestructive Interference Method". *Trans. IECE Japan.,* **E60**: 702, 1977.

Krug, P. A., J. Canning and D. Y. Stepanov, "Gratings for WDM Systems - Review of Applications and Critical Measurements", *NIST Digest Symposium on Optical Fiber Measurements (OFM'98)*, Boulder, Colorado, USA: 143-148, 1998.

Krug, P. A., B. J. Eggleton, P. Coll and K. O. Hill, "Growth of Holographically Written Optical Fibre Bragg Gratings". *Eighteenth Australian Conference on Optical Fibre Technology*, Institute of Radio and Electrics Engineers, Edgecliff, Australia, 59-62, 1993.

Krug, P. A., R. Stolte and R. Ulrich, "Measurement of Index Modulation Along an Optical Fiber Bragg Grating". *Optics Letters,* **20** (17): 1767-1769, 1995.

Laakkonnen, P., M. Kuittinen and J. Turunen, "Coated Phase Masks for Proximity Printing of Bragg Gratings". *Optics Communications,* **192**: 153 - 159, 2001.

Lambelet, P., P. Y. Fonjallaz, H. G. Limberger, R. P. Salathe, C. Zimmer and H. H. Gilgen, "Bragg Grating Characterization by Optical Low-Coherence Reflectometry". *IEEE Photonics Technology Letters,* **5**: 565-567, 1993.

Latimer, P., "Talbot Plane Patterns: Grating Images or Interference Effects?" *Applied Optics,* **32** (7): 1078-1083, 1993.

Latimer, P., "Talbot Effect and Cornu's Spiral". *Applied Optics,* **33** (22): 4983-4987, 1994.

Lemaire, P. J., G. R. Atkins, V. Mizrahi and W. A. Reed, "High Presure H_2 Loading as a Technique for Achieving Ultrahigh UV Photosensiticity and Thermal Sensitivity in GeO_2 Doped Optical Fibres". *Electronics Letters,* **29**: 1191-1193, 1993.

Li, X., L. Ge, Y. Ishikawa and G. D. Peng,*Post-Seismic Structural Integrity Monitoring System Based on Optical Fibre and GPS Sensors.* [Online, Internet]. Eos Transactions, American Geophysical Union, West Pacific Geophysics Meeting, Supplement Available: http:www.agu.org/meetings/wp02-pdf/wp02-SE31A.pdf, Accessed 10 March 2003.

Liaw, S. K. and S. Chi, "Gain-Flattened Optical Limiting Amplifier Modules for Wavelength Division Multiplexing Transmission". *Fiber & Integrated Optics,* **18** (2): 69-77, 1999.

Linares, J. and E. M. Lopez-Lago, C. Prieto, X., "Interferometric Characterization Method of Lateral Ion Exchange for Refractive Waveguide Elements". *Pure and Applied Optics,* **5**: 919-928, 1996.

Lines, M. E., "Scattering Losses in Optic Fiber Materials. I. A New Parametrization". *Journal of Applied Physics,* **55** (11): 4052-4057, 1984.

Liu, Y., J. A. R. Williams, L. Zhang and I. Bennion, "Abnormal Spectral Evolution of Fiber Bragg Gratings in Hydrogated Fibers". *Optics Letters,* **27** (8): 586-588, 2002.

Loh, W. H., F. Q. Zhou and J. J. Pan, "Novel Designs for Sampled Grating-Based Multiplexers-Demultiplexers". *Optics Letters,* **24** (21): 1457-1459, 1999.

Luc, B. J., Single Mode Fiber Optics: Principles and Applications. Marcel Dekker, New York, 1990.

Mabrouk, M. and H. F. El-Bawab, "Refractive Index Profile of GRIN Optical Fibre Considering the Area under the Interference Fringe Shift: I. The Matching Case". *Pure and Applied Optics,* **6**: 247-256, 1997.

MacChesney, J. B., "Working Knowledge: Optical Fibers". *Scientific American*: 96, 1997.

Malo, B., F. Bilodeau, J. Albert, D. C. Johnson, K. O. Hill, Y. Hibino and M. Abe, "Photosensitivity in Optical Fiber and Silica on Substrate Waveguides". *SPIE,* **2024**: 46-54, 1993.

Malo, B., D. C. Johnson, F. Bilodeau, J. Albert and K. O. Hill, "Single-Excimer-Pulse Writing of Fiber Gratings by Use of a Zero-Order Nulled Phase Mask - Grating Spectral Response and Visualization of Index Perturbations". *Optics Letters,* **18** (15): 1277-1279, 1993.

Malo, B., K.O. Hill, F. Bilodeau, D.C. Johnson and J. Albert, "Point-by Point Fabrication of Micro-Bragg Gratings in Photosensitive Fibre Using Single Excimer Pulse Refractive Index Modification Techniques", *Electronics Letters*, 29(18): 1668-1669, 1993.

Marcuse, D., *Principle of Optical Fiber Measurements*. Academic Press, New York, USA, Chapter 1, 1981.

Marcuse, D., *Theory of Dielectric Optical Waveguides*. Academic, New York, 1991.

Marhic, M. E., P. S. Ho and N. Epstein, "Nondestructive Refractive Index Profile Measurements of Cladd Optical Fibers". *Applied Physics Letters,* **26** (10): 574-575, 1975.

Meltz, G., W. W. Morey and W. H. Glenn, "Formation of Bragg Gratings in Optical Fibers by a Transverse Holographic Method". *Optics Letters,* **14** (15): 823-825, 1989.

Meyers, R. A., Ed. *Optical Fiber Communications*, Encyclopaedia of Physical Science and Technology, 1992.

Mihailov, S. J. and M. C. Gower, "Periodic Cladding Surface Structures Induced when Recording Fiber Bragg Reflectors with a Single Pulse from a KrF Excimer Laser". *Applied Physics Letters,* **65** (21): 2639 - 2641, 1994a.

Mihailov, S. J. and M. C. Gower, "Recording of Efficient High-Order Bragg reflectors in Optical Fibres by Mask Image Projection and Single Pulse Exposure with an Excimer Laser". *Electronics Letters,* **30**: 707-709, 1994b.

Mills, J. D., C. W. J. Hillman, B. H. Blott and W. S. Brocklesby, "Imaging of Free-Space Interference Patterns Used to Manufacture Fiber Bragg Gratings". *Applied Optics,* **39** (33): 6128-6135, 2000.

Mills, J. D., C. W. J. Hillman, W. S. Brocklesby and B. H. Blott, "Evanescent Field Imaging of an Optical Fiber Bragg Grating". *Applied Physics Letters,* **75** (26): 4058-4060, 1999.

Minski, M. "Microscopy Apparatus". U.S. Patent:3013467. 1957

Minski, M., "Memoir on Inventing the Confocal Scanning Microscope". *Scanning,* **10** (4): 128-138, 1988.

Morey, W. W., G. A. Ball and G. Meltz, "Photoinduced Bragg Gratings in Optical Fibers". *Optical Photonic News,* **5**: 8-14, 1994.

Morey, W. W., G. Meltz and W. H. Glenn, "Fibre Bragg Grating Sensors". *Proceedings of SPIE - The International Society for Optical Engineering,* **1169**: 98 - 100, 1989.

Morey, W. W., G. Meltz and W. H. Glenn, "Holographically Generated Gratings in Optical Fibres". *Optics & Photonics News,* **1** (7): 8-14, 1994.

Nellen, P. M., P. Mauron, A. Frank, U. Sennhauser, K. Bohnert, P. Pequignot, P. Bodor and H. Brandle, "Reliability of Fiber Bragg Grating Sensors for Downhole Applications". *Sensors and Actuators A,* **103**: 364 - 376, 2003.

Nomarski, G. "Interferometre a Polarisation". Brevet d'Invention Francais. No. 1,059,123 (see also US Patent No. 2,924,142 in 1960). 1952

Nomarski, G., "Microinterferometre Differential a Ondes Polarisees". *J. Phys. Radium,* **16** (9s), 1955.

Norman, H. F. and Y. Matt, "Two-Dimensional Index Profiling of Fibers and Waveguides". *Applied Optics,* **38** (33): 6836-6844, 1999.

Nugent, K. A., "A Phase Odyssey". *Physics Today,* **54** (8): 27 - 32, 2001.

Othonos, A. and K. Kalli, Bragg Gratings: Fundamentals and Applications in Telecommunications and Sensing. Artech House Inc., London, p.95 - 99, 1999a.

Othonos, A. and K. Kalli, Fiber Bragg Gratings: Fundamentals and Applications in Telecommunications and Sensing. Artech House Optoelectronics Library, London, 1999b.

Othonos, A., K. S. Lee and R. M. Measures, "Superimposed Multiple Bragg Gratings". *Electronics Letters,* **30**: 1972-1973, 1994.

Paganin, D., "Studies in Phase Retrieval". PhD Thesis, University of Melbourne, Melbourne, Australia, 1999.

Pastor, D., J. Capmany, D. Ortega, V. Tatay and J. Marti, "Design of Apodized Linearly Chirped Fiber Gratings for Dispersion Compensation". *Journal of Lightwave Technology,* **14** (11): 2581-2588, 1996.

Patorski, K., "The Self Imaging Phenomenon and its Applications". In *Progress in Optics*, E. Wolf (Ed.), XXVII, Amsterdam: North Holland Pub. Co., Amsterdam. 1 - 108, 1989.

Perez, I, H-L. Cui and E. Udd, "Acoustic Emission Detection using Fiber Bragg Gratings" In *Proceedings of the SPIE*, 4328. 209-216, 2001.

Petermann, I., S. Helmfrid and A. T. Friberg, "Limitations of the Interferometric Side Diffraction Technique for Fibre Bragg Grating Characterization". *Optics Communications,* **201** (4 - 6): 301 - 308, 2002.

Piston, D. W., "Choosing Objective Lenses: The importance of Numerical Aperture and Magnification in Digital Optical Microscopy". *Biological Bulletin,* **195** (1): 1-4, 1998.

Pluta, M., "Interference Microscopy of Polymer Fibres". *Journal of Microscopy,* **96** (3): 309-332, 1972.

Pluta, M., "Variable Wavelength Interferometry. I. Fringe-Field Method for Transmitted Light". *Optica Applicata,* **15** (4): 375-393, 1985.

Pluta, M., "Variable Wavelength Interferometry. VI. Some Useful Modifications of the VAWI - 2 Technique". *Optica Applicata,* **17** (2): 141-151, 1987a.

Pluta, M., "Variable Wavelength Microinterferometry of Sections, Layers, Thin Films and Other Like Objects". *Journal of Microscopy,* **145** (2): 191-206, 1987b.

Pluta, M., "Variable Wavelength Interferometry of Birefringent Retarders". *Optical Lasers Technology,* **20** (2): 81-88, 1988.

Pluta, M., "Advanced Light Microscopy: Specialized Methods". In *Advanced Light Microscopy: Specialized Methods*, M. Pluta (Ed.), 2, Elsevier, Amsterdam, 1989.

Pluta, M., "Quasi-Object-Adapted Variable-Wavelength Double-Refracting Microscope Interferometry". *Optical Engineering,* **31** (3), 1992.

Pluta, M., *Manual of Automatic Computer-Aided Microinterferometer.* Institute of Applied Optics, Warsaw, 1996.

Pohl, D. W., W. Denk and M. Lanz, "Optical Stethoscopy: Imaging Recording with Resolution $\lambda/20$". *Applied Physics Letters,* **44**: 651-653, 1984.

Poladian, L., "Resonance Mode Expansions and Exact Solutions for Nonuniform Gratings". *Physical Review E,* **54**: 2963-2975, 1996.

Poladian, L., "Group-Delay Reconstruction for Fiber Bragg Gratings in Reflection and Transmission". *Optics Letters,* **22** (20): 1571-1573, 1997.

Poladian, L., "Simple Grating Synthesis Algorithm". *Optics Letters,* **25(11)**: 787-789, 2000.

Poumellec, B., P. Guenot, P. Riant, P. Sansonetti, P. Niay, P. Bernage and J. F. Bayon, "UV Induced Densification During Bragg Grating Inscription in Ge:SiO_2 Preforms". *Optical Materials,* **4**: 441 - 449, 1995b.

Poumellec, B., P. Niay, M. Douay and J. F. Bayon, "The UV-Induced Refractive Index Grating in Ge:SiO_2 Preforms: Additional CW Experiments and the Macroscopic Origin of the Change in Index". *Journal of Physics D: Applied Physics,* **29**: 1842 - 1856, 1996.

Poumellec, I., P. Riant, P. Niay, P. Bernage and J. F. Bayon, "UV Induced Densification During Bragg Grating Inscription in Ge:SiO_2 Preforms: Interferometric Microscopy Investigations". *Optical Materials,* **4**: 404 - 409, 1995.

Presby, H. M., R. D. Standley, J. B. MacChesney and P. B. O'Connor, "Material Structure of Germanium-Doped Optical Fibers and Preforms". *Bell Systems Technical Journal,* **54** (10): 1681-1692, 1975.

Preza, C., "Phase Estimation Using Rotational-Diversity Phase Estimation for Differential-Interference-Contrast Microscopy". Doctor of Science Dissertation, Sever Institute of Washington University, Saint Louis, Missouri, USA, 2000a.

Preza, C., "Rotational-Diversity Phase Estimation from Differential-Interference-Contrast Microscopy Images". *Journal of the Optical Society of America A-Optics \& Image Science,* **17** (3): 415-424, 2000b.

Preza, C., D. L. Snyder and J. A. Conchello, "Imaging Models for Three-Dimensional Transmitted-Light DIC Microscopy". In *Proceedings of the ISET/SPIE Symposium on Electronic Imaging, Science and Technology*, C. J. Cogswell, G. S. Kino and T. Wilson (Ed.), 2655. 245-257, 1996.

Preza, C., D. L. Snyder and J. A. Conchello, "Theoretical Development and Experimental Evaluation of Imaging Models for Differential-Interference-Contrast Microscopy". *Journal of the Optical Society of America A Optics \& Image Science,* **16** (9): 2185-2199, 1999.

Prohaska, J. D., E. Snitzer and J. T. Winthorp, "Theoretical Description of Fiber Bragg Reflectors Prepared by Fresnel Diffraction Images". *Applied Optics,* **33** (18): 3896-3900, 1994.

Rabin, M. W., W. C. Swann and S. L. Gilbert, "Interleaved, Sampled Fiber Bragg Gratings for Use in Hybrid Wavelength References". *Applied Optics,* **41** (34): 7193-7196, 2002.

Raine, K. W., "A Microscope for Measuring Axial Stress Profiles with High Spatial Resolution and Low Noise". *Proceedings of the Fourth Optical Fiber Measurement Conference*, National Physical Laboratory, Teddington, UK, 269-272, 1997.

Raine, K. W., J. G. N. Baines and D. E. Putland, "Refractive Index Profiling- State of the Art". *Journal of Lightwave Technology,* **7** (8): 1162-1169, 1989.

Raine, K. W., R. Feced, E. Kanellopoulos and V. A. Handerek, "to be found". *Proceedings of the Fourth Optical Fiber Measurement Conference*, National Physical Laboratory, Teddington, UK, 200, 1997.

Raine, K. W., R. Feced, S. E. Kanellopoulos and V. A. Handerek, "Measurement of Axial Stress at High Spatial Resolution in Ultravioloet-Exposed Fibers". *Applied Optics,* **38** (7): 1086-1095, 1999.

Rao, Y. J., "In-Fibre Bragg Grating Sensors [Review]". *Measurement Science & Technology,* **8** (4): 355-375, 1997.

Rao, Y. J., "Recent Progress in Applications of In-Fibre Bragg Grating Sensors". *Optics & Lasers in Engineering,* **31** (4): 297-324, 1999.

Rayleigh, L., "On The Manufacture and Theory of Diffraction Grating". *Philosophical Magazine,* **11**: 196-205, 1881b.

Renner, H., "Effective-Index Increase, Form Birefringence and Transition Losses in UV-Side-Illuminated Photosensitive Fibers". *Optics Express,* **9** (11): 546 - 560, 2001.

Renner, H., D. Johlen and E. Brinkmeyer, "Modal Field Deformation and Transition Losses in UV-Side Written Optical Fibers". *Applied Optics,* **39** (6): 933 - 940, 2000.

Rhodes, S. K., A. Barty, A. Roberts and K. A. Nugent, "Sub-Wavelength Characterisation of Optical Focal Structures". *Optics Communications,* **145** (1): 9-14, 1998.

Riant, I., "Fiber Bragg Gratings for Optical Telecommunications". *Comptes Rendus Physique,* **4**: 41-49, 2003.

Richards B. and E. Wolf, "Electromagnetic Diffraction in Optical Systems II. Structure of the Image Field in an Aplanatic System", *Proceedings of the Royal Society*, **253**, 358 – 379, 1959.

Rizvi, N. H. and M. C. Gower, "Production of Submicron Period Bragg Gratings in Optical Fibers using Wavefront Division With a Biprism and an Excimer Laser Source". *Applied Physics Letters,* **67** (6): 739-741, 1995.

Roberts, A., E. Ampem-Lassen, A. Barty, K. A. Nugent, G. W. Baxter, N. M. Dragomir and S. T. Huntington, "Refractive-Index Profiling of Optical Fibers with Axial Symmetry by Use of Quantitative Phase Microscopy". *Optics Letters,* **27** (23): 2061-2063, 2002.

Roberts, A., K. Thorn, M. L. Michna, N. M. Dragomir, P. M. Farrell and G. W. Baxter, "Determination of Bending-Induced Strain Optical Fibers by Use of Quantitative Phase Imaging". *Optics Letters,* **27** (2): 86-88, 2002.

Rose, A. H., "Devitrification in Annealed Optical Fiber". *Journal of Lightwave Technology,* **15** (5): 808 - 815, 1997.

Rose, A. H., C.-M. Wand and S. D. Dyer, "Fiber Bragg Grating Metrology Round Robin: Telecom Group". *Symposium on Optical Fiber Measurements (SOFM)*, National Institute of Standards and Technology, Boulder, Colorado, USA, 161-164, 2000.

Roussel, N., S. Magne, C. Martinez and P. Ferdinand, "Measurement of Index Modulation Along Fiber Bragg Gratings by Side Scattering and Local Heating Techniques". *Optical Fiber Technology,* **5**: 119-132, 1999.

Roy, P., F. Brechet, P. Leproux, J. Marcou and D. Pagnoux, "Characterization of the Guiding Properties of a Bragg Type Photonic-Band-Gap Fiber". *Symposium on Optical Fiber Measurements*, NIST, OSA, Boulder, Colorado, USA, 7-10, 2000.

Salik, E., "Photosensitivity of Germanium-doped Optical Fibres and its Enhancement by Strain". PhD, University of Southern California, Los Angeles, 2001.

Sceats, M. G., G. R. Atkins and S. B. Poole, "Photolytic Index Changes in Optical Fibers". *Annual Review of Material Science,* **23**: 381 - 410, 1993.

Scherer, G. W., "Stress Induced Profile Distortion in Optical Waveguides". *Applied Optics,* **19** (12): 200-2006, 1980.

Schulz, W. L., J. P. Conte, E. Udd and J. M. Seim, "Seismic Damage Identification using Long Gage Fiber Bragg Grating Sensors". *Second Workshop on Advanced Technologies in Urban Earthquake Disaster Mitigation* Kyoto, Japan, Article available on line at: http://www.bluerr.com/publications, July 2000.

Sheppard, C.J.R., and H.J. Matthews, "Imaging in High-Aperture Optical Systems", *Journal of the Optical Society of America* A, **4**, 1354-1360, 1987.

Shu, X., Y. Liu, D. Zhao, B. Gwandu, F. Floreani, L. Zhang and I. Bennion, "Dependence of Temperature and Strain Coefficients on Fiber Grating and its Application to Simultaneous Temperature and Strain Measurement". *Optics Letters,* **27** (9): 701-703, 2002.

Sidiroglou, F., S. A. Wade, N. Dragomir, M., G. W. Baxter and S. F. Collins, "Effects of High Temperature Heat treatment on Nd^{3+}-Doped Optical Fibers for Use in Fluorescence Intensity Ratio Based Temperature Sensing". *Review of Scientific Instruments*: **74** (7): 3524 - 3530, 2003.

Sidiroglou, F., S. A. Wade, N. Dragomir, M., S. F. Collins and G. W. Baxter, "Potential for Very High Temperature Sensing using Neodymium and Ytterbium Doped Silica Fibres". *The Inaugural Australasian Workshop onStructural Health Monitoring* Monash University, Melbourne, Australia, 2002.

Skaar, J., "Synthesis and Characterization of Fiber Bragg Gratings". Ph D, Institute of Physical Electronics, Stockholm, Norway, 2000.

Smith, K. C. A., "Charles Oatley: Pioneer of Scanning Electron Microscopy". *Annual Conference of the Electron Microscope Group of the Institute of Physics: EMAG '97*, Institute of Physics, University of Cambridge, UK, 1997.

Snyder, A. W., "Asymptotic Expressions for Eigenfunctions and Eigenvalues of a Dielectric or Optical Waveguide". *IEEE Transactions on Microwave Theory,* **MTT - 17**: 1130 - 1138, 1969.

Snyder, A. W. and J. D. Love, *Optical Waveguide Theory*. Chapman and Hall, London, 1983.

Sochacka, M., "Optical Fibers Profiling by Phase-Stepping Transverse Interferometry". *Journal of Lightwave Technology,* **12** (1): 19-23, 1994.

Sochacki, J., "Accurate Reconstruction of Refractive-Index Profile of Fibers and Preform Rods from Transverse Interferometric Data". *Applied Optics,* **25** (19): 3473-3482, 1986.

Sokkar, T. Z. N., M. A. Mabrouk and H. F. El-Bawab, "Refractive Index Profile of GRIN Optical Fibre Considering the Area under the Interference Fringe Shift: II. The Mismatching Case". *Journal of Optics A: Pure and Applied Optics,* **1**: 64-72, 1999.

Spagnolo, S., G. and D. Ambrosini, "Talbot Effect Application: Measurement of Distance with a Fourier Transform Method". *Measurement Science and Technology,* **11**: 77-82, 2000.

Starodumov, A. N., L. A. Zenteno and B. S. Mendoza, "Fibre as Phase-Object Approximation in Light Scattering Experiments". *Journal of Modern Optics,* **45** (8): 1629 - 1635, 1998.

Stevenson, A. J., D. D. Garchev , N. M. Dragomir, B. R. Walter, G. W. Baxter and P. M. Farrell "Effects of Differential Thermal Dopant Diffusion on Splice Loss Arising inMode Mismatch between Dissimilar FIbres". *25th Australian Conference on Optical Fibre Technology*, Information, Telecommunications & Electronics Engineering Society, Canberra, Australia, 71-73, 2000.

Stewart, W. J., "A New Technique for Measuring the Refractive Index Profiles of Graded Optical Fibres". *Technical Digest - IOOC (IECE)* Tokyo, 395-398, 1977.

Stone, J. and H. E. Earl, "Optical Fiber Refractometry by Interference Microscopy: A Simplified Method". *Applied Optics,* **17** (22): 3647-3652, 1978.

Sun, T., Z. Y. Zhang and K. T. V. Gratan, "Erbium/Ytterbium Fluorescence Based Fiber Optic Temperature Sensor System". *Review of Scientific Instruments,* **71** (11): 4017-4022, 2000.

Sun, T., Z. Y. Zhang, K. T. V. Grattan, A. W. Palmer and B. T. Meggitt, "Ytterbium-Based Fluorescence Decay Time Fiber Optic Temperature Sensors Systems". *Review of Scientific Instruments,* **69** (12): 4179 - 4185, 1998.

Talbot, H. F., "Facts Relating to Optical Science. No. IV". The London and Edinburgh Philosophical Magazine and Journal of Science (Third Series), **9**: 401-407, 1836.

Teague, M. R., "Deterministic Phase Retrieval: A Green's Function Solution". *Journal of the Optical Society of America A-Optics & Image Science,* **76**: 1434 - 1441, 1983.

Tsai, D. P., Y. L. Chung and A. Othonos, "Study of Optical Fiber Structure Using Atomic Force Microscopy and Scanning Near-Field Optical Microscopy". *Proceedings of SPIE - The International Society for Optical Engineering,* **2695**: 204-210, 1996.

Van Munster, E. B., L. J. Vanvliet and J. A. Aten, "Reconstruction of Optical Pathlength Distributions from Images Obtained by a Wide-Field Differential Interference Contrast Microscope". *Journal of Microscopy (Oxford),* **188** (Part 2): 149-157, 1997.

Wade, S., S. F. Collins and G. W. Baxter, "The Fluorescence Intensity Ratio Technique for Optical Fiber Temperature Sensing". *Journal of Applied Physics*: submitted, 2003.

Wade, S. A., S. F. Collins, G. W. Baxter, T. Sun, Z. Y. Zhang, K. T. V. Gratan and G. Monnom, "The Fluorescence Intensity Ratio Technique for Optical Fiber Temperature Sensing". *13th International Conference on Optical Fibre Sensors* Kyongju, Korea, 200-203, 1999.

Wade, S. A., N. Dragomir, M., K. T. V. Gratan, P. M. Farrell and G. W. Baxter, "Analysis of Physical Changes to Optical Fibre Resulting from Annealing Processes". *Sensors and their Applications XI*, Institute of Physics, Bristol, UK, City University, London, 347 - 353, 2001.

Wagreich, R. B., W. A. Atia, H. Singh and J. S. Sirks, "Effects of Diametric Load on Fibre Bragg Gratings Fabricated in Low Birefringence Fibre". *Electronics Letters,* **32** (13): 1223 - 1226, 1996.

Wang, H., C. Zhou, S. Zhao, P. Xi and L. Liu, "The Temporal Fresnel Diffractive Field of a Grating Illuminated by an Ultrashort Pulsed-Laser Beam". *Journal of Optics A: Pure and Applied Optics,* **3** (3): 159-163, 2001.

Wei, C. Y., C. C. Ye, S. W. James, P. E. Irving and R. P. Tatam, "AFM Observation of Surface Topography of Fibre Bragg Gratings Fabricated in Germanium-Boron Doped Fibres and Hydrogen -Loaded Fibres". *Optical Materials,* **20**: 283 -294, 2002a.

Wei, C. Y., C. C. Ye, S. W. James, R. P. Tatam and P. E. Irving, "The Influence of Hydrogen Loading and the Fabrication Process on the Mechanical Strength of Optical Fibre Bragg Gratings". *Optical Materials,* **20**: 241 - 251, 2002b.

White, K. I., "Practical Application of the Refractive Near Field Technique for the Measurement of Optical Fiber Refractive Index Profiles". *Optical and Quantum Electronics,* **11**: 185-196, 1979.

Williams, D. L., B. J. Ainslie, J. R. Armitage, R. Kashyap and R. J. Campbell, "Enhanced Photosensitivity in Germanium Doped Silica Fibers for Future Optical Networks". *ECOC'92*, Proceedings of the 18th European Conference on Optical Communications, 425 - 428, 1992.

Williams, D. L., S. T. Davey, R. Kashyap, J. R. Armitage and B. J. Ainslie, "Ultraviolet Absorption Studies on Photosensitive Germanosilicate Preforms and Fibers". *Applied Physics Letters,* **59**: 762 - 764, 1991.

Williamson, R.. L., L. J Brereton, and M. J. Miles "Are Artifacts in Scanning Near-Field Optical Microscopy Related to the Misuse of Shear Force?". *Ultramicroscopy,* **71**: 165 - 175, 1998.

Willsch, R., "Technical Trends, Potential Applications and Market Development in Optical Fibre Sensor Technology". In *Business Briefing: Global Optical Communications*, (Ed.). 110 - 117, 2001.

Wilson, T., "The Role of The Pinhole In Confocal Imaging Systems", J. B. Pawley, *The Handbook of Biological Confocal Microscopy*, WI, IMR Press: 99-114, 1989.

Wilson, T. and C. J. R. Sheppard, *Theory and Practice of Scanning Optical Microscopy*. Academic Press, London, UK, 1984.

Winthorp, J. T. and C. R. Worthington, "Theory of Fresnel Images. I. Plane Periodic Objects in Monochromatic Light". *Journal of the Optical of Society of America,* **55**: 373-381, 1965.

Wojcik, G., J. J. Mould, R. Ferguson, M. R. and K. K. Low, "Some Image Modeling Issues For I-Line, 5 X Phase Shifting Masks", T. A. Brunner, *Optical Laser Microlithography VII*, Proc SPIE, **2197**: 455-465, 1994.

Xie, W. X., M. Douay, P. Bernage, P. Niay, J. F. Bayon and T. Georges, "Second Order Diffraction Efficiency of Bragg Gratings Written within Germanosilicate Fibres". *Optics Communications,* **101** (1 - 2): 85 - 88, 1993.

Xie, W. X., P. Niay, P. Bernage, M. Douay, J. F. Bayon, T. Georges, M. Monerie and B. Poumellec, "Experimental Evidence of two Types of Photorefractive Effects Occuring During Photoinscription of Bragg Gratings within Germanosilicate Fibers". *Optics Communications,* **104** (1-3): 185 - 195, 1993.

Xiong, Z., G. D. Peng, B. Wu and P. L. Chu, "Effects of the Zeroth-Order Diffraction of a Phase Mask on Bragg Gratings". *Journal of Lightwave Technology,* **17** (11): 2361-2367, 1999.

Yeh, P., A. Yariv and E. Marom, "Theory of Bragg Fiber". *Journal of the Optical Society of America,* **68** (9): 1196-1201, 1978.

Young, M., "Calibration Technique for Refracted Near-Field Scanning of Optical Fibers". *Applied Optics,* **19** (15): 2479-2480, 1980.

Young, M., "Optical Fiber Index Profiles by the Refracted -Ray Method (Refracted Near Field Scanning)". *Applied Optics,* **20** (19): 3415-3422, 1981.

Zhang, Q., D. A. Brown, L. Reinhart and T. F. Morse, "Simple Prism-Based Scheme for Fabricating Bragg Gratings in Optical Fibres". *Optics Letters,* **19** (23): 2030-2032, 1994.

Zhang, Z. Y., K. T. V. Gratan and B. T. Meggitt, "Thulim-Based Fiber Optic Decay-Time Temperature Sensors: Characterization of High Temperature Performance". *Review of Scientific Instruments,* **71** (4): 1614-1620, 2000.

Zhang, Z. Y., K. T. V. Gratan, A. W. Palmer and B. T. Meggitt, "Spectral Characteristics and Effects of Heat Treatment on Intrinsic Nd-doped Fiber Thermometer Probes". *Review of Scientific Instruments,* **69** (1): 139-145, 1998.

Zhong, Q. and D. Innis, "Characterization of the Lightguiding Structure of Optical Fibers by Atomic Force Microscopy". *Journal of Lightwave Technology,* **12** (9): 1517-1523, 1995.

Zhu, Y. H., E. Simova, P. Berini and C. P. Grover, "A Comparison of Wavelength Dependent Polarization Dependent Loss Measurements in Fiber Gratings". *IEEE Transactions on Instrumentation & Measurement,* **49** (6): 1231-1239, 2000.